Timescales and Error Estimates in Dynamical Systems

Ferdinand Verhulst

Mathematisch Instituut, University of Utrecht, PO Box 80.010, 3508 TA Utrecht,
The Netherlands
(E-mail: `f.verhulst@uu.nl`)

Abstract. The method of multiple timescales is widely used in engineering and
mathematical physics. In this note we draw attention to the literature on the tech-
niques and comparison of various perturbation methods. The emphasis is on au-
tonomous ODEs and ODEs with periodic coefficients. We indicate where we can
obtain an advantage from the concept of timescales and we present examples from
bifurcation theory where the anticipation of timescales is not straightforward and
multiple timing is in danger of being deficient. The paper is tutorial but new results
are presented in section 6.
Keywords: .

1 Introduction

Many problems in physics and engineering can be formulated as a perturbation
problem, i.e. as a small perturbation of a problem that we know how to solve.
Usually a small, positive parameter ε plays a part in the formulation; we will
assume $0 \leq \varepsilon \ll 1$. We start with some examples to illustrate the concept of
timescales.

Example 1 *Consider the harmonic equation with a slight perturbation (detun-
ing) of the frequency 1:*

$$\ddot{x} + (1 + \varepsilon)x = 0.$$

It is easy to solve the perturbed equation, we find the general solution

$$x(t) = A\cos(\sqrt{1 + \varepsilon}t) + B\sin(\sqrt{1 + \varepsilon}t)$$

*with arbitrary constants A and B which are for instance determined by initial
conditions. Expanding with respect to ε in a Taylor series, we find*

$$\cos(\sqrt{1 + \varepsilon}t) = \cos t - \frac{\varepsilon t}{2}\sin t + \frac{\varepsilon^2 t}{8}\sin t - \frac{\varepsilon^2 t^2}{8}\cos t + \varepsilon^3 \dots$$

and for $\sin t$ *a similar expression. The exact solution is periodic with respect to* t, *but the Taylor expansion with respect to* ε *is not. In fact, the expansion contains terms that are unbounded with time, so-called* secular *terms. These secular terms assume different forms and are called time-like variables or* timescales. *In this elementary problem, the timescales* $t, \varepsilon t$ *and* $\varepsilon^2 t$ *play a part, at higher order more timescales appear.*

Example 2 *We know the damped harmonic oscillator*

$$\ddot{x} + \mu\dot{x} + x = 0, \ \mu > 0,$$

and its solutions with usually μ *rather small to avoid quenching the oscillation too quickly. Suppose now that we are considering a mechanical process where, for some reason, the damping slowly increases from (say)* $\mu = \varepsilon$ *to* $\mu = 2\varepsilon$. *For this oscillator, we propose the equation*

$$\ddot{x} + \varepsilon(2 - e^{-\varepsilon t})\dot{x} + x = 0.$$

Note that already in the equation a timescale, εt, *is present, but maybe the dynamics of this oscillator will produce more timescales. If* $t = 0$, *we have the damped oscillator given above for* $\mu = \varepsilon$; *if we let* t *tend to infinity, we have this oscillator with* $\mu = 2\varepsilon$. *What happens for the time in between? If* $\varepsilon = 0$, *the independent variable is time* t. *It is natural to assume that as the damping varies with* εt, *an approximation of the problem can be achieved by assuming that two* timescales, *play a part:* t *and* εt. *We will show how we will handle such a problem.*

The picture of timescales as in the examples above is not always so simple. Consider for instance an example of the classical Euler equation:

Example 3

$$t^2\ddot{x} - t\dot{x} + (1 + \varepsilon)x = 0.$$

The so-called Euler-index λ *is obtained by substituting* $x(t) = t^\lambda$. *This produces the index-equation*

$$\lambda^2 - 2\lambda + 1 + \varepsilon = 0,$$

with

$$\lambda = 1 \pm i\sqrt{\varepsilon}.$$

So, independent solutions are $t\cos(\sqrt{\varepsilon}\ln t)$ *and* $t\sin(\sqrt{\varepsilon}\ln t)$ *with timescales* t *and* $\sqrt{\varepsilon}\ln t$. *However, ignoring the exact solution, and putting* $\varepsilon = 0$ *in the equation, gives the index-equation*

$$\lambda^2 - 2\lambda + 1 = 0,$$

with double roots 1. *The independent solutions if* $\varepsilon = 0$ *are* t *and* $t\ln t$ *which have not much in common with the perturbed solutions.*
This is a so-called bifurcation problem for the index-equation. This equation has two coincident solutions that bifurcate to two different solutions by adding a small parameter. Usually, problems in applications contain parameters that at specific values produce bifurcation phenomena. As these correspond with qualitative changes in the solutions and also in the physical applications, bifurcation phenomena merit special interest.

The examples until now are all concerned with linear equations; in some cases we have found so-called 'natural timescales', but sometimes we have already in a linear problem unexpected phenomena. Examples 1 and 2 will be typical for the theory to be developed in the sequel.

2   The general formulation of perturbation problems

A rather general problem formulation is to consider ordinary differential equations (ODEs) that contain a small positive parameter ε as in

$$\dot{x} = f(t, x, \varepsilon), \ x \in \mathbb{R}^n, \tag{1}$$

depending to some order smoothly on x and t for $t_0 \leq t < \infty$ and ε for $0 \leq \varepsilon \leq \varepsilon_0$; the dot represents differentiation with respect to t. We assume we can Taylor-expand:

$$\dot{x} = f_0(t, x) + \varepsilon f_1(t, x) + \varepsilon^2 f_2(t, x) + \varepsilon^3 \ldots \tag{2}$$

For such a general problem, we usually cannot formulate explicit solutions of the equation in terms of elementary functions, but we assume that the equation can be solved, at least to some extent, if $\varepsilon = 0$. 'To some extent' may also mean that we are able to extract certain special solutions, equilibria or periodic, if $\varepsilon = 0$. By expanding in a neighbourhood of such a solution we can obtain so-called variational equations.

In our analysis we hope for the presence of certain typical timescales like $t, \varepsilon t, \varepsilon^2 t, \ldots$, which we called 'natural' in the Introduction, on which approximate solutions depend; in some problems we have similar choices for spatial variables. Contrasting with this approach of *anticipating timescales* is averaging, a normal form method, where no apriori assumption on the form of time-dependence is made. This contrasting approach also holds for the renormalization method. It will be clear that an apriori choice of timescales should be linked with apriori knowledge of the nature of the solutions.

The idea of anticipating timescales was introduced in Kiev by Krylov and Bogoliubov in 1935 [9]; the first application (as far as we are aware) was by Kuzmak in 1959 [10]. After 1960, the idea of multiple timescales was advocated and studied by Kevorkian [6], Cochran [4] and Nayfeh, see for instance [15]. The method, also called multiple timing, is intuitively clear and became very popular, especially in engineering.

The Kiev school of approximation theory for nonlinear ODEs was very influential so it is interesting to find out why they dropped the idea of multiple timing after the work of Kuzmak. When asked for a reason, Yu.A. Mitropolsky, a prominent member of the Kiev school, told me "because it is not a good method" [12]. This seems somewhat exaggerated as the validity of the method can be demonstrated in a great many cases. But it is true, as we shall see, that for a large number of important research problems, multiple timing can be misleading.

Apart from the literature cited above, introductions to the multiple timescale method can be found in [2], [15], [19] and [24]. A comparison of averaging and

multiple timing by a number of important examples can be found in [7]. There have appeared many papers on the approximation of solutions of ODEs, we can cite only a few of them.

The relation between multiple timing and the renormalization method was discussed in [2], [3] and [13], however on a formal level only. In [16], Perko established the equivalence of the averaging method and multiple timing for standard equations like

$$\dot{x} = \varepsilon f(t, x)$$

on intervals of time of order $1/\varepsilon$. This was a major step forward. See also the extensive discussions in [14] and [19].

Asymptotic equivalence of methods would imply that, considering a solution $x(t)$ of a differential equation, expressions $\bar{x}_1(t)$ and $\bar{x}_2(t)$ obtained by different methods, would both represent an approximation of $x(t)$ with error $\delta(\varepsilon) = o(1)$ as $\varepsilon \to 0$ on the same interval of time (for instance of size $1/\varepsilon$). Such results extend beyond the formal level.

Often, we will indicate that an approximation with error $\delta(\varepsilon)$ is valid on an interval of size $1/\varepsilon$. A more precise statement is that the error estimate is valid for $t_0 \leq \varepsilon t \leq t_0 + L$ with t_0, L constants independent of ε. It was shown in [16] that the approximations obtained by averaging and by multiple timing are equivalent to $O(\varepsilon)$ on intervals of time of order $1/\varepsilon$.

We will restrict ourselves to a discussion of ODEs. In [24] one can find a discussion and references of a number of PDE problems.

3   The basic idea for two timescales

As stated above, many small ε parameter problems are studied using timescales like $t, \varepsilon t, \varepsilon^2 t$ and in general $\varepsilon^n t$ with $n \in \mathbb{N}$. In the perturbation problem of eq. (2), the form of the solution for $\varepsilon = 0$ plays a part.

3.1   The variational equation

Ideally, we know the solution of the equation

$$\dot{x} = f_0(t, x)$$

explicitly, say $x(t)|_{\varepsilon=0} = \psi(t, c)$ with c a constant n-vector. We transform the solution of eq. (2) as follows. Put

$$x(t) = \psi(t, y),$$

and substitute into eq. (2) (this is Lagrange's method of variation of contants). We find:

$$\dot{x} = \frac{\partial \psi}{\partial t} + \frac{\partial \psi}{\partial y}\dot{y} = f_0(t, \psi(t, y)) + \varepsilon f_1(t, \psi(t, y)) + \varepsilon^2 \ldots$$

Assuming that we can invert the matrix $\partial \psi/\partial y$, we derive:

$$\dot{y} = \varepsilon \left(\frac{\partial \psi}{\partial y}\right)^{-1} f_1(t, \psi(t, y)) + \varepsilon^2 \ldots$$

This is the so-called variational equation in standard form.

In a number of problems we have less explicit knowledge of the solutions of the unperturbed problem. We may know an explicit solution which can be used to start a perturbation formulation. Another possibility is the presence of one or more integrals of motion of the unperturbed problem. These integrals can also be used as new variables for perturbation equations.

3.2   Two-timing

A simple but typical approach for two timescales runs as follows. Consider the variational equation in standard form

$$\dot{x} = \varepsilon f(t, x) \tag{3}$$

with $f(t, x)$ T-periodic in t, the initial value $x(0)$ is given. As we will see below, we can also start our multiple timing process directly for eq. (2) (direct two-timing). We will look for solutions of the form

$$x(t) = x_0(t, \tau) + \varepsilon x_1(t, \tau) + \varepsilon^2 \ldots \tag{4}$$

with $\tau = \varepsilon t$, the dots represent the higher order expansion terms. As the unknown functions $x_0, x_1, \ldots$ are supposed to depend on two variables, we have to transform the differential operator; we have to first order in ε:

$$\frac{d}{dt} = \frac{\partial}{\partial t} + \varepsilon \frac{\partial}{\partial \tau}.$$

Using this differential operator and the expansion we find

$$\frac{\partial x_0}{\partial t} + \varepsilon \frac{\partial x_0}{\partial \tau} + \varepsilon \frac{\partial x_1}{\partial t} + \varepsilon^2 \ldots = \varepsilon f(t, x_0(t, \tau) + \varepsilon x_1(t, \tau) + \varepsilon^2 \ldots)$$

Suppose we can Taylor-expand the function f to a certain order, collecting then the terms of order 1 and ε, we find the simple partial differential equations

$$\frac{\partial x_0}{\partial t} = 0,$$
$$\frac{\partial x_1}{\partial t} = -\frac{\partial x_0}{\partial \tau} + f(t, x_0).$$

The first equation produces

$$x_0(t, \tau) = A(\tau), A(0) = x(0),$$

with $A(\tau)$ still an unknown function; A will be determined at the next step. For x_1 we find by integration

$$x_1(t, \tau) = \int_0^t \left(-\frac{\partial A(\tau)}{\partial \tau} + f(s, A(\tau)) \right) ds + B(\tau).$$

The function $B(\tau)$ is unknown and has to satisfy $B(0) = 0$. If we are looking for bounded solutions of eq. (3), or even for periodic solutions, the integral

$$\int_0^t \left(-\frac{\partial A(\tau)}{\partial \tau} + f(s, A(\tau)) \right) ds$$

has to be bounded. This is called the *secularity condition*. We can achieve this by determining $A(\tau)$ such that

$$\frac{dA}{d\tau} = \frac{1}{T} \int_0^T f(s, A(\tau)) ds. \tag{5}$$

Assuming that $f(t, x)$ has a Fourier expansion is a natural condition as it means that the 'constant' term of the expansion vanishes. The determination of $A(\tau)$ implies that satisfying the secularity condition corresponds with averaging the function $f(t, x)$ while keeping x constant. This idea can be traced to the end of the 18th century, for instance in the writings of Lagrange (see [19]).

The condition (5) is exactly the condition for averaging. Starting with the standard form (3), and initial condition $x(0) = x_0$, the initial value problem

$$\tilde{x} = \varepsilon \frac{1}{T} \int_0^T f(t, \tilde{x}) dt, \ \tilde{x}(0) = x_0,$$

produces an approximation $x(t) = \tilde{x}(t) + O(\varepsilon)$ on intervals of time $O(1/\varepsilon)$. This establishes the equivalence of two-timing and averaging to first order in ε.

Note that both two-timing and averaging assume boundedness of the solutions resulting in the secularity condition. If the solutions are unbounded it makes no sense to apply a secularity condition.

3.3 Direct two-timing

The standard form eq. (3) was our starting point. In some cases, for instance for the perturbed harmonic equation:

$$\ddot{x} + x = \varepsilon f(t, x, \dot{x}),$$

it may be easier to transform the original equation using the differential quotients with respect to time. Assuming the presence of the timescales t and εt, we compute:

$$\frac{d}{dt} = \frac{\partial}{\partial t} + \varepsilon \frac{\partial}{\partial \tau}, \text{ and } \frac{d^2}{dt^2} = \frac{\partial^2}{\partial t^2} + 2\varepsilon \frac{\partial^2}{\partial t \partial \tau} + \varepsilon^2 \frac{\partial^2}{\partial \tau^2}. \tag{6}$$

Substitution into the equation produces to first order in ε:

$$(\frac{\partial^2}{\partial t^2} + 2\varepsilon \frac{\partial^2}{\partial t \partial \tau})(x_0 + \varepsilon x_1) + x_0 + \varepsilon x_1 = \varepsilon f(t, x_0 + \varepsilon x_1, (\frac{\partial}{\partial t} + \varepsilon \frac{\partial}{\partial \tau})(x_0 + \varepsilon x_1)) + \varepsilon^2 \dots.$$

Collecting equal powers of ε we find to zero order

$$\frac{\partial^2 x_0}{\partial t^2} + x_0 = 0,$$

with general solution

$$x_0(t, \tau) = A(\tau) \cos t + B(\tau) \sin t.$$

To first order in ε we find:

$$\frac{\partial^2 x_1}{\partial t^2} + x_1 = 2\left(\frac{dA}{d\tau} \sin t - \frac{dB}{d\tau} \cos t\right) + f(t, x_0, \frac{\partial x_0}{\partial t}).$$

We have to apply the secularity condition to this first order equation to determine $A(\tau)$ and $B(\tau)$.

We demonstrate this for example 2.

Example 4 *Consider again the problem of example 2:*

$$\ddot{x} + \varepsilon(2 - e^{-\varepsilon t})\dot{x} + x = 0.$$

Introducing $\tau = \varepsilon t$, the differential operators (6) and the expansion (4) into the equation we find to zero order

$$\frac{\partial^2 x_0}{\partial t^2} + x_0 = 0,$$

with general solution

$$x_0(t, \tau) = A(\tau) \cos t + B(\tau) \sin t.$$

The unknown functions $A(\tau), B(\tau)$ will be determined at next order of ε:

$$\frac{\partial^2 x_1}{\partial t^2} + 2\frac{\partial^2 x_0}{\partial t \partial \tau} + (2 - e^{-\tau})\frac{\partial x_0}{\partial t} + x_1 = 0.$$

Using the expression for x_0 we can write this as:

$$\frac{\partial^2 x_1}{\partial t^2} + x_1 = 2\left(\frac{dA}{d\tau} \sin t - \frac{dB}{d\tau} \cos t\right) + (2 - e^{-\tau})(A \sin t - B \cos t).$$

The solutions of the inhomogeneous harmonic equation produces unbounded (secular) terms unless

$$2\frac{dA}{d\tau} + (2 - e^{-\tau})A = 0, \ 2\frac{dB}{d\tau} + (2 - e^{-\tau})B = 0.$$

Solving the equations for A and B we find to first order for $x(t)$:

$$e^{-\tau - \frac{1}{2}e^{-\tau} + \frac{1}{2}}(A(0) \cos t + B(0) \sin t).$$

$A(0)$ and $B(0)$ are determined by the initial conditions. As expected, the damping factor increases.

It is interesting to compare the two-timing result with the approximation obtained by averaging; see [19], introductions can be found in [23] and [24]. Averaging produces in the solution the same damping factor, as expected. The result of Perko [16] implies that the two methods both yield an $O(\varepsilon)$ approximation, valid on an interval of time of size $1/\varepsilon$. So any difference must be beyond this interval or at higher order approximations.

4   Algebraic timescales for bifurcations

Analytic and numerical approximation theory gives us useful details, but one of the basic questions of engineering and mathematical physics is to obtain a global picture of the behaviour of the dynamical system studied; this is tied in with the study of qualitative changes when the parameters of the system pass certain critical values. Such changes are called bifurcations, they may entail stability changes, branching or vanishing of solutions, transitions from periodic solutions to tori, emergence of chaos and other phenomena. As we shall see, it is important in these problems to avoid making apriori assumptions on timescales.

In the analysis of bifurcations, approximation theory is used, combined with linearization and matrix calculations. A typical computation for an equation of the form $\dot{x} = f(x, t, \varepsilon)$ will be to identify an equilibrium or special solution $\psi(t)$ and study the behaviour of this solution as the parameters are changing; this leads to the calculation of eigenvalues, Lyapunov exponents and characteristic multipliers.

A typical example of a corresponding bifurcation diagram is displayed in fig. 1 describing bifurcations in a three degrees of freedom mechanical system with damping parameter b and self-excitation magnitude β. The curves in the b, β-diagram correspond with bifurcations as for example Hopf (H), Chenciner (CH), Neimark-Sacker (NS) etc. The system is studied in [1].
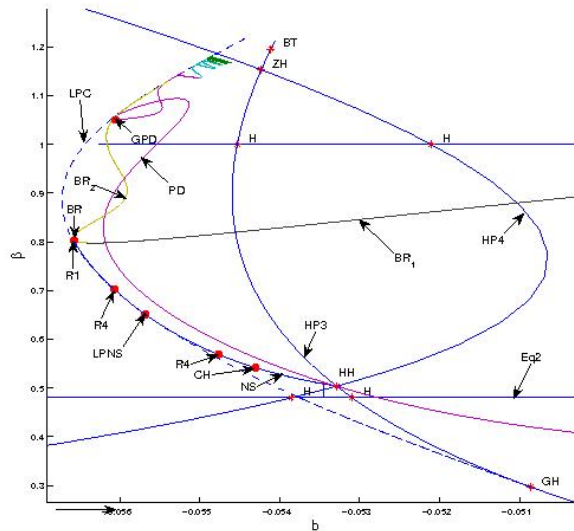

Fig. 1. Bifurcation diagram of a 6-dimensional system with damping b and self-excitation β. The curves correspond with bifurcations in parameter-space, see [1].

Bifurcation phenomena in ODEs lead by local linearization to studying systems of the form:

$$\dot{x} = A(\varepsilon)x, \tag{7}$$

where we can expand the $n \times n$-matrix A:

$$A(\varepsilon) = A_0 + \varepsilon A_1 + \varepsilon^2 A_2 + \varepsilon^3 \ldots$$

The $n \times n$-matrices A_n do not depend on ε; ε^n before a matrix should be interpreted as a diagonal $n \times n$-matrix with diagonal elements ε^n. If we have started with the standard form (3), we will have $A_0 = 0$. More in general, we have A_0 derived from the unperturbed problem, A_1 is produced by perturbation methods, by a special effort we may know A_2 and we will have some knowledge about higher order terms. An important question is then what the eigenvalues of A_0 and $A_0 + \varepsilon A_1$ tell us about the eigenvalues of $A(\varepsilon)$. This question is tied in with the structural stability of the matrices and whether eigenvalues are single or multiple. Failure of structural stability and the appearance of multiple eigenvalues is characteristic for bifurcation phenomena and so merit special attention. For instance in the bifurcation diagram of fig. 1, H corresponds with the presence of two purely imaginare eigenvalues, CH with one zero and two imaginary eigenvalues; for an extensive description see [11].

A $n \times n$ matrix is called *structurally stable* if it is nonsingular and all eigenvalues have nonzero real part. If we have a zero eigenvalue or purely imaginary eigenvalues, we can expect bifurcations. Apart from this, the presence of multiple eigenvalues affects the form of the expansions and the timescales.

Example 5 *We start with an example derived from an equation in standard form (3) where we have the expansion of $A(\varepsilon)$ until A_2:*

$$\dot{x} = \varepsilon^2 y, \ x(0) = 0,$$
$$\dot{y} = -\varepsilon x, \ y(0) = 1.$$

A_0 has vanished, A_1 has zero eigenvalues, $\varepsilon A_1 + \varepsilon^2 A_2$ has eigenvalues $\pm \varepsilon^{\frac{3}{2}} i$. The solution of the initial value problem is

$$x(t) = \varepsilon^{\frac{1}{2}} \sin(\varepsilon^{\frac{3}{2}} t), \ y(t) = \cos(\varepsilon^{\frac{3}{2}} t).$$

As can be seen from the eigenvalues, the timescale $\varepsilon^{\frac{3}{2}} t$ plays a part. Expanding the trigonometric functions on an interval of time of size $1/\varepsilon$, we find that the timescales t and εt can be used to obtain asymptotic estimates. On a longer interval of time, for instance $1/\varepsilon^2$, we need the timescale $\varepsilon^{\frac{3}{2}} t$ to obtain asymptotic estimates.

For bifurcations, local linearization leads to eigenvalue problems associated with eq. (7), so algebraic timescales are natural phenomena. Can we predict the form $\varepsilon^q t$ with q rational of such algebraic timescales? The following questions and results are classical.

Consider the matrix expansion obtained by a perturbation method:

$$A(\varepsilon) = A_0 + \varepsilon A_1 + \varepsilon^2 A_2 + \varepsilon^3 \ldots$$

- Can the eigenvalues be expanded in a convergent series of the form

$$\lambda = \lambda_0 + \varepsilon\lambda_1 + \varepsilon^2 \cdots ,$$

  where λ_0 is an eigenvalue of the matrix A_0 ? If this is the case, we expect timescales of the form $t, \varepsilon t, \varepsilon^2 t. \ldots$
- If we are in the critical case of bifurcations where λ_0 is zero or purely imaginary, how do the perturbations affect the eigenvalues and thus the qualitative behaviour of the solutions of the differential equations?

If A_0 vanishes, we extract ε and treat A_1 as perturbed matrix. We refer to [24] for references and summarize some basic results:

- If λ_0 is single, we have

$$\lambda(\varepsilon) = \lambda_0 + \varepsilon\lambda_1 + \varepsilon^2 \ldots$$

  If $\lambda_0 = 0$, this means we have an $O(\varepsilon)$ size eigenvalue.
- According to Newton and Puisieux:
  If λ_0 is multiple, the expansion is in fractional powers of ε.

Example 6 *Consider the equation $\dot{x} = A(\varepsilon)x$ with for the matrix $A(\varepsilon)$:*

$$A(\varepsilon) = \begin{pmatrix} 0 & 0 & 1 \\ 0 & 0 & 0 \\ 0 & 0 & 0 \end{pmatrix} + \varepsilon \begin{pmatrix} 0 & 0 & 0 \\ 1 & 0 & 0 \\ 3 & 0 & 0 \end{pmatrix} + \varepsilon^2 \begin{pmatrix} 0 & 0 & 0 \\ 0 & 0 & 0 \\ 0 & -1 & 0 \end{pmatrix} .$$

The characteristic equation to $O(\varepsilon)$ is:

$$\lambda^3 - 3\varepsilon\lambda = 0$$

with eigenvalues $\lambda_1 = 0, \lambda_{2,3} = \pm 3\sqrt{\varepsilon}$. The matrix $A_0 + \varepsilon A_1$ is not structurally stable so we add the $O(\varepsilon^2)$ term. This leads to the characteristic equation:

$$\lambda^3 - 3\varepsilon\lambda + \varepsilon^3 = 0.$$

with Newton-Puisieux expansion for the eigenvalues

$$\lambda_1 = \frac{1}{3}\varepsilon^2 + \frac{1}{81}\varepsilon^5 + \cdots , \lambda_{2,3} = \pm 3\sqrt{\varepsilon} - \frac{1}{6}\varepsilon^2 + \cdots .$$

Including the $O(\varepsilon^2)$-terms we have structural stability. Solving the equation we have time-like variables (timescales) of the form

$$\sqrt{\varepsilon}t, \varepsilon^2 t, \varepsilon^5 t$$

and from the expansion also higher order timescales.

The discussion has some relevance for the analysis of the nonlinear problem

$$\dot{x} = A(\varepsilon)x + \varepsilon f(x),$$

where $f(x)$ is a nonlinear vector field with an expansion starting with quadratric terms near $x = 0$. The zero eigenvalue to $O(\varepsilon)$ suggests the presence of a center manifold associated with the corresponding eigenvector. The calculation of eigenvalues to $O(\varepsilon^2)$ destroys this picture.

Similar problems may arise for other codimension one and two bifurcations triggered by the matrix $A(\varepsilon)$.

In the sequel we will consider a number of bifurcation problems arising in applications.
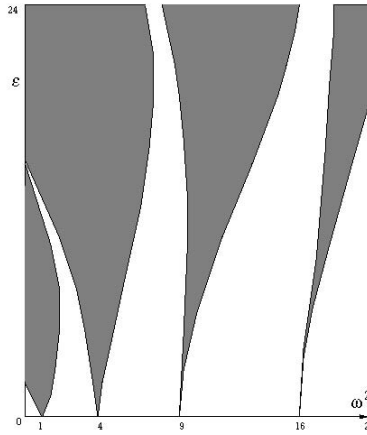
5   Application: the Mathieu-equation

Fig. 2. The gray Floquet tongues denote for which parameter values ω and ε the trivial solution of the Mathieu equation is unstable. In our approximations we have described the lower part of the tongue emerging from $\omega = 1$ as in eq. (8).

We consider the Mathieu equation which plays a part in many engineering problems:

$$\ddot{x} + (\omega^2(\varepsilon) + \varepsilon \cos \nu t)x = 0,$$

in its fundamental $1 : 2$-resonance with a slight detuning:

$$\ddot{x} + (1 + \varepsilon a + \varepsilon^2 b + \varepsilon \cos 2t)x = 0, \tag{8}$$

a and b are free parameters independent of ε, $\omega^2 = 1 + \varepsilon a + \varepsilon^2 b$. We apply Lagrange variation of constants

$$x = y_1 \cos t + y_2 \sin t, \; \dot{x} = -y_1 \sin t + y_2 \cos t.$$

The slowly-varying equations for (y_1, y_2) are, after averaging, of the form $\dot{y} = A(\varepsilon)y$; this (averaging) normal form approach produces to first order in ε:

$$A(\varepsilon) = +\varepsilon \begin{pmatrix} 0 & \frac{1}{2}(a - \frac{1}{2}) \\ -\frac{1}{2}(a + \frac{1}{2}) & 0 \end{pmatrix} + O(\varepsilon^2).$$

The eigenvalues are

$$\lambda_{1,2} = \pm \frac{1}{2}\sqrt{\frac{1}{4} - a^2},$$

the two approximate independent solutions for (y_1, y_2) can be written as

$$e^{\pm\frac{1}{2}\sqrt{\frac{1}{4}-a^2}\,\varepsilon t}.$$

This leads to the well-known result that for $a^2 > \frac{1}{4}$ the solutions of the Mathieu equation are stable (the approximate solutions are trigonometric) and for $a^2 < \frac{1}{4}$ they are unstable. The approximations with appropriate initial values have error estimate $O(\varepsilon)$ on a long time-interval $O(1/\varepsilon)$. In this approximation, the timescales for $x(t)$ are t and εt. The boundary of the instability domains, the Floquet tongues, are the bifurcation curves where the transition from unstable to stable solutions takes place in (ω^2, ε)-parameter space; see fig. 2.

5.1   What happens at the tongue boundary?

What happens at the transition values, for instance at $\omega^2 = 1 + \varepsilon a$ where $a = \frac{1}{2}$? In this case, we have for the normal form to first order:

$$A_1 = \begin{pmatrix} 0 & 0 \\ -\frac{1}{2} & 0 \end{pmatrix},$$

a typical degenerate matrix from bifurcation theory. Following [19] or [24] we perform a second-order averaging normalization to find:

$$A_2 = \begin{pmatrix} 0 & \frac{1}{64} + \frac{1}{2}b \\ \frac{7}{64} - \frac{1}{2}b & 0 \end{pmatrix}.$$

We find for the eigenvalues of $A(\varepsilon)$ to this order of approximation

$$\lambda^2 = -\frac{1}{4}\left(b + \frac{1}{32}\right)\varepsilon^3 + \frac{1}{4}\left(b + \frac{1}{32}\right)\left(\frac{7}{32} - b\right)\varepsilon^4.$$

The $O(\varepsilon^3)$-term dominates, $b = -\frac{1}{32}$ produces a more precise location of the Floquet tongue.

If $b > -\frac{1}{32}$ we have stability, if $b < -\frac{3}{32}$ we have instability.
The second order approximations of the solutions for (y_1, y_2) are a linear combination of $\exp.(+\lambda t)$ and $\exp.(-\lambda t)$. With appropriate initial values they yield approximations of the solutions of the Mathieu equation (8) with error estimate $O(\varepsilon^2)$ on a long time-interval $O(1/\varepsilon)$.

It is remarkable that the timescale $\varepsilon^{\frac{3}{2}}t$ plays a part in this problem because near the boundary of the Floquet tongue we have that $\lambda^2 = O(\varepsilon^3)$. The timescales characterizing the flow near the Floquet tongue are until second order

$$t,\ \varepsilon t,\ \varepsilon^{\frac{3}{2}}t,\ \varepsilon^2 t.$$

The presence of the timescale $\varepsilon^{\frac{3}{2}}t$ was noted for the Mathieu equation in [2], using the renormalization method. It is also noted in [2] that, using multiple timing with timescales $t, \varepsilon t, \varepsilon^2 t$, this extra timescale is not discovered. It arises from a bifurcation problem with multiplicity two eigenvalues

The tongue boundaries in fig. 2 correspond with parameter values where the Mathieu equation has periodic solutions. They indicate the transition from unstable to stable trivial solution, the eigenvalues on the boundaries show the nature of the bifurcations.

6 Application: resonance manifolds

Many dynamical systems, both dissipative and conservative, can be put in the form:

$$\begin{cases} \dot{x} = \varepsilon X(\phi, x) + \varepsilon^2 \dots, \\ \dot{\phi} = \Omega(x) + \varepsilon \dots \end{cases} \tag{9}$$

x is an n-vector (amplitudes) and ϕ an angle-vector (think of gyroscopic systems or in the case of Hamiltonian systems of actions and angles).
ϕ is time-like in domains where $\Omega(x) \neq 0$.

In a neighbourhood of $\Omega(x) = 0$, ϕ is not time-like and we have a resonance manifold.

6.1 Simple examples

Consider as an example a one degree of freedom system:

Example 7 *The equation to be studied is*

$$\ddot{x} + \omega^2 x = \varepsilon f(x, \dot{x}),$$

with (positive) constant frequency ω. Putting $\dot{x} = \omega y$ and introducing amplitude-angle variables $x, y \to r, \phi$ by

$$x = r \sin \phi, \ y = r \cos \phi,$$

we find the equations

$$\dot{r} = \varepsilon \frac{\cos \phi}{\omega} f(r \sin \phi, \omega r \cos \phi),$$

$$\dot{\phi} = \omega - \frac{\sin \phi}{\omega r} f(r \sin \phi, \omega r \cos \phi).$$

One observes that the righthand sides are 2π-periodic in ϕ and a perturbation scheme can be started, for instance by averaging over ϕ.
Apply this for instance to the damped, Duffing equation where $f(x, \dot{x}) = -a\dot{x} - bx^3$.

For the theory we refer to [19] and [24]. New phenomena may emerge in the case of more degrees of freedom. We borrow some examples from [24].

Example 8 *After suitable transformations in a problem, we have obtained the system:*

$$\dot{x} = \varepsilon x(\cos \phi_1 + \cos \phi_2 + \cos(2\phi_1 - \phi_2)),$$
$$\dot{\phi}_1 = x,$$
$$\dot{\phi}_2 = 2.$$

We have one amplitude, x, two angles ϕ_1 and ϕ_2; in addition the combination angle $\psi = 2\phi_1 - \phi_2$. We could consider the angles $\phi_1, \phi_2, 2\phi_1 - \phi_2$ as time-like variables and average over them; this is also called 'averaging over a torus'. This would result in an average zero for the righthand side of $\dot{x}$. Is this a correct strategy? The answer is affirmative in the cases that the three angles are indeed time-like but not in the cases when

$$\dot{\phi}_1 = 0, \ \dot{\phi}_2 = 0, \ 2\dot{\phi}_1 - \dot{\phi}_2 = 0.$$

As $2\dot{\phi}_1 - \dot{\phi}_2 = 2(x - 1)$ we have to consider separately the cases $x = 0$ and $x = 1$. The domains near $x = 0$ and $x = 1$ are called the resonance zones in x-space. Outside the resonance zones, the average of $\dot{x}$ over the two angles and the combination angle vanishes, so $x(t)$ is nearly constant there. What happens in a resonance zone? In this example $x = 0$ is an exact solution, consider instead a neighbourhood of $x = 1$ by rescaling:

$$x - 1 = \delta(\varepsilon)\xi.$$

Here, ξ is the new, local variable; $\delta(\varepsilon) = o(1)$ as $\varepsilon \to 0$, but we still have to find out what the size of $\delta(\varepsilon)$ and the resonance zone is. Introducing ξ and ψ in the equations produces:

$$\begin{aligned}
\delta(\varepsilon)\dot{\xi} &= \varepsilon(\cos\phi_1 + \cos\phi_2 + \cos\psi) + O(\varepsilon\delta(\varepsilon)), \\
\dot{\phi}_1 &= 1 + O(\delta(\varepsilon)), \\
\dot{\phi}_2 &= 2 \\
\dot{\psi} &= 2\delta(\varepsilon)\xi.
\end{aligned}$$

To first order, ϕ_1 and ϕ_2 are time-like in this resonance zone, ψ is not. The equations for ξ and ψ show the same size of terms on choosing $\delta(\varepsilon) = \sqrt{\varepsilon}$. The equations become with this choice:

$$\begin{aligned}
\dot{\xi} &= \sqrt{\varepsilon}(\cos\phi_1 + \cos\phi_2 + \cos\psi) + O(\varepsilon), \\
\dot{\phi}_1 &= 1 + O(\sqrt{\varepsilon}), \\
\dot{\phi}_2 &= 2 \\
\dot{\psi} &= 2\sqrt{\varepsilon}\xi.
\end{aligned}$$

We average now over the time-like variables ϕ_1 and ϕ_2 to find the leading equations and terms in this resonance zone:

$$\dot{\xi} = \sqrt{\varepsilon}\cos\psi, \ \dot{\psi} = 2\sqrt{\varepsilon}\xi.$$

Differentiating ψ we get the pendulum equation for the combination angle:

$$\ddot{\psi} - 2\varepsilon\cos\psi = 0.$$

The pendulum equation has a centre point and a saddle. It can be shown that the stationary solutions of this resonance zone equation correspond with a stable and an unstable periodic solution of the original system. Note that in this example we had to localize in space to size $O(\sqrt{\varepsilon})$, the natural timescale in the resonance zone is $\sqrt{\varepsilon}t$, outside the resonance zones it is εt.
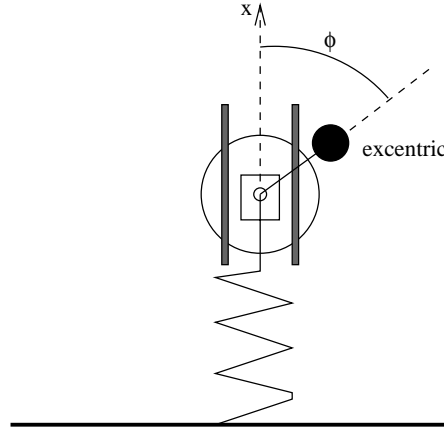
Fig. 3. Excentric flywheel, rotating on elastic foundation

6.2   Rotation of an excentric flywheel

An application in [24], example 12.11 (with more references there), describes a slightly excentric flywheel, see fig. 3; the analysis is based on the thesis of Van den Broek [22], see also [21]. The vertical displacement x of a small mass on the flywheel and its rotation angle ϕ are given by

$$\begin{cases} \ddot{x} + x = \varepsilon(-x^3 - \dot{x} + \dot{\phi}^2 \cos\phi) + O(\varepsilon^2), \\ \ddot{\phi} = \varepsilon(\frac{1}{4}(2 - \dot{\phi}) + (1 - x)\sin\phi) + O(\varepsilon^2). \end{cases} \tag{10}$$

To analyse the system and to put it in standard perturbation form, we introduce:

$$x = r\sin\phi_2, \dot{x} = r\cos\phi_2, \phi = \phi_1, \dot{\phi}_1 = \Omega,$$

with $r, \Omega > 0$. We find to $O(\varepsilon)$ a system with two angles, ϕ_1, ϕ_2, and slowly varying variables r and Ω:

$$\dot{r} = \varepsilon\cos\phi_2(-r^3\sin^3\phi_2 - r\cos\phi_2 + \Omega^2\cos\phi_1),$$

$$\dot{\Omega} = \varepsilon(\frac{1}{4}(2 - \Omega) + \sin\phi_1 - r\sin\phi_1\sin_2),$$

$$\dot{\phi}_1 = \Omega,$$

$$\dot{\phi}_2 = 1 + \varepsilon(r^2\sin^4\phi_2 + \frac{1}{2}\sin 2\phi_2 - \frac{\Omega^2}{r}\cos\phi_1\sin\phi_2).$$

Evaluating the trigonometric terms in the slowly varying equations for r and Ω we find the angles $\phi_1, \phi_2, 2\phi_2, 4\phi_2$ and the combination angles $\phi_1 - \phi_2, \phi_1 + \phi_2$. The righthand sides of the equations for the angles are positive, so the only resonance zone that can be active is when $\dot{\phi}_1 - \dot{\phi}_2 \approx 0$. As

$$\frac{d}{dt}(\phi_1 - \phi_2) = \Omega - 1 + O(\varepsilon),$$

this happens if Ω is near 1. Note that the analysis included $O(\varepsilon)$ terms only, if we add higher order terms, more (but smaller) resonance zones may be found. Outside the resonance zone we average over the angles to find an approximation from

$$\begin{cases} \dot{r} = -\frac{\varepsilon}{2}r, \\ \dot{\Omega} = \frac{\varepsilon}{4}(2 - \Omega). \end{cases} \tag{11}$$

Although simple looking, this result is already of interest. The deflection x of the flywheel will go exponentially fast to zero outside the resonance zone; outside resonance, $\Omega(t)$, the rotation speed, will tend to 2, but if $\Omega(0) < 1$, the flywheel will pass through the resonance zone, the averaged equations 11 do not apply in this zone. What happens there? As in example 8 above, we rescale locally in a neighbourhood of $\Omega = 1$ and introduce the combination angle ψ:

$$\Omega = 1 + \delta(\varepsilon)\omega, \ \psi = \phi_1 - \phi_2.$$

We find

$$\dot{r} = O(\varepsilon),$$
$$\delta(\varepsilon)\dot{\omega} = \varepsilon(\frac{1}{4} + \sin \phi_1 - \frac{1}{2}r \cos \psi + \frac{1}{2}r \cos(2\phi_1 - \psi)) + \dots,$$
$$\dot{\phi}_1 = 1 + \dots,$$
$$\dot{\psi} = \delta(\varepsilon)\omega + \dots$$

The dots represent higher order terms. The equations for ω and ψ show the same size of terms if

$$\delta(\varepsilon) = \sqrt{\varepsilon},$$

which determines the size of the resonance zone. Averaging over the remaining angle ϕ_1 and noting that $r(t)$ varies $O(\varepsilon)$ in the resonance zone, we find to $O(\sqrt{\varepsilon})$ (neglecting terms of $O(\varepsilon\sqrt{\varepsilon})$):

$$\dot{\omega} = \sqrt{\varepsilon}(\frac{1}{4} - \frac{1}{2}r \cos \psi),$$
$$\dot{\psi} = \sqrt{\varepsilon}\omega.$$

Differentiating the equation for ψ we find again a pendulum equation describing the dynamics in the resonance zone:

$$\ddot{\psi} + \frac{1}{2}\varepsilon r(0) \cos \psi = \frac{1}{4}\varepsilon.$$

So it turns out that the resonance zone near $\Omega = 1$ is of size $O(\sqrt{\varepsilon})$, the timescale of the dynamics is $\sqrt{\varepsilon}t$. The centre equilibrium of the pendulum equation corresponds with a stable periodic solution, the saddle with an unstable one. A periodic solution that is Lyapunov stable only does not attract. By including second order aproximations, we find that if we start at $0 < \Omega(0) < 1$, there exist initial values $\Omega(0)$ so that the solution is trapped in the resonance

zone, resulting in periodic deflections of the flywheel. To describe this behaviour analytically, we have to obtain a second order approximation with respect to ε (described in [21]). This second order approximation adds negative real values $O(\varepsilon^2)$ to the purely imaginary eigenvalues. For a numerical illustration see fig. 4.
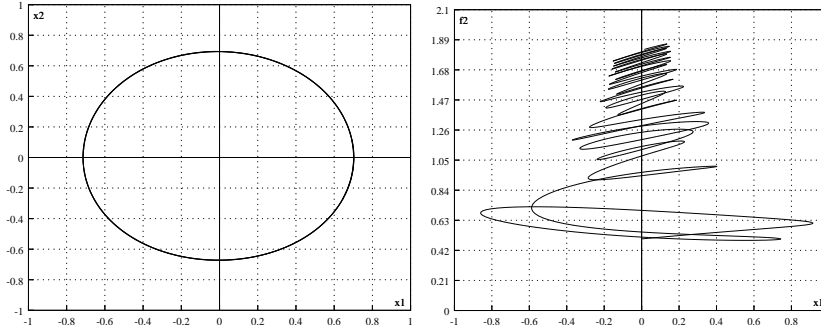

Fig. 4. Orbits for the excentric flywheel. Left: capture into resonance ($x1 = x, x2 = \dot{x}$); $\phi_1(0) - \phi_2(0) = 1.13, \phi_2(0) = 0, \varepsilon = 0.1$. Right: transition through the resonance zone, vertical $f2 = \phi_2$; $\phi_1(0) - \phi_2(0) = 0.5, \phi_2(0) = 0.5, \varepsilon = 0.1$.

It turns out that at this level of approximation, there are three open sets of initial values of the combination angle ψ that lead the corresponding solutions to trapping into the resonance zone. If $\varepsilon = 0.01$, the sets are for $\phi_1(0) - \phi_2(0) = \psi(0)$: $[1.049, 1.232]$, $[2.840, 3.047]$ and $[4.763, 4.863]$. In [21] this result is established analytically and confirmed numerically.

The results are dependent on the value of ε. It is an open question how the number of 'channels' leading to trapping in the resonance zone depends on the level of approximation; narrower channels may exist at higher order.

Problems where averaging over angles (a torus) has to be used, arise in many fields of application, for instance in gyroscopic systems, also in Hamiltonian mechanics. Algebraic timescales of the form $\varepsilon^q t$ with q a rational number, are natural in this context; see also [24] for the general theory and more examples.

6.3   Application: resonance manifolds in Hamiltonian systems

Higher order resonance turns out to be a natural application of the asymptotics of resonance manifolds. For an application in two degrees-of-freedom Hamiltonian systems, in particular the elastic pendulum, see [20].

Consider the two degrees-of-freedom Hamiltonian in local coordinates with Taylor-expansion:

$$H = H_2 + \varepsilon H_3 + \varepsilon^2 H_4 + \dots,$$

with H_k homogeneous of degree k in position and momentum (p, q). H_2 takes the standard form

$$H_2 = \frac{m}{2}(q_1^2 + p_1^2) + \frac{n}{2}(q_2^2 + p_2^2),$$

with the integers m, n positive and relative prime. The phase-flow in a neighbourhood of the origin takes place on compact manifolds parametrised by the Hamiltonian (energy) integral.

Most of the attention in the literature went to the primary resonance $1 : 2$ and to the secondary resonances $1 : 1$ and $1 : 3$. In these resonance cases, the dominant part of the phase-flow is characterised by the timescales $t, \varepsilon t, \varepsilon^2 t$ and the time intervals of validity of approximation $1/\varepsilon$ and $1/\varepsilon^2$, see [19].

6.4   The higher order normal form

The cases where $m + n \geq 5$ are called higher order resonances. Studying these resonances requires the computation of higher order normal forms and involves intervals of time longer than $1/\varepsilon^2$. In the Hamiltonian normal form, the first resonant term, involving both actions and angles, arrives from H_{m+n} at $O(\varepsilon^{m+n-2})$.

The first basic approach to higher order resonance was given in [17] with applications in [18]. In [20] an improvement of the estimates has been given, together with a number of applications, among which the elastic pendulum (a pendulum where the suspending, inflexible string is replaced by a linear spring). Introducing action-angle variables $p_i, q_i \rightarrow \tau_i, \phi_i$, $i = 1, 2$, the normal form will be of the form:

$$H = m\tau_1 + n\tau_2 + \varepsilon_2 P_2(\tau_1, \tau_2) + \ldots + \varepsilon^{m+n-2} D(\tau_1^n \tau_2^m)^{\frac{1}{2}} \cos \chi,$$

with resonance combination angle $\chi = n\phi_1 - m\phi_2 + \alpha$. The dots represent terms depending on τ_1, τ_2 only, the terms in so-called Birkhoff normal form. A consequence from the corresponding equations of motion is that the actions are constant until terms of order $O(\varepsilon^{m+n-2})$ are taken into account, for the combination angle we have

$$\dot{\chi} = \varepsilon^2 \left(n \frac{\partial P_2}{\partial \tau_1} - m \frac{\partial P_2}{\partial \tau_2} \right) + \varepsilon^3 \ldots$$

6.5   The phase-flow of higher order resonance

Consider the *higher order* resonances defined by $m + n \geq 5$. It turns out there are two domains in phase-space where the dynamics is very different and is characterised by different timescales:

- The *resonance domain D_I*, which is a neighborhood of the resonance manifold M. The resonance manifold, if it exists, arises from the condition that $P_2(\tau_1, \tau_2)$ and maybe higher order Birkhoff normal forms vanish. In D_I the variations of the actions and the combination angle may interact significantly. In terms of singular perturbations, this is the *inner* boundary layer of the Hamiltonian system. In [20] it has been shown that the size of the resonance domain is $O(\varepsilon^{\frac{m+n-4}{2}})$, the interaction of the actions takes place on a time interval of order $O(\varepsilon^{-\frac{m+n}{2}})$

- The remaining part of phase-space, outside the resonance domain, is D_0, the *outer* domain. In the domain D_0, there is, to a certain approximation, little variation of the actions, and so hardly any exchange of energy between the two degrees of freedom.

It is shown in [20] that for Hamiltonians derived from a potential, we have $\alpha = 0$, and that for the elastic pendulum, after the first order $2 : 1$-resonance, the higher order $4 : 1$-resonance is the most prominent one with resonance manifold of size $O(\varepsilon^{\frac{1}{2}})$ and time interval of interaction $O(\varepsilon^{-\frac{5}{2}})$; for a Poincaré map of the $1 : 6$-resonance of the elastic pendulum see fig. 5.
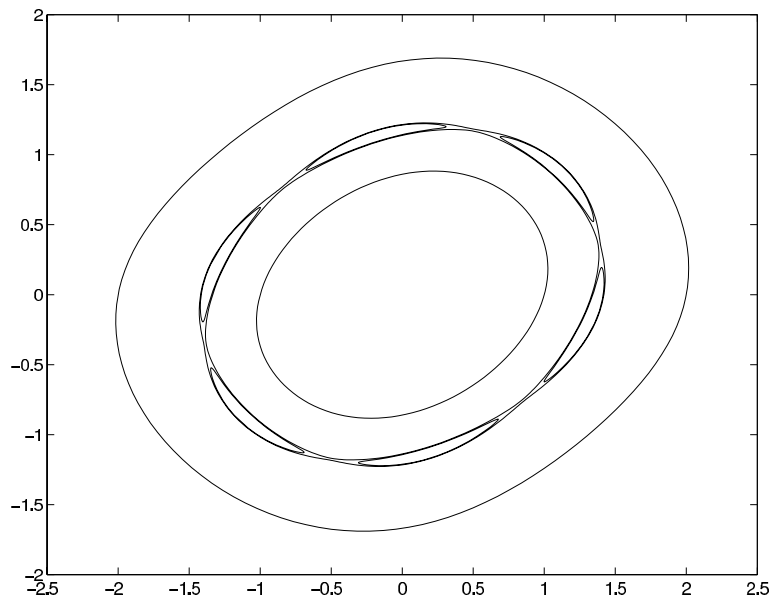
Fig. 5. The Poincaré map for the $1 : 6$-resonance of the elastic pendulum ($\varepsilon = 0.75$, large for illustration purposes). In the resonance domain, the saddles are connected by heteroclinic cycles and inside the cycles are 6 center fixed points, see [20].

6.6   The Hénon-Heiles family

A well-known model for orbits in axi-symmetric galaxies is the family of Hénon-Heiles potential problems

$$H = \frac{m}{2}(q_1^2 + p_1^2) + \frac{n}{2}(q_2^2 + p_2^2) - \varepsilon \left(\frac{a_1}{3} q_1^3 + a_2 q_1 q_2^2 \right). \qquad (12)$$

In the literature, most of the attention is on the $m : n = 1 : 1$- and $2 : 1$-resonances. In [20] it is noted that the $m : n = 1 : 2$-resonance degenerates because of the discrete symmetry in the second degree of freedom, it is treated

as a $2 : 4$ higher order resonance. In this case the resonance manifold, for the parameter values where it exists, has size $O(\varepsilon)$, the timescale of interaction is $\varepsilon^3 t$.

Is the degenerate $1 : 2$-resonance the most prominent higher order resonance? Other candidates are the $2 : 3$- and the $4 : 1$-resonances, the $3 : 2$- and $1 : 4$-resonances are degenerate because of the discrete symmetry of the potential.

If $a_2 = 0$, the equations decouple, so we assume $a_2 \neq 0$. Assuming $m+n \geq 5$ we find the normal form from [18] or [20]. As explained above, we find for the actions $\tau_1 = \frac{1}{2}(q_1^2 + p_1^2), \tau_2 = \frac{1}{2}(q_2^2 + p_2^2)$:

$$\dot{\tau}_1 = O(\varepsilon^3), \; \dot{\tau}_2 = O(\varepsilon^3).$$

For the combination angle $\chi = n\phi_1 - m\phi_2$ we have:

$$\dot{\chi} = \varepsilon^2 \left(-\frac{5n}{12}a_1^2 + \frac{m}{4}a_1 a_2 + \frac{m}{30}a_2^2\right) 2\tau_1 + \varepsilon^2 \left(-\frac{n}{2}a_1 a_2 - \frac{n}{15}a_2^2 + \frac{29m}{120}a_2^2\right) 2\tau_2. \tag{13}$$

For the Hénon-Heiles family, one usually puts $\lambda = a_1/3a_2$, producing:

$$\dot{\chi} = 6a_2^2 \varepsilon^2 \left(-\frac{5n}{4}\lambda^2 + \frac{m}{4}\lambda + \frac{m}{90}\right) \tau_1 + 6a_2^2 \varepsilon^2 \left(-\frac{n}{2}\lambda - \frac{n}{45} + \frac{29m}{360}\right) \tau_2. \tag{14}$$

The resonance manifold, if it exists, is determined by the equation

$$\left(-\frac{5n}{4}\lambda^2 + \frac{m}{4}\lambda + \frac{m}{90}\right) \tau_1 + \left(-\frac{n}{2}\lambda - \frac{n}{45} + \frac{29m}{360}\right) \tau_2 = 0. \tag{15}$$

The approximate energy integral is given by

$$m\tau_1 + n\tau_2 = E_0, \; 0 \leq \tau_1 \leq \frac{E_0}{m}, \; 0 \leq \tau_2 \leq \frac{E_0}{n}.$$

We will consider the prominent higher order resonances for the original Hénon-Heiles problem [5] and the potential often used by Contopoulos, see [18]. As mentioned, the candidates for this are the $2 : 3$- and the $4 : 1$-resonances. If they exist, the size of the resonance manifolds are in these cases $O(\varepsilon^{\frac{1}{2}})$, the interaction of the degrees of freedom in the resonance manifold takes place on an interval of order $O(\varepsilon^{-\frac{5}{2}})$.

6.7   The Hénon-Heiles case

In this model we have $a_1 = 1$, $a_2 = -1$, $\lambda = -1/3$ (in the original problem we have $m = n = 1$, see [5]). From eq. (15) and the approximate energy integral we find if $m + n \geq 5$ the conditions:

$$-\left(\frac{5n}{18} + \frac{13m}{90}\right) \tau_1 + \left(\frac{13n}{45} + \frac{29m}{180}\right) \tau_2 = 0$$

and

$$m\tau_1 + n\tau_2 = E_0, \; 0 \leq \tau_1 \leq \frac{E_0}{m}, \; 0 \leq \tau_2 \leq \frac{E_0}{n}.$$

The $2:3$-resonance

Putting $m = 2$, $n = 3$ we find that the resonance manifold exists near:

$$\tau_1 = \frac{107}{517}E_0, \ \ \tau_2 = \frac{101}{517}E_0.$$

The $4:1$-resonance

Putting $m = 4$, $n = 1$ we find that this resonance manifold also exists; it is found near:

$$\tau_1 = \frac{84}{413}E_0, \ \ \tau_2 = \frac{77}{413}E_0.$$

In both resonance cases we find islands with stable and unstable periodic solutions. Generically, the stable and unstable manifolds of the unstable solution will cross, producing homoclinic chaos.

6.8   The Contopoulos case

In this model we have $a_1 = 0$, $\lambda = 0$. From eq. (15) we find the condition:

$$\frac{m}{2}\tau_1 + \left(-n + \frac{29m}{8}\right)\tau_2 = 0.$$

So we have for existence the requirement $n > 29m/8$; the $2 : 3$- and the $4 : 1$-resonances will not be present at this potential; also not the degenerate $1 : 2$-resonance which can be seen as a $2 : 4$-resonance. The higher order resonances that exist have to satisfy the requirement and will have smaller resonance manifolds than in the Hénon-Heiles potential. An example is the $2 : 9$-resonance with resonance manifold size $O(\varepsilon^{\frac{7}{2}})$, time interval of interaction $O(\varepsilon^{-\frac{11}{2}})$. The homoclinic chaos in the resonance zones will be smaller in size than in the Hénon-Heiles model.

References

1.T. Bakri, Yu.A. Kuznetsov and F. Verhulst, *Torus bifurcations in a mechanical system*, to be publ. in J. Dynamics and Differential Equations.

2.Lin-Yuan Chen, N. Goldenfeld and Y. Oono, *Renormalization group and singular perturbations: multiple scales, boundary layers, and reductive perturbation theory*, Phys. Rev. E 54, 376-394 (1996).

3.H. Chiba, *Extension and unification of singular perturbation methods for ODEs based on the renormalization group method*, SIAM J. Applied Dynamical Systems 8, 1066-1115 (2009).

4.J.A. Cochran, *Problems in singular perturbation theory*, Stanford University (1962).

5.M. Hénon and C. Heiles, *The applicability of the third integral of motion: some numerical experiments*, Astron. J. 69, 73-79 (1964).

6.J. Kevorkian, *The uniformly valid asymptotic representation of the solution of certain nonlinear differential equations*, Thesis Calif. Institute Techn., Pasadena (1961).

7.J. Kevorkian, *Perturbation techniques for oscillatory systems with slowly varying coefficients*, SIAM Review 29, 391-461 (1987).

8.E. Kirkinis, *The renormalization group: a perturbation method for the graduate curriculum*, SIAM Review 54, 374-388 (2012).

9.N. Krylov and N. Bogoliubov, *Méthodes approchées de la mécanique nonlinéaire dans leur application a l'étude de la perturbation des mouvements périodiques et de divers phénomènes de résonance s'y rapportant*, Ac. Sciences Ukraine 14 (1935).

10.G.E. Kuzmak, *Asymptotic solutions of nonlinear second order differential equations with variable coefficients*, J. Appl. Math. Mechanics (PMM) 10, 730-744 (1959).

11.Yu.A. Kuznetsov, *Elements of applied bifurcation theory*, 3d ed. Springer (2004).

12.Yu.A. Mitropolsky, *Private communication*, Kiev (1981).

13.B. Mudavanhu and R.E. O'Malley, *A new renormalization method for the asymptotic solution of weakly nonlinear vector systems*, SIAM J. Appl. Math. 63, 373-397 (2002).

14.J.A. Murdock, *Perturbations, theory and methods*, SIAM Classics in Applied Mathematics 27 (1999) (republ. with corrections from John Wiley ed. 1991).

15.A.H. Nayfeh, *Perturbation Methods*, Wiley-Interscience (1973).

16.L.M. Perko, *Higher order averaging and related methods for perturbed periodic and quasi-periodic systemss*, SIAM J. Appl. Math. 17, 698-724 (1969).

17.J.A. Sanders, *Are higher order resonances really interesting*, Celestial Mech. 16, 421-440 (1977).

18.J.A. Sanders and F. Verhulst, *Approximations of higher order resonances with an application to Contopoulos' model problem*, in Asymptotic Analysis, from Theory to Application (F. Verhulst, ed.) Lecture Notes in Math. 711, 209-228, Springer (1979).

19.J.A. Sanders, F. Verhulst and J. Murdock, *Averaging methods in nonlinear dynamical systems*, 2nd ed. Springer (2007).

20.J.M. Tuwankotta and F. Verhulst, *Symmetry and resonance in Hamiltonian systems*, SIAM J. Appl. Math. 61, 1369-1385 (2000).

21.B. van den Broek and F. Verhulst, *Averaging techniques and the oscillator-flywheel problem*, Nieuw Archief voor Wiskunde 5, pp. 186-206 (1987).

22.B. van den Broek, *Studies in nonlinear resonance, applications of averaging*, thesis University of Utrecht (1988).

23.Ferdinand Verhulst, *Nonlinear differential equations and dynamical systems*, Springer (2000).

24.Ferdinand Verhulst, *Methods and applications of singular perturbations*, Springer (2005).

Panjer Randomized Fibonacci Model and Dynamic Instabilities in Population Growth Models

Maria de Fátima Brilhante[1,4], Maria Ivette Gomes[2,4], and Dinis Pestana[3,4]

[1] Universidade dos Açores, Ponta Delgada, Açores, Portugal
   (E-mail: `fbrilhante@uac.pt`)
[2] Universidade de Lisboa, Faculdade de Ciências, DEIO, Portugal, and
   Instituto de Investigação Científica Bento da Rocha Cabral, Lisboa, Portugal
   (E-mail: `ivette.gomes@fc.ul.pt`)
[3] Universidade de Lisboa, Faculdade de Ciências, DEIO, Portugal, and
   Instituto de Investigação Científica Bento da Rocha Cabral, Lisboa, Portugal
   (E-mail: `dinis.pestana@fc.ul.pt`)
[4] CEAUL — Centro de Estatística e Aplicações da Universidade de Lisboa,
   Portugal

Abstract. Although Fibonacci's numbers play an important role in modeling phenomena in a wide variety of subjects, their use as descriptors of population growth has clearly been rather restricted after the introduction of the Verhulst logistic model and its numerous modifications and extensions. In fact, in the very unrealistic Fibonacci model neither population extinction nor bounded growth are possible, only quasi-exponential unbounded population growth can result. We present a modified model assuming that the number of direct offsprings of each ancestor is a Bernoulli random variable, hence with positive probability of 0 count, and thus accommodating both extinction and possible sustainable growth. We compare algebraic and numerical treatment of equations using the fixed point method in the framework of instabilities of numerical algorithms for finding roots of equations. On the othe hand, branching processes are natural models for random population growth in many situations. Here we use basic count models whose probability mass function satisfies Panjer iteration, and investigate randomly stopped sums and collective risk when the subordinator random variable and the summands are independent and identically distributed basic count random variables.
Keywords: Fibonacci model, Verhulst model, Bernoulli offsprings, branching processes, fixed point algorithm instabilities, branching processes, Panjer iteration, basic count models.

1 Introduction

Let $N(t)$ denote the size of some population at time t. Two main issues in population dynamics deal with the probability of extinction and with the total size of the progeny of an ancestor.

Fibonacci (c. 1170 – c. 1250) in his *Liber Abaci* posed and solved a problem involving the growth of a population of rabbits based on idealized and very unrealistic assumptions. As a consequence, a population with Fibonacci's growth pattern never dies out, while we know that the total progeny of some ancestor is in many real circumstances finite, cf. for instance Lotka [15] example (p. 123–136) on the extinction of surnames, using branching processes. However, Fibonacci's numbers are still a very active research area, since they (mainly the initial numbers of the sequence) can approximate quite well counts in many natural systems, and have been applied successfully in very diverse situations and areas, namely aesthetic (the golden ratio is pervasive in all form of plastic arts, and is even used by aesthetic surgeons in beauty improvement), including for instance Lindenmayer grammars, cf. Prusinkiewicz and Hanan [20], used by Pestana [18] for an initial investigation of music composition with repetitive structures.

1.1 Fibonacci population growth model

Fibonacci (c. 1170 – c. 1250) in his *Liber Abaci* posed and solved a problem involving the growth of a population of rabbits based on idealized and very unrealistic assumptions. The solution, generation by generation, was a sequence of numbers $\{F_n\}_{n\geq 0}$ later known as Fibonacci numbers, starting with $\{0,1\}$, such that $F_{n+2} = F_n + F_{n+1}$. Using Binet's formula

$$F_n = \frac{(1 + \sqrt{5})^n - (1 - \sqrt{5})^n}{2^n \sqrt{5}}$$

the computation of any member of the Fibonacci sequence is straightforward.

Although the wide success of Fibonacci's sequence as an approximate model for the first few generations is still praised in many branches of Biology, the very unrealistic assumption that any couple of rabbits gives birth to exactly one couple of rabbits as offsprings, and this in each of exactly two successive mating periods, cannot accommodate important real features in population dynamics, such as sustainable growth or even population extinction, as studied successfully for instance by Lotka [14] using the more realistic sustainable growth logistic model introduced by Verhulst. In fact, rewriting $F_{n+2} = F_n + F_{n+1} = 2F_{n+1} - F_{n-1} \Longrightarrow F_{n+2} - F_{n+1} = F_{n+1} - F_{n-1}$, the closely associated differential equation $\frac{\mathrm{d}}{\mathrm{d}t} N(t) = \frac{\partial^2}{\partial t^2} N(t)$ shows that Fibonacci's growth is approximately exponential. Indeed, we get an approximate geometric growth with ratio $\frac{1+\sqrt{5}}{2}$. Even for moderate values such as $n = 11$, say, $F_{12} = 144 \approx F_{11}\frac{1+\sqrt{5}}{2} = 144.005$ (recall that $\frac{1+\sqrt{5}}{2}$ is the "golden ratio" limit of $\frac{F_{n+1}}{F_n}$).

1.2 Verhulst sustainable growth logistic model and extensions

Imposing some natural regularity conditions on $N(t)$, namely that $\frac{\mathrm{d}}{\mathrm{d}t} N(t) = \sum_{k=0}^{\infty} A_k [N(t)]^k$, Verhulst ([27], [28], [29]) used the second order approximation

$\frac{d}{dt}N(t) = A_1 N(t) + A_2 [N(t)]^2$, with $A_1 > 0$ and $A_2 < 0$, which can be rewritten as

$$\frac{d}{dt}N(t) = r\,N(t)\left[1 - \frac{N(t)}{K}\right], \tag{1}$$

(where $r > 0$ is frequently interpreted as a Malthusian instantaneous growth rate parameter, whenever modeling natural breeding populations, and $K > 0$ as the equilibrium limit size of the population) to develop a broadly successful "logistic" population growth model, much more realistic to model sustainable growth. In fact, an initial period of exponential growth if followed by moderate approximately linear growth, with exponential steep exponential moderation when limitation of natural resources (or success of predators or competing species) ultimately curb down growth to sustainable values.

Moreover, and since in many species there exist periodic mating periods, using Euler's ideas on the interplay of differential equations and difference equations in numerical methods, the associated difference equation

$$x_{n+1} = \alpha\,x_n\,(1 - x_n), \tag{2}$$

(where it is convenient to deal with the assumption $x_n \in [0,1]$, $n = 1, 2, \dots$) made his way in modeling population dynamics.

The equilibrium $x_{n+1} = x_n$ leads to a simple second order algebraic equation with positive root $1 - 1/\alpha$, and to a certain extent it is surprising that anyone would care to investigate its numerical solution using the fixed point method, which indeed brings in many pathologies when a steep curve — i.e., for some values of the iterates $|\alpha\,(1 - 2\,x_n)| > 1$ — is approximated by an horizontal straight line. This numerical investigation, apparently devoid of interest, has however been at the root of many theoretical advances when $\alpha \notin [1,3]$ (namely Feigenbaum bifurcations and ultimate chaotic behavior), and *a posteriori* led to many interesting breakthroughs in the understanding of population dynamics. Due to its close association with the differential equation (1), whose solution is a logistic function

$$N(t) = \frac{K\,N_0}{N_0 + (K - N_0)\,e^{-rt}}, \tag{3}$$

the parabola $x\,(1 - x)$ appearing in the discretization (2) is very often called the "logistic parabola".

Up to a multiplicative constant, the logistic parabola is the $Beta(2,2)$ probability density function. In Aleixo *et al.* [1], and in Rocha *et al.* [23] several extensions of population growth models tied to more general $Beta(p,q)$ densities have been investigated, and in Pestana *et al.* [17] the factor $1 - x$ has been considered the linear truncation of $-\ln x$, so obtaining differential functions whose solution exhibits Paretian tail behaviour and ultimately extreme value models (*Gumbel*, *Fréchet* or *Weibull*) solutions for the associated differential equation $\frac{d}{dt}N(t) = r\,N(t)\,(-\ln(N(t))^{1+\gamma}$. Tsoularis [26] and Waliszewski and Konarski [30] must be credited for the *Gompertz* (or *Gumbel*) solution when in the associated differential equation $\gamma = 0$. Tsoularis [26] is a very informative state-of-the-art on population growth models. Brilhante *et al.* ([3], [4]) provide

the connection between the solution of the above extensions of the original Verhulst equation to extreme value and Rachev and Resnick [21] geo-extreme value (i.e., when the original sequence is subject to Rényi's [22] rarefaction, equivalent in its final results to Kovalenko's [12] and Kozubowski's [13] geometric thinning).

1.3   Modified Fibonacci models

We shall discuss, using branching processes, several modifications of the Fibonacci model, so that more realistic possibilities, such as limited growth or even extinction, may occur:

1. A framework very similar to the original description posed by Fibonacci: each ancestor can produce direct offsprings only in the first two consecutive reproducing periods. However, instead of deterministically producing exactly one offspring in each reproducing epoch, the number of offsprings is a random $X \frown Bernoulli(p)$.
2. A simple modification, which has the advantage of affordable algebraic treatment, is to consider that the progeny (it is indifferent whether we count individuals in the case of non-sexual reproduction, or couples in the case of sexual reproduction) is a random $Y \frown Geometric(p)$. The hypothesis that in sexual reproduction we consider that the progeny is solely of couples, and that each of those behaves as a faithful couple, is indeed as unrealistic as what has been taken for granted as an assumption in the original Fibonacci model. But the wider variability of the number of offsprings of each ancestor at each reproducing period, with sensible choices so that the mean value $\mathbb{E}(Y) = (1 - p)/p$ is rather small, can produce more realistic results.
   Observe, further, that while the Bernoulli random variable is underdispersed, i.e $Var(X)/\mathbb{E}(X) < 1$, the Geometric random variable is overdispersed, So, it can accommodate more realistic wider variability.
3. An almost similar framework as the one described in item 1 is investigated explicitly assuming removing each progenitor from the system after two reproduction periods, using randomly stopped sums.

Aside from presenting models allowing for extinction and limited growth, and hence more realistic than the unlimited quasi-exponential growth of the original Fibonacci model, our aim is to compare whenever possible algebraic solutions to numerical solutions using the fixed point method. These indeed exhibit instabilities whenever the function is too steep in a neighborhood of the root we wish to calculate.

Although those instabilities are qualitatively quite different from the celebrated Feigenbaum bifurcations and ultimate chaos that the discretization of the Verhulst model brought to the limelights of the structural investigation of dynamical systems, it seems worthwhile to discuss them, since the philosophical controversy whether pathologies observed in the numerical solution of equations $x = f(x)$ using the fixed point algorithm are an essential feature or solely an inherent consequence of instabilities to be expected when $|f'(x)| > 1$ in the vicinity of the equation root is far from being settled.

In this first paper, we shall discuss in depth the Bernoulli randomized model described in item 1, postponing for a second part other randomizations.

2 Modified Randomized Fibonacci Models: Bernoulli(p) Offsprings in Each Reproduction Epoch

Let us assume that the process starts with one ancestor (single or couple, according to the reproduction characteristics of the species). In each of the two initial reproduction epochs each unit produces $X \frown Bernoulli(p)$ offsprings, and is removed from the process after the the second reproduction epoch. On the other hand, each offspring becomes an ancestor in the next step, behaving exactly in the some fashion.

Let Z_1 denote the number of units in the system in the first step of the process, i.e. exactly when the initial ancestor is removed from the system:

$$Z_1 = \begin{cases} 0 & 1 & 2 & 3 \\ (1-p)^2 & p(1-p)(2-p) & 2p^2(1-p) & p^3 \end{cases} \tag{4}$$

The probability generating function is

$$\mathcal{G}_{Z_1}(t) = (1-p)^2 + p(1-p)(2-p)t + 2p^2(1-p)t^2 + p^3 t^3, \tag{5}$$

and hence the mean value, expressed as a function of p, is

$$\mathbb{E}(Z_1) = p(1-p)(2-p) + 4p^2(1-p) + 3p^3, \tag{6}$$

which is greater than 1 for $p \in (\sqrt{2}-1, 1] \approx (0.414214, 1]$.

If $\mathbb{E}(Z_1) < 1$, extinction is almost sure.

If $\mathbb{E}(Z_1) > 1$, defining iteratively $x_n = \mathcal{G}_{Z_1}(x_{n-1})$, with initial value $x_1 = \mathbb{P}[Z_1 = 0] = (1-p)^2$, x_n is the probability that the process terminates at or before the n-th generation, cf. Feller [5], Theorem p. 297.

The sequence $\{x_n\}$ is increasing, its limit $x \leq 1$ being the solution of the equation

$$x = \mathcal{G}_{Z_1}(x)$$

In the model at hand, the probability of extinction is therefore

$$x \equiv x_p = \min \left\{ 1, \frac{(p-2)p^2 + \sqrt{p^3(4-4p+p^3)}}{2p^3} \right\}, \tag{7}$$

On the other hand, the total number os descendants from the initial ancestor up to the n-th generation is $Y_n = 1 + Z_1 + Z_2 + \cdots + Z_n$, where Z_k denotes de number of units in the k-th generation. Following Good [7] (an argument that inspired Feller [5], XII.5), $R_1(t) = t\,\mathcal{G}(t)$ and iteratively $R_n(t) = t\,R_{n-1}(t)$, we obtain the probability generating functions for the successive generations.

This is a decreasing sequence, whose limit $\rho(s)$ satisfies $\rho(s) = s\,\mathcal{G}(\rho(s))$ and which may be found solving $t = s\,\mathcal{G}(t)$. Each coefficient r_k in the MacLaurin's expansion of $\rho(s)$ is the probability that the total progeny consists of k elements, and therefore if $\sum r_k = \rho(1) < 1$, this is the probability of extinction.
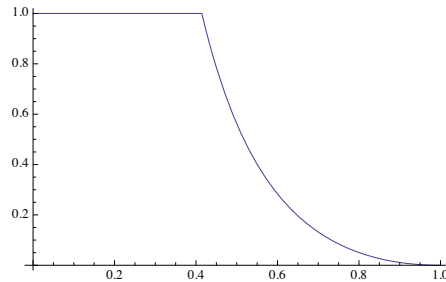
Fig. 1. Extinction probability x_p, in (7), as a function of p in the Bernoulli(p) off-springs randomized Fibonacci model.

The total progeny is finite whenever the expected value $\mu = \mathbb{E}(Z_1) < 1$. Therefore, as $\mathbb{E}(Z_n) = \mu^n$, it follows that the expected value of the total progeny is $\sum_{n=0}^{\infty} \mu^n = \frac{1}{1-\mu}$.

In this randomized Bernoulli Fibonacci modified model, from solving $t = s\,\mathcal{G}(t)$ we get

$$\rho(s) = \frac{2(-p^2 s + p^3 s)}{3\,p^3 s} - \frac{(1 - i\sqrt{3})A(s)}{32^{2/3}\,p^3 s\,\left((B(s) + \sqrt{4A^3(s) + B^2(s)})\right)^{1/3}} - \frac{(1 + i\sqrt{3})}{6 2^{1/3}\,p^3 s}\left((B(s) + \sqrt{4A^3(s) + B^2(s)})\right)^{1/3} \tag{8}$$

where $A(s) = -3p^3 s + (2p^4 - p^5 - p^6)s^2$, and $B(s) = 18(1 - p)p^5 s^2 + (7p^6 - 12p^7 + 3p^8 + 2p^9)s^3$.

Plotting the the real part of the above function $\rho(s)$, in (8), for $s = 1$, which indeed coincides with (7), we obtain a visual grasp of the probability of extinction as a function of p, exactly the one given in Fig. 1, using now a more complex definition of the function to be plotted.

Observe that the equilibrium point $p = \rho(p)$ is 0.513376. The observation that this is approximately the proportion of male offsprings in the observed equilibrium of human reproduction is surely circumstantial, or at least we do not devise any bond tying that empirical observation.

On the other hand, $\mu < 1$ for $p < \sqrt{2} - 1 \approx 0.414214$. Below, in Table 1 we register for a few values of p the expected size of the total progeny:

We now compare this analytic solution with the numerical results defining iteratively $x_n = \mathcal{G}_{Z_1}(x_{n-1})$, the probability that extinction does occur at or before the n-th generation, with initial value $x_1 = \mathbb{P}[Z_1 = 0] = (1 - p)^2$.

The successive repeated compositions of a function with itself can be computed using for instance the command "Nest" in *Mathematica*, and the corresponding evaluation at the appropriate point can then generate a list of coordinates with the command "Flatten".

In Table 2 we illustrate the result for the choices 0.1(0.1)0.9, and also for the extreme choices 0.01 and 0.99, and finally for the equilibrium value 0.513376 (using 200 points and 300 iterated compositions of the function with itself.

p	μ	Expected size $\frac{1}{1-\mu}$
0.1	0.21	1.26582
0.2	0.44	1.78571
0.3	0.69	3.22581
0.4	0.96	25
.41421	0.99999...	99246.7

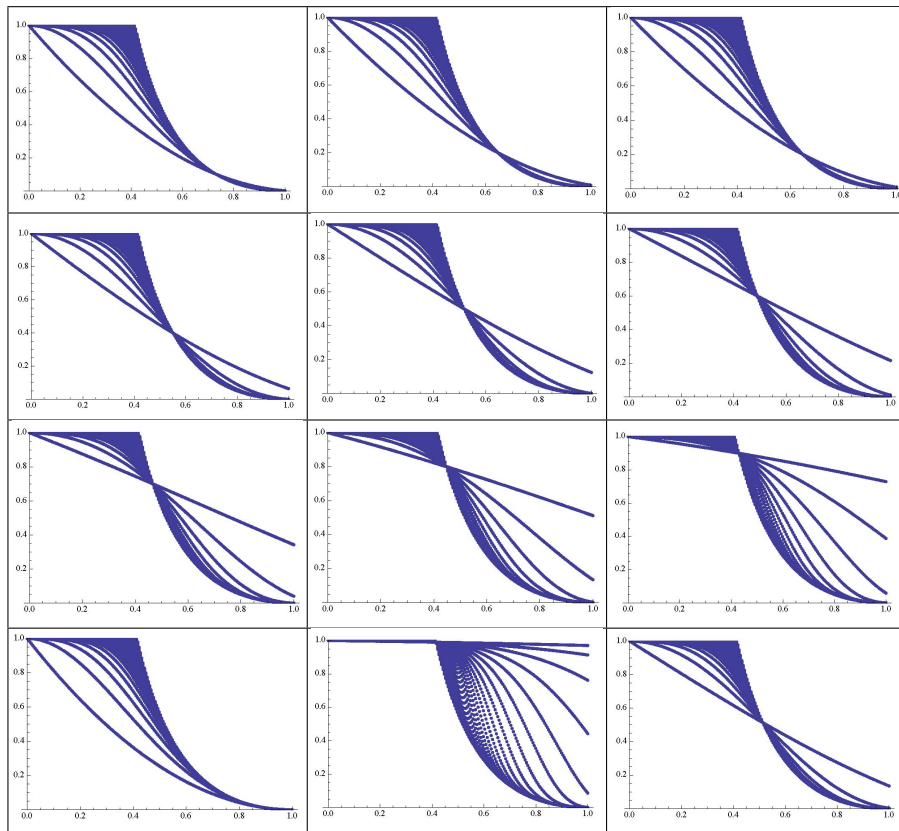**Table 1.** Expected total progeny when $\mu < 1$ in the modified Bernoulli randomized Fibonacci model.

Table 2. Graphical representation of 300 compositions of the generating function with itself; from left to right and top to bottom, initial 0.1, 0.2, 0.3, 0.4, 0.5, 0.6, 0.7, 0.8, 0.9, 0.01, 0.99, 0.513376.

From those graphics it is obvious that the use of the fixed point method leads to instabilities, that seem quite different in nature from the Feigenbaum bifurcations encountered in the discretization of the Verhulst model and its various extensions we have mentioned. Further research is needed to interpret those pathologies in the context of dynamical models.

3   Randomizing the Fibonaccy Population Growth Model Via Branching Processes

Let $\{f_n\}_{n \in \mathcal{S}_X}$ denote the probability mass function (pmf) of a discrete random variable (rv) X with support $\mathcal{S}_X \subset \mathbb{N}$. The corresponding probability generating function (pgf) is $m_X(t) = E(t^X) = \sum_{n=0}^{\infty} f_n t^n$.

If N is a discrete rv, $X_0 = 0$ and $X_1, X_2, \ldots$ independent replicas of X, with N and X_k independent, and we define the "compound" rv $Y = \sum_{k=0}^{N} X_k$, then

$$m_Y(t) = \sum_{j \in \mathcal{S}_Y} m_X^j(t)\, \mathbb{P}[N = j] = m_N(m_X(t)). \tag{9}$$

From this, we may easily compute mean value and variance of the rv Y. An alternative designation for the concept of compounding rv's is the concept of randomly stopped sums, which can have the advantage of explicitly indicating the type of the subordinator rv.

If in particular X_k, $k = 1, 2, \ldots$ are independent replicas of a count rv X modeling the number of direct descendants of each individual (or each female) in the population, and we define

$$Y_0 = 1, \qquad Y_1 = X_1, \qquad Y_2 = \sum_{k=0}^{Y_1} X_k, \quad \ldots \quad Y_{n+1} = \sum_{k=0}^{Y_n} X_k, \quad \ldots \tag{10}$$

we may interpret Y_k as the number of direct offsprings in the k-th generation, and $Z_n = \sum_{j=0}^{n} Y_j$ as the total progeny of some ancestor until the n-th generation. Let us denote $m(t) = m_1(t)$ the pgf of $Y_1 \overset{\mathrm{d}}{=} X$, $m_n(t)$ the pgf of Y_n; then $m_n(t) = m(m_{n-1}(t) = m^{\otimes(n)}(t)$, where $m^{\otimes(n)}$ denotes the n-fold composition of m with itself.

Following Good [7] (an argument that inspired Feller [5], XII.5), $m_{Z_1}(t) = t\, m_X(t)$ and iteratively $m_{Z_n}(t) = t\, m_{Z_{n-1}}(t)$, we obtain the probability generating functions for the number of descendants up to each successive generation.

This is a decreasing sequence, whose limit $\rho(s)$ satisfies $\rho(s) = s\, m_X(\rho(s))$ and which may be found solving $t = s\, m_X(t)$. Each coefficient r_k in the MacLaurin's expansion of $\rho(s)$ is the probability that the total progeny consists of k elements, and therefore if $\sum r_k = \rho(1) < 1$, this is the probability of extinction.

$\{Y_0, Y_1, ...\}$ is usually called a Galton–Watson branching process, or a cascade process. Simple examples of branching processes, and basic results on important problems such as extinction probability and size of a population can be found in Feller [5]. Namely, in what concerns extinction:

Theorem 1. *If $\mathbb{E}(Y) = \mu \leq 1$, the process almost surely dies out, and its expected size is $\dfrac{1}{1-\mu}$ when $\mu < 1$, and infinite when $\mu = 1$. If $\mu > 1$, the probability f_n that the process terminates at or before the n-th generation tends to the unique root $x < 1$ of the equation $x = m_Y(x)$.*

And, in what concerns the total progeny:

Theorem 2. *Denoting ρ_k the probability that the total progeny has k individuals,*

1. *the extinction probability is $\displaystyle\sum_{k=1}^{\infty} \rho_k$.*

2. *The pgf $\rho(s) = \displaystyle\sum_{k=1}^{\infty} \rho_k s^k$ is given by the unique positive root of $t = s\, m_Y(t)$, and $\rho(s) \leq x$.*

More extensive monographies on branching processes, with deeper results, are Harris [8], Athreya and Ney [2] or Jaegers [10]. Gnedenko and Korolev [6] present interesting examples of random infinite divisibility and random stability using branching processes, and they establish necessary and sufficient conditions for the convergence of randomly stopped sums, and limit theorems for super-critical (i. e., $\mu = \mathbb{E}(X) > 1$) Galton–Watson processes.

The $Y \frown Geometric(p)$ model for the number of direct descendants, with pmf $\{f_n = p\,(1-p)^n\}_{n\in\mathbb{N}}$, provides an algebraic simple treatment. In fact, writing $q = 1 - p$, $m_Y(t) = \dfrac{p}{1-qt}$, and

$$
m_{Y_n}(t) = \begin{cases} p\,\dfrac{q^n - p^n - (q^{n-1} - p^{n-1})\,q\,t}{q^{-1}n - p^{n-1} - (q^n - p^n)\,q\,t} & p \neq q \\[4mm] \dfrac{n - (n-1)t}{n + 1 - nt} & p = q = \frac{1}{2} \end{cases} \tag{11}
$$

is easily computed.

Both the $Bernoulli(p)$ and the $Geometric(p)$ pmf's satisfy the recursive expression

$$
f_{n+1} = \left(a + \frac{b}{n+1}\right) f_n, \quad \forall n \geq k, \quad f_n = 0 \text{ for } 0 \leq n \leq k-1 \tag{12}
$$

(in the case of $X \frown Bernoulli(p)$, $a = \dfrac{p}{p-1}$ and $b = \dfrac{2p}{1-p}$, and in the case of $X \frown Geometric(p)$, $a = q$ and $b = 0$). As we shall state in the following section, the above recursive expression is valid for the pmf of a broad class of rv's, known as Panjer rv's, that play an important role on the theory of collective risk. We investigate some consequences of using simple Panjer direct progeny models in branching processes.

4   Basic Count Models

We shall say that X is a Panjer rv if its pmf $\{f_n\}_{n \in \mathcal{S}_X}$ satisfies the recursive expression

$$f_{n+1} = \left(a + \frac{b}{n+1}\right) f_n, \quad \forall n \geq k, \quad f_n = 0 \text{ for } 0 \leq n \leq k-1. \qquad (13)$$

We denote $Panjer(a, b, k)$ the class of all pmf's satisfying (13).

This expression has been used by several authors, with $k = 0$, before Panjer [16], but it was in this seminal paper that the consequences for the iterative computation of the density of the collective risk process have been established.

In fact, Panjer [16] considered only the case $k = 0$ — for which the non degenerate types are the underdispersed binomial, the overdispersed negative binomial, and the Poisson in between —, but immediatly Sundt and Jewell [25] published the extension for $k = 1$, with the logarithmic and the extended negative binomial solutions.

Finally Hess *et al.* [9] defined the general class, with the recursion starting with $k \geq 0$, the $f_0, ..., f_{k-1}$ being free parameters (for $k = 0$, f_0 can be considered the starting jump of a hurdle process); it is also known as the class of basic count distributions, or class of basic claim distributions. For more details, cf. Rolsky *et al.* [24], Klugman *et al.* [11], and Pestana and Velosa [19].

Theorem 3. *Let* $\{f_n\}_{n \in \mathcal{S}_X}$ *be the pmf of a non degenerate count rv* X. *For* a, $b \in \mathbb{R}$ *the statements that follow are equivalent:*

(a) $\{f_n\}_{n \in \mathcal{S}_X}$ *is a* $Panjer(a, b; k)$ *pmf.*
(b) for $\ell \in \mathbb{N}^+$, *the pgf* $m_X(t) = \sum_{n=0}^{\infty} f_n t^n$ *satisfies the differential equations*

$$(1 - at)h^{(\ell)}(t) = (\ell a + b)h^{(\ell-1)}(t) + f_k \binom{k}{\ell}\ell! \, t^{k-1},$$

$t \in [0, 1)$ *and* $h^{(j)}(0) = 0$ *for* $j \leq k - 1$.
(c) m_X *satisfies the differential equation*

$$(1 - at)h^{(k+1)}(t) = ((k+1)a + b)h^{(k)}(t),$$

$t \in [0, 1)$ *and* $h^{(j)}(0) = 0$ *for* $j \leq k - 1$.

Further, $Q = Panjer(a, b; k) \implies (k+1)a + b > 0$, *and on the other hand* $a + b \geq 0 \Rightarrow a < 1$ *and* $a + b < 0 \Rightarrow a \leq 1$.

From this it is easy to conclude that the Panjer class has the following non degenerate elements:

1. The $Binomial(\nu, p)$, $\nu \in \mathbb{N}^+$, $p \in (0,1)$, which is $Panjer(\frac{p}{p-1}, \frac{(\nu+1)\,p}{1-p}, 0)$.
   Its variation index $\mathcal{I}(X) = \dfrac{\text{var}(X)}{\mathbb{E}(X)} = 1 - p < 1$, i.e., X is underdispersed.

2. The $Poisson(\mu)$, $\mu > 0$ is $Panjer(0, \mu, 0)$. Its dispersion index is 1.

3. The overdispersed $NegativeBinomial(\alpha, p)$, $\alpha > 0$, $p \in (0,1)$, with pmf $\left\{ \binom{\alpha+n-1}{n} p^n (1-p)^\alpha \right\}_{n \in \mathbb{N}}$, is $Panjer(p, (\alpha-1)\,p, 0)$.

4. The $ExtendedNegativeBinomial(\alpha, p, k)$, $\alpha \in (-k, -k+1)$, $p \in (0,1), k \in \mathbb{N}^+$, with pmf

$$f_n = \frac{\dbinom{\alpha+n-1}{n} p^n}{(1-p)^{-\alpha} - \sum_{j=0}^{k-1} \dbinom{\alpha+j-1}{j} p^j}, \quad n = k, k+1, ..., \qquad (14)$$

   in the support $\mathcal{S}_X = \{k, k+1, \dots\}$, is $Panjer(p, (\alpha-1)\,p, k)$. In the expression above the extended binomial coefficients $\dbinom{\alpha+n-1}{n}$ are defined as $\dbinom{\alpha+n-1}{n} = \dbinom{-\alpha}{n} = \dfrac{\Gamma(\alpha+n)}{\Gamma(\alpha)\,n!}$.

5. The $ExtendedLogarithmic(p, k)$, $p \in (0,1), k \in \mathbb{N}^+$, with pmf

$$f_n = \frac{\dfrac{p^n}{\dbinom{n}{m}}}{\displaystyle\sum_{j=m}^{\infty} \dfrac{p^j}{\dbinom{j}{m}}}, \quad n = k, k+1, ..., \qquad (15)$$

   is $Panjer(p, -kp, k)$.

6. If $X \frown Panjer(a, b, k)$, truncating $\{k, k+1, ..., \ell-1\} \subset \mathcal{S}_X$ we obtain a truncated rv $X^* \frown Panjer(a, b, \ell)$.

The special "unit" cases $Bernoulli(p) \equiv Binomial(1, p)$, $Geometric(p) \equiv NegativeBinomial(1, p))$, $ExtendedNegativeBinomial(\alpha, p, 1)$ whose pmf has the simple form $\dfrac{1 - (1 - q\,t)^{-\alpha}}{1 - p^{-\alpha}}$, $t \le \frac{1}{q}$), and $Panjer(p, -p, 1)$ or $Logarithmic(p)$ (or $ExtendedLogarithmic(1, p)$, with pgf $\dfrac{\ln(1 - pt)}{\ln(1 - p)}$), do have specially nice properties in each of the corresponding subclasses.

   In particular, $NegativeBinomial(\alpha, p)$ — and hence, as a special case $Geometric(p)$ — that result from a $Gamma$ randomization of the $Poisson(\Lambda)$, i.e., an hierarchic model with $\Lambda \frown Gamma(\alpha, 1)$ — are successfully used to

model the descendance of populations when the distribution of direct offsprings exhibits large variation, and both the the $ExtendedNegativeBinomial(\alpha, p, 1)$ and the $Logarithmic(p)$ distributions have been used to provide close fit to some natural populations.

In Table 2 below we sumarize results, indicating also the pgf $m_Q(t)$:

Table 3. Panjer distributions.

X	a	b	k	$m_Q(t)$
$Binomial(m, p)$	$\frac{p}{p-1}$	$\frac{(m+1)p}{1-p}$	0	$(1 - p + pt)^m$
$Poisson(\mu)$	0	μ	0	$e^{\mu(t-1)}$
$NegativeBinomial(\alpha, p)$	p	$(\alpha - 1)p$	0	$\left(\frac{1-pt}{1-p}\right)^{-\alpha}$
$ExtendedNegativeBinomial(\alpha, p, k)$	p	$(\alpha - 1)p$	k	$\frac{(1-pt)^{-\alpha} - \sum_{j=0}^{k-1}\binom{\alpha+j-1}{j}(pt)^j}{(1-p)^{-\alpha} - \sum_{j=0}^{k-1}\binom{\alpha+j-1}{j}p^j}$
$ExtendedLogarithmic(p, k)$	p	$-kp$	k	$\frac{\sum_{n=k}^{\infty}\binom{n}{k}^{-1}(pt)^n}{\sum_{n=k}^{\infty}\binom{n}{k}^{-1}p^n}$

5   Randomly Stopped Sums with Panjer Subordinator

The importance of the Panjer class is a consequence of the implications that the recursive expression (13) has on the recursive computation of the density of randomly stopped sums subordinated by Panjer rv's. This results from the following theorem:

Theorem 4. *Let $\{q_n\}_{n\in\mathbb{N}}$ be the pmf of a count distribution Y, and $\{f_n\}_{n\in\mathbb{N}}$ denote the pmf of a claim number distribution X whose support is a subset of the positive integers, i. e. $f_0 = 0$. Consider the randomly stopped sum*

$$T = \sum_{n=\inf \mathcal{S}_Y}^{Y} X_n,$$ *with Y and the replicas X_n of X independent.*

Then the following statements are equivalent:

1. $Y \frown Panjer(a, b, k)$;
2. *For any claim number rv* X *and any* $\ell \geq 1$, m_T *satisfies the differential equation*

$$(1 - a\, m_X(t))h^{(\ell)}(t) = \sum_{i=1}^{\ell} \binom{\ell}{i} (a + b\frac{i}{\ell})\, h^{(\ell-i)}(t)\, m_X^{(i)}(t) + q_k\, m_T^{(\ell)}(t),$$

$t \in [0, 1)$, *with the initial conditions* $h^{(j)}(0) = 0$ *for* $j \leq k - 1$.

From this, we can compute the pmf of a compound rv T with Panjer subordinator Y and count summands independent replicas of X, as defined above, by observing that for $\ell \geq 1$

$$(1 - a\, m_X(t))\, m_T^{(\ell)}(t) = \sum_{i=1}^{\ell} \binom{\ell}{i} \left(a + b\frac{i}{\ell}\right) m_T^{(\ell-i)}(t)\, m_X^{(i)}(t) + q_k\, [m_X^k(t)]^{(\ell)}.$$

In fact, the main consequence of Panjer's theory is the following result:

Theorem 5. *Let* $\{q_n\}_{n\in\mathbb{N}}$ *be the pmf of a count distribution* Y, *and* $\{f_n\}_{n\in\mathbb{N}}$ *denote the pmf of a claim number distribution* X *whose support is a subset of the positive integers. Consider the randomly stopped sum* $T = \sum_{n\in\mathcal{S}_Y} X_n$, *with* Y *and the replicas* X_n *of* X *independent. Then*

$$\mathbb{P}[T = n] = g_n = \begin{cases} m_Y(m_X(0)) = m_T(f_0) & n = 0 \\[2ex] \dfrac{1}{1 - a\, f_0} \left[\sum_{i=1}^{n} \left(a + b\frac{i}{n}\right) g_{n-i} f_i \right] + q_k f_n^{*k} & n \geq 1 \end{cases} \tag{16}$$

where f_n^{*k} *stands for the k-th iterated convolution of the sequence* $\{f_n\}$ *with itself.*

(There exists a simple extension for the density when the summands are absolutely continuous, but it is not relevant in the context of branching processes.)

6   Discussion and Conclusions

With the exception of *Poisson* or of *Geometric* subordinator — i.e., of a $Panjer(0, \mu, 0)$ or a $Panjer(p, 0, 0)$, respectively, cf. Pestana and Velosa [19] on the simplicity of these cases when compared to the complexity of others — we couldn't obtain any close expressions for the n-fold composition of the pgf for any other Panjer subordinators. Aside from those two cases, the only one for which we got more promising results has been — as predictable — the

Logarithmic(p). Moreover, when the aim is to extend the Fibonacci sequence using branching randomization, in case we want to remove individuals from the population after two mating epochs, we have the extra burden of subtracting, the two rv's used being dependent.

Happily, compound pgf's are amenable to compute mean values and variances, and in what concerns the mean value we have the extra facility that the mean value of the difference is the difference of the means values, regardless whether the random variables are dependent or independent. So, it is easy to follow the process on average, and the relation of the sequence of expected values to the sequence of Fibonacci numbers simple.

The quantities of interest — extinction probability and expected total size in the supercritical case, size of the n-th generation, total size of the population up to the n-th generation — can be dealt with computationally. When the fixed point method is used to compute roots of some equation $F(x) = x$, numerical instabilities are a rule whenever F is too steep, and the sufficient convergence conditions are not met.

References

1. Aleixo, S., Rocha, J.L., and Pestana, D., Probabilistic Methods in Dynamical Analysis: Population Growths Associated to Models Beta (p,q) with Allee Effect, in Peixoto, M. M; Pinto, A.A.; Rand, D.A.J., editors, *Dynamics, Games and Science, in Honour of Maurício Peixoto and David Rand*, vol II, Ch. 5, pages 79–95, New York, 2011, Springer Verlag.
2. Athreya, K. B., and Ney, P. E. *Branching processes*, New York, 2004, Dover.
3. Brilhante, M.F., Gomes, M.I., and Pestana, D., BetaBoop Brings in Chaos. *Chaotic Modeling and Simulation*, 1: 39–50, 2011.
4. Brilhante, M.F., Gomes, M.I., and Pestana, D., Extensions of Verhulst Model in Population Dynamics and Extremes, in Ch. Skiadas (eds) Proceedings, 5th Chaotic Modeling and Simulation International Conference, 115–122, 2012.
5. Feller, W., *An Introduction to Probability Theory and Its Applications*, vol. I, New York, 1968, Wiley.
6. Gnedenko, B. V., and Korolev, V. Yu. *Random Summation. Limit Theorems and Applications*, Boca Raton and New York, 1996, CRC Press.
7. Good, I.J., The number of individuals in a cascade process, *Proc. Cambridge Philos. Soc.* **45**, 360–363, 1949.
8. Harris, H. *Theory of Branching Processes*, Englewood Cliffs, 1963, Prentice-Hall.
9. Hess, K. Th., Liewald, A., and Schmidt, K. D. An Extension of Panjer's Recursion, *Astin Bulletin* **32**, 283–297, 2002.
10. Jaegers, P. *Branching Processes with Biological Applications*, London-New York-Sydney-Toronto, 1975, Wiley.
11. Klugman, S. A., Panjer, H. H., and Willmot, G. E. *Loss Models*, New York and Chichester, 1998, Wiley.
12. Kovalenko, I.N., On a class of limit distributions for rarefied flows of homogeneous events, *Lit. Mat. Sbornik* **5**, 569–573, 1965. (Transation: On the class of limit distributions for thinning streams of homogeneous events, *Selected Transl. Math. Statist. and Prob.* **9**, 75– 81, 1971, Providence, Rhode Island.)
13. Kozubowski, T.J., Representation and properties of geometric stable laws, *Approximation, Probability, and Related Fields*, New York, 321–337, 1994, Plenum.

14. Lotka, A.J., *Elements of Physical Biology*, Baltimore, 1925, Williams and Wilkins Co (reprinted under the title *Elements of Mathematical Biology*, New York, 1956, Dover).

15. Lotka, A.J., *Thorie Analytique des Associations Biologiques, II*, Paris, 1939, Herman.

16. Panjer, H. H. Recursive Evaluation of a Family of Coumpound Distributions, *Astin Bulletin* **12**, 22–26, 1981.

17. Pestana, D., Aleixo, S., and Rocha, J.L., Regular variation, paretian distributions, and the interplay of light and heavy tails in the fractality of asymptotic models. In C. H. Skiadas, I. Dimotikalis and C. Skiadas, editors, *Chaos Theory: Modeling, Simulation and Applications*, pages 309–316, Singapore 2011. World Scientific.

18. Pestana, P., Lindenmayer Systems and the Harmony of Fractals, *Chaotic Modeling and Simulation* (CMSIM) 1: 91–99, 2012.

19. Pestana, D., and Velosa, S. Extensions of Katz–Panjer Families of Discrete Distributions, *REVSTAT Statistical Journal* **2**, 145–162.

20. Prusinkiewicz, P., and Hanan, J., *Lindenmayer Systems, Fractals, and Plants* (Lecture Notes in Biomathematics). Springer-Verlag, 1989.

21. Rachev, S.T., and Resnick, S., Max-geometric infinite divisibility and stability, *Communications in Statistics — Stochastic Models*, 7:191–218, 1991.

22. Rényi, A., A characterization of the Poisson process, *MTA Mat. Kut. Int. Kzl.* **1**, 519–527, 1956. (English translation in *Selected Papers of Alfred Rényi, 1, 1948–1956*, P. Turán, editors, 622–279 Akadémiai Kiadó, Budapest).

23. Rocha, J.L., Aleixo, S., and Pestana, D., Beta(p,q)-Cantor Sets: Determinism and Randomness. In C.H. Skiadas, I. Dimotikalis and C. Skiadas (Eds.), Chaos Theory: Modeling, Simulation and Applications, World Scientific Books, 333–340, 2011.

24. Rolski, T. , Schmidli, H. , Schmidt, V. , and Tengels, J. *Stocastic Processes for Insurance and Finance*, New York and Chichester, 1998, Wiley.

25. Sundt, B., and Jewell, W. S. Further Results on Recursive Evaluation of Coumpound Distributions, *Astin Bulletin* **12**, 27–39, 1981.

26. Tsoularis, A., Analysis of logistic growth models. *Res. Lett. Inf. Math. Sci.*, vol. 2:23–46, 2001.

27. Verhulst, P.-F., Notice sur la loi que la population poursuit dans son accroissement. *Corresp. Math. Physics* 10:113–121, 1838. (easily available in `http://books.google.pt/books?id=8GsEAAAAYAAJ&printsec=frontcover&hl=pt-PT&source=gbs_ge_summary_r&cad=0#v=onepage&q&f=false`

28. Verhulst, P.-F., La loi de l'accroissement de la population, *Nouveaux Mémoires de l'Académie Royale des Sciences et Belles-Lettres de Bruxelles*, 18:1–42, 1845. (available at `http://gdz.sub.uni-goettingen.de/dms/load/img/`.)

29. Verhulst, P.-F., Deuxième mémoire sur la loi d'accroissement de la population. *Mémoires de l'Académie Royale des Sciences, des Lettres et des Beaux-Arts de Belgique* 20:1–32, 1847. (`http://gdz.sub.uni-goettingen.de/dms/load/img/`)

30. Waliszewski, J., and Konarski, J., A Mystery of the Gompertz Function, in G.A. Losa, D. Merlini, T. F .Nonnenmacher and E.R. Weibel, editors, *Fractals in Biology and Medicine*, Basel, 277–286, 2005, Birkhäuser.

Exploring Sullivan's Health Status Index of Mortality and Morbidity

Christos H Skiadas[1] and Charilaos Skiadas[2]
[1]ManLab, Technical University of Crete, Chania, Crete, Greece
Email: skiadas@cmsim.net
[2]Department of Mathematics and Computer Science, Hanover College, Indiana, USA

Sullivan proposed the most used index of mortality and morbidity, a relatively simple and easy to apply method as an extension of the classical life table. In his study he had also estimated the disability free life expectancy for USA the year 1965. Although the estimated healthy life years lost from disability by Sullivan are only a small proportion of the recent estimates we further check the related estimates done in 1971 because in these days the disability estimates were focused mainly on the severe disability causes resulting in no active years of life. We have tested Sullivan's results for USA (1965) with one of our hitting time models and found significant differences for the healthy age at birth but very good approach for the healthy age at 65 years of age. Related study was published for New Zealand (2006) and the results are in a very good agreement with ours. In the latter case we have estimated the active life expectancy for 34 countries from the human mortality database. The advantage of our method is that we use only population and death data without the use of results from health questionnaires.

Introduction

Daniel F. Sullivan introduced a remarkable method for estimating the healthy life expectancy based on the classical Life Table. The seminal paper on "A Single Index of Mortality and Morbidity" was published in 1971 in Health Services and Mental Health Administration (HSMHA) Health Reports. Reading his paper you understand the deep insight on the subject from the author leading to his remarkable work. Furthermore, few years ago (1966), he had done an extensive analysis on the definition and estimation of the population health status. Sanders (1964) explored the measurement of community health levels. Chiang (1965) work directed towards mathematical models for the health status and George W. Torrance (1976) proposed a unified mathematical approach to the health status index models including a detailed bibliographic search of the existing models.
Between all models presented the Sullivan model was already a quite promising model from the applied point of view. Sullivan in his 1971 work already had estimated the loss of healthy life years for USA by using his method. This was a

very important point to promote his health status index. It was an index providing results. Not a theoretical one.

The missing point when launching questionnaires is that the expected replies will based on people's experience on what we call health; good health, bad health or death. Replies express our experience on health based on the data already known by individuals. These data include deaths and population and the inevitable decline of the known population by means people of the same or similar age to be in good or bad condition or dead. That we ask people is already included in our databases for the existing population by year of age and the related number of deaths at every year of age.

However, a question arises regarding the health status or the health state of individuals. As we have only population and death data where is the information for the health state hidden?

The reply is as simple as the replies received from people when we launch questionnaires. People have similar data from a closed of course environment. The health state estimated comes mainly as a comparison with the main event; death and less as a measure of disabilities. Of course people have a way to understand the way disabilities lead to a lower and lower health status and finally death. But why does not exist a mathematical model or method to produce similar results as the replies of people to questionnaires? As people make simple estimates we can search for not a very complicated model. A simple but yet quite important was proposed by Torrance (1976). The basis was a simple procedure expressing by 1 the alive and by 0 death persons. He considered the state of functioning of an organism by adding intermediate cases with levels of disability. This was a model mainly directed towards the direction of collecting disability data via a health system or questionnaires.

However, the most important point of his study was the definition of the Health Status over time t of a population denoted by $H(t)$. He suggests that this Health Status will come as a summation of the related health status $h(t)$ of every individual into the population with a related weight when appropriate.

As the health status of an individual is a stochastic process the next point should be the derivation of the health status of a population as the probability density function of the health status stochastic process from the barrier which could be set as zero for simplicity. However, Torrance (1976) probably was not aware for the developments in this direction already done in a very theoretical level from 1971 to 1976 (for an analysis see [2, 4-15]). Even today only few researchers enter into the complicated world of the first exit or hitting time processes. Instead Torrance and mainly Sullivan preferred the leading system used by actuaries and demographers the last four centuries that is the Classical Life Tables. They thus established a quite strong and relatively easy to apply system which turned out to be the preferred method to estimate the health status or health status index in very many countries and for several time periods with a cost of an enormous statistical survey system all over the world.

Two main points where missing:

1. The proposal of a hitting time model expressing the health status of a population something done by Janssen and Skiadas (1995) and the publications by Skiadas and Skiadas from 2007 until today (5-15).
2. The finding of a method to estimate the health status of a population from death and population data only, thus providing a useful tool for comparisons between countries and regions avoiding the bias resulting from the way people with different cultures and way of living respond to the health questionnaires.

The task of this paper is to insert a Sullivan like method to the already proposed Health State Life Table thus providing an extra tool for estimating the healthy life expectancy and the loss of healthy life years without using data from questionnaires. The simplest first exit time model used was proposed by Skiadas and Skiadas (2010) [8, 9]. The model is expressed by the following formula for the hitting time probability density function $g(t)$ at time t

$$g(t) = k(l + (c-1)(bt)^c)(t)^{-3/2} e^{-\frac{(l-(bt)^c)^2}{2t}}$$

where b, l, c, k are parameters. The Health State Function is

$$H(t) = l - (bt)^c$$

This is a declining function for the *health state of a population* as we have called the analogous *health status of population* in terms of Sullivan. The slight different terminology was accepted to distinguish the estimates done by using models and modeling from the estimates based on questionnaires. However, both terms will tend to express the same as both methods tend to provide similar results. The first attempt is presented in this paper. We use the model for the Health State of a population to estimate the fraction of people with disabilities per year of age, thus enabling the estimation of the Active Live Expectancy (ALE) via a Health State Life Table. This is the classical life table in which we have added a Sullivan like part for the healthy life expectancy estimation. Both abridged and complete Health State Life Tables were constructed. Due to space limits only the abridged table is included (see Table I).
The proportion of the loss of healthy life years is estimated with the method illustrated in Figures 1 and 2. Figure 1 illustrates the case of USA females the year 1965. The blue curve is the estimated from the hitting time procedure health state function $H(t)$ of the population. The line AB expresses the optimum case (no deaths) with no disabilities and other health declining phenomena whereas the curve ADC expresses the real situation.
That is immediately clear is that the area ABCDA represents the total loss of health of the population whereas the area ADCOA expresses the Healthy region. As a consequence the fraction ABCDA/ABCOA provides the net loss of health of the population from zero to 110 years of age. This is the important information enabling us to estimate the Active Life Expectancy (ALE) and the

Loss of Active Life Years (LALY) according to the terminology used by the Ministry of Health and Statistics New Zealand (2008) in a published discussion paper [3]. For our application we use the classical Life Table expanded for the estimation of the Active Life Expectancy.

TABLE I

| Abridged Health State Life Table (0 - 85+) for New Zealand (males 2006)										
The Abridged Life Table Including Life Expectancy and Active Life Expectancy Estimation										
Life Expectancy Estimation						Active Life Expectancy Estimation				
Age	Mortality	100.000 population Sx and Number of Deaths dx		Survivorship	Tx=S(Lx)	Life Expectancy	Fraction of Loss of Active Life Years	Survivorship without disability	Txd=S(Lxd)	Active Life Expectancy	Loss of Active Life Years
x	qx	Sx	dx	Lx	Tx	ex	px_active	Lxd_total	Txd_total	ALE	LALY
0	0,0059	100000	589	99.470	7.803.206	78,0	0,000	99.470	7.488.886	74,9	3,1
1	0,0011	99411	112	397.419	7.703.736	77,5	0,000	397.419	7.389.416	74,3	3,2
5	0,0008	99299	79	496.295	7.306.317	73,6	0,000	496.294	6.991.997	70,4	3,2
10	0,0008	99219	80	495.895	6.810.022	68,6	0,000	495.885	6.495.703	65,5	3,2
15	0,0044	99139	436	494.604	6.314.127	63,7	0,000	494.555	5.999.818	60,5	3,2
20	0,0045	98703	440	492.413	5.819.523	59,0	0,000	492.246	5.505.263	55,8	3,2
25	0,0047	98262	465	490.150	5.327.110	54,2	0,001	489.702	5.013.017	51,0	3,2
30	0,0051	97798	501	487.736	4.836.960	49,5	0,002	486.714	4.523.315	46,3	3,2
35	0,0059	97297	571	485.057	4.349.224	44,7	0,004	482.978	4.036.601	41,5	3,2
40	0,0079	96726	765	481.716	3.864.167	39,9	0,008	477.851	3.553.623	36,7	3,2
45	0,0125	95961	1.198	476.810	3.382.451	35,2	0,014	470.119	3.075.773	32,1	3,2
50	0,0186	94763	1.758	469.421	2.905.641	30,7	0,023	458.520	2.605.654	27,5	3,2
55	0,0300	93005	2.792	458.046	2.436.220	26,2	0,037	441.222	2.147.133	23,1	3,1
60	0,0492	90213	4.435	439.979	1.978.174	21,9	0,056	415.364	1.705.911	18,9	3,0
65	0,0772	85778	6.620	412.341	1.538.195	17,9	0,083	378.311	1.290.548	15,0	2,9
70	0,1266	79158	10.020	370.740	1.125.854	14,2	0,118	326.830	912.237	11,5	2,7
75	0,2034	69138	14.064	310.531	755.114	10,9	0,166	258.992	585.407	8,5	2,5
80	0,3246	55074	17.874	230.685	444.583	8,1	0,228	178.145	326.415	5,9	2,1
85	1	37200	37.200	213.899	213.899	5,8	0,307	148.270	148.270	4,0	1,8
		100.000						*Developed by Christos H Skiadas 19 April 2014*			
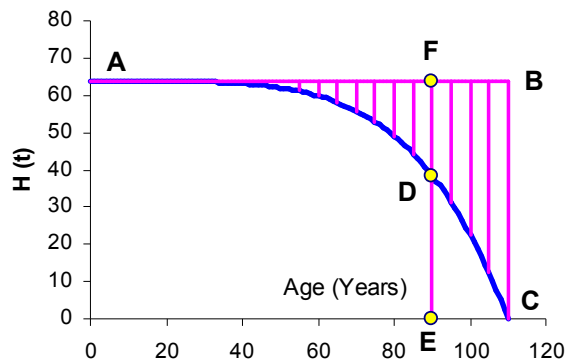
Figure 1. Health State of USA Population (females, 1965)

The estimates at an age level $x=t$ provide the formula for the fraction of the loss of active life years p_x

$$p_x=(DF)/(EF)$$

It is clear that $p_x=0$ at zero age and 1 at the end of the life time. The resulting fraction of the loss of active life years during age is presented in Figure 2.
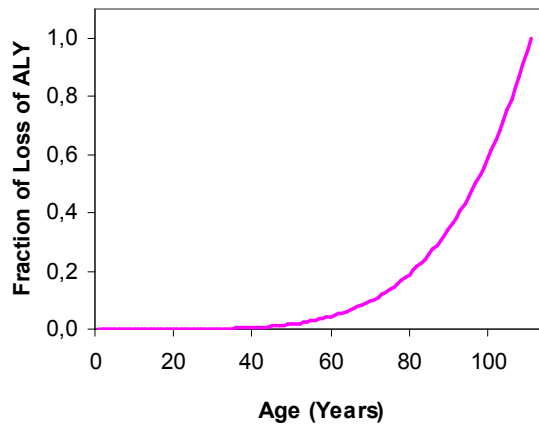

Figure 2. The fraction of the loss of active life years

TABLE II					
Comparisons of our model with Sullivan's results					
	Life Expectancy, Healthy Life Expectancy and Loss of Healthy Life Years at Birth (USA 1965)				
	Sullivan	Model	Sullivan	Model	Sullivan	Model
Both	70.2	70.1	64.9	66.5	5.3	3.6
Males	66.8	66.7	61.6	62.7	5.2	4.0
Females	73.7	73.8	68.4	70.6	5.3	3.2
	Life Expectancy, Healthy Life Expectancy and Loss of Healthy Life Years at Age 65 (USA 1965)				
	Sullivan	Model	Sullivan	Model	Sullivan	Model
Both	14.6	14.6	11.3	11.4	3.3	3.2
Males	12.9	12.8	9.4	9.5	3.5	3.3
Females	16.2	16.3	13.1	13.3	3.1	3.0

Our method is tested with the results presented in Sullivan's paper for USA 1965. Table II summarizes the results and Table III includes the parameter estimates for the model used. For the healthy life expectancy at birth our method underestimates Sullivan's results, whereas the findings for both methods are

almost identical for the healthy life expectancy at age 65 for males, females and both.

TABLE III						
Four Parameter Hitting Time Model						
	Model Parameters				Statistics	
USA 1965	b	l	k	c	SSE	R^2
Both	0.0250	13.41	0.367	4.00	0.000654	0.944
Males	0.0293	13.96	0.366	3.45	0.000820	0.926
Females	0.0200	13.85	0.367	4.65	0.000494	0.965

TABLE IV						
Comparisons of our model with New Zealand's results						
	Life Expectancy, Healthy Life Expectancy and Loss of Healthy Life Years at Birth for ALE (Active Life Expectancy)					
	Life Expectancy at Birth (LE)		Active Life Expectancy (ALE)		Years without Active Life	
Males 2006	New Zealand	Model	New Zealand	Model	New Zealand	Model
0	78.1	78.0	74.9	74.9	3.2	3.1
15	63.7	63.7	60.7	60.5	3.0	3.2
25	54.2	54.2	51.3	51.0	2.9	3.2
45	35.3	35.2	32.5	32.1	2.8	3.1
65	18.0	17.9	15.5	15.0	2.5	2.9
Females 2006	New Zealand	Model	New Zealand	Model	New Zealand	Model
0	82.1	82.0	78.4	78.9	3.7	3.1
15	67.6	67.5	64.0	64.4	3.6	3.1
25	57.8	57.7	54.4	54.6	3.4	3.1
45	38.5	38.3	35.2	35.2	3.3	3.1
65	20.6	20.4	17.5	17.5	3.1	2.9

We had another opportunity to test our model results with relatively more recent findings for New Zealand for Active Life Expectancy for males and females in 2006. The comparative study is presented in Table IV. The findings are in perfect agreement with the related study for New Zealand [3].

Discussion

The estimation for the active life expectancy with our method provides very good results because the method is based on the dramatic loss of health during the few last years of the life span easily provided by the model. Similar results we have explored in several countries for 2006 (see Table V). Other

transformations will make possible the estimation of other disability life periods including of healthy life years from moderate or light disability causes.

Country	Males 2006			Females 2006		
	LE	ALE	LALY	LE	ALE	LALY
Australia	79.1	75.7	3.4	84.1	80.4	3.7
Austria	77.0	74.0	3.0	83.1	79.8	3.3
Belarus	63.3	59.4	3.9	75.3	72.4	2.9
Belgium	76.5	73.6	2.9	82.5	79.3	3.3
Bulgaria	69.1	65.4	3.7	76.1	73.6	2.5
Canada	78.2	74.7	3.5	83.2	79.3	3.9
Czech Republic	73.3	70.0	3.3	79.9	77.0	2.9
Denmark	75.8	72.2	3.6	80.8	76.7	4.1
Estonia	67.3	63.0	4.3	78.5	75.7	2.8
Finland	75.7	72.7	3.0	83.1	80.0	3.1
France	77.3	74.1	3.2	84.8	81.0	3.8
Germany	76.9	73.6	3.3	82.7	79.2	3.5
Hungary	69.0	64.2	4.8	77.5	74.5	3.0
Ireland	77.2	73.5	3.7	82.1	78.0	4.1
Israel	78.4	74.1	4.3	82.3	77.8	4.5
Italy	78.5	74.9	3.6	84.4	80.2	4.2
Japan	78.9	75.1	3.8	86.4	82.0	4.4
Latvia	65.6	60.8	4.8	76.3	73.8	2.5
Lithuania	65.2	60.5	4.7	76.9	74.5	2.4
Luxemburg	76.9	73.8	3.1	82.6	79.8	2.8
Netherlands	77.6	74.2	3.4	82.1	79.0	3.1
New Zealand	78.0	74.7	3.3	82.5	79.1	3.4
Norway	78.1	75.2	2.9	83.0	80.0	3.0
Poland	70.7	66.6	4.1	79.4	76.3	3.1
Portugal	75.3	72.5	2.8	82.3	78.4	3.9
Russia	60.2	56.4	3.8	73.1	70.6	2.5
Slovakia	70.3	66.4	3.9	78.3	75.3	3.0
Slovenia	74.2	70.8	3.4	81.7	78.2	3.5
Spain	77.4	74.1	3.3	84.4	80.4	4.0
Sweden	78.7	75.7	3.0	83.2	80.0	3.2
Switzerland	79.1	75.7	3.4	84.6	80.9	3.7
UK	77.1	73.5	3.6	81.7	77.7	4.0
Ukraine	62.2	58.3	3.9	73.6	71.1	2.5
USA	75.3	71.9	3.4	80.7	76.9	3.8

TABLE V - Active Life Expectancy Estimation

References

1. Chiang, C. L., An Index of Health: Mathematical Models, U.S. Department of HEW, Public Health Service, Publication No. lCXK). Series 2, No. 5 (May 1965).

2. Janssen J, Skiadas CH (1995) Dynamic modelling of life-table data. Applied Stochastic Models and Data Analysis, 11, 1:35-49

3. Ministry of Health and Statistics New Zealand. (2008). Health Expectancy: Toward Tier 1 official statistic status. Wellington: Ministry of Health and Statistics New Zealand. Discussion paper, November 2008.

4. Sanders, B. S., (1964) "Measuring Community Health Levels," American Journal of Public Health, Vol. 54, pp. 1063-1070.

5. Skiadas CH (1 Oct 2011) A Life Expectancy Study based on the Deterioration Function and an Application to Halley's Breslau Data. arXiv:1110.0130v1 [q-bio.PE]

6. Skiadas CH (4 Dec 2011) Life Expectancy at Birth, Estimates and Forecasts in the Netherlands (Females). arXiv:1112.0796v1 [q-bio.PE]

7. Skiadas CH, Skiadas C (2007) A modeling approach to life table data. In Recent Advances in Stochastic Modeling and Data Analysis. C. H. Skiadas, Ed. (World Scientific, Singapore), 350–359

8. Skiadas CH, Skiadas C (2010) Comparing the Gompertz Type Models with a First Passage Time Density Model. In Advances in Data Analysis, C. H. Skiadas Ed. (Springer/Birkhauser, Boston), 203-209

9. Skiadas CH, Skiadas C (2010) Development, Simulation and Application of First Exit Time Densities to Life Table Data. Communications in Statistics 39, 444-451

10. Skiadas CH, Skiadas C (2011) Exploring life expectancy limits: First exit time modelling, parameter analysis and forecasts. In Chaos Theory: Modeling, Simulation and Applications, C. H. Skiadas, I. Dimotikalis and C. Skiadas, Eds. (World Scientific, Singapore), 357–368

11. Skiadas CH, Skiadas C (10 Jan 2011) Properties of a Stochastic Model for Life Table Data: Exploring Life Expectancy Limits. arXiv:1101.1796v1 [nlin.CD]

12. Skiadas CH, Skiadas C (Jan 2013) The Health State Function of a Population. Athens http://www.amazon.com/Health-State-Function-Population/dp/6188046505/ref=sr_1_1?s=books&ie=UTF8&qid=1364343495&sr=1-1

13. Skiadas CH, Skiadas C (Dec 2013) Supplement: The Health State Function of a Population, Athens http://www.amazon.com/Supplement-Health-State-Function-Population/dp/6188069831/ref=sr_1_13?s=books&ie=UTF8&qid=1391111075&sr=1-13&keywords=christos+h+skiadas

14. Skiadas CH, Skiadas C (2014) The First Exit Time Theory applied to Life Table Data: the Health State Function of a Population and other Characteristics. Communications in Statistics-Theory and Methods, 43: pp. 1585-1600.

15. Skiadas CH, Skiadas C (2014) Exploring the State of a Stochastic System via Stochastic Simulations: An Interesting Inversion Problem and the Health State Function, Methodology and Computing in Applied Probability (accepted).

16. Sullivan, D. F., (May 1966) Conceptual Problems in Developing an Index of Health, U.S. Department of HEW, Public Health Service Publication No. 1000, Series 2, No. 17.

17. Sullivan, D. F. (April 1971) (National Center for Health Statistics): A single index of mortality and morbidity. HSMHA Health Reports, Vol. 86, pp. 347-354.

18. Torrance G. W. (1976) Health Status Index Models: A Unified Mathematical View, Management Science, 22(9): pp. 990-1001.

Synchronization in von Bertalanffy's models

J. Leonel Rocha[1], Sandra M. Aleixo[1] and Acilina Caneco[2]

[1] Instituto Superior de Engenharia de Lisboa - ISEL, ADM and CEAUL, Rua Conselheiro Emídio Navarro, 1, 1959-007 Lisboa, Portugal
(E-mail: `jrocha@adm.isel.pt, sandra.aleixo@adm.isel.pt`),
[2] Instituto Superior de Engenharia de Lisboa - ISEL, ADM and CIMA-UE, Rua Conselheiro Emídio Navarro, 1, 1959-007 Lisboa, Portugal
(E-mail: `acilina@adm.isel.pt`)

Abstract. Many data have been useful to describe the growth of marine mammals, invertebrates and reptiles, seabirds, sea turtles and fishes, using the logistic, the Gompertz and von Bertalanffy's growth models. A generalized family of von Bertalanffy's maps, which is proportional to the right hand side of von Bertalanffy's growth equation, is studied and its dynamical approach is proposed. The system complexity is measured using Lyapunov exponents, which depend on two biological parameters: von Bertalanffy's growth rate constant and the asymptotic weight.

Applications of synchronization in real world is of current interest. The behavior of birds flocks, schools of fish and other animals is an important phenomenon characterized by synchronized motion of individuals. In this work, we consider networks having in each node a von Bertalanffy's model and we study the synchronization interval of these networks, as a function of those two biological parameters. Numerical simulation are also presented to support our approaches.
Keywords: Von Bertalanffy's models, synchronization, Lyapunov exponents.

1 Introduction and motivation

Several mathematical equations have been used to describe the growth of marine populations, namely fishes, seabirds, marine mammals, invertebrates, reptiles and sea turtles. Among these equations, three of the most familiar are the logistics, the Gompertz and the von Bertalanffy models, see [8] and references therein. For a certain population, the growth of an individual, regarded as an increase in its length or weight with increasing age, is commonly modeled by a mathematical equation that represents the growth of an "average" individual in the population. One of the most popular functions that have been used to analyze the increase in average length or weight of fish is von Bertalanffy's model, see for example [2] and [5].

Synchronization is a fundamental nonlinear phenomenon, which can be observed in many real systems, in physics, chemistry, mechanics, engineering, secure communications or biology, see for example [1]. It can be observed in

living beings, on the level of single cells, physiological subsystems, organisms and even on the level of large populations. Sometimes, this phenomenon is essential for a normal functioning of a system, e.g. for the performance of a pacemaker, where the synchronization of many cells produce a macroscopic rhythm that governs respiration and heart contraction. Sometimes, the synchrony leads to a severe pathology, e.g. in case of the Parkinson's disease, when locking of many neurons leads to the tremor activity. Biological systems use internal circadian clocks to efficiently organize physiological and behavioral activity within the 24-hour time domain. For some species, social cues can serve to synchronize biological rhythms. Social influences on circadian timing might function to tightly organize the social group, thereby decreasing the chances of predation and increasing the likelihood of mating, see [4]. Almost all seabirds breed in colonies; colonial and synchronized breeding is hypothesized to reduce predation risk and increases social interactions, thereby reducing the costs of breeding . On the other hand, it is believed that synchronization may promote extinctions of some species. Full synchronism may have a deleterious effect on population survival because it may lead to the impossibility of a recolonization in case of a large global disturbance, see [16]. Understand the aggregate motions in the natural world, such as bird flocks, fish schools, animal herds, or bee swarms, for instance, would greatly help in achieving desired collective behaviors of artificial multi-agent systems, such as vehicles with distributed cooperative control rules.

The layout of this paper is as follows. In Sec.2, we present a new dynamical approach to von Bertalanffy's growth equation, a family of unimodal maps, designated by von Bertalanffy's maps. In Sec.3, we present the network model having in each node a von Bertalanffy's model. The synchronization interval is presented in terms of the network connection topology, expressed by its Laplacian matrix and of the Lyapunov exponent of the network's nodes. In Sec.4, we give numerical simulations on some kinds of lattices, evaluating its synchronization interval. We present some discussion on how this interval changes with the increasing of the number of neighbors of each node, with the increasing of the total number of nodes and with the intrinsic growth rate. We also observe and discuss some desynchronization phenomenon.

2   Von Bertalanffy's growth dynamics approach

An usual form of von Bertalanffy's growth function, one of the most frequently used to describe chick growth in marine birds and in general marine growths, is given by

$$W_t = W_\infty \left(1 - e^{-\frac{K}{3}(t-t_0)} \right)^3, \qquad (1)$$

where W_t is the weight at age t, W_∞ is the asymptotic weight, K is von Bertalanffy's growth rate constant and t_0 is the theoretical age the chick would have at weight zero. The growth function, Eq.(1), is solution of the von Bertalanffy's
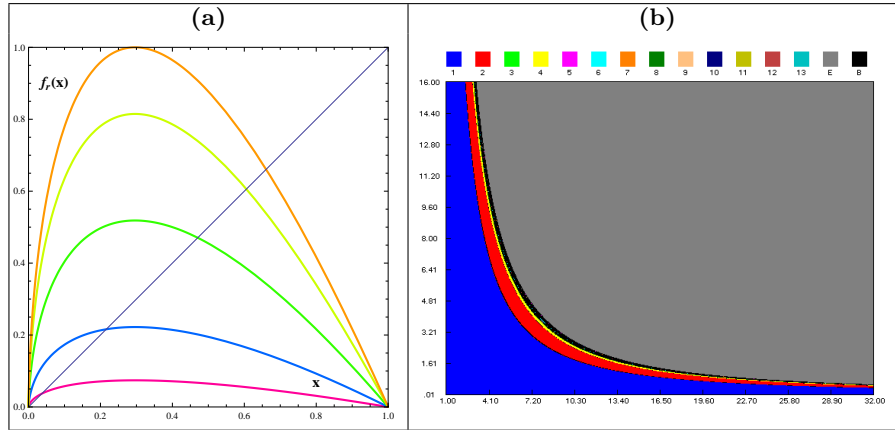
Fig. 1. (a) Graphics of von Bertalanffy's maps $f_r(x)$, Eq.(4), for several values of intrinsic growth rate r (0.5 (magenta), 1.5, 3.5, 5.5 and 6.75 (orange)); (b) Bifurcation diagram of von Bertalanffy's maps $f_r(x)$ in the (K, W_∞) parameter plane. The blue region is the stability region. The period doubling and chaotic regions correspond to the cycles shown on top of figure. The gray region is the non admissible region.

growth equation,

$$g\left(W_t\right) = \frac{dW_t}{dt} = \frac{K}{3} \; W_t^{\frac{2}{3}} \left(1 - \left(\frac{W_t}{W_\infty}\right)^{\frac{1}{3}}\right), \tag{2}$$

introduced by von Bertalanffy to model fish weight growth, see [17] and [18]. The *per capita* growth rate, associated to this growth model, is given by

$$h\left(W_t\right) = \frac{g\left(W_t\right)}{W_t} = \frac{K}{3} \; W_t^{-\frac{1}{3}} \left(1 - \left(\frac{W_t}{W_\infty}\right)^{\frac{1}{3}}\right). \tag{3}$$

In this paper, we consider a family of unimodal maps, the von Bertalanffy maps, which is proportional to the right hand side of von Bertalanffy's equation, Eq.(2), $f_r : [0, 1] \to [0, 1]$, defined by

$$f_r\left(x\right) = r \; x^{\frac{2}{3}} \left(1 - x^{\frac{1}{3}}\right), \tag{4}$$

with $x = \frac{W_t}{W_\infty} \in [0, 1]$ the normalized weight and $r = r(K, W_\infty) = \frac{K}{3} \times W_\infty^{\frac{2}{3}} > 0$ an intrinsic growth rate of the individual weight, see Fig.1(a).

Remark that, the family of maps that we will study depends on two biological parameters: von Bertalanffy's growth rate constant K and the asymptotic weight W_∞. The following conditions are satisfied:

(A1) f_r is continuous on $[0, 1]$;

(A2) f_r has an unique critical point $c = (2/3)^3 \in \,]0, 1[$;

(A3) $f_r'(x) \neq 0, \forall x \in \,]0, 1[\, \backslash \{c\}, \; f_r'(c) = 0$ and $f_r''(c) < 0$;

(A4) $f_r \in C^3\left(]0,1[\right)$ and the Schwarzian derivative of f_r, denoted by $S\left(f_r(x)\right)$, verifies $S\left(f_r(x)\right) < 0, \forall x \in]0,1[\setminus\{c\}$ and $S\left(f_r(c)\right) = -\infty$.

Conditions $(A1)-(A4)$ are essential to prove the stability of the only positive fixed point, [15]. In particular, the negative Schwarzian derivative ensures a "good" dynamic behavior of the models. In general, the growth models studied have negative Schwarzian derivative and the use of unimodal maps is usual, see for example [12] and [13].

The dynamical complexity of the proposed models is displayed at (K, W_∞) parameter plane, depending on the variation of the intrinsic growth rate r. The analysis of their bifurcations structure is done based on the bifurcation diagram, see Fig.1(b). For these models, the extinction region and the semistability curve have no expressive meaning. Because it is difficult to identify *per capita* growth rates, Eq.(3), less than one for all densities, to the extinction case, and *per capita* growth rates strictly less than one for all densities, except at one population density, to the semistability case, except at most a set of measure zero. We verify that, $\lim_{x \to 0^+} f_r'(x) > 1$ and the origin's basin of attraction is empty, except at most a set of measure zero. The fixed point 0 is unstable.

A behavior of stability is defined when a population persists for intermediate initial densities and otherwise goes extinct. The *per capita* growth rate of the population, Eq.(3), is greater than one for an interval of population densities. The lower bound of these densities correspond to the positive fixed point

$$A_{K,W_\infty} \equiv A_r = \left(\frac{r}{r+1}\right)^3,$$

of each function f_r, Eq.(4), see Fig.1(a). Furthermore, attending to $(A2)$ and $(A3)$ we have that $f_r^2(c) > 0$, then there is a linearly stable fixed point $A_r \in]0,1[$, whose basin of attraction is $]0,1[$. For more details see [15].

The symbolic dynamics techniques prove to be a good method to determine a numerical approximation to the stability region (in blue), see Fig.1(b). For more details about symbolic dynamics techniques see for example [12]. In the (K, W_∞) parameter plane, this region is characterized by the critical point iterates that are always attracted to the fixed point sufficiently near of the super stable or super attractive point $\tilde{A}_r$, defined by $f_r(c) = c$. Let $\bar{A}_r \in]0,1[$ be the fixed points sufficiently near of $\tilde{A}_r$, then

$$\lim_{n \to \infty} f_r^n(c) = \bar{A}_r, \quad \text{for} \quad \left(3K^{-1}A_r^{\frac{1}{3}}\left(1 - A_r^{\frac{1}{3}}\right)\right)^{\frac{3}{2}} < W_\infty(K) < \hat{W}_\infty(K)$$

where $\hat{W}_\infty(K)$ represents the super stable curve of the cycle of order 2, given in implicit form by $f_r^2(c) = c$. In this parameter plane, the set of the super stable or super attractive points $\tilde{A}_r$ defines the super stable curve of the fixed point. In the region before reaching the super stable curve, the symbolic sequences associated to the critical points orbits are of the type CL^∞. After this super stable curve, the symbolic sequences are of the type CR^∞. In this parameter region, the topological entropy is null, [10].

The period doubling region corresponds to the parameters values, to which the population weight oscillates asymptotically between 2^n states, with $n \in \mathbb{N}$.

In period-doubling cascade, the symbolic sequences correspondent to the iterates of the critical points are determined by the iterations $f_r^{2^n}(c) = c$. Analytically, these equations define the super-stability curves of the cycle of order 2^n. The period doubling region is bounded below by the curve of the intrinsic growth rate values where the period doubling starts, $\hat{W}_\infty(K)$, correspondent to the 2-period symbolic sequences $(CR)^\infty$. Usually, the upper bound of this region is determined using values of intrinsic growth rate r, corresponding to the first symbolic sequence with non null topological entropy. Commonly, the symbolic sequence that identifies the beginning of chaos is $\left(CRLR^3\right)^\infty$, a 6-periodic orbit, see for example [12] and [13]. The unimodal maps in this region, also have null topological entropy, [10].

In the chaotic region of the (K, W_∞) parameter plane, the evolution of the population size is *a priori* unpredictable. The maps are continuous on the interval with positive topological entropy whence they are chaotic and the Sharkovsky ordering is verified. The symbolic dynamics are characterized by iterates of the functions f_r that originate orbits of several types, which already present chaotic patterns of behavior. The topological entropy is a non-decreasing function in order to the parameter r, until reaches the maximum value $\ln 2$ (consequence of the negative Schwartzian derivative). In [12] and [13] can be seen a topological order with several symbolic sequences and their topological entropies, which confirm this result to others growth models. This region is bounded below by the curve of the intrinsic growth rate values where the chaos starts. The upper bound is the *fullshift* curve or chaotic semistability curve, defined by $f_r(c) = 1$. This curve characterizes the transition between the chaotic region and the non admissible region. In the non admissible region, the graphic of any function f_r is no longer totally in the invariant set $[0, 1]$. The maps under these conditions no longer belong to the studied family functions and are not good models for populations dynamics.

The above explanations are summarized in the next result:

Lemma 1. *Let $f_r(x)$ be von Bertalanffy's maps, Eq.(4), with $r \in \mathbb{R}^+$ and satisfying $(A1) - (A4)$.*

(i) *(Stability region of the fixed point A_r) If $0 < r < 5$, then there is a linearly stable fixed point $A_r \in]0, 1[$ whose basin of attraction is $]0, 1[$;*

(ii) *(Period doubling and chaotic regions) If $5 < r < \frac{3^3}{2^2}$, then the interval $[f_r^2(c), f_r(c)]$ is forward invariant with basin of attraction $]0, 1[$;*

(iii) *(Chaotic semistability curve) If $r = \frac{3^3}{2^2}$, then $[0, 1]$ is invariant and verifies that*

$$\bigcup_{n \geq 0} f_r^n(x) = [0, 1] \quad and \quad \lim_{n \to \infty} \frac{1}{n} |Df_r^n(x)| > 0,$$

for Lebesgue almost every $x \in [0, 1]$.

For more analytical details of the proof see [14] and [15].

3   Synchronization and Lyapunov exponents

Consider a general network of N identical coupled dynamical systems, described by a connected, undirected graph, with no loops and no multiple edges. In each node the dynamics of the system is defined by the maps f_r given by Eq.(4). The state equations of this network, in the discretized form, are

$$x_i(k+1) = f_r(x_i(k)) + c \sum_{j=1}^{N} l_{ij} x_j(k), \text{ with } i = 1, 2, ..., N \qquad (5)$$

where c is the coupling parameter and $L = (l_{ij})$ is the Laplacian matrix or coupling configuration of the network. The Laplacian matrix is given by $L = D - A$, where A is the adjacency matrix and $D = (d_{ij})$ is a diagonal matrix, with $d_{ii} = k_i$, being k_i the degree of node i. The eigenvalues of L are all real and non negatives and are contained in the interval $[0, \min\{N, 2\Delta\}]$, where Δ is the maximum degree of the vertices. The spectrum of L may be ordered, $\lambda_1 = 0 \le \lambda_2 \le \cdots \le \lambda_N$. The network (5) achieves asymptotical synchronization if

$$x_1(t) = x_2(t) = ... = x_N(t) \underset{t \to \infty}{\to} e(t),$$

where $e(t)$ is a solution of an isolated node (equilibrium point, periodic orbit or chaotic attractor), satisfying $\dot{e}(t) = f(e(t))$.

One of the most important properties of a chaotic system is the sensitivity to initial conditions. A way to measure the sensitivity with respect to initial conditions is to compute the average rate at which nearby trajectories diverge from each other. Consider the trajectories x_k and y_k, starting, respectively, at x_0 and y_0. If both trajectories are, until time k, always in the same linear region, we can write

$$|x_k - x_k| = e^{\lambda k}|x_0 - y_0|, \text{ where } \lambda = \frac{1}{k} \sum_{j=0}^{k-1} \ln|f_r'(x_j)|.$$

The Lyapunov exponents of a trajectory x_k is defined by

$$h_{\max} = \lim_{k \to +\infty} \frac{1}{k} \sum_{j=0}^{k-1} \ln|f_r'(x_j)| \qquad (6)$$

whenever it exists. The computation of the Lyapunov exponent $h_{\max}$ gives the average rate of divergence (if $h_{\max} > 0$), or convergence (if $h_{\max} < 0$) of the two trajectories from each other, during the time interval $[0, k]$, see for example [6]. We note that, the Lyapunov exponents depend on two biological parameters: von Bertalanffy's growth rate constant and the asymptotic weight. See in Fig.2 the Lyapunov exponents estimate for von Bertalanffy's maps Eq.(4).

If the coupling parameter c belongs to the synchronization interval

$$\left] \frac{1 - e^{-h_{\max}}}{\lambda_2}, \frac{1 + e^{-h_{\max}}}{\lambda_N} \right[\qquad (7)$$

then the synchronized states $x_i(t)$, $(i = 1, ...N)$ are exponentially stable, [9]. The second eigenvalue λ_2 is know as the algebraic connectivity or Fiedler value
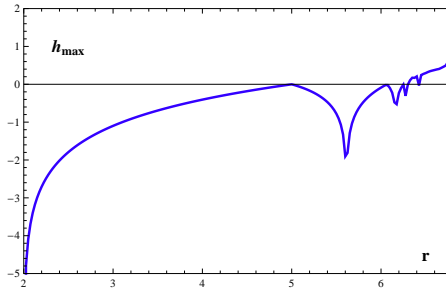
Fig. 2. Lypunov exponents estimates for von Bertalanffy's maps Eq.(4), as a function of the intrinsic growth rate r.

and plays a special role in the graph theory. As bigger is λ_2, more easily the network synchronizes. As much larger λ_2 is, more difficult is to separate the graph in disconnected parts. The graph is connected if and only if $\lambda_2 \neq 0$. In fact, the multiplicity of the null eigenvalue λ_1 is equal to the number of connected components of the graph. Fixing the topology of the network, the eigenvalues of the Laplacian λ_2 and λ_N are fixed, so the synchronization only depends on the Lyapunov exponent of each node, $h_{\max}$, which in turn depends on the two biological parameters: von Bertalanffy's growth rate constant and the asymptotic weight.

4   Numerical simulation and conclusions

To support our approaches, we consider a regular ring lattice, a graph with N nodes, each one connected to k neighbors, $\frac{k}{2}$ on each side, having in each node the same model, the von Bertalanffy maps f_r given by Eq.(4). See in Fig.3 some example of lattices. If, for instance, $N = 6$ and $K = 4$, see Fig.3c), the
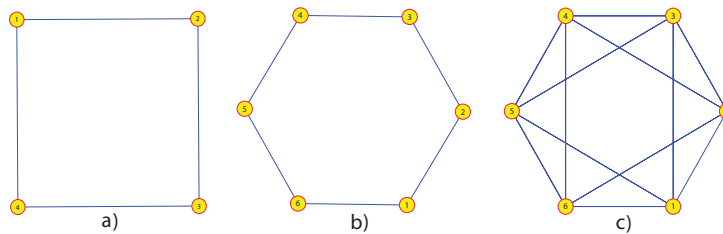
Fig. 3. Lattices. In a) with $N = 4$ nodes and $k = 2$, in b) with $N = 6$ nodes and $k = 2$ and in c) with $N = 6$ nodes and $k = 4$. From (a) to (b) the total number of vertices of the network increases maintaining the number of neighbors of each node, and from (b) to (c) increases the number of neighbors of each node, but the total number of vertices of the network remains the same.

adjacency matrix A and the Laplacian matrix L are

$$A = \begin{bmatrix} 0 & 1 & 1 & 0 & 1 & 1 \\ 1 & 0 & 1 & 1 & 0 & 1 \\ 1 & 1 & 0 & 1 & 1 & 0 \\ 0 & 1 & 1 & 0 & 1 & 1 \\ 1 & 0 & 1 & 1 & 0 & 1 \\ 1 & 1 & 0 & 1 & 1 & 0 \end{bmatrix} \quad \text{and} \quad L = D - A = \begin{bmatrix} 4 & -1 & -1 & 0 & -1 & -1 \\ -1 & 4 & -1 & -1 & 0 & -1 \\ -1 & -1 & 4 & -1 & -1 & 0 \\ 0 & -1 & -1 & 4 & -1 & -1 \\ -1 & 0 & -1 & -1 & 4 & -1 \\ -1 & -1 & 0 & -1 & -1 & 4 \end{bmatrix}.$$

So, the network correspondent to the graph in Fig.3 c) is defined by the system,

$$\begin{cases} \dot{x}_1 = f_r(x_1) + c(4x_1 - x_2 - x_3 - x_5 - x_6) \\ \dot{x}_2 = f_r(x_2) + c(-x_1 + 4x_2 - x_3 - x_4 - x_6) \\ \dot{x}_3 = f_r(x_3) + c(-x_1 - x_2 + 4x_3 - x_4 - x_5) \\ \dot{x}_4 = f_r(x_4) + c(-x_2 - x_3 + 4x_4 - x_5 - x_6) \\ \dot{x}_5 = f_r(x_5) + c(-x_1 - x_3 - x_4 + 4x_5 - x_6) \\ \dot{x}_6 = f_r(x_6) + c(-x_1 - x_2 - x_4 - x_5 + 4x_6) \end{cases}.$$

For this lattice the eigenvalues of the Laplacian matrix are $\lambda_1 = 0$, $\lambda_2 = \lambda_3 = \lambda_4 = 4$ and $\lambda_5 = \lambda_6 = 6$. If we consider, for instance, $r = 6.60$, the Lyapunov exponent of $f_r(x)$ is 0.377, Eq.(6). Then, attending to Eq.(7), this lattice synchronizes if $\frac{1-e^{-0.377}}{4} < c < \frac{1+e^{-0.377}}{6} \Leftrightarrow 0.079 < c < 0.281$ and the amplitude of the synchronization interval is 0.202. For more examples see Table 1. The lattice correspondent to the Fig.3 b) has eigenvalues of the Laplacian matrix $\lambda_1 = 0$, $\lambda_2 = \lambda_3 = 1$, $\lambda_4 = \lambda_5 = 3$ and $\lambda_6 = 4$. Thus, for the same $r = 6.60$, the lattice synchronizes if $0.313 < c < 0.421$ and the amplitude of this interval is 0.107. Moreover, to the lattice in Fig.3 a), the eigenvalues of the Laplacian matrix are $\lambda_1 = 0$, $\lambda_2 = \lambda_3 = 2$ and $\lambda_4 = 4$. For the same $r = 6.60$, the lattice synchronizes if $0.157 < c < 0.421$ and the amplitude of this interval is 0.264. In Table 1 are presented more examples, where we computed the synchronization interval for several values of the intrinsic growth rate r, for all these lattices a), b) and c) of Fig.3. The results of Table 1 allow us to claim:

(C1) From the lattice a) to lattice b) in Fig.3, the total number of vertices of the network increases maintaining the number of neighbors of each node. We verify that the synchronization is worse, not only because it begins to synchronize at a higher value of the coupling parameter c, but also, because the synchronization interval is shorter.

(C2) Comparing the results for the lattices b) and c) in Fig.3, we may conclude that maintaining the total number of vertices of the network, but increasing the number of neighbors of each node, the synchronization is better, not only because it begins to synchronize at a lower value of the coupling parameter c, but also, because the synchronization interval is larger.

(C3) Observing the columns of Table 1, we verify that, as the intrinsic growth rate r increases, the synchronization is worse, not just because it begins to synchronize at a higher value of the coupling parameter c, but also, because the synchronization interval is shorter.

(C4) Note that, for the intrinsic growth rate $r = 6.74$ and $r = 6.75$, for the lattice b), the upper bound of the synchronization interval is lower than the lower

r	h_{max}	Synchronization Interval			Amplitude		
		Lattice a)	Lattice b)	Lattice c)	Lattice a)	Lattice b)	Lattice c)
6.50	0.297	]0.128, 0.436[	]0.257, 0.436[	]0.064, 0.291[	0.308	0.179	0.226
6.55	0.347	]0.147, 0.427[	]0.293, 0.427[	]0.073, 0.285[	0.280	0.134	0.211
6.60	0.377	]0.157, 0.421[	]0.313, 0.421[	]0.079, 0.281[	0.264	0.107	0.202
6.65	0.406	]0.167, 0.417[	]0.334, 0.417[	]0.083, 0.278[	0.250	0.083	0.194
6.70	0.463	]0.185, 0.407[	]0.371, 0.407[	]0.093, 0.272[	0.222	0.037	0.179
6.73	0.506	]0.199, 0.401[	]0.397, 0.401[	]0.099, 0.267[	0.202	0.003	0.168
6.74	0.533	]0.207, 0.397[	(*)	]0.103, 0.265[	0.190	(*)	0.161
6.75	0.598	]0.225, 0.388[	(*)	]0.112, 0.258[	0.163	(*)	0.146

Table 1. Lyapunov exponent, h_{max}, synchronization interval, $\left] \frac{1-e^{-h_{\max}}}{\lambda_2}, \frac{1+e^{-h_{\max}}}{\lambda_N} \right[$, and amplitude of this interval, $\frac{1+e^{-h_{\max}}}{\lambda_N} - \frac{1-e^{-h_{\max}}}{\lambda_2}$, for several intrinsic growth rates r, for the lattices a), b) and c) of Fig.3.(*) In this case, the desynchronization phenomenon occurs, see (C4).

bound. This means that, there is no synchronization for any value of the coupling parameter c. This desynchronization phenomenon was expected because the network (5) synchronizes only if $h_{max} < \ln(2R+1)$, where $R = \frac{\lambda_1 - \lambda_2}{\lambda_2 - \lambda_N}$, see [9]. In the case of lattice b), we have $\ln(2R+1) = 0.511$, so there is synchronization only if $h_{max} < 0.511$, which do not happens for $r = 6.74$ and $r = 6.75$. In all the other studied cases, the Lyapunov exponent verifies $h_{max} < \ln(2R+1)$, so we have a non empty synchronization interval.

Acknowledgment

References

1.A. Balanov, N. Janson, D. Postnov and O. Sosnovtseva. Synchronization: From Simple to Complex, Springer, 2009.
2.G.M. Cailliet, W.D. Smith, H.F. Mollet and K.J. Goldman. Age and growth studies of chondrichthyan fishes: the need for consistency in terminology, verification, validation, and growth function fitting. *Environ. Biol. Fish.*, 77: 211–228, 2006.

3. A.B. Cooper. A Guide to Fisheries Stock Assessment. From Data to Recommendations. New Hampshire Sea Grant, 2006.

4. A.J. Davidson and M. Menaker, Birds of a feather clock together sometimes: social synchronization of circadian rhythms. *Curr. Opin. Neurobiol.*, 13 (6): 765–769, 2003.

5. T.E. Essington, J.F. Kitchell and C.J. Walters. The von Bertalanffy growth function, bioenergetics, and the consumption rates of fish. *Can. J. Fish. Aquat. Sci.*, 58: 2129–2138, 2001.

6. M.Hasler and Y.L. Maistrenko, An introduction to the synchronization of chaotic systems: coupled skew tent maps. *IEEE Trans. on Circ. Syst. – I*, 44 (10): 856–866, 1987.

7. J.A. Hutchings and J.D. Reynolds. Marine fish population collapses: consequences for recovery and extinction isk. *BioSci.*, 54: 297–309, 2004.

8. V.S. Karpouzi and D. Pauly. Life-History Patterns in Marine Birds. In M.L.D. Palomares and D. Pauly, editors, *Fisheries Center Research Reports 16 (10), Von Bertalanffy Growth Parameters of Non-Fish Marine Organisms*, pages 27-43, Canada, 2008. The Fisheries Center, University of British Columbia.

9. X. Li and G. Chen, Synchronization and desynchronization of complex dynamical networks: An engineering viewpoint. *IEEE Trans. on Circ. Syst. –I*, 50 (11): 1381–1390, 2003.

10. D. Lind and B. Marcus. An Introduction to Symbolic Dynamics and Codings. 2nd edition, Cambridge University Press, Cambridge, 1999.

11. J.A. Musick. Criteria to define extinction risk in marine fishes. *Fisheries*, 24: 6–14, 1999.

12. J.L. Rocha and S.M. Aleixo. An extension of gompertzian growth dynamics: Weibull and Fréchet models. *Math. Biosci. Eng.*, 10: 379–398, 2013.

13. J.L. Rocha and S.M. Aleixo. Dynamical analysis in growth models: Blumberg's equation. *Discrete Contin. Dyn. Syst.-Ser.B*, 18: 783–795, 2013.

14. J.L. Rocha, S.M. Aleixo and A. Caneco. Synchronization in Richards' chaotic systems. *Journal of Applied Nonlinear Dynamics*, to appear.

15. S.J. Schreiber. Chaos and population disappearances in simple ecological models. *J. Math. Biol.*, 42: 239–260, 2001.

16. J.A.L. Silva and F.T. Giordani, Density-dependent migration and synchronism in metapopulations. *Bull. of Math. Biol.*, 68: 451465, 2006.

17. L. Von Bertalanffy. A quantitative theory of organic growth. *Human Biology*, 10: 181–213, 1938.

18. L. Von Bertalanffy. Quantitative laws in metabolism and Growth. *The Quarterly Review of Biology*, 32: 217–231, 1957.

Stability and Bifurcation in the Hénon Map and its Generalizations

O. Ozgur Aybar[1], I. Kusbeyzi Aybar[2], and A. S. Hacinliyan[3]

[1] Gebze Institute of Technology, Department of Mathematics, Kocaeli, Turkey
  Yeditepe University, Department of Information Systems and Technologies,
  Istanbul, Turkey
  (E-mail: `oaybar@yeditepe.edu.tr`)
[2] Yeditepe University, Department of Computer Education and Instructional
  Technology, Istanbul, Turkey
  (E-mail: `ikusbeyzi@yeditepe.edu.tr`)
[3] Yeditepe University, Department of Information Systems and Technologies,
  Istanbul, Turkey
  Yeditepe University, Department of Physics, Istanbul, Turkey
  Bogazici University, Department of Physics, Istanbul, Turkey
  (E-mail: `ahacinliyan@yeditepe.edu.tr`)

Abstract. The Hénon map, its higher iterates and generalizations as given in [1] are studied in this work in the sense of stability and bifurcation analysis

$$x_{n+1} = 1 + y_n - ax_n^2$$
$$y_{n+1} = bx_n^k. \tag{1}$$

Instances of several forms bifurcations are observed. The second iteration of the generalized Hénon map is of interest since period doubling bifurcation is a prominent mechanism as revealed by the bifurcation map. As we proceed to higher iterations, the position of the bifurcations remain essentially unchanged, the nature of the bifurcations change to include saddle node, Hopf, period doubling bifurcations[1–4]. It is also shown that the delayed version of the Hénon map can be reduced to the logistic map if $k = 1$ and bifurcation scenarios in the one dimensional logistic map, such as period doubling are also observed in the Hénon map.
Keywords: Hénon map, Chaos, Stability, Bifurcation.

1 Introduction

Both iterated maps and flows are used as models for chaotic behavior. It is well known that flows have the same equilibrium points with the maps to which they are related by discretization. The classical example is the logistic map. As a differential equation it has a simpler behavior, however when converted to a map it indicates period doubling bifurcation.

Bifurcation analysis for both the generalized Hénon map and its higher iterations involving the 2^n fold iteration gives rich structures[1]. The generalized Hénon map and the higher iterates as first studied by Skiadas et al. are taken into consideration in this work [2,5]. The relation between the original Hénon map and the logistic map are also studied and the results given are consistent with the bifurcation diagrams of the original Hénon map[5,6].

In our previous work continuous and discrete versions of predator prey models were studied[7,8]. A similar analysis is done in this work for the iterated Hénon map, its higher iterates and the generalized form and bifurcation properties with rich properties [9,10].

The Hénon map and its generalization is given by the system 1 for $k \geq 1$. In the following sections we give explicit results of stability and bifurcation analysis for various values of k and higher iterations of this dynamical system which defines a generalized version of the Hénon map. For the special case that $k = 1$ this system is known as the original Hénon map which sets an example as a chaotic map for given parameter values. We further generalize the y update formula to $y_{n+1} = bx_{n+1}^k$.

2   Stability and bifurcation properties of the first and second iterations of the original Hénon map

The first iteration of the generalized Hénon map introduced in the previous section for $k = 1$ is considered as the original Hénon map given by:

$$x_{n+1} = 1 + y_n - ax_n^2$$
$$y_{n+1} = bx_n. \tag{2}$$

The equilibrium points of this system are

$$(x_1, y_1) = (\frac{b - 1 - \beta}{2a}, \frac{b(b - 1 - \beta)}{2a})$$
$$(x_2, y_2) = (\frac{b - 1 + \beta}{2a}, \frac{b(b - 1 + \beta)}{2a}) \tag{3}$$

and the eigenvalues at these equilibrium points are

$$\lambda_{1,2} = \{\frac{1}{2}(1 - b + \beta \mp \sqrt{4\beta + (1 + b - \beta)^2}\} \tag{4}$$

and

$$\lambda_{3,4} = \{\frac{1}{2}(1 - b - \beta \mp \sqrt{-4\beta + (1 + b + \beta)^2}\}. \tag{5}$$

where $\beta = \sqrt{4a + (b - 1)^2}$.

The original Hénon map can be considered as a quadratic map in one dimension if y_{n+1} is updated first, i.e.:

$$x_{n+1} = bx_n + 1 - ax_n^2. \tag{6}$$

This is an implied delay of one step. A quadratic map can be reduced to the functional form of the logistic map by a linear transformation $x = cy + d$ for appropriate values of the parameters.[11–13]

The Hénon map has two equilibrium points

$$x_{1,2} = \frac{b - 1 \pm \sqrt{(1-b)^2 + 4a}}{2a}, \tag{7}$$

Hence these equilibrium points are real if

$$\sqrt{(1-b)^2 + 4a} > 0. \tag{8}$$

It can also be shown that one of these equilibrium points is stable for the positive sign before the radical, the other one is always unstable.

The parameter values known to exhibit chaotic behavior are $a = 1.4$ and $b = 0.3$ and the two equilibrium points of the system for these parameter values are $(-1.13135, -0.339406)$ and $(0.631354, 0.189406)$. The eigenvalues at the first equilibrium point are $\{2.25982, -1.09203\}$ and the eigenvalues at the second equilibrium point are $\{-2.92374, -0.844054\}$. Hence the first one is a saddle point and the second one is clearly a stable equilibrium point.

Theorem 1. *A quadratic map where the coefficient of the quadratic term is negative can always be reduced to the functional form of the logistic map $y_{n+1} = \lambda y_n(1 - y_n)$ by a linear transformation of the form $x = cy + d, c \neq 0$. It should be noted that the linear transformation does not respect the unit interval condition of the logistic map, however the Hénon map itself does not stay in $0 < x < 1$, $0 < y < 1$.*

Proof. After substitution of the linear transformation $x = cy + d$ in the system the constant term should vanish. We have:

$$y_n^2(ac^2) + y_n(2acd - bc) + ad^2 - bd + cy_{n+1} + d - 1 = 0. \tag{9}$$

The condition for vanishing constant term coincides with the condition that gives the equilibrium points, namely:

$$d_{1,2} = \frac{b - 1 \pm \sqrt{(1-b)^2 + 4a}}{2a}. \tag{10}$$

Hence $y_{n+1} = \lambda y_n(1 - y_n)$ is obtained where $\lambda = \pm\sqrt{(1-b)^2 + 4a} + 1$ for both solutions of d.

This theorem is important since it shows that a quadratic map can be converted to the logistic map provided that the logistic map variable remains in the unit interval. Furthermore a quadratic map can also be converted to a tent map where the codimension is incremented by one since the logistic map is reduced to tent map for $\lambda = 4$.

An iterated map and differential equation can be converted to one another by using a specific discretization. However the differential equation obtained by

any discretization is invertible by the implicit function theorem while the corresponding map is usually non-invertible. This of course implies codimension is decreased by one upon conversion to map[14,15].

The formula for x_{n+1} with $y_n = bx_n$ substituted in the same way as the step leading to $x_{n+1} = 1 + bx_n - ax_n^2$ of the first iteration can be factorized as follows

$$x_n - f^2(x_n) = (x_n - f(x_n))(a^2 x_n^2 - abx_n - ax_n - a + 1) \qquad (11)$$

as expected where $f^2(x_n) = f(f(x_n))$. Theorem 1 then guarantees that both factors can be transformed into either the logistic map or its version with the reversed sign $x_{n+1} = \lambda(x_n^2 - x_n)$.

In the numerical analysis literature, one of the possible variations for successive iteration is the commonly known Jacobi iteration, and the second one is the Gauss-Seidel iteration. The difference lies in the fact that whether all variables are updated at the end of an iteration or the newer values for a variable are immediately used in later equations of the same iteration. The two-dimensional map

$$x_{n+1} = f(x_n, y_n)$$
$$y_{n+1} = g(x_n, y_n) \qquad (12)$$

is an instance of the Jacobi variant. The Gauss-Seidel variant uses $y_{n+1} = g(x_{n+1}, y_{n+1})$ for the second term.

According to the Jacobi variant the second iteration of the original Hénon map is given by:

$$x_{n+1} = -a^3 x_n^4 + 2a^2 x_n^2 y_n + 2a^2 x_n^2 - ay_n^2 - 2ay_n - a + bx_n + 1$$
$$y_{n+1} = b(-ax_n^2 + y_n + 1). \qquad (13)$$

The system has four equilibrium points two of which are inherited from the original Hénon map and the other equilibrium points are

$$\left(-\left(\frac{b-1}{2a}\right) \pm \sqrt{\frac{1}{a} - 3\left(\frac{b-1}{2a}\right)^2}, \; -b\left(\frac{b-1}{2a} \pm \sqrt{\frac{1}{a} - 3\left(\frac{b-1}{2a}\right)^2}\right)\right). \qquad (14)$$

The eigenvalues that are inherited from the original Hénon map are

$$\{\pm\beta(b-1) \pm \sqrt{2\alpha} + 2a + b^2 - b + 1\}, \qquad (15)$$

and the eigenvalues of the third and fourth equilibrium points are

$$\{\pm 2\sqrt{a^2 - 2ab^2 + 3ab - 2a + b^4 - 3b^3 + 4b^2 - 3b + 1} - 2a + 2b^2 - 3b + 2\}$$

where $\beta = \sqrt{4a + (b-1)^2}$ and

$$\alpha = ((2ab - 2a + b^3 - 2b^2 + 2b - 1)\beta + 2a^2 + 4ab^2 - 6ab + 4a + b^4 - 3b^3 + 4b^2 - 3b + 1).$$

We proceed by giving the detailed stability results for the original Hénon map. We recall that the original Hénon map has two real equilibrium points for $a > -\frac{(b-1)^2}{4}$[3,4].

Lemma 1. *For $a = -\frac{(b-1)^2}{4}$ and $\beta = 0$ the original Hénon map has a unique equilibrium point at $(\frac{-2}{b-1}, \frac{-2b}{b-1})$ with the eigenvalues $\{1, -b\}$ indicating saddle node bifurcation[3,4].*

Proof. By substituting $a = -\frac{(b-1)^2}{4}$ and $\beta = 0$ in Equation 3 the two equilibrium points are found to overlap each other at $(\frac{-2}{b-1}, \frac{-2b}{b-1})$. The Jacobian of the system at the equilibrium point is

$$\begin{pmatrix} 1-b & 1 \\ b & 0 \end{pmatrix}$$

and hence the eigenvalues are $\{1, -b\}$.

We consider the saddle node bifurcation with a numerical example. For $b = 0.3$ and $a = -0.1225$ the equilibrium point of the system is $(2.8571, 0.8571)$ indicating a saddle node bifurcation with a stable and an unstable branch shown in Figure 1. The range for a along the stable branch is between $-0.1225 \le a \le 0.3675$.
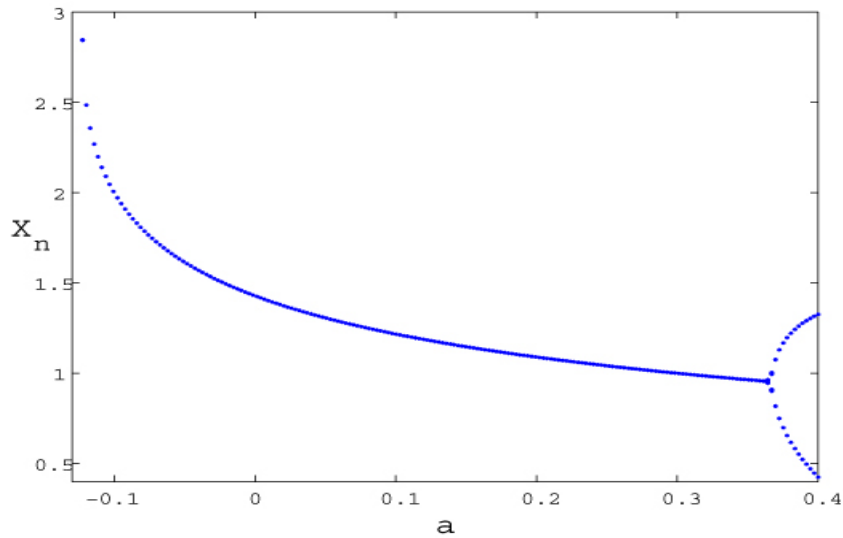
Fig. 1. Bifurcation diagram of the original Hénon map for $-0.15 \le a \le 0.4$ and $b = 0.3$.

For the special case that $a = \frac{3(b-1)^2}{4}$ period doubling bifurcation is observed for the original Hénon map. At this period doubling point the original Hénon map and the second iteration of the original Hénon map have completely overlapped equilibrium points at $(\frac{2}{b-1}, \frac{2b}{b-1})$. The eigenvalues for the original Hénon map are $\{-1, b\}$ and $\{\frac{\pm\sqrt{9b^2-14b+9}-3(b-1)}{2}\}$ and the

eigenvalues for the second iteration of the original Hénon map are $\{1, b^2\}$ and $\{\frac{\pm 3\sqrt{9b^2-14b+9}|b-1|+9b^2-16b+9}{2}\}$.

Lemma 2. *The first and second iterations of the original Hénon map show Hopf bifurcation for $a = -0.982051$ and $a = 2.48205$ while $b = -1$.*

Proof. For $b = -1$ and $a = -0.982051$ the equilibrium points of the original Hénon map are $(1.1546, -1.1546)$ and $(0.88185, -0.88185)$ and the eigenvalues are $\{1.6686, 0.5992\}$ and $\{\frac{\sqrt{3}}{2} \pm \frac{i}{2}\}$. The equilibrium points of the second iteration of the original Hénon map are the same of those of the original Hénon map and the eigenvalues are $\{0.35913, 2.7844\}$ and $\{\frac{1}{2} \pm \frac{i\sqrt{3}}{2}\}$.

For $b = -1$ and $a = 2.48205$ the equilibrium points of the original Hénon map are $(0.3489, -0.3489)$ and $(-1.1547, -1.1547)$ and the eigenvalues are $\{0.18011, 5.5519\}$ and $\{\frac{-\sqrt{3}}{2} \pm \frac{i}{2}\}$. The equilibrium points of the second iteration of the original Hénon map are the same of those of the original Hénon map and the eigenvalues are $\{0.03244, 30.8239\}$ and $\{\frac{1}{2} \pm \frac{i\sqrt{3}}{2}\}$.
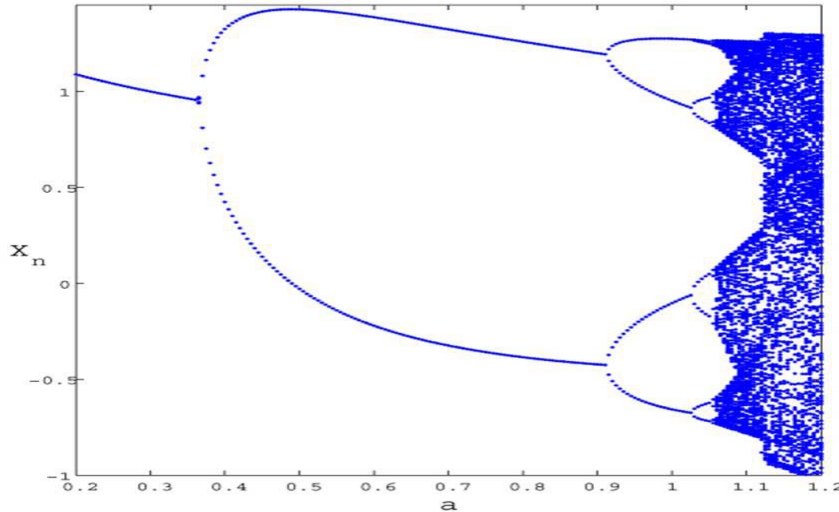
Fig. 2. Bifurcation diagram of the original Hénon map for $0.2 \leq a \leq 1.2$ and $b = 0.3$.

The first iteration of the original Hénon map exhibits a period doubling bifurcation and transition to chaos about $a = 0.2$ as shown in Figure 2 demonstrating an example of stable branch. Further stability analysis for the parameter value $a = 0.2$ gives the two equilibrium points $(1.08945, 0.326836)$ and $(-4.58945, -1.376836)$ and the eigenvalues $\{0.371580, -0.80736213\}$ and $\{1.986779, -0.1509981\}$ respectively. The first equilibrium point is a stable sink and the second equilibrium point is a saddle point. For the same parameter val-
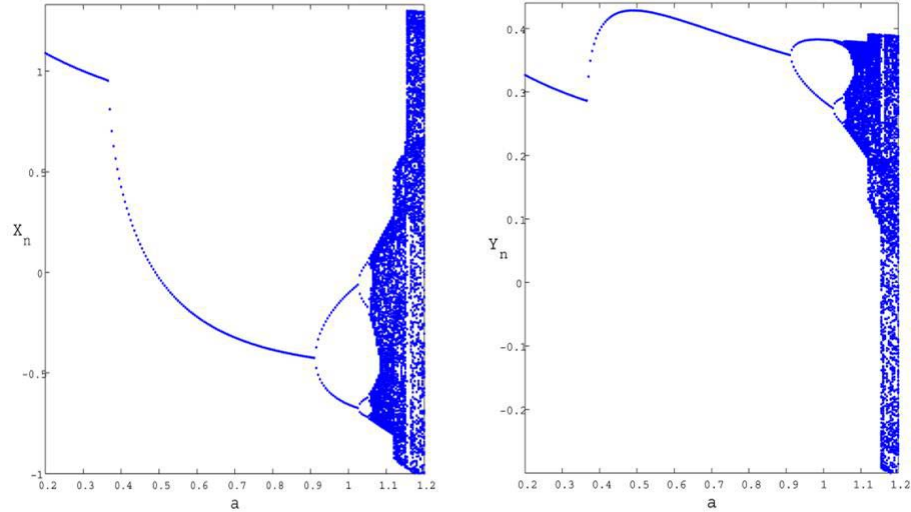
Fig. 3. Bifurcation diagram of the second iteration of the original Hénon map for $0.2 \leq a \leq 1.2$ and $b = 0.3$ for both x and y.

ues the second iteration of the original Hénon map has four equilibrium points, two of them are complex conjugates, i.e. $(1.75 \pm 2.046338i, 0.525 \mp 0.6139i)$ and the others are inherited from the original Hénon map respectively. The eigenvalues of the complex conjugate equilibrium points are $\{1.7072, 0.05271\}$, the eigenvalues of the third equilibrium point are $\{0.138072, 0.6518336\}$ and the eigenvalues of the fourth equilibrium point are $\{0.0228, 3.9472\}$. The complex conjugate equilibrium points are saddles, the third equilibrium point is a stable sink and the fourth equilibrium point is a saddle as expected and the bifurcation diagram is shown in Figure 3. When a approaches 0.3675, a period-2 orbit is observed. The equilibrium points at $a = 0.3675$ are $(0.95238, 0.285714)$ and $(-2.857142, -0.857142)$ and the eigenvalues corresponding to these equilibrium points are $\{0.3, -1\}$ and $\{2.234271, -0.134271\}$. Hence the first equilibrium point gives the beginning of the period doubling bifurcation and the second equilibrium point is a saddle point[16].

In the second iteration period doubling bifurcation occurs when the equilibrium points of the first iterate $f(x_n)$ lose their stability but the second iteration $f^2(x_n)$ develops a pair of new stable equilibrium points $x_{n\pm}$ such that $f^2(x_{n\pm}) = x_{n\pm}$ while f forms a period-2 attractor $f(x_{n\pm}) = x_{n\mp}$. The second iteration can not move $x_{n\pm}$ to $x_{n\mp}$ hence one of the branches for $f(x_n)$ becomes invisible for $f^2(x_n)$. Furthermore the special form of the Hénon map where y_n is calculated as the iterated value of x_n causes x_n and y_n to switch branches for f^2. This fact applies for $0.3625 \leq a \leq 0.9125$. At $a = 0.9125$ a period-4 attractor occurs as shown in Figure 3.

For $a = 1$ the equilibrium points are $(0.70948, 0.21284)$ and $(-1.40948, -0.42284)$ and the eigenvalues are $\{0.186824, -1.60578\}$ and $\{2.921643, -0.102681\}$ respectively. Both of the equilibrium points are saddle points. The bifurcation
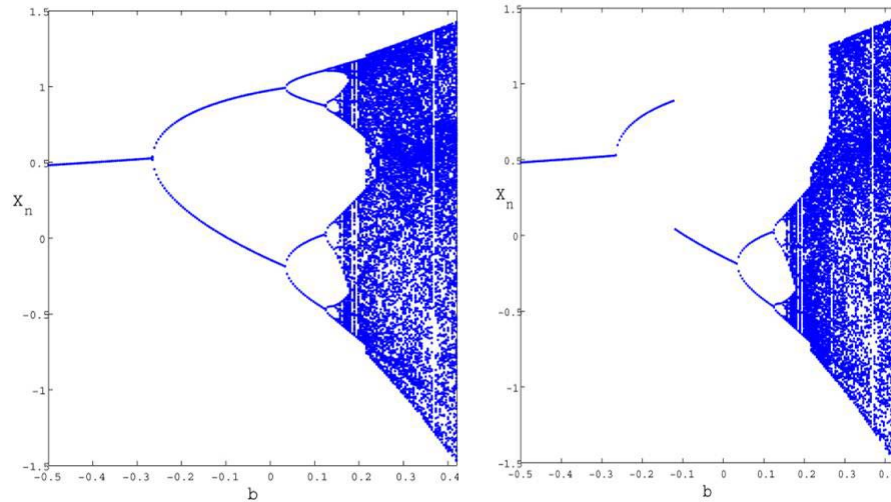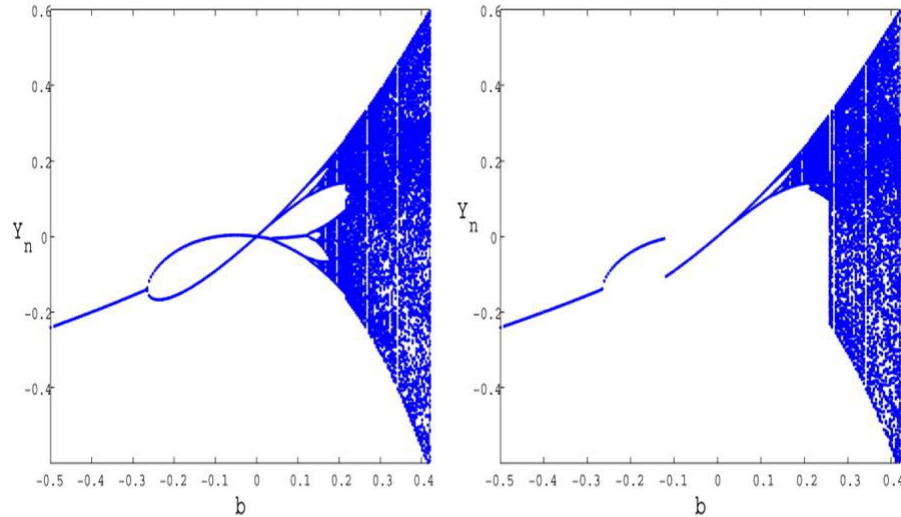

Fig. 4. Bifurcation diagram of the first and second iterations of the original Hénon map for $-0.5 \le b \le 0.42$ and $a = 1.2$ for x.

diagram of the first and second iterations of the original Hénon map for $-0.5 \le b \le 0.419$ and $a = 1.2$ is given in Figures 4 and 5. For $a = 1.2$ and $b = -0.1$ the equilibrium points are $(0.563137, -0.0563137)$ and $(-1.4798, 0.14798)$ and the eigenvalues are $\{-0.0785562, -1.2729739\}$ and $\{0.0283838, 3.523146\}$ respectively. Both of the equilibrium points are saddles. About the first equilibrium point period-2 orbit is observed. Considering the second iteration of the original Hénon map with same conditions there are four equilibrium points of which two are the same as the first iteration. The eigenvalues are $\{1.620462, 0.0061710\}$ and $\{12.41256, 0.000805\}$. Again both equilibrium points are saddle points. The system hides its periodic behavior that is observed for the first iteration and the increase in the iteration of the system makes the system a more chaotic and complex one instead of a multiperiodic one.

3   Conclusion

In this paper we investigated the bifurcation analysis and stability structure of the generalized Hénon map and its higher iterations[17,18]. The second iteration of the generalized Hénon map is of interest since period doubling bifurcation is a prominent mechanism as revealed by the bifurcation map. The

Fig. 5. Bifurcation diagram of the first and second iterations of the original Hénon map for $-0.5 \leq b \leq 0.42$ and $a = 1.2$ for y.

second iteration can either be done on the original Hénon map or on the delayed version as proposed by Skiadas[2]. The two options correspond to the Jacobi and Gauss-Seidel iterations in numerical analysis where all variables are either updated following a complete iteration or each updated value is used for the subsequent equations in the same iterations. As we proceed to higher iterations, the position of the bifurcations remain essentially unchanged, the nature of the bifurcations change to include virtually all kinds of bifurcations. The generalization of the y_n updating formula to the form x_n^2 does not qualitatively change the nature. The bifurcation scenario is not sensitive to k. When we increase the value of k, we notice that the bifurcation diagrams do not change their general properties. The stability analysis related to these results are also investigated. Generally magnitude of one eigenvalue is less than 1 and the other is greater than 1. Therefore we have a saddle for these kinds of equilibrium points. On the other hand, we have stable sinks for other type of eigenvalues. As we look generally, we do not observe any bifurcation out of the range $0.2 \leq a \leq 1.875$ so that we can obtain similar results according to the Gauss-Seidel iteration.

References

1. M. Hénon, A two-dimensional mapping with a strange attractor, *Commun. Math. Phys.* 50:69–77, 1976.
2. C.H. Skiadas, C. Skiadas, Chaotic Modelling and Simulation Analysis of Chaotic Models, Attractors and Forms, Taylor & Francis Group, LLC, 2009.

3. E. Zeraoulia, J.C. Sprott, World Scientific Series on Nonlinear Science Series A 73 (2010).

4. J.C. Sprott, High-Dimensional Dynamics in the Delayed Hénon Map, *Elec J.of Theo. Phys.* 3:19–35, 2006.

5. D. Blackmore, J. Chen, J. Perez, M. Savescu, Dynamical properties of discrete LotkaVolterra equations, *Chaos Soliton Fract.* 12:2553–2568, 2001.

6. D.K. Arrowsmith, C.M. Place, Dynamical systems. Differential equations, maps and chaotic behavior, Chapman & Hall, London, 1992.

7. I. Kusbeyzi, O.O. Aybar, A.S. Hacinliyan, Stability and bifurcation in two species predator-prey models , *Nonlinear Anal. RWA* 12:377-387, 2011.

8. I. Kusbeyzi, O.O. Aybar, A.S. Hacinliyan, A predator-prey model with the non-linear self interaction coupling $x^k y$, *Chaos Theory, Modeling, Simulation and Applications* (CHAOS2010), World Scientific, ISBN: 978-981-4350-33-4, 2011.

9. D. Sterling, H.R. Dullin, J.D. Meiss, Homoclinic Bifurcations for the Hénon Map, *Physica D* 134:153–184, 1999.

10. Ed. D. Estep, S. Tavener, Collected Lectures on the Preservation of Stability under Discretization, SIAM, Philadelphia, 2002.

11. A. Margaris, M. Adamopoulos, Identifying Fixed Points of Hénon Map Using Artificial Neural Networks, *Chaotic Systems, Theory and Applications*(CHAOS 2009), World Scientific, ISBN:978-981-4299-71-8, 2010.

12. E. Li, G. Li, G. Wen, H. Wang, Hopf bifurcation of the third-order Hénon system, *Nonlinear Anal. TMA* 70:3227–3235, 2009.

13. H.R. Dullin, J.D. Meiss, Generalized Hénon Maps: the Cubic Polynomial. Diffeomorphisms of the Plane, *Physica D* 143:262–289, 2000.

14. J.F. Selgrade, J.H. Roberds, Period-doubling bifurcations for systems of difference equations and applications to models in population biology, Nonlinear Anal. TMA 29 (2) (1997) 185-199.

15. J.E. Fornss, B. Weickert, A quantized henon map, *Discrete Contin. Dyn. Syst.* 6:723–740, 2000.

16. J-M. Grandmont, Nonlinear difference equations, bifurcations and chaos: An introduction, *Res.in Eco.* 62:122–177, 2008.

17. Y. Cao, S. Kiriki, The basin of the strange attractors of some Hénon maps, *Chaos Soliton Fract.* 11:729–734, 2000.

18. Z. He, X. Lai, Bifurcation and chaotic behavior of a discrete-time predatorprey system, *Nonlinear Anal. RWA* 12:403–417, 2011.

A Mathematical Model of the Metabolism of a Cell.

Self-organization and Chaos[*]

Valerii I. Grytsay[a], Iryna V. Musatenko[b]

[a]Bogolyubov Institute for Theoretical Physics, Kyiv, Ukraine
E-mail: vgrytsay@bitp.kiev.ua
[b]Taras Shevchenko National University of Kyiv, Faculty of Cybernetics, Kyiv, Ukraine
E-mail: ivmusatenko@gmail.com

Abstract: Using the classical tools of nonlinear dynamics, we study the process of self-organization and the appearance of the chaos in the metabolic process in a cell with the help of a mathematical model of the transformation of steroids by a cell *Arthrobacter globiformis*. We constructed the phase-parametric diagrams obtained under a variation of the dissipation of the kinetic membrane potential. The oscillatory modes obtained are classified as regular and strange attractors. We calculated the bifurcations, by which the self-organization and the chaos occur in the system, and the transitions "chaos-order", "order-chaos," "order-order," and "chaos-chaos" arise. Feigenbaum's scenarios and the intermittences are found. For some selected modes, the projections of the phase portraits of attractors, Poincaré sections, and Poincaré maps are constructed. The total spectra of Lyapunov indices for the modes under study are calculated. The structural stability of the attractors is demonstrated. A general scenario of the formation of regular and strange attractors in the given metabolic process in a cell is found. The physical nature of their appearance in the metabolic process is studied.
Keywords: Mathematical model, Metabolic process, Self-organization, Phase portrait, Deterministic chaos, Regular attractor, Strange attractor, Bifurcation, Poincaré section, Poincaré map, Lyapunov indices.

1. Introduction

In the present work, we continue the study of the mathematical model of the metabolic process in a cell *Arthrobacter globiformis*. It is based on the process of transformation of steroids in a bioreactor, which is well investigated in experiments [1]. The constructed mathematical model allows us to determine the internal and external parameters, with which the model describes the stationary modes of a bioreactor. The studies within the model showed that autooscillations must appear in the biochemical reaction under certain conditions [2-17]. These autooscillations predicted as early as in 1985 [2] were found experimentally in [18, 19].

Analogous autooscillations are observed in the processes of photosynthesis, glycolysis, variations of the calcium concentration in a cell, oscillations in heart muscle, and other biochemical systems [20-24].

The study of such autooscillations will allow one to investigate the internal dynamics of metabolic processes in cells, to find the structural-functional connections in a cell, by which its vital activity runs, and to clarify the evolution of the formation of these connections. The application of the mathematical apparatus of nonlinear dynamics to the study of metabolic processes will allow one to develop the general methods of synergetics considering the physical laws of self-organization in the Nature.

2. The Mathematical Model

The mathematical model of the metabolic process running in a cell *Arthrobacter globiformis* at the transformation of steroids is constructed according to the general scheme of this process presented in Fig. 1. The model is based on the results of experimental studies of the process under flowing-through conditions with a fermenter in porious granules with immobilized cells *Arthrobacter globiformis* [3, 4].
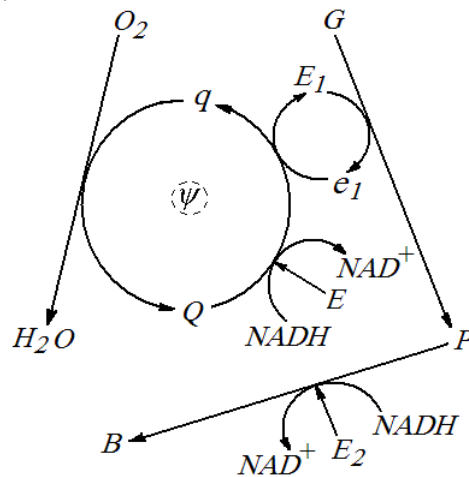
Fig. 1. General scheme of the metabolic process in a cell *Arthrobacter globiformis*.

The variation of the concentration of hydrocortisone (G) is described by the equation

$$\frac{dG}{dt} = \frac{G_0}{N_3 + G + \gamma_2 \psi} - l_1 V(E_1)V(G) - \alpha_3 G. \tag{1}$$

Under the action of the diffusion and the flow into pores of a macroporous granule to cells, hydrocortisone comes to the region of localization of the

enzyme 3-ketosteroid-Δ-dehydrogenase (E_1) (term $\dfrac{G_0}{N_3 + G + \gamma_2 \psi}$) and is transformed by this enzyme into prednisolone (term $l_1 V(E_1)V(G)$). A part of hydrocortisone is taken out from the biosystem by the flow (term $\alpha_3 G$).

Here and below, the function $V(X)$ characterizes the adsorption of the enzyme in the region of local binding into active complexes; $V(X) = X/(1 + X)$.

The variation of the concentration of prednisolone (P):

$$\frac{dP}{dt} = l_1 V(E_1)V(G) - l_2 V(E_2)V(N)V(P) - \alpha_4 P. \tag{2}$$

Prednisolone formed in the process (term $l_1 V(E_1)V(G)$) is transformed by the enzyme 20β-oxysteroid-dehydrogenase (E_2) to its 20β-oxyderivative (term $l_2 V(E_2)V(N)V(P)$). Under the action of a flow (term $\alpha_4 P$), a part of prednisolone goes out into the external solution.

The variation of the concentration of 20β-oxyderivative of prednisolone (B):

$$\frac{dB}{dt} = l_2 V(E_2)V(N)V(P) - k_1 V(\psi)V(B) - \alpha_5 B. \tag{3}$$

The increase of the concentration of B occurs as a result of the transformation of prednisolone (term $l_2 V(E_2)V(N)V(P)$). Its decrease is due to the use of 20β-oxyderivative by cells in one of the possible modifications of the Krebs cycle (term $k_1 V(\psi)V(B)$), which increases the level of $NAD \cdot H$. Under the action of a flow (term $\alpha_5 B$), B is washed out into the external solution.

The variation of the concentration of the oxidized form of 3-ketosteroid-Δ-dehydrogenase (E_1):

$$\frac{dE_1}{dt} = E_{10} \frac{G^2}{\beta_1 + G^2}(1 - \frac{P + mN}{N_1 + P + mN}) - $$
$$- l_1 V(E_1)V(G) + l_4 V(e_1)V(Q) - \alpha_1 E_1. \tag{4}$$

The biosynthesis of the enzyme is described by the term $E_{10} \dfrac{G^2}{\beta_1 + G^2}(1 - \dfrac{P + mN}{N_1 + P + mN})$, which is defined by the activation by the substrate G and the inhibition by the reaction products P and N. The decrease of the concentration of this form of the enzyme in the process of transformation of hydrocortisone is given by the term $l_1 V(E_1)V(G)$, and its increase in the process of reduction of the respiratory chain corresponds to the

term $l_4 V(e_1)V(Q)$. The inactivation of the enzyme due to the proteolysis is described by the term $\alpha_1 E_1$.

The variation of the concentration of the reduced form of 3-ketosteroid-Δ-dehydrogenase (e_1):

$$\frac{de_1}{dt} = -l_4 V(e_1)V(Q) + l_1 V(E_1)V(G) - \alpha_1 e_1. \tag{5}$$

Its level decreases in the process of reduction of the respiratory chain (term $-l_4 V(e_1)V(Q)$) and due to the inactivation (term $\alpha_1 e_1$) and increases at the transformation of hydrocortisone (term $l_1 V(E_1)V(G)$).

The variation of the level of the oxidized form of the respiratory chain (Q)

$$\frac{dQ}{dt} = 6lV(2-Q)V(O_2)V^{(1)}(\psi) - l_6 V(e_1)V(Q)_1 - l_7 V(Q)V(N), \tag{6}$$

where $V^{(1)}(\psi) = 1/(1 + \psi^2)$. We accept that the concentration of menaquinone $Q^0 + q^0 = 2$, where q is the reduced form of the respiratory chain.

The respiratory chain is oxidized by oxygen (term $6lV(2-Q)V(O_2)V^{(1)}(\psi)$) and is reduced with the help of e_1 (term $-l_6 V(e_1)V(Q)$) and due to the high level of $NAD \cdot H$ (term $-l_7 V(Q)V(N)$).

The variation of the concentration of oxygen (O_2):

$$\frac{dO_2}{dt} = \frac{O_{20}}{N_5 + O_2} - lV(2-Q)V(O_2)V^{(1)}(\psi) - \alpha_7 O_2. \tag{7}$$

Under the action of a flow (terms $\dfrac{O_{2_0}}{N_5 + O_2}$ and $\alpha_7 O_2$), the level of aeration of a cell is changed. The concentration of oxygen decreases at the oxidation of the respiratory chain (term $-lV(2-Q)V(O_2)V^{(1)}(\psi)$).

The variation of the concentration of 20β-oxysteroid-dehydrogenase (E_2):

$$\frac{dE_2}{dt} = E_{20} \frac{P^2}{\beta_2 + P^2} \frac{N}{\beta + N} (1 - \frac{B}{N_2 + B}) - \\ - l_{10} V(E_2)V(N)V(P) - \alpha_2 E_2 \tag{8}$$

The increase of the level of the given enzyme occurs due to the biosynthesis:
$E_{20} \dfrac{P^2}{\beta_2 + P^2} \dfrac{N}{\beta + N}(1 - \dfrac{B}{N_2 + B})$. Prednisolone and $NAD \cdot H$ are activators of this process, and 20β-oxyderivative is an inhibitor. The decrease of the level of the given enzyme occurs as a result of the inactivation ($-\alpha_2 E_2$) and the process of transformation of prednisolone ($-l_{10}V(E_2)V(N)V(P)$).

$$\frac{dN}{dt} = -l_2 V(E_2)V(N)V(P) - l_7 V(Q)V(N) +$$
$$+ k_2 V(B) \frac{\psi}{K_{10} + \psi} + \frac{N_0}{N_4 + N} - \alpha_6 N. \tag{9}$$

The level of the co-enzyme N decreases in the process of transformation $P \Rightarrow B$, in the process of reduction of the respiratory chain ($-l_7 V(Q)V(N)$), and due to a flow ($-\alpha_6 N$). It increases at the use of B by cells in the Krebs cycle as a substrate ($k_2 V(B) \dfrac{\psi}{K_{10} + \psi}$) and in the presence of endogenous substrates ($\dfrac{N_0}{N_4 + N}$) in the environment.

The variation of the level of kinetic membrane potential (ψ):

$$\frac{d\psi}{dt} = l_5 V(E_1)V(G) + l_8 V(N)V(Q) - \alpha \psi. \tag{10}$$

The kinetic membrane potential arises at the transformation of hydrocortisone ($l_5 V(E_1)V(G)$) and the reduction of the respiratory chain ($l_8 V(N)V(Q)$) at a high level of $NAD \cdot H$ and decreases due to other metabolic processes ($-\alpha \psi$). The variation of the level of ψ changes its regulatory role (1), (3), (6), (7), (9). If the potential is high, the respiratory chain is blocked and held in the reduced state.

The main parameters of the system, with which we fit the relevant experimental data, are as follows: $l = l_1 = k_1 = 0.2$; $l_2 = l_{10} = 0.27$; $l_5 = 0.6$; $l_4 = l_6 = 0.5$; $l_7 = 1.2$; $l_8 = 2.4$; $k_2 = 1.5$; $E_{10} = 3$; $\beta_1 = 2$; $N_1 = 0.03$; $m = 2.5$; $\alpha = 0.033$; $a_1 = 0.007$; $\alpha_1 = 0.0068$; $E_{20} = 1.2$; $\beta = 0.01$; $\beta_2 = 1$; $N_2 = 0.03$; $\alpha_2 = 0.02$; $G_0 = 0.019$; $N_3 = 2$; $\gamma_2 = 0.2$; $\alpha_5 = 0.014$; $\alpha_3 = \alpha_4 = \alpha_6 = \alpha_7 = 0.001$; $O_{20} = 0.015$; $N_5 = 0.1$; $N_0 = 0.003$; $N_4 = 1$; $K_{10} = 0.7$.

The study of solutions of the given mathematical model was carried out with the help of the theory of nonlinear differential equations [25-27].

In the numerical solution of this autonomous system of nonlinear differential equations, we used the Runge--Kutta--Merson method. The accuracy of calculations was set to be 10^{-8}. To attain the reliability of a solution, when the system passes from the initial transient phase onto the asymptotic solution with an attractor, the duration of calculations was taken to be 10^6. For this time interval, the trajectory "sticks" onto the appropriate attractor.

The various types of autooscillatory modes are studied with the help of the construction of exact phase-parametric diagrams. We found the scenarios of appearance of bifurcations at the transition of the dynamical process from one type of an attractor to another one. For the most characteristic modes, we calculated the total spectra of Lyapunov indices (Table 1).

To construct a phase-parametric diagram, we used the method of section. In the phase space of trajectories of the system, we place a cutting plane with $P = 0.2$. Such choice is explained by the symmetry of oscillations relative to this point of this variable in multiple modes. If the trajectory $P(t)$ crosses this plane in a certain direction, we mark the value of chosen variable (e.g., G) on the phase-parametric diagram. In such way, we have the point corresponding to the section of a trajectory by the two-dimensional plane. If the multiple periodic limiting cycle appears, we obtain a number of points, which will be coincide in a period. If a deterministic chaos arises, the points of intersection of trajectories by the plane will be placed chaotically.

In order to uniquely identify the form of an attractor for the chosen points, we calculated the total spectrum of Lyapunov indices and determined their sum

$$\Lambda = \sum_{j}^{10} \lambda_j$$ (see Table 1). The calculation was carried out by Benettin's

algorithm with orthogonalization of the vectors of perturbation by the Gram--Schmidt method [26, 28, 29].

3. Results of Studies

We now consider the dynamics of modes within the mathematical model (1)-(10) under a variation of the dissipation of a kinetic membrane potential α (10) [16, 17]. We found the autooscillatory and chaotic modes with various multiplicities. The projections of their phase portraits have a characteristic form shown in Fig. 2,a,b.
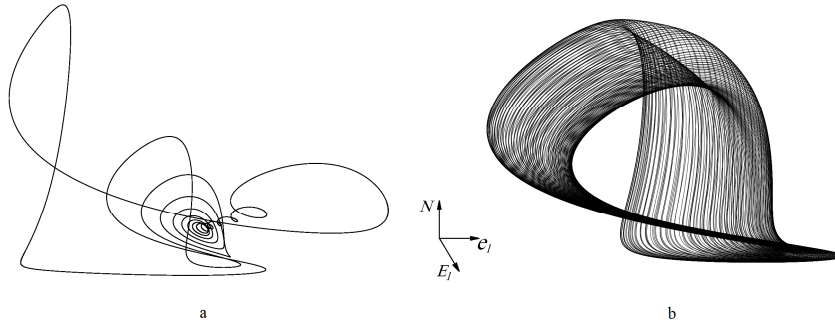
Fig. 2. Projections of the phase portraits of regular attractors: a – autoperiodic cycle $14 \cdot 2^0$ for $\alpha = 0.033$; b – quasiperiodic cycle $\approx 31 \cdot 2^0$ for $\alpha = 0.0321375$.

Let us consider a part of the bifurcation diagram not studied earlier. In Fig. 3, we show the bifurcation diagram for $\alpha \in (0.032159, 0.32166)$.
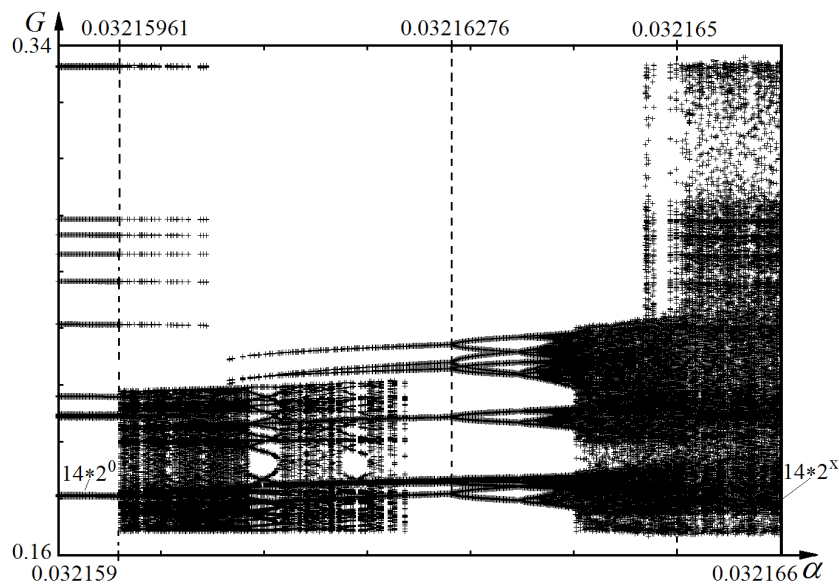

Fig. 3. Bifurcation diagram of the system for $\alpha \in (0.032159, 0.32166)$.

For $\alpha \in (0.0321590, 0.03215960)$, the regular attractor of the 14-fold period $14 \cdot 2^0$ is kept in the system. For $\alpha = 0.03215961$, we observe the appearance of the period doubling bifurcation with the generation of the regular attractor $14 \cdot 2^1$ (Table 1). Then for $\alpha = 0.03215962$, there arises the bifurcation of the generation of a two-dimensional torus (the Neimark bifurcation). The configuration of kinetic curves is instantly changed, and the quasiperiodic

attractor with n-fold period is established on the toroidal surface $\approx n \cdot 2^0 (t)$ (Figs. 4,a and 5,a).
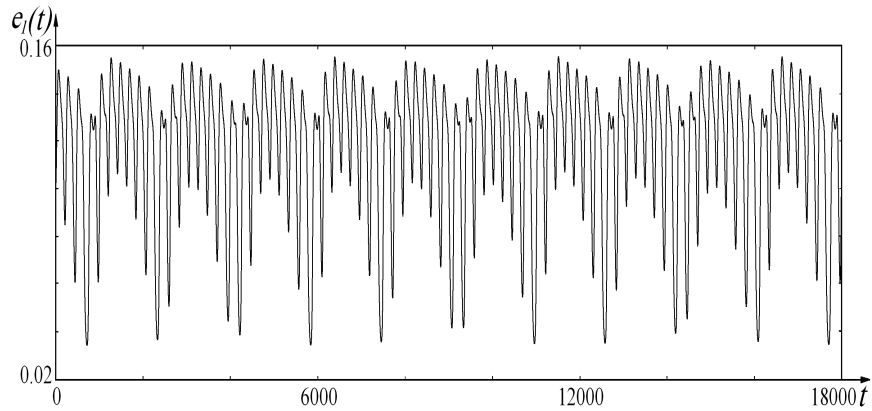
a - regular attractor of the quasiperiodic cycle $\approx n*2^0$ on the toroidal surface for $\alpha = 0.03215962$.
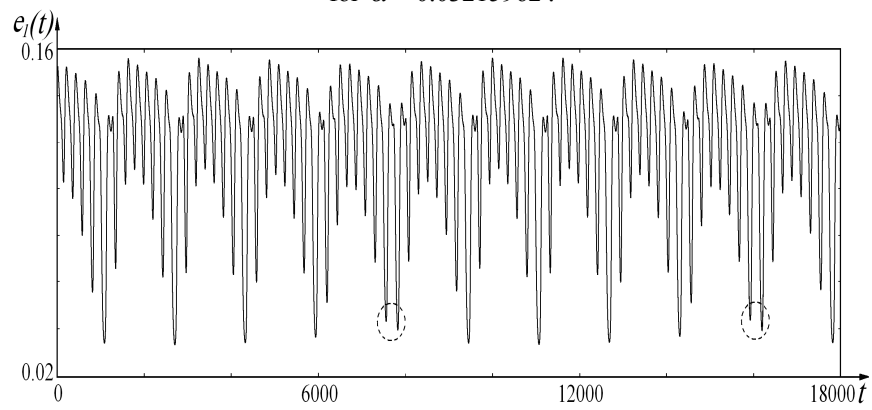
b - regular attractor $36 \cdot 2^0$ for $\alpha = 0.032162$.

Fig. 4. Kinetic curve of the variable $e_1(t)$.
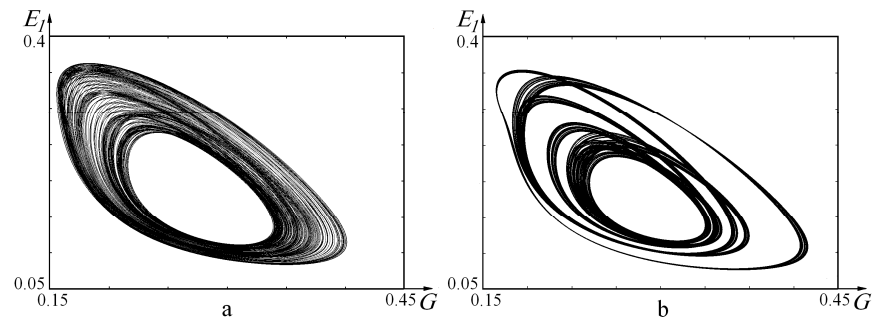
Fig. 5. Projections of phase portraits: a – regular attractor of the quasiperiodic cycle $\approx n \cdot 2^0$ on the toroidal surface for $\alpha = 0.03215962$; b – strange attractor $7 \cdot 2^x$ for $\alpha = 0.032164$.

As α increases, the given attractor loses the stability, by passing periodically to the 14-fold limiting cycle ($\alpha = 0.032160$), which corresponds to the gaps in Fig. 3,a. In addition, other various multiple modes arise. For example, for $\alpha =$ 0.032161, 0.0321615, and 0.032162, the regular attractors $29 \cdot 2^0$, $7 \cdot 2^0$, and 362^0 appear, respectively (Fig. 4,b). As α increases, we see the appearance of bifurcations of the limiting cycle. Moreover, the instant structural rearrangement of the type "order-order" occurs; i.e., as a result of the self-organization, the regular attractor of some form is replaced instantly by a regular attractor of some other form. In this case, the trajectories leave the region of attraction of the attractor and are drawn in the region of attraction of another regular attractor.

The interesting scenario of the metabolic process is observed in the interval $\alpha \in (0.0321626, 0.032164)$. In Fig. 6, we present a magnified part of the bifurcation diagram in Fig. 3.
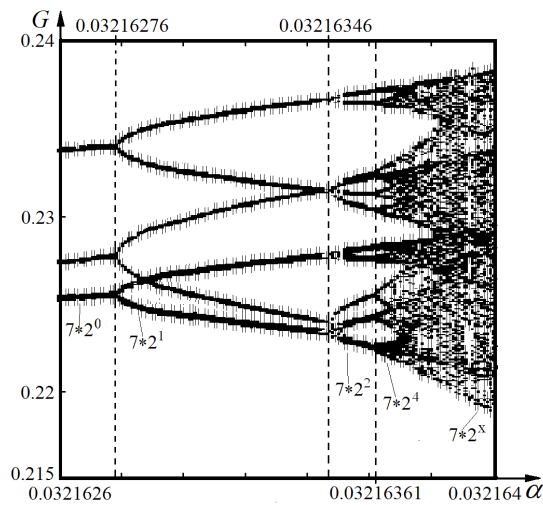
Fig. 6. Phase-parametric diagram of the system for $\alpha \in (0.0321626, 0.32164)$, where Feigenbaum's scenario is observed.

At the beginning of the interval at $\alpha = 0.0321626$, the regular attractor $7 \cdot 2^0$ is formed on the toroidal surface. For $\alpha_j = 0.03216276$, the bifurcation yields the doubling of the period, and the regular attractor $7 \cdot 2^1$ arises on the toroidal surface. For $\alpha_{j+1} = 0.03216346$ and $\alpha_{j+2} = 0.03216361$, we see the attractors

$7 \cdot 2^2$ and $7 \cdot 2^4$, respectively. This sequence of bifurcations satisfies the relation

$$\lim_{t \to \infty} \frac{\alpha_{j+1} - \alpha_j}{\alpha_{j+2} - \alpha_{j+1}} \approx 4.667 .$$

This number is very close to Feigenbaum's universal constant $\delta = 4.669211660910\ldots$ characterizing the infinite cascade of bifurcations at the transition to a deterministic chaos. Thus, as the coefficient of dissipation α increases in this region, the period of a complicated regular attractor on the torus is doubled by Feigenbaum's scenario [37-40].

The further increase in α causes a deviation from the given scenario and the formation of the strange attractor $7 \cdot 2^x$ ($\alpha = 0.032164$, Fig. 5,b) as a result of the intermittency. But then, for $\alpha = 0.032174$, the strange attractor $14 \cdot 2^x$ appears (Fig. 7,b). In the interval $\alpha \in (0.032164, 0.032174)$ as a result of the intermittency of these chaotic cycles, we observe the transition between them: $(7 \leftrightarrow 14) \cdot 2^x$. In Fig. 7,a for $\alpha = 0.032165$, we show a projection of the phase portrait of a mutual transition of the given strange attractors. Figure 8 presents the kinetic curve for the variable $e_1(t)$ for tis mode. We observe the transition "chaos-chaos": $(7 \leftrightarrow 14) \cdot 2^x$. Moreover, the strange attractor $7 \cdot 2^x$ on the left and the strange attractor $14 \cdot 2^x$ on the right move toward each other. Since there are no other attractors of the system in this region, the trajectory is chaotically kept in the region of attraction of the strange attractor $14 \cdot 2^x$ or the strange attractor $7 \cdot 2^x$ Under the effect of bifurcations, the trajectory is aperiodically drawn in one of the regions of the given strange attractors after the transient process. According to the values of higher Lyapunov indices (Table 1), the formed limiting set is unstable by Lyapunov.
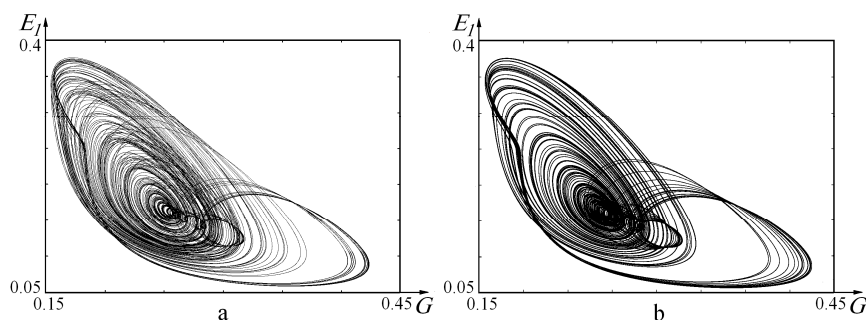
Fig. 7. Projections of the phase portraits: a – strange attractor of the mutual transition $(7 \leftrightarrow 14) \cdot 2^x$ for $\alpha = 0.032165$; b – strange attractor $14 \cdot 2^x$ for $\alpha = 0.032174$.
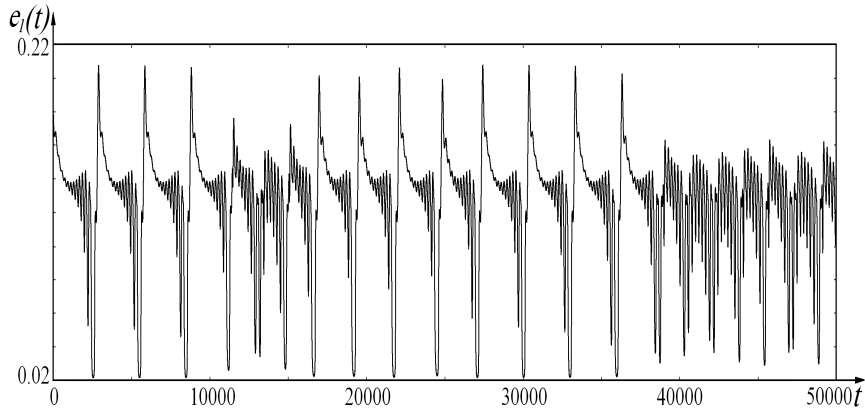
Fig. 8. Kinetic curve of the variable $e_1(t)$ of the mutual transition of the strange attractors $(7 \leftrightarrow 14) \cdot 2^x$ for $\alpha = 0.032165$.

For the given strange attractor, we constructed a projection of the section by the plane $P = 0.2$ and the Poincaré map in Fig. 9,a,b. The choice of a cutting surface was made to attain the maximum number of intersections of the given component and the phase trajectory $P(t)$, as the former decreases, without contacts.
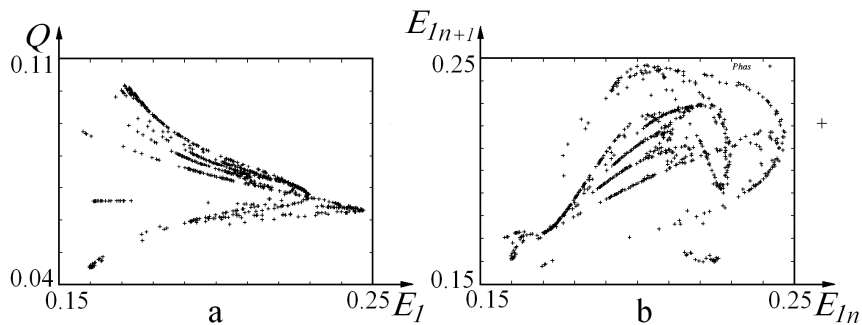

Fig. 9. Projection of the section by the plane $P = 0.2$ (a) and Poincaré map (b) of the strange attractor formed during the mutual transition $(7 \leftrightarrow 14) \cdot 2^x$ for $\alpha = 0.032165$.

The obtained points of intersections and the Poincaré maps are grouped along several curves that form a geometric self-similarity. On the projection, we see clearly the fractality of this strange attractor. In addition, these curves do not create a quasistrip structure. Their number increases permanently with the duration of numerical integration of the system. This testifies to the impossibility of any reduction of the given complicated mathematical model to some one-dimensional discrete approximation without loss of the information about the dynamics of the metabolic process in a cell. We note that the general

scheme (Fig. 2) includes only the main parts of the metabolic process running in any cell with substrate-enzyme reactions and in the respiratory chain. Therefore, the model gives a rather general qualitative representation of the dynamics of the internal self-organization of the metabolic process in a cell.

Table 1. Total spectra of Lyapunov indices for attractors of the system under study (λ_4 - λ_{10} are not important for our investigation).

α	Attractor	λ_1	λ_2	λ_3	Λ
0.0321590	$14 \cdot 2^0$	.000056	-.000214	-.003250	-.898509
0.0321596	$14 \cdot 2^0$	.000040	-.000142	-.003306	-.898550
0.03215961	$14 \cdot 2^1$	.000078	-.000150	-.003394	-.899865
0.03215962	$\approx n \cdot 2^0(t)$	.000063	.000026	-.000274	-.905553
0.032160	$14 \cdot 2^0$	.000040	-.000146	-.003365	-.899368
0.032161	$29 \cdot 2^0$	.000051	-.000142	-.000123	-.905352
0.0321615	$7 \cdot 2^0$	.000062	-.000596	-.000576	-.902277
0.032162	$36 \cdot 2^0$	.000064	-.000171	-.000155	-.905320
0.0321626	$7 \cdot 2^0(t)$	.000063	-.000097	-.001180	-.902078
0.03216276	$7 \cdot 2^1(t)$	.000062	-.000005	-.001267	-.902189
0.03216346	$7 \cdot 2^2(t)$	.000047	.000025	-.001252	-.902056
0.03216361	$7 \cdot 2^3(t)$	.000048	-.000023	-.001265	-.902267
0.032164	$7 \cdot 2^x$	.000367	.000018	-.001641	-.902164
0.032165	$(7 \leftrightarrow 14) \cdot 2^x$	.000363	-.000004	-.001598	-.904005
0.032174	$14 \cdot 2^x$	.000693	.000020	-.003534	-.901422

4. Conclusions

We have constructed a mathematical model of the metabolic process in a cell *Arthrobacter globiformis* at the transformation of steroids. With the help of the given model, we have found the autooscillations in agreement with experiment, which show the complicated internal dynamics in a cell. The model is optimized by the number of variables of the system required for a qualitative description of the metabolic process under study. The given model involves the general regularities characteristic of any cell consuming a substrate, on the whole. The autooscillations arise on the level of the substrate-enzyme interaction with participation of the redox process in the respiratory chain and characterize the times of such interactions. At the synchronization of the given processes, the autooscillations characterizing the self-organization of the metabolic process on the whole are observed. At the desynchronization of the given processes, we see the adaptation of the metabolic process in a cell to varying external conditions in the environment with conservation of its functionality. The scenario of the

transitions "order-chaos", "chaos-order", "order-order", and "chaos-chaos" is studied with the help of Poincaré sections and maps. The total spectra of Lyapunov indices are calculated, and the structural stability of the obtained attractors is studied. Feigenbaum's scenario and the Neimark bifurcation are found. The results will allow one to carry on the search for metabolic oscillations in a cell and to clarify the physical laws of self-organization.

References

1. A. A. Akhrem and Yu. A. Titov. *Steroids and Microorganisms*, Nauka, Moscow, 1970 (in Russian).

2. V. P. Gachok and V. I. Grytsay. Kinetic model of macroporous granule with the regulation of biochemical processes. *Dokl. Akad. Nauk SSSR* 282: 51-53, 1985.

3. V. P. Gachok, V. I. Grytsay, A. Yu. Arinbasarova, A. G. Medentsev, K. A. Koshcheyenko and V. K. Akimenko. Kinetic Model of Hydrocortisone 1-en Dehydrogenation by *Arthrobacter globiformis*. *Biotechn. Bioengin.* 33: 661-667, 1989.

4. V. P. Gachok, V. I. Grytsay, A. Yu. Arinbasarova, A. G. Medentsev, K. A. Koshcheyenko and V. K. Akimenko. A kinetic model for regulation of redox reactions in steroid transformation by *Arthrobacter globiformis* cells. *Biotechn. Bioengin.* 33: 668-680, 1989.

5. V. I. Grytsay. Self-organization in the macroporous structure of the gel with immobilized cells. Kinetic model of bioselective membrane of biosensor. *Dopov. Nats. Akad. Nauk Ukr.* No 2: 175-179, 2000.

6. V. I. Grytsay. Self-organization in a reaction-diffusion porous media. *Dopov. Nats. Akad. Nauk Ukr.* No. 3: 201-206, 2000.

7. V. I. Grytsay. Ordered structure in a mathematical model biosensor. *Dopov. Nats. Akad. Nauk Ukr.* No. 11: 112–116, 2000.

8. V. I. Grytsay. Self-organization of biochemical process of immobilized cells bioselective of membrane biosensor. *Ukr. J. Phys.* 46: 124-127, 2001.

9. V. V. Andreev and V. I. Grytsay. Modeling of inactive zones in porous granules of a catalyst and in a biosensor. *Matem. Modelir.* 17**,** no. 2: 57-64, 2005.

10. V. V. Andreev and V. I. Grytsay. Influence of heterogeneity of diffusion-reaction process for the formation of structures in the porous medium. *Matem. Modelir.* 17, no. 6: 3-12, 2005.

11. V. I. Grytsay and V. V. Andreev. The role of diffusion in the active structures formation in porous reaction-diffusion media. *Matem. Modelir.* 18, no. 12: 88-94, 2006.

12. V. I. Grytsay. Unsteady Conditions in Porous Reaction-Diffusion. *Roman. J. Biophys.* 17, no. 1: 55-62, 2007.

13. V. I. Grytsay. The uncertainty in the evolution structure of reaction-diffusion medium bioreactor. *Biofiz. Visn.* No.2: 92-97, 2007

14. V. I. Grytsay. Formation and stability of morphogenetic fields of immobilized cell in bioreactor. *Biofiz. Visn.* No. 2: 25-34, 2008.

15. V. I. Grytsay. Structural instability of a biochemical process. *Ukr. J. Phys.* 55: 599-606, 2010.

16. V. I. Grytsay and I. V. Musatenko. Self-oscillatory dynamics of the metabolic process in a cell. *Ukr. Biochem. J.* 85, no. 2: 93 – 104, 2013.

17. *V. I. Grytsay and I. V. Musatenko*. The structure of a chaos of strange attractors within a mathematical model of the metabolism of a cell. *Ukr. J. Phys*. 58: 677-686, 2013.

18. A. G. Dorofeev, M. V. Glagolev, T. F. Bondarenko and N. S. Panikov. Unusual growth kinetics of *Arthrobacter globiformis* and its explanation. *Mikrobiol.* 61**,** no. 1: 33-42, 1992.

19. A. S. Skichko and E. M. Koltsova. A mathematical model to describe the fluctuations biomass of bacteria. *Teor. Osnov. Khim. Tekhn.* 40, no. 5: 540-550, 2006.

20. E. E. Selkov. Self-oscillations in glycolysis. *Europ. J. Biochem.* 4: 79-86, 1968.

21. B. Hess and A. Boiteux. Oscillatory phenomena in biochemistry. *Ann. Rev. Biochem.* 40: 237-258, 1971.

22. A. Goldbeter and R. Lefer. Dissipative structures for an allosteric model. Application to glycolytic oscillations. *Biophys J.* 12: 1302-1315, 1972.

23. A. Godlbeter and R. Caplan. Oscillatory enzymes. *Ann. Rev. Biophys. Bioeng.* 5: 449–476, 1976.

24. *Chaos in Chemical and Biochemical Systems*. Field R., Györgyi L. (eds.), World Scientific, Singapore, 1993.

25. V. S. Anishchenko. *Complex Oscillations in Simple Systems*, Nauka, Moscow, 1990 (in Russian).

26. S. P. Kuznetsov, *Dynamical Chaos*, Nauka, Moscow, 2001 (in Russian).

27. T. S. Krasnopol'skaya and A. Yu. Shvets, *Regular and Chaotic Dynamics of Systems with Bounded Excitation*, R&C Dynamics, Moscow-Izhevsk, 2008 (in Russian).

28. I. Shimada and T. Nagashima. *Progr. Theor. Phys*. 61: 1605-1616, 1979.

29. M. Holodniok, A. Klic, M. Kubicek, M. Marek. *Methods of Analysis of Nonlinear Dynamical Models*, Academia, Praha, 1986. (in Czech).

Mutual information rate and topological order in networks

J. Leonel Rocha[1] and Acilina Caneco[2]

[1] Instituto Superior de Engenharia de Lisboa - ISEL, ADM and CEAUL, Rua Conselheiro Emídio Navarro, 1, 1959-007 Lisboa, Portugal
   (E-mail: `jrocha@adm.isel.pt`),
[2] Instituto Superior de Engenharia de Lisboa - ISEL, ADM and CIMA-UE, Rua Conselheiro Emídio Navarro, 1, 1959-007 Lisboa, Portugal
   (E-mail: `acilina@adm.isel.pt`)

Abstract. In this paper we study the evolution of the information flow associated with a topological order in networks. The amount of information produced by a network may be measure by the mutual information rate. This measure and the synchronization interval are expressed in terms of the transversal Lyapunov exponents. The networks are constructed by successively joining one edge, maintaining the same number of nodes, and the topological order is described by the monotonicity of the network topological entropy. The network topological entropy measures the complexity of the network topology and it is expressed by the Perron value of the adjacency matrix. We conclude that, as larger the network topological entropy, the larger is the rate with which information is exchanged between nodes of such networks. To illustrate our ideas we present numerical simulations for several networks with a topological order established.
Keywords: Mutual information rate, topological entropy, networks.

1 Introduction and motivation

Information theory is an area of mathematics and engineering, concerning the quantification of information and it benefits of matters like mathematics, statistics, computer science, physics, neurobiology and electrical engineering. Information theory and synchronization are directly related in a network. The entropy is a fundamental measure of information content and the topological entropy can describe the character of complexity of a network, see for example [10]. In [6], using the mutual information rate to measure the information flow, we have proved that the larger the synchronization is, the larger is the rate with which information is exchanged between nodes in the network. Although the important growth in the field of complex networks, it is still not clear which conditions for synchronization implies information transmission and it is still not known which topology is suitable for the flowing of information.

Nevertheless, we conclude with this study that, the more complex is a network, expressed by its topological entropy, the larger is the flux of information.

In this work we study the relationship between the topological order in networks and the transmission of information. The topological order in networks is described by the monotonicity of the network topological entropy. The concept of the network topological entropy was previously introduced in [10]. However, there are several concepts of network entropy, see [7]. We will use the one based on symbolic dynamics. In Sec.2, we present some preliminaries concepts to be used in the following, such as: fundamental notions of graphs theory, conditions for complete synchronization, comunication channel and mutual information rate. Sec.3 is devoted to the study of topological order in networks, using the definition of the network topological entropy. In Sec.4, numerical simulations are presented for several networks with a topological order established. Finally, in Sec.5, we discuss our study and provide some relevant conclusions.

2   Preliminaries concepts

In this section, we introduce some notions and basic results on graphs and networks theory. Mathematically, networks are described by graphs (directed or undirected) and the theory of dynamical networks is a combination of graph theory and nonlinear dynamics. From the point of view of dynamical systems, we have a global dynamical system emerging from the interactions between the local dynamics of the individual elements. The tool of graph theory allows us to analyze the coupling structure between them.

A graph G is an ordered pair $G = (V, E)$, where V is a nonempty set of N vertices or nodes v_i and E is a set of edges or links, e_{ij}, that connect two vertices v_i and v_j. We will only consider the case of undirected graphs, that means that the edge e_{ij} is the same as the edge e_{ji}. If the graph G is not weighted, the adjacency matrix $A = A(G) = [a_{ij}]$ is defined as follows:

$$a_{ij} = \begin{cases} 1, & \text{if } v_i \text{ and } v_j \text{ are connected} \\ 0, & \text{if } v_i \text{ and } v_j \text{ are not connected} \end{cases}.$$

The degree of a node v_i is the number of edges incident on it and is denoted by k_i. For more details in graph theory see [4].

Consider a network of N identical chaotic dynamical oscillators, described by a connected and undirected graph, with no loops and no multiple edges. In each node the dynamics of the oscillators is defined by $\dot{x}_i = f(x_i)$, with $f : \mathbb{R}^n \to \mathbb{R}^n$ and $x_i \in \mathbb{R}^n$ is the state variables of the node i. The state equations of this network are

$$\dot{x}_i = f(x_i) + \sigma \sum_{j=1}^{N} l_{ij} \, x_j, \quad \text{with} \quad i = 1, 2, ..., N \tag{1}$$

where $\sigma > 0$ is the coupling parameter, $L = [l_{ij}] = A - D$ is the Laplacian matrix or coupling configuration of the network. One of the most important subjects under investigation is the network synchronizability. It may be studied fixing the connection topology and varying the local dynamics or fixing the local

dynamic and varying the connection topology [5]. In [9] it was establish that complete synchronization can be achieved provided that all the conditional Lyapunov exponents are negative. In Sec.4, we use this result to determine the synchronization interval. The negativity of the conditional Lyapunov exponents is a necessary condition for the stability of the synchronized state, [3]. It is also a mathematical expression of the decreasing to zero of the logarithm average of the distance of the solutions on the transverse manifold to the solutions on the synchronization manifold.

A communication channel represents a pathway through which information is exchanged. In this work, a communication channel is considered to be formed by a transmitter S_i and a receiver S_j, where the information about the transmitter can be measured. In a network, each one of the links between them, i.e., each one of the edges of the corresponding graph, represents a communication channel. In [1], it is defined $I_C(S_i, S_j)$, the mutual information rate (MIR) between one transmitter S_i and one receiver S_j, by

$$I_C(S_i, S_j) = \begin{cases} \lambda_\parallel - \lambda_\perp \,, \text{ if } \lambda_\perp > 0 \\ \\ \lambda_\parallel \qquad \,, \text{ if } \lambda_\perp \leq 0 \end{cases}, \tag{2}$$

where $\lambda_\parallel$ denotes the positive Lyapunov exponents associated to the synchronization manifold and $\lambda_\perp$ denotes the positive Lyapunov exponents associated to the transversal manifold, between S_i and S_j. $\lambda_\parallel$ represents the information (entropy production per time unit) produced by the synchronous trajectories and corresponds to the amount of information transmitted. On the other hand, $\lambda_\perp$ represents the information produced by the nonsynchronous trajectories and corresponds to the information lost in the transmission, the information that is erroneously retrieved in the receiver. For more details and references see for example [1] and [2]. In [6], we prove that, as the coupling parameter increases, the mutual information rate increases to a maximum in the synchronization interval and then decreases.

3   Topological order in networks

In this section we study a topological order in networks, which are constructed by successively joining one edge, maintaining the same number of nodes. This topological order is described by the monotonicity of the network topological entropy. The introduction of the network topological entropy concept was made in [10], which requires a strict and long construction, using tools of symbolic dynamics and algebraic graph theory. However, we present some basic aspects of this definition. The topological entropy $h_{top}(X)$ of a shift dynamical system (X, σ) over some finite alphabet $\mathcal{A}$ is defined by

$$h_{top}(X) = \lim_{n \to \infty} \frac{\log Tr\left(A^n(X)\right)}{n}$$

and $h_{top}(X) = 0$ if $X = \emptyset$, where $A(X)$ is the transition matrix of X, [8]. We remark that the transition matrix $A(X)$ describes the dynamics between

the nodes of the network, which is represented by a graph G. The Perron-Frobenius Theorem states that, if the adjacency matrix $A \neq 0$ is irreducible and λ_A is the Perron value of A, then $h_{top}(X) = \log \lambda_A$. We calculate the topological entropy of the associated dynamical system, which is equal to the logarithm of the growth rate of the number of admissible words, [8]. If we have a network associated to a graph G, which determine the shift space X, we will call network topological entropy of G the quantity $h_{top}(X)$, i.e.,

$$h_{top}(G) = h_{top}(X) = \log \lambda_A. \tag{3}$$

The following result establishes a topological order in networks.

Proposition 1. *Let G_1 and G_2 be two undirected graphs, with the same number of vertices N, and G_1 be a not complete graph. If the graph G_2 is obtained from the graph G_1 by joining an edge, then $h_{top}(G_2) > h_{top}(G_1)$.*

Proof. Let $A = [a_{ij}]$ and $B = [b_{ij}]$ be the adjacency matrices of the graphs G_1 and G_2, respectively. If the graph G_2 is obtained from the graph G_1 by joining an edge, then the adjacency matrix B is obtained from the adjacency matrix A by replacing some entry $a_{ij} = 0$ by $b_{ij} = 1$. As the graphs G_1 and G_2 are not directed, then the matrices A and B are symmetric, and $b_{ji} = 1$. Thus, the matrix B is equal to the matrix A plus some matrix with non negative entries. For any power n, we have $B^n = A^n + C$, for some matrix C whose entries are all non negative. As $Tr(C) \geq 0$ and $Tr(B^n) = Tr(A^n) + Tr(C)$, then $Tr(B^n) > Tr(A^n)$. Consequently, we obtain $\frac{\log \ Tr(B^n)}{n} > \frac{\log \ Tr(A^n)}{n}$, for all integers n. From the definition of network topological entropy, Eq.(3), we have $h_{top}(G_2) > h_{top}(G_1)$.

4   Numerical simulations

In this section we will consider, as an example, a network with $N = 6$ nodes, having in each node the same skew-tent map, $f : [0, 1] \to [0, 1]$, defined by

$$f(x) = \begin{cases} \frac{x}{a} & \text{, if } 0 \leq x \leq a \\ \frac{1-x}{1-a} & \text{, if } a < x \leq 1 \end{cases}, \tag{4}$$

with $0.5 \leq a < 1$, see [6]. See Fig.1 where we present some examples of these networks. We start with a network of 7 edges and without the edges e_{12}, e_{35}, e_{56}, e_{34}, e_{46}, e_{25}, e_{36}, e_{24} and each time we add the last edge of this list, we evaluate the eigenvalues of the Jacobian matrix, the Lyapunov exponents, the region where all transversal Lyapunov exponents are negatives, the synchronization interval and the mutual information rate for all communication channels of these networks. In order to compare the results, as we add one edge, we consider for all studied cases the same value $a = 0.9$ of the skew-tent map parameter. For this network, the region where all transversal Lyapunov exponents are negatives do not intersect the line $a = 0.9$. So, for this value of a there is no synchronization interval, see 1) of Fig.2 and we do not evaluate the mutual information rate in this case.
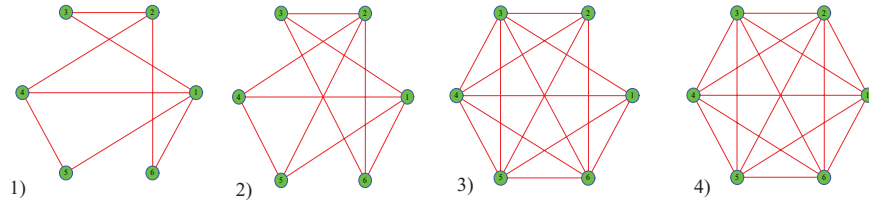
Fig. 1. Construction of networks by successively joining one edge, with 8, 10, 14 and 15 edges and $N = 6$ nodes.

We present the details for the network with 8 edges shown in 1) of Fig.1. The adjacency matrix A and the Laplacian matrix L of this network are:

$$A = \begin{bmatrix} 0 & 0 & 1 & 1 & 1 & 1 \\ 0 & 0 & 1 & 1 & 0 & 1 \\ 1 & 1 & 0 & 0 & 0 & 0 \\ 1 & 1 & 0 & 0 & 1 & 0 \\ 1 & 0 & 0 & 1 & 0 & 0 \\ 1 & 1 & 0 & 0 & 0 & 0 \end{bmatrix} \quad \text{and} \quad L = A - D = \begin{bmatrix} -4 & 0 & 1 & 1 & 1 & 1 \\ 0 & -3 & 1 & 1 & 0 & 1 \\ 1 & 1 & -2 & 0 & 0 & 0 \\ 1 & 1 & 0 & -3 & 1 & 0 \\ 1 & 0 & 0 & 1 & -2 & 0 \\ 1 & 1 & 0 & 0 & 0 & -2 \end{bmatrix},$$

where D is the diagonal matrix with entries $d_{ii} = k_i$, beeing k_i the degree of each node i. This network is defined by the following system,

$$\begin{cases} \dot{x}_1 = f(x_1) + \sigma(-4x_1 + x_3 + x_4 + x_5 + x_6) \\ \dot{x}_2 = f(x_2) + \sigma(-3x_2 + x_3 + x_4 + x_6) \\ \dot{x}_3 = f(x_3) + \sigma(x_1 + x_2 - 2x_3) \\ \dot{x}_4 = f(x_4) + \sigma(x_1 + x_2 - 3x_4 + x_5) \\ \dot{x}_5 = f(x_5) + \sigma(x_1 + x_4 - 2x_5) \\ \dot{x}_6 = f(x_6) + \sigma(x_1 + x_2 - 2x_6) \end{cases},$$

where σ is the coupling parameter. The Jacobian matrix is given by,

$$J = \begin{bmatrix} c - 4\sigma & 0 & \sigma & \sigma & \sigma & \sigma \\ 0 & c - 3\sigma & \sigma & \sigma & 0 & \sigma \\ \sigma & \sigma & c - 2\sigma & 0 & 0 & 0 \\ \sigma & \sigma & 0 & c - 3\sigma & \sigma & 0 \\ \sigma & 0 & 0 & \sigma & c - 2\sigma & 0 \\ \sigma & \sigma & 0 & 0 & 0 & c - 2\sigma \end{bmatrix},$$

being $c = c(x)$ the slope of f, Eq.(4), given by $c(x) = \frac{1}{a}$, if $x \leq a$ and $c(x) = -\frac{1}{1-a}$ if $x > a$. The eigenvalues of the Jacobian are $\mu_1 = c$, $\mu_2 = c - 4\sigma$, $\mu_3 = c - 3\sigma$, $\mu_4 = c - 2\sigma$, $\mu_5 = c - \frac{7}{2}\sigma - \frac{\sqrt{17}}{2}$ and $\mu_6 = c - \frac{7}{2}\sigma - \frac{\sqrt{17}}{2}$. The first eigenvector is $(1, 1, 1, 1, 1, 1)$ and it corresponds to the parallel Lyapunov exponent $\lambda_\parallel$. The others eigenvectors correspond to the transversal Lyapunov exponents $\lambda_{\perp_i}$, with $i = 2, 3, 4, 5, 6$. So, the parallel Lyapunov exponent is

$$\lambda_\parallel = \int \ln|\mu_1| = \int_0^a \ln\frac{1}{a} + \int_a^1 \ln\left|\frac{-1}{1-a}\right| = -a \ln a - (1-a)\ln(1-a) \quad (5)$$
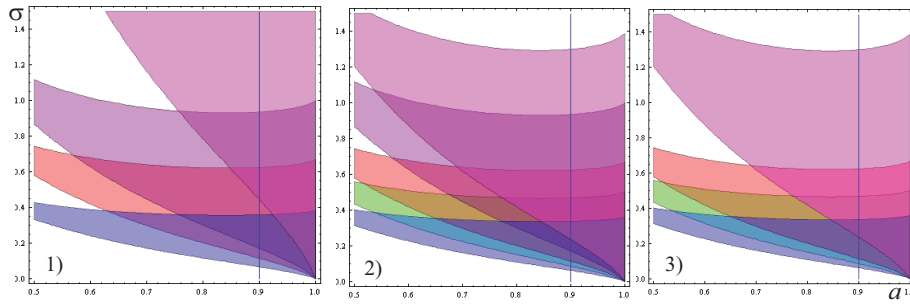
Fig. 2. Regions where the transversal Lyapunov exponents are negatives. The synchronization region is the intersection of these regions. In the vertical axis is the coupling parameter σ and in the horizontal axis is the tent map parameter a. In 1) is the network with 7 edges, in 2) with 8 edges, and in 3) with 9 edges. The image in 1) shows that for $a = 0.9$ there is no synchronization interval because the intersection of the regions where all transversal Lyapunov exponents are negatives does not occur for $a = 0.9$.
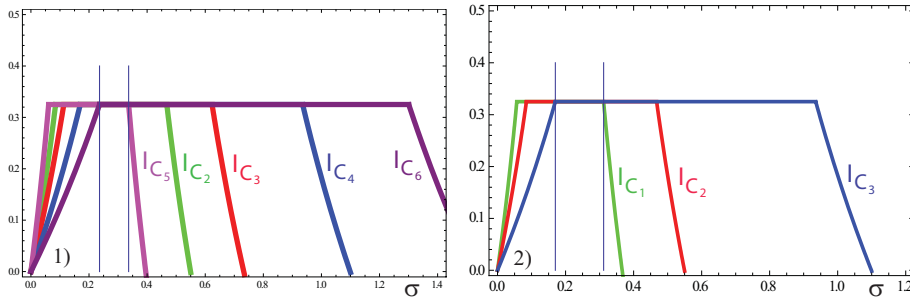
Fig. 3. I_{C_i} for the network with 8 edges in 1) of Fig.1 and with 10 edges in 2) of Fig.1.

and the transversal Lyapunov exponents are

$$\lambda_{\perp_i} = a \ln \left| \frac{1}{a} - \nu_i \sigma \right| + (1-a) \ln \left| -\frac{1}{1-a} - \nu_i \sigma \right|, \quad \text{with} \quad i = 2, 3, 4, 5, 6$$

where $\nu_2 = 4$, $\nu_3 = 3$, $\nu_4 = 2$, $\nu_5 = \frac{7}{2}\sigma + \frac{\sqrt{17}}{2}$ and $\nu_6 = \frac{7}{2}\sigma - \frac{\sqrt{17}}{2}$. In order to have synchronization, all transversal Lyapunov exponents must be negatives, see 2) in Fig.2. In this figure, each color corresponds to a region where one of the transversal Lyapunov exponents is negative. For example, if $a = 0.9$, then the synchronization interval is $]0.236, 0.336[$, where all the transversal Lyapunov exponents $\lambda_{\perp_i}$ are negative. See also 3) in Fig.2 for the network with 9 edges. To evaluate the mutual information rate (MIR), according to Eq.(2), for each $\lambda_{\perp_i}$ we obtain the interval $]a_i, b_i[$ where $\lambda_{\perp_i} < 0$, thus

$$I_{C_i} = \begin{cases} -a \ln a - (1-a)\ln(1-a) - a \ln \left| \frac{1}{a} - \nu_i \sigma \right| - (1-a)\ln \left| -\frac{1}{1-a} - \nu_i \sigma \right|, \\ \qquad \qquad \text{if} \quad \sigma < a_i \quad \text{or} \quad \sigma > b_i \\ -a \ln a - (1-a)\ln(1-a), \quad \text{if} \quad a_i < \sigma < b_i \end{cases}$$

with $a = 0.9$ and $i = 2, 3, 4, 5, 6$. See in 1) of Fig.3 the plots of these I_{C_i}. The MIR attains its maximum $0.325...$, in an interval of lenght 1.028 and the network topological entropy, given by Eq.(3), is $\log \lambda_A = 1.02835...$.

The second case that we study in detail is the network with 10 edges and without the edges e_{12}, e_{35}, e_{56}, e_{34}, e_{46}, see 2) of Fig.1. The adjacency matrix A and the Laplacian matrix L are given by,

$$A = \begin{bmatrix} 0 & 0 & 1 & 1 & 1 & 1 \\ 0 & 0 & 1 & 1 & 1 & 1 \\ 1 & 1 & 0 & 0 & 0 & 1 \\ 1 & 1 & 0 & 0 & 1 & 0 \\ 1 & 1 & 0 & 1 & 0 & 0 \\ 1 & 1 & 1 & 0 & 0 & 0 \end{bmatrix} \quad \text{and} \quad L = A - D = \begin{bmatrix} -4 & 0 & 1 & 1 & 1 & 1 \\ 0 & -4 & 1 & 1 & 1 & 1 \\ 1 & 1 & -3 & 0 & 0 & 1 \\ 1 & 1 & 0 & -3 & 1 & 0 \\ 1 & 1 & 0 & 1 & -3 & 0 \\ 1 & 1 & 1 & 0 & 0 & -3 \end{bmatrix}.$$

This network is defined by the system,

$$\begin{cases} \dot{x}_1 = f(x_1) + \sigma(-4x_1 + x_3 + x_4 + x_5 + x_6) \\ \dot{x}_2 = f(x_2) + \sigma(-4x_2 + x_3 + x_4 + +x_5 + x_6) \\ \dot{x}_3 = f(x_3) + \sigma(x_1 + x_2 - 3x_3 + x_4) \\ \dot{x}_4 = f(x_4) + \sigma(x_1 + x_2 - 3x_4 + x_5) \\ \dot{x}_5 = f(x_5) + \sigma(x_1 + x_2 + x_4 - 3x_5) \\ \dot{x}_6 = f(x_6) + \sigma(x_1 + x_2 + x_3 - 3x_6) \end{cases},$$

and the Jacobian matrix is given by

$$J = \begin{bmatrix} c-4\sigma & 0 & \sigma & \sigma & \sigma & \sigma \\ 0 & c-4\sigma & \sigma & \sigma & \sigma & \sigma \\ \sigma & \sigma & c-3\sigma & \sigma & 0 & 0 \\ \sigma & \sigma & \sigma & c-3\sigma & \sigma & 0 \\ \sigma & \sigma & 0 & \sigma & c-3\sigma & 0 \\ \sigma & \sigma & \sigma & 0 & 0 & c-3\sigma \end{bmatrix}.$$

The eigenvalues of the Jacobian matrix are $\mu_1 = c$, $\mu_2 = c - 6\sigma$, $\mu_3 = \mu_4 = \mu_5 = c - 4\sigma$ and $\mu_5 = c - 2\sigma$. Thus, the parallel Lyapunov exponent is identical to the previous case, Eq.(5), and the transversal Lyapunov exponents are

$$\lambda_{\perp_i} = a \ln \left| \frac{1}{a} - \nu_i \sigma \right| + (1-a) \ln \left| -\frac{1}{1-a} - \nu_i \sigma \right|, \quad \text{with } i = 2, 3, 4$$

where $\nu_2 = 6$, $\nu_3 = 4$ and $\nu_4 = 2$. See 1) in Fig.4 the regions where these transversal Lyapunov exponents are negatives. For $a = 0.9$, this network synchronizes if $\sigma \in]0.170, 0.312[$. We compute the I_{C_i} like in the previous case and we plot its graphics in 2) of Fig.3. The MIR attains its maximum $0.325...$, in an interval of lenght 1.216 and the network topological entropy is $\log \lambda_A = 1.21559....$ Figs.4, 5 and Table 1 contain information similar to the other cases analyzed in this topological order.

5   Conclusions and discussion

We started our simulations, considering the network with 8 edges and without the edges e_{12}, e_{35}, e_{56}, e_{34}, e_{46}, e_{25}, e_{36} and in each step we add the last edge
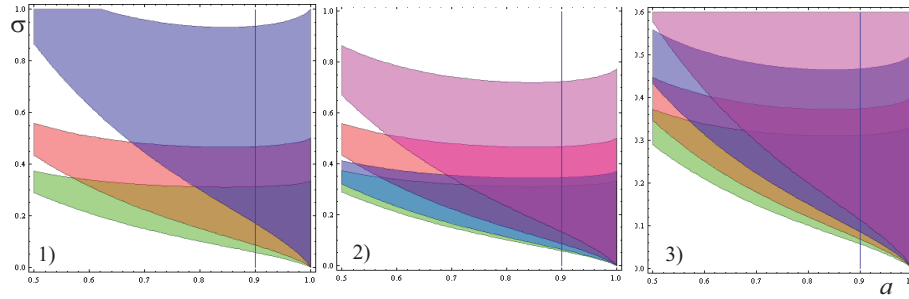
Fig. 4. Regions where the transversal Lyapunov exponents are negatives. The synchronization region is the intersection of these regions. In 1) is the network with 10 edges, in 2) with 11 edges, and in 3) with 12 edges. For the same value of a, the amplitude of the synchronization interval increases.
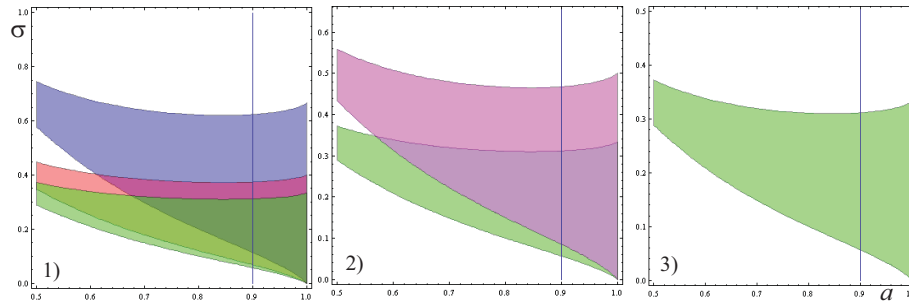

Fig. 5. Regions where the transversal Lyapunov exponents are negatives. The synchronization region is the intersection of these regions. In 1) is the network with 13 edges, in 2) with 14 edges and in 3) with 15 edges (complete network). For the same value of a, the amplitude of the synchronization interval increases.

Edges	$\mu_i = c - \nu_i\sigma$ $(i=2,3,4,5,6)$	Sync. interv.	Ampl.	$\log\lambda_A$
8	$\nu_2=4,\ \nu_3=3,\ \nu_4=2,\ \nu_5=\frac{7+\sqrt{17}}{2},\ \nu_6=\frac{7-\sqrt{17}}{2}$	$]0.236,0.336[$	0.100	1.028
9	$\nu_2=\nu_3=4,\ \nu_4=3,\ \nu_5=\frac{7+\sqrt{17}}{2},\ \nu_6=\frac{7-\sqrt{17}}{2}$	$]0.236,0.336[$	0.100	1.127
10	$\nu_2=6,\ \nu_3=\nu_4=\nu_5=4,\ \nu_6=2$	$]0.170,0.312[$	0.142	1.216
11	$\nu_2=6,\ \nu_3=\nu_4=4,\ \nu_5=4+\sqrt{2},\ \nu_6=4-\sqrt{2}$	$]0.131,0.312[$	0.181	1.312
12	$\nu_2=\nu_3=6,\ \nu_4=5,\ \nu_5=4,\ \nu_6=3$	$]0.113,0.312[$	0.199	1.403
13	$\nu_2=\nu_3=\nu_4=6\ \nu_5=\nu_6=4$	$]0.085,0.312[$	0.227	1.475
14	$\nu_2=\nu_3=\nu_4=\nu_5=6\ \nu_6=4$	$]0.085,0.312[$	0.227	1.548
15	$\nu_2=\nu_3=\nu_4=\nu_5=\nu_6=6$	$]0.057,0.312[$	0.255	1.609

Table 1. Jacobian eigenvalues, μ_i, for $(i=2,3,4,5,6)$, which correspond to the transversal Lyapunov exponents, synchronization interval, its amplitude, network topological entropy and the number of edges from 8 to 15 (complete network).

of this list. In each step of this construction, we obtain the Laplacian matrix and compute the eigenvalues μ_i $(i=1,2,3,4,5,6)$ of the Jacobian matrix, the parallel and transversal Lyapunov exponents, the synchronization interval, the network topological entropy and the I_{C_i} for the networks with 8, 9, 10, 11, 12, 13, 14 and 15 edges (complete network). For all these cases $\mu_1 = c$
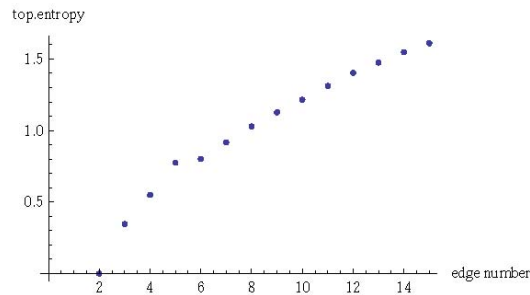
Fig. 6. The network topological entropy increases as the the number of edges of the network increases.

and this eigenvalue correspond to the synchronization manifold. The others μ_i correspond to the transversal Lyapunov exponents and are presented in Table 1. In this table is also presented the synchronization interval and the network topological entropy, for all these cases. See in Figs.2, 4 and 5 the synchronization regions, in terms of the skew-tent map parameter a and of the coupling parameter σ. In Fig.6 we may see that the network topological entropy increases as we add one edge sucessively to the network, which confirms Proposition 1.

From the numerical simulations shown in figures and Table 1, we conclude that, with the topological order established, the interval where the mutual information rate attains its maximum, the synchronization interval, increases its amplitude. Thus, we claim that:

Conjecture: As larger the network topological entropy, the larger is the rate with which information is exchanged between nodes in the network.

Acknowledgment

References

1. M. S. Baptista and J. Kurths, Chaotic channel, *Phys. Rev. E*, **72**, 045202R, (2005).
2. M. S. Baptista and J. Kurths, Information transmission in active networks, *Phys. Rev. E*, **77**, 026205, (2008).
3. S. Boccaletti, J. Kurths, G. Osipov, D.L. Valladares and C.S. Zhou, The synchronization of chaotic systems, *Physics Reports*, **366**, 1-101, (2002).
4. B. Bollobás and O.M. Riordan, *Handbook of Graphs and Networks: From the Genome to the Internet*, Wiley-VCH, 2003.
5. A. Caneco, S. Fernandes, C. Grácio and J.L. Rocha, Networks synchronizability, local dynamics and some graph invariants, *Dynamics, Games and Science I, Springer Proceedings in Mathematics*, **1**, 221-238, (2011).

6.A. Caneco and J.L. Rocha, Synchronization and information transmission in networks, *submited*.

7.L. Ji, B.-H. Wang , W.-X. Wang and T. Zhou , Network entropy based on topology configuration and its computation to random networks, *Chin. Phys. Lett.*, **25**, 11, 4177, (2008).

8.D. Lind and B. Marcus, *Symbolic Dynamics and Coding*, Cambridge University Press, 1995.

9.L. M. Pecora and T. L. Carroll, Driving systems with chaotic signals, *Phys. Rev. A*, **44**, 2374-2383, (1991).

10.J.L. Rocha, C. Grácio, S. Fernandes, A. Caneco, Spectral and dynamical invariants in a complete clustered network, *submited*.

Chaos In a Modified Cardiorespiratory Model

Tatyana S. Krasnopolskaya [1]
Evgeniy D. Pechuk [2]

[1] Institute of Hydromechanics NASU, Kyiv, Ukraine
E-mail: t.krasnopolskaya@tue.nl
[2] Institute of Hydromechanics NASU, Kyiv, Ukraine
E-mail: uzuzun@i.ua

Abstract: A new modified cardiorespiratory model based on the famous DeBoer beat-to-beat model and Zaslavsky map (which describes dynamics of the respiratory system as a generator of central type) was studied in details. In this case the respiratory tract was firstly modeled by the self-oscillating system under the impulsive influence of heartbeat. The steady-state regimes of the modified model are investigated by methods of the dynamical system theory. The regular (periodic and quasi-periodic) and chaotic regimes typical for functioning of the cardiosystem are found and studied.
Keywords: A beat-to-beat model, Cardiorespiratory system, DeBoer model, Zaslavsky map, Nonlinear dynamics, Chaotic regimes.

1. Introduction

The human cardiovascular system closly interacts with different organs and systems of organism. Realized self-oscillations in a cardiovascular system are under an activity of practically entire organism (see [2-5, 9-11]). Physiological rhythms are not isolated processes. There are numerous interactions of rhythms between itself and with an internal and external environment. Cardiac and respiratory rhythms form up during embryo development, and even the brief break of these rhythms after a birth results in death.

Existence of breathing and heart rhythm synchronization effect, found experimentally in the cardiovascular system both for healthy people and with pathologies, is well-proven in work Toledo [10] in 2002. It is well known, the dynamic process of mutual synchronization can be realized only in a case of presence of a subsystem mechanical interaction. Therefore, the indicated effect display testifies the presence of both direct and feedback interactions between the cardiovascular and respiratory systems.

A heart system and organism of man in general have one of major descriptions of activity, such as a blood pressure dynamics. His time-history, along with electrocardiogram (ECG), is an important information generator for research and diagnostics of laws and pathologies of the cardiovascular system. The task of mathematical model construction, describing the dynamics of arterial blood pressure, is far from completion. Complications of such design are related to the necessity of taking into account of influence on the cardiac rhythms not only the cardiovascular system but also other organs and systems of organism, in particular a respiratory system.
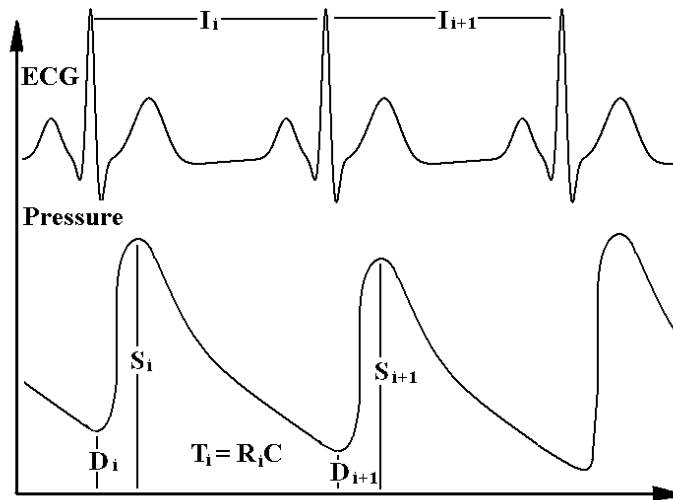
Fig. 1. Characteristics of the heartbeat in DeBoer model.

2. The mathematical model of a direct and reverse interactions

The DeBoer model of a cardiovascular system is under direct action of a respiratory systems (what corresponds to experimental data) [3]. This model was substantially developed in future. The sinus node responsiveness (and other detailed factors) is taking into account in the work of Seidel and Herzel [9] (the so-called SH-model). In this model chaotic dynamics was found in dynamics of a cardiosystem.

The models of both DeBoer and SH only considered direct respiratory influence on heartbeats. The SH-model got further development [5], where an effect of heartbeat and the resultant changes in the baroreceptor afferent activitiy to the SH-model are added and the cardiorespiratory sinchronization found due to this modification. Interaction of blood pressure and amplitudes of breathing oscillations revealed in accordance with principles of optimum control in the DeBoer model is investigated in the Grinchenko-Rudnitsky model [2]. This model allowed, in particular, to explain appearance of a peak on the Meyer frequency in the spectrums of pressure oscillations and synchronization of cardiac and respirator rhythms.

However, this model does not consider the reverse mechanical influence effect of the heartbeat changes on a breathing phase (frequency). In the present study, we add to the DeBoer model a self-oscillating system (which describes dynamics of the respiratory system as a generator of central type [4]) which is under impulsive influence of heartbeat.
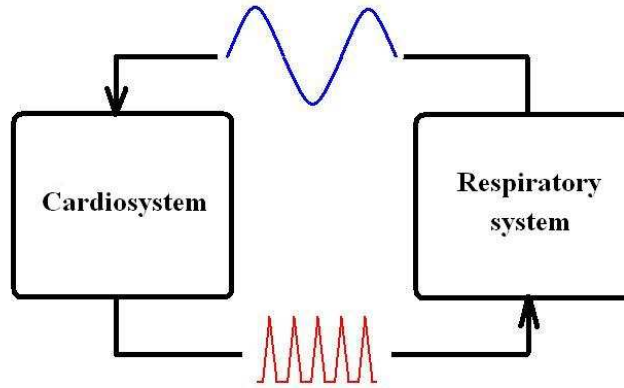
Fig. 2. Interaction of the cardiovascular and respiratory system

The DeBoer model describes the followings main characteristics of the heartbeat (see Figure 1) system: systolic pressure S , diastolic pressure D, R-R interval I and arterial time constant T (in a state of rest for a healthy man S=120 mmHg, D=80 mmHg, I=800 ms, T=1500 ms). This mathematical model is a system of five discrete nonlinear maps. This model contains only a direct mechanical influence of the respirator system on the cardiosystem and can be written in the form:

$$D_i' = S_{i-1}' \exp\left(-\frac{2}{3}\frac{I_{i-1}'}{T_{i-1}'}\right),$$

$$S_i' = D_i' + \gamma \frac{T_0}{S_0} I_{i-1}' + \frac{A}{S_0}\sin\left(2\pi f T_0 t_i\right) + \frac{c_2}{S_0},$$

$$I_i' = G_v \frac{S_0}{T_0}\hat{S}_{i-\tau_v}' + G_\beta \frac{S_0}{T_0} F(\hat{S}',\tau_\beta) + \frac{c_3}{T_0},$$

$$T_i' = 1 + G_\alpha \frac{S_0}{T_0} - G_\alpha \frac{S_0}{T_0} F(\hat{S}',\tau_\alpha),$$

$$\hat{S}_i' = 1 + \frac{18}{S_0}\arctan\frac{S_0(S_i'-1)}{18},$$

where $i \geq 1$, $D' = D/S_0$, $S' = S/S_0$, $\hat{S}' = \hat{S}/S_0$, $I' = I/T_0$, $T' = T/T_0$, $F(\hat{S},\tau) = 1/9(\hat{S}_{i-\tau-2} + 2\hat{S}_{i-\tau-1} + 3\hat{S}_{i-\tau} + 2\hat{S}_{i-\tau+1} + \hat{S}_{i-\tau+2})$, $t_i = \sum_{k=0}^{i-1} I_k'$ is a real time, A=3 mmHg is a breathing amplitude, f=0.25 Hz is a breathing frequency, $c_2 = S_0 - D_0 - \gamma I_0$, $c_3 = I_0 - S_0(G_v + G_\beta)$, $\gamma = 0.016$ mmHg, $G_\alpha = 18$

ms/mmHg, $G_\beta = 9$ ms/mmHg, $G_v = 9$ ms/mmHg, $\tau_\alpha = \tau_\beta = 4$, $\tau_v = 0$, is equal to 0 if frequency of heartbeat is less then 75 beat/min, and τ_v is equal to 1, if frequency is more then 75 beat/min.

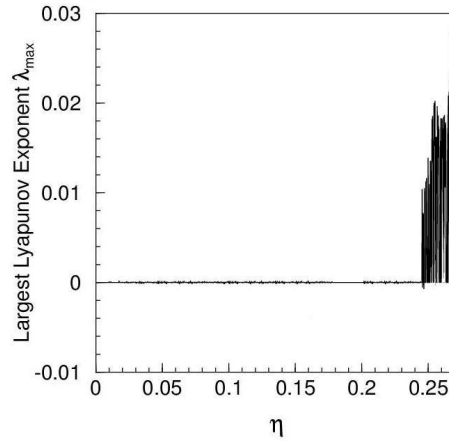Fig. 3.Largest Lyapunov exponent of the modified system

We suppose that a healthy man at rest breathes periodically with a permanent frequency and an amplitude of motions of thorax. In that case a breathing process can be described as the self-oscillating system [4], which has a steady limit cicle. Thus for the mathematical modeling of a such system equations of the Zaslavskiy map could be used. Famous Zaslavsky map is the system of equations [8, 12] which describes the dynamics of an amplitude r_n and a phase φ_n of the system (in which periodic self-oscillations with a frequency ω are realized) which is under T-periodic impulsive action of constant intensity η. Te system has the following form:

$$r_{n+1} = \left(r_n + \eta \sin \varphi_n \right) \exp\{-\kappa T\},$$

$$\varphi_{n+1} = \varphi_n + \omega T + v \left(r_n + \eta \sin \varphi_n \right) \frac{1 - \exp\{-\kappa T\}}{\kappa},$$

where κ, v are constant parameters.

a) $\eta = 0.22$

b) $\eta = 0.23$

c) $\eta = 0.24$

d) $\eta = 0.25$
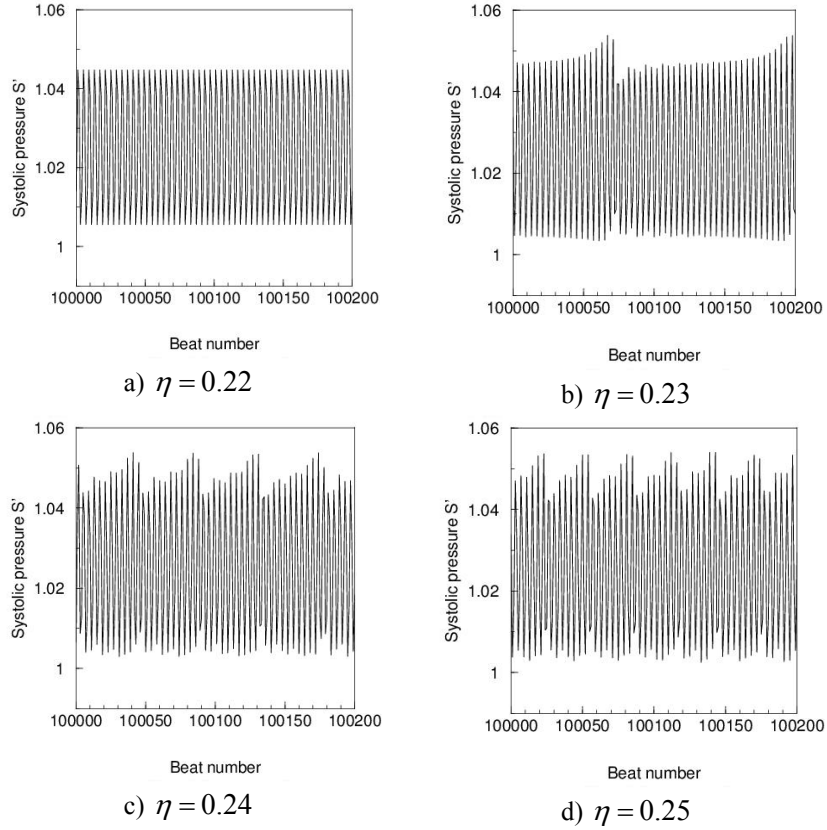
Fig. 4. Simulated systolic pressure data (cases a, b, c and d)

In our approach these equations are used to describe changes of an amplitude and phase of a respiratory system effect for every R-R interval with an intensity proportional to systolic pressure: $-\eta(S_n - S_0)$

$$r_{n+1} = \left(r_n - \eta(S_n - S_0)\sin\varphi_n \right)\exp\{-\kappa I_n\},$$

$$\varphi_{n+1} = \varphi_n + 2\pi f I_n + \nu\left(r_n - \eta(S_n - S_0)\sin\varphi_n \right)\frac{1 - \exp\{-\kappa I_n\}}{\kappa},$$

where I is R-R interval, $\eta > 0$, κ, ν are constant parameters of interaction.

Thus, we study the dynamics of the modified model of cardiorespiratory system, which consists of the DeBoer model with direct respiratory influence $(A + r_i)\sin\varphi_i$, and with reverse influence modeled by the Zaslavskiy map system (see Figure 2).

a) $\eta = 0.23$ b) $\eta = 0.24$

c) $\eta = 0.25$
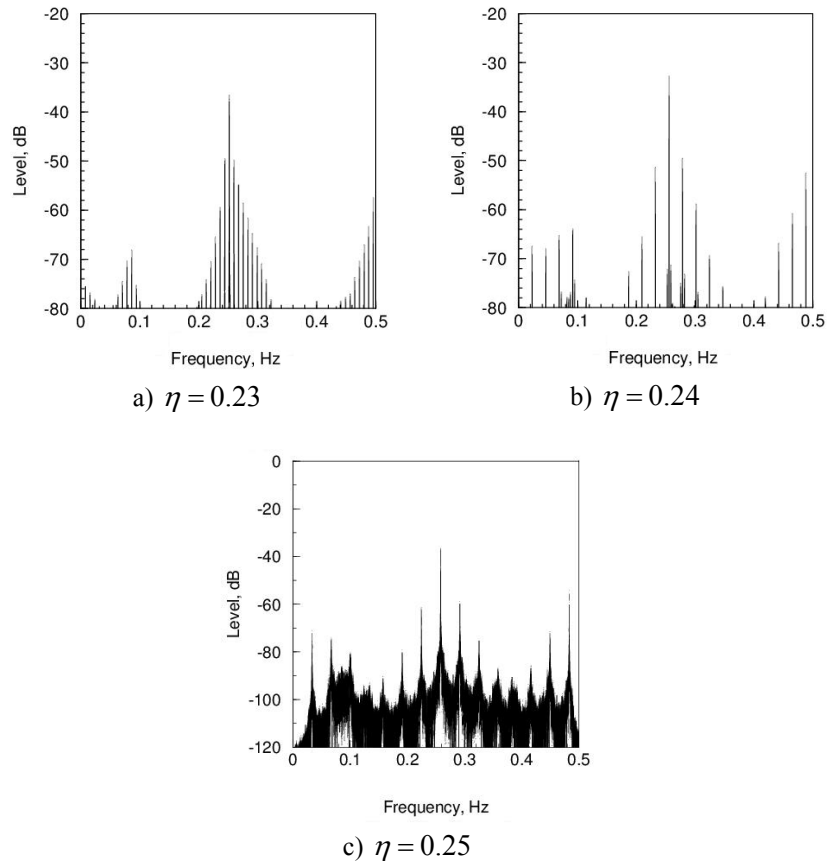
Fig. 5. Power spectra computed from systolic pressure data (cases a, b and c)

3. Numerical simulations results

In accordance with physiology of healthy man, the followings values of variables and constants are used in our numerical simulations: $I'[0] = 0.53$, $S'[-j] = 1.08$, $j = 0,...,6$, $r'[0] = 0$, $\varphi'[0] = 0$, $\kappa = 0.001$ 1/ms, $\nu = 0.001$ 1/msmmHg. In order to study steady-state regimes first of all the largest Lyapunov exponent [1, 6, 7] was found. The dependence of the largest Lyapunov exponent of the modified system on values of the bifurcation parameter η is shown in Figure 3. The dynamics of the system changes with increasing of this parameter. There is the region where Lyapunov exponent positive ($\eta > 0.245$) that means transition to chaos occurs. We emphasize that η describes intensity of heart influence on a respiratory system. The next Figure 4 illustrates a behaviour of systolic pressure data in the modified model. Power spectra computed from these data are shown in Figure 5. The spectrum in Figure 5.a and in Figure 5.b have discrete peaks which are situated equidistantly with a frequency difference. So that, graphs indicate that there are regular regimes in the modified system.

Finally, for the steady-state regimes, when the largest Lyapunov exponent is positive and the chaotic regime is realized, the power spectrum is continuous (Figure 5.c).

Phase portrait projections on the plane of the simulated systolic pressure and R-R interval data are presented in Figure 6. The phase portrait in the Figure 6.a represents a singular solid curve and corresponds to quasiperiodic regime. There are only several points in the phase portrait in Figure 6.b which means that at $\eta = 0.24$ the modified system has regular periodic regime. And in Figure 6.c when $\eta = 0.25$ the phase portrait has numerous lines (the number of which increases in time) and corresponds to chaotic steady-state regime. So we have found such steady-state basic regimes as:

1. at $\eta = 0.22$, periodic regime (Figure 4.a);

2. at $\eta = 0.23$, quasiperiodic regime (Figure 4.b, Figure 5.a, Figure 6.a);

3. at $\eta = 0.24$, periodic regime (Figure 4.c, Figure 5.b, Figure 6.b);

4. at $\eta = 0.25$, chaotic regime (Figure 4.d, Figure 5.c, Figure 6.c).

a) $\eta = 0.23$ b) $\eta = 0.24$

c) $\eta = 0.25$
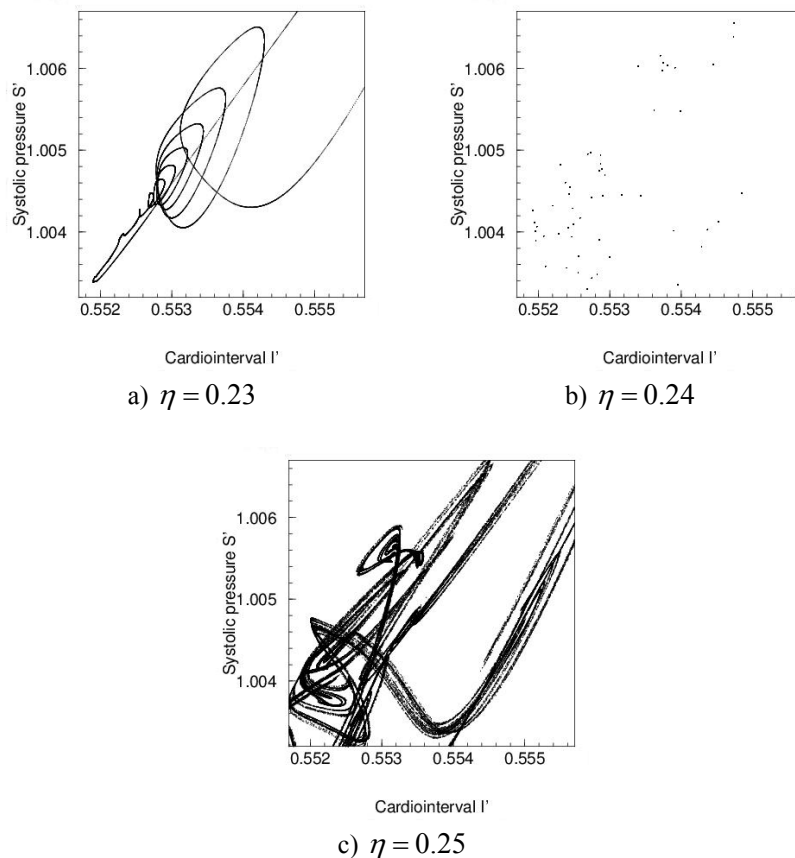
Fig. 6. The parts of phase portraits simulated systolic pressure and R-R interval data (cases a, b and c)

4. Conclusions

On the basis of the DeBoer model an interaction of the heartbeat and the respiratory system as dissipative Zaslavskiy map is studied and the modified model of cardiosystem is built out. This model takes into account both direct and reverse influence of subsystems – cardiovascular and respiratory.

The methods of modern theory of the dynamical systems are used to study laws of the steady-state regimes of the modified model. Firstly the chaotic regimes were found out. Analysis of bifurcational curves of the largest Lyapunov exponent, projections of phase portraits, temporal realizations and power spectrums allowed to investigate the basic laws of dynamics of the model. The dynamics of heartbeat and respiratory systems are in good correspondence with experimental information of healthy man. Found irregularities of phase trajectories of the modified model depend on intensity of heart rhythm influence on breathing, what is well known characteristic for the dynamics of the cardiovascular system of healthy man.

References

1. V. S. Anishshenko. *Acquaintance with nonlinear dynamic,* Institute of Computer Science, Moscow-Izhevsk, 2002.

2. V. T. Grinchenko and A. G. Rudnitskiy. A model of interection of the cardiovascular and respiratory systems, *Acoustic Journal*, vol. 9, no. 3, 16-26, 2006.

3. R. W. DeBoer, J. M. Karemaker, J. Strakee. Hemodynamic fluctuations and baroreflex sensitivity in humans: A beat-to-beat model, *Amer. J. Physiol.*, vol. 253, H680-H689, 1987.

4. L. Glass, M. C. Mackey. *From Clocks to Chaos. The rhythms of life,* Princeton University Press, Princeton, 1988.

5. K. Kotani [et al.]. Model for cardiorespiratory synchronization in humans, *Physical Review E.*, vol. 65, 051923-051932, 2002.

6. S. P. Kouznetsov. *Dynamic chaos*, Physmatlit, Moscow, 2001.

7. T. S. Krasnopolskaya, A. Yu. Shvets. *Regular and chaotic dynamics of the systems with limited excitation,* Institute of Computer Science, Moscow-Izhevsk, 2008.

8. R. Z. Sagdeev, D. A. Usikov and G. M. Zaslavsky. *Nonlinear Physics: From the Pendulum to Turbulence and Chaos*, Harwood Academic Publishers, New-York, 1988.

9. H. Seidel and H. Herzel. Bifurcations in a nonlinear model of the baroreceptor-cardiac reflex, *Acoustic Journal*, vol. 115D, 145-160, 1998.

10. E. Toledo [et al.]. Does synchronisation reflect a true interaction in the cardiorespiratory system, *Med. Engng Phys.*, vol. 24, 45-52, 2002.

11. T. Yang, M. D. Jacobstein, M. N. Levy. Synchronization of automatic cells in S-A node during vagal stimulation in dogs, *Am. J. Physiol.*, n. 246, H585-H591, 1984.

12. G. M. Zaslavsky. The simplest case of a strange attractor, *Phys. Lett. A*, vol. 69, 145-147, 1978.

Chaos Cryptography: Relation Of Entropy With Message Length and Period

George Makris[1], Ioannis Antoniou[2]

Complex Systems Analysis Laboratory, Mathematics Department, Aristotle University, 54124, Thessaloniki, Greece
[1]E-mail: geormak@outlook.com
[2]E-mail: iantonio@math.auth.gr

Abstract: Chaos cryptography is implemented by torus automorphisms with strictly positive entropy production. For any given entropy production $h > 0$ we explicitly construct integer valued automorphisms with entropy $h(S) \geq h$. We identify compatibility conditions between the values of the entropy production and the lengths of the messages in terms of the grid size and we propose constructive ways to encrypt messages of arbitrary length in terms of torus automorphisms with any given desired entropy production. We moreover prove that the restrictions of chaotic maps with the same entropy have the same period for a fixed grid size.

Keywords: Entropy, Cryptography, Chaos, Cryptography with Chaos.

1. Introduction

Chaos cryptography was proposed by Shannon in his classic 1949 mathematical paper on Cryptography where used chaotic maps as models - mechanisms for symmetric key encryption. Of course Shannon did not employ the term Chaos which emerged in the 1970s. This remarkable intuition was based on the paradigm of the Baker's map introduced by Hopf in 1934 as a simple deterministic mixing model with statistical regularity. Shannon observed that using chaotic maps, encryption is achieved via successive mixing of the initial information which is uniformly "spread" all over the available state space. In this way it is becoming exponentially hard to recover the initial message if the reverse transformation is not known. Baker's map is the simplest example of chaotic Torus Automorphisms with constant Entropy production equal to one bit at every step. The Entropy production theory of Torus Automorphisms and general Chaotic maps was developed later by Kolmogorov and his group [Arnold and Avez, 1968; Katok ea, 1995; Lasota ea, 1994], following Shannon's earlier foundation of Information Theory in 1948. Baker's map has also served as a toy model for understanding the problem of Irreversibility in Statistical Mechanics [Prigogine, 1980]. Chaos cryptography with 2-dimensional maps deal with image encryption [Guan D. ea, 2005; Xiao G. ea , 2009] and text encryption [Kocarev ea, 2003; Kocarev ea, 2004; Kocarev L. and Lian S., 2011;Li S., 2003]. We have proposed a new implementation method for

Chaos Cryptography based on Chaotic torus automorphisms, applicable for both image and text encryption simultaneously [Makris G, Antoniou I, 2012a] and designed torus automorphisms with desired entropy production [Makris G, Antoniou I, 2012b]. Part of these results is summatized in section 1.

As the grid discretizations of chaotic Torus automorphisms are periodic, for effective implementation we have to examine the conditions for reliable cryptography implementation. The objectives of this work are: a) to examine the dependence of the period on the entropy production and on the grid size (Section 2), b) to provide conditions for admissible grid discretizations (Section 3) and c) to provide algorithms for the construction of integer torus automorphims with desired entropy production (Appendix A) and for adapting the image size to the appropriate grid size (Appendix B) for customized implementation of chaotic cryptography).

The automorphisms of the 2-torus $Y = [0,1) \times [0,1)$ are defined by the formula:

$$S : Y \to Y : \begin{bmatrix} x_{n+1} \\ y_{n+1} \end{bmatrix} = A \begin{bmatrix} x_n \\ y_n \end{bmatrix} (mod\, 1), n \in \mathrm{N} \;\textbf{(1)}$$

Where $A = \begin{bmatrix} a & b \\ c & d \end{bmatrix}$ is a real invertible matrix with inverse:

$$A^{-1} = \frac{1}{ad - bc} \begin{bmatrix} d & -b \\ -c & a \end{bmatrix}$$

Chaotic Torus automorphisms (1) have one eigenvalue greater than 1, according Pesin's 1977 Formula.

Lemma:

1) The class of chaotic automorphisms (1) with $ad - bc = 1$ consists of the matrices:

$$A = \begin{bmatrix} a & b \\ \dfrac{ad-1}{b} & d \end{bmatrix}, a \in \mathrm{R}, b \in \mathrm{R} - \{0\}, d > 2 - a \quad \textbf{(2)}$$

2) The entropy production of the Chaotic automorphisms (2) is:

$$h = \log_2 \lambda_1 = \log_2 \frac{(a+d) + \sqrt{(a+d)^2 - 4}}{2} = \log_2 \frac{tr(A) + \sqrt{(tr(A))^2 - 4}}{2},$$
$$a \in \mathrm{R}, b \in \mathrm{R}, d > 2 - a \;(or\; tr(A) > 2) \quad \textbf{(3)}$$

3) The chaotic automorphisms (2) are expressed in terms of the entropy production as a parameter h by the formula:

$$A = \begin{bmatrix} a & b \\ \dfrac{a \cdot (2^h + 2^{-h} - a) - 1}{b} & 2^h + 2^{-h} - a \end{bmatrix}, a \in \mathrm{R}, b \in \mathrm{R} - \{0\}, h > 0 \quad \textbf{(4)}$$

4) For the class of chaotic automorphisms A with one eigenvalue greater than 1 and $ad - bc = -1$ we have the corresponding formulas:

$$A = \begin{bmatrix} a & b \\ \dfrac{ad+1}{b} & d \end{bmatrix}, a \in \mathrm{R}, b \in \mathrm{R} - \{0\}, d > -a \quad \textbf{(5)}$$

$$\mathsf{h} = \log_2 \lambda_1 = \log_2 \frac{(a+d) + \sqrt{(a+d)^2 + 4}}{2} = \log_2 \frac{tr(A) + \sqrt{(tr(A))^2 + 4}}{2},$$
$$a \in \mathrm{R}, b \in \mathrm{R}, d > -a \ (\text{or } tr(A) > 0) \quad \textbf{(6)}$$

$$A = \begin{bmatrix} a & b \\ \dfrac{a \cdot \left(2^h - 2^{-h} - a\right) + 1}{b} & 2^h - 2^{-h} - a \end{bmatrix}, a \in \mathrm{R}, b \in \mathrm{R} - \{0\}, \mathsf{h} > 0 \ \textbf{(7)}$$

Formulas (2),(3),(4) are proven in [Makris G, Antoniou I, 2012b]. The corresponding formulas for the case $ad - bc = -1$ are obtained in a similar way. From formulas (3),(6) we see that

Corollary

Two Chaotic Torus Automorphisms have the same Entropy Production (are isomorphic), if and only if they have the same trace

2. Entropy production and the period of the discretization restrictions of integer Torus Automorphisms

The implementation of cryptographic algorithms requires discretization of the chaotic maps onto the selected $N \times N$ grid. In order to preserve the grid structure we shall consider torus automorphisms with integer matrix elements. Given a desired entropy production value not less than h we may construct integer torus automorphisms with entropy production h from formulas (4),(7) using the algorithms presented in appendix A.

The coordinates of pixels are elements of the NxN lattices $\Lambda_N \times \Lambda_N$. The restriction of any integer torus automorphism to $\Lambda_N \times \Lambda_N$ (mod N):

$$\begin{bmatrix} x' \\ y' \end{bmatrix} = A \begin{bmatrix} x \\ y \end{bmatrix} (\mathrm{mod}\, N) = \begin{bmatrix} a & b \\ c & d \end{bmatrix} \begin{bmatrix} x \\ y \end{bmatrix} (\mathrm{mod}\, N) \ \textbf{(8)}$$

is a periodic transformation, called the NxN discretization automorphism of (1). The period of the discretization automorphisms (8) is the minimal number T which satisfies the formula:

$$\begin{bmatrix} a & b \\ c & d \end{bmatrix}^T (\mathrm{mod}\, N) = \mathrm{I}_2 = \begin{bmatrix} 1 & 0 \\ 0 & 1 \end{bmatrix} (9)$$

Theorem 1: All discretization automorphisms (8) with the same trace have the same period T which depends only on the size N of the grid.

Proof:
First we shall show that the discretization automorphisms (8) of isospectral matrices have the same period. It is enough to show that the matrices A (9) and

$$\Delta = \begin{bmatrix} \lambda_1 & 0 \\ 0 & \lambda_2 \end{bmatrix} (10)$$

define discretization automorphisms (8) with the same period.
We have:

$$A = B^{-1} \cdot \Delta \cdot B$$

Where B is a diagonalization transformation of A.
If T is the period of (8), from (9) and (10) we have:

$$A^T = \left(B^{-1} \cdot \Delta \cdot B \right)^T = B^{-1} \cdot \Delta^T \cdot B$$

and:

$$\begin{bmatrix} a & b \\ c & d \end{bmatrix}^T (\mathrm{mod}\, N) = \left(B^{-1} \begin{bmatrix} \lambda_1^T & 0 \\ 0 & \lambda_2^T \end{bmatrix} B \right)(\mathrm{mod}\, N) = \begin{bmatrix} 1 & 0 \\ 0 & 1 \end{bmatrix}$$

Therefore:

$$\begin{bmatrix} \lambda_1^T & 0 \\ 0 & \lambda_2^T \end{bmatrix}(\mathrm{mod}\, N) = \begin{bmatrix} 1 & 0 \\ 0 & 1 \end{bmatrix}$$

Therefore the discretizations (8) of Δ and A have the same period T. From the eigenvalue formulas (3) and (6), we see that the eigenvalues λ_1, λ_2 depend only on the trace of A. Therefore any two matrices with the same trace define discretizations (8) with the same period. ∎

3. Entropy Production and Grid size

We observe that torus automorphisms with different entropy production may have identical discretizations (8). For example, applying formula (6) we see that

the torus automorphisms with matrices $A_1 = \begin{bmatrix} 2 & 1 \\ 4093 & 2047 \end{bmatrix}$ and

$A_2 = \begin{bmatrix} 2 & 1 \\ 93 & 47 \end{bmatrix}$ have entropy productions $h_1 = 11.0007$

and $h_2 = 5.6141$ correspondingly. However their discretizations (8) to the grid 100×100 are identical:

$$\begin{bmatrix} 2 & 1 \\ 4093 & 2047 \end{bmatrix} \mathrm{mod}\, 100 \equiv \begin{bmatrix} 2 & 1 \\ 93 & 47 \end{bmatrix} \mathrm{mod}\, 100 .$$

The same is true for the grids 200×200, 500×500, 1000×1000 and others.
This is an undesirable fact because only equivalent chaotic torus automorphisms should have identical grid discretization (8). We found that this requirement is true only for certain values of the entropy production h and grid size N. The result is the following:

Theorem 2: An necessary and sufficient condition for   one to one correspondence between torus automorphisms and their grid discretizations (8) is: $N > \max\{a,b,c,d\}$ **(11)**

Equivalently in terms of entropy production, using (3) and (6) we have the conditions:

$$N > \max\left\{a,b,2^h+2^{-h}-a,\frac{a\cdot\left(2^h+2^{-h}-a\right)-1}{b}\right\} \text{ for } \det(A)=1 \text{ (12)}$$

$$N > \max\left\{a,b,2^h-2^{-h}-a,\frac{a\cdot\left(2^h-2^{-h}-a\right)+1}{b}\right\} \text{ for } \det(A)=-1 \text{ (13)}$$

Prof:

$$\begin{bmatrix} a & b \\ c & d \end{bmatrix}\begin{bmatrix} x \\ y \end{bmatrix}(\bmod N) = \begin{bmatrix} a\ (\bmod N) & b\ (\bmod N) \\ c\ (\bmod N) & d\ (\bmod N) \end{bmatrix}\begin{bmatrix} x \\ y \end{bmatrix}(\bmod N) =$$

$$= \begin{bmatrix} \upsilon_\alpha & \upsilon_b \\ \upsilon_c & \upsilon_d \end{bmatrix}\begin{bmatrix} x \\ y \end{bmatrix}(\bmod N)$$

As the remainders $\upsilon_\alpha, \upsilon_b, \upsilon_c, \upsilon_d$ are always not greater than a,b,c,d

correspondingly, we have: $tr\begin{bmatrix} a & b \\ c & d \end{bmatrix} = a+d \geq \upsilon_\alpha + \upsilon_d = tr\begin{bmatrix} \upsilon_\alpha & \upsilon_b \\ \upsilon_c & \upsilon_d \end{bmatrix}$

Therefore, from (3) and (6) we have: $h\begin{bmatrix} a & b \\ c & d \end{bmatrix} \geq h\begin{bmatrix} \upsilon_\alpha & \upsilon_b \\ \upsilon_c & \upsilon_d \end{bmatrix}$

$h\begin{bmatrix} a & b \\ c & d \end{bmatrix} = h\begin{bmatrix} \upsilon_\alpha & \upsilon_b \\ \upsilon_c & \upsilon_d \end{bmatrix}$ if and only if: $a < N$ and $b < N$ and $c < N$ and $d < N$,

from which follows the desired result. ∎

The natural question now arises what are the possible values of entropy production for automorphisms satisfying (11)

Without significant loss of generality we consider the simpler class of integer torus automorphisms with $b=1$. Formulas (12) and (13) are written :

$$\boxed{h < \log_2\left[(a+N)+\sqrt{(a+N)^2-4}\right]-1 \ , \ 0 < a < N}, \ \det(A)=1 \text{ (14)}$$

$$\boxed{h < \log_2\left[(a+N)+\sqrt{(a+N)^2+4}\right]-1, \ 0 < a < N}, \ \det(A)=-1 \text{ (15)}$$

Therefore given the grid size N we know the maximal entropy production from (14),(15) for automorphisms with b=1 and conversely given a desired entropy

production value we know the minimal grid size from (12),(13). The relation between entropy production and grid size is shown in figure 1. We shall call the discretizations (8) with grid size $N \times N$ admissible discretizations if and only if the conditions (12) , (13) hold.
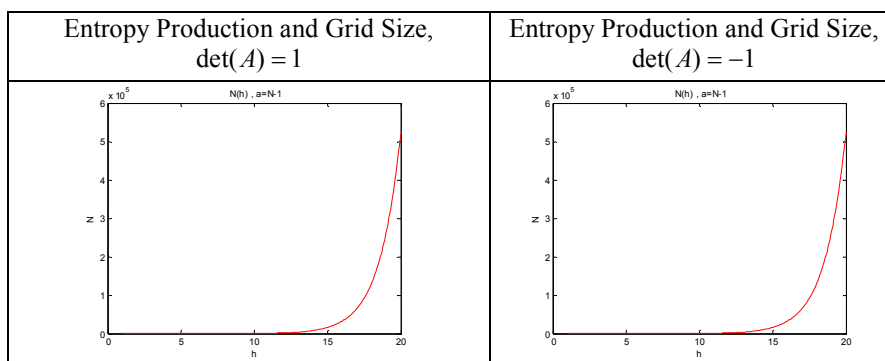
Entropy Production and Grid Size, $\det(A) = 1$	Entropy Production and Grid Size, $\det(A) = -1$

Figure 1: Entropy Production and Grid Size

In case the grid $N \times N$ for admissible discretization (8) of the constructed torus automorphisms is larger than the message size $n \times m$ we may enlarge and adapt the message size to the grid size using the algorithm presented in appendix B.

5. Conclusions

After extending our previous results [Makris G, Antoniou I, 2012b] on the entropy production on torus automorphisms (Lemma and Corollary), we show that the period of grid discretizations of chaotic automorphisms depends only on the entropy production and on the grid size (Theorem 1). In order to avoid the undesirable fact that torus automorphisms with different entropy production may have the same discretization, we provide a necessary and sufficient condition of admissible grid discretizations (Theorem 2). For customized implementation of chaotic cryptography, we provide algorithms for the construction of integer torus automorphims with desired entropy production (Appendix A) and for adapting the image size to the appropriate grid size (Appendix B). These results are necessary for implementation of chaotic cryptographic algorithms of desired entropy production. Based on Theorem 2 and Appendix B we can automatically adapt the message size to admissible discretization for effective cryptography.

References

1. Akritas P., Antoniou I., Pronko G., "On the Torus Automorphisms: Analytic Solution, Computability and Quantization", Chaos, Solitons and Fractals 12,(2001) 2805-2814

2. Arnold, V. I. and Avez, A., Ergodic Problems of Classical Mechanics Benjamin, New York , 1968

3. Guan Z. H., Huang F., and Guan W.. Chaos-based image encryption algorithm. Physics Letters A, Vol. 346, Issues 1-3,(2005), pp 153-157.

4. Dyson FJ, Falk H., Period of a discrete cat mapping. Am Math Monthly 1992;2(99):603-14

5. Hopf E., On Causality, Statistics and Probability, J. Math. and Phys. 13, (1934), 51-102.

6. Katok A., Hasselblatt B., Introduction to the Modern Theory of Dynamical Systems, Cambridge University Press, Cambridge, UK , 1995

7. Kocarev L., Sterjev M., Amato P., RSA ENCRYPTION ALGORITHM BASED ON TORUS AUTOMORPHISMS, IEEE, ISCAS (2004), IV 577-580.

8. Kocarev L., Tasev Z., and Makraduli J., "Public-Key Encryption and Digital-Signature Schemes Using Chaotic Maps", 16th European Conference on Circuits Theory and Design, September 1 – September 4, 2003, Krakow, Poland, ECCTD 2003.

9. Kocarev, L., Lian, S., Chaos-Based Cryptography. Theory, Algorithms and Applications,Studies in Computational Intelligence, Vol. 354, (2011), ISBN 978-3-642-20542-2, Berlin.

10. Lasota A. and Mackey M., Chaos, Fractals, and Noise, Springer-Verlag New York, 1994.

11. Li, S., Analyses and New Designs of Digital Chaotic Ciphers. Ph.D. thesis, School of Electronic and Information Engineering, Xi'an Jiaotong University, Xi'an, China, 2003

12. Makris G., Antoniou I., 2012, "Cryptography with Chaos", Chaotic Modeling and Simulation (CMSIM), VOL 1: 169-178, 2012, ISSN 2241-0503.

13. Makris G., Antoniou I., 2012, "Cryptography with Entropy Producing Maps", 6th World Congress of NonLinear Analysts, IFNA 2012, 25 June - 1 July, Athens, Greece

14. Pesin Ya. B., Characteristic Lyapunov exponents and smooth ergodic theory, Russ. Math. Surv. 32:4, (1977), 55-112

15. Prigogine I., From Being to Becoming, Freeman, New York, 1980

16. Shannon C. , A Mathematical Theory of Communication. Bell System Technical Journal, vol. 27, pp. 379–423, 623–656 (1948); Shannon C. and Weaver W., Mathematical Theory of Communication, Univ of Illinois Press, Urbana, Ill (1949).

17. Shannon, C., Communication Theory of Secrecy Systems. Bell System Technical Journal, Vol.28, Issue 4, (1949), pp 656–715.

18. Smale S., "Differentiable dynamical systems". Bulletin of the American Mathematical Society 73: (1967) 747–817.

19. Smale S., Finding a horseshoe on the beaches of Rio, Mathematical Intelligencer 20, (1998), 39-44

20. Xiao, D., Liao, X., Wei, P., Analysis and improvement of a chaos-based image encryption algorithm. Chaos, Solitons & Fractals, Vol. 40, Issue 5, (2009), pp 2191-2199.

Appendix A: Construction of integer torus automorphisms with entropy production not less than any desired positive real number

Torus automorphisms have been applied to NxN grids and the periods has been related to the grid size N [Vivaldi, 1989; Dyson FJ and Falk H, 1992; Akritas ea, 2001; Antoniou ea, 1997; Xiao ea, 2009]. According to formula (2) we should have $\dfrac{ad-1}{b} \in Z$ for any integer values a,b,d. , ie. : $(ad) \bmod b = 1$

For any given entropy production $h > 0$ we construct integer matrixes A with entropy $h(A) \geq h$ according to the following algorithm.

Algorithm 1. Construction of integer matrices A with $\det(A) = 1$

Step 0: inputs: $h \in (0, \infty)$, a,$b \in Z$

Step 1: Set $x = \lceil tr(A) \rceil = \lceil 2^h + 2^{-h} \rceil$, $\lceil z \rceil$ is the ceiling of z

Step 2: Set d=x-a

Step 3: if [d>2-a and (b=1 or $(ad) \bmod b = 1$)] goto Step 9

Step 4: if [a $\bmod$ $b \neq 0$ and b $\bmod$ $a \neq 0$] goto Step 7

Step 5: Set x=x+1 and d=x-a

Step 6: goto Step 3

Step 7: Set a=a+1 and d=x-a

Step 8: goto Step 3

Step 9: return $A = \begin{bmatrix} a & b \\ \dfrac{ad-1}{b} & d \end{bmatrix}$

Step 10: return $\lambda_1(A) = \dfrac{(a+d) + \sqrt{(a+d)^2 - 4}}{2}$

Step 11: return $h(A) = \log_2 \lambda_1(A)$

Input			Output		
h	a	b	$A = \begin{bmatrix} a & b \\ \dfrac{ad-1}{b} & d \end{bmatrix}$	$\lambda_1(A)$	$h(A)$
1.2	1	1	$A = \begin{bmatrix} 1 & 1 \\ 1 & 2 \end{bmatrix}$	2.6180	**1.3885**
1.2	2	3	$A = \begin{bmatrix} 2 & 3 \\ 1 & 2 \end{bmatrix}$	3.7321	**1.9000**
3.5	1	1	$A = \begin{bmatrix} 1 & 1 \\ 10 & 11 \end{bmatrix}$	11.9161	**3.5748**
3.5	5	1	$A = \begin{bmatrix} 5 & 1 \\ 34 & 7 \end{bmatrix}$	11.9161	**3.5748**
3.5	5	3	$A = \begin{bmatrix} 5 & 3 \\ 13 & 8 \end{bmatrix}$	11.9161	**3.5748**
11	2	1	$A = \begin{bmatrix} 2 & 1 \\ 4093 & 2047 \end{bmatrix}$	2049	**11.0007**

Table 1: Examples of **Algorithm 1**

According to formula (4) we should have $\dfrac{ad+1}{b} \in Z$ for any integer values

a,b,d. , ie. : $(ad+1)\,mod\,b = 0 \Rightarrow (ad)\,mod\,b = b-1$

Algorithm 2. Construction of integer matrices A with $\det(A) = -1$

Step 0: inputs: $h \in (0,\infty)$, $a, b \in Z$

Step 1: Set $x = \lceil tr(A) \rceil = \lceil 2^h - 2^{-h} \rceil$, $\lceil z \rceil$ is the ceiling of z

Step 2: Set d=x-a

Step 3: if [d>-a and (b=1 or $(ad)\,mod\,b = b-1$)] goto Step 9

Step 4: if [a $mod\ b \neq 0$ and $b\,mod\,a \neq 0$] goto Step 7

Step 5: Set x=x+1 and d=x-a

Step 6: goto Step 3

Step 7: Set a=a+1 and d=x-a

Step 8: goto Step 3

Step 9: return $A = \begin{bmatrix} a & b \\ \dfrac{ad+1}{b} & d \end{bmatrix}$

Step 10: return $\lambda_1(A) = \dfrac{(a+d) + \sqrt{(a+d)^2 + 4}}{2}$

Step 11: return $h(A) = \log_2 \lambda_1(A)$

Input			Output		
h	a	b	$A = \begin{bmatrix} a & b \\ \dfrac{ad+1}{b} & d \end{bmatrix}$	$\lambda_1(A)$	$h(A)$
1.2	1	1	$A = \begin{bmatrix} 1 & 1 \\ 2 & 1 \end{bmatrix}$	2.4142	**1.2716**
1.2	2	3	$A = \begin{bmatrix} 2 & 3 \\ 1 & 1 \end{bmatrix}$	3.3028	**1.7237**
3.5	1	1	$A = \begin{bmatrix} 1 & 1 \\ 12 & 11 \end{bmatrix}$	12.0828	**3.5949**
3.5	5	1	$A = \begin{bmatrix} 5 & 1 \\ 36 & 7 \end{bmatrix}$	12.0828	**3.5949**
3.5	5	3	$A = \begin{bmatrix} 5 & 3 \\ 12 & 7 \end{bmatrix}$	12.0828	**3.5949**
11	2	1	$A = \begin{bmatrix} 2 & 1 \\ 4093 & 2046 \end{bmatrix}$	2048	**11.0000**

Table 2: Examples of **Algorithm 2**

Appendix B: Algorithm to Enlarge image size from $(n \times m)$ to $(N \times N)$:

Step 0: inputs: $(image, N, c)$, N: new image size, c: color of new pixels

Step 1: calculate (n, m) =image size

Step 2: $W_h = N - n$

Step 3: Create an new blank image1 with size $\left(\dfrac{W_h}{2} \times m \right)$ and color c to every pixel.

Step 4: Create an new image2 with vertical quote of three images:
$image2 = \begin{pmatrix} image1 \\ image \\ image1 \end{pmatrix}$. Image2 size= $(N \times m)$

Step 5: $W_w = N - m$

Step 6: Create a new blank image3 with size $\left(\dfrac{W_w}{2} \times N \right)$ and color c to every pixel.

Step 7: Create a new_image with horizontal quote of three images :
$new\_image = (image3 \quad image2 \quad image3)$. new_mage size$=(N \times N)$

Image (342 x 454)	Image1 (79 x 454)	Image2 (500 x 454)	Image3 (500 x 23)
Inputs	**New_image** (500 x 500)		**Output**
Image N=500 c=white Calculations $W_h = N - n = 158$ $W_w = N - m = 46$			New_image

The advantage of adding pixels in an image is to keep the original information.

Chaotic Neural Networks with a Random Topology Can Achieve Pattern Recognition*

Ke Qin[1] and B. J. Oommen[2,3]

[1] University of Electronic Science & Technology of China, Chengdu, China. 611731
   (E-mail: `qinke@uestc.edu.cn`)
[2] Carleton University, Ottawa, ON, Canada. K1S 5B6
[3] University of Agder, Postboks 509, 4898 Grimstad, Norway.
   (E-mail: `oommen@scs.carleton.ca`)

Abstract. This paper confirms the fascinating result that we can design chaotic Neural Networks (NNs) that have a *random* topology and that these NNs can achieve *chaotic* Pattern Recognition (PR). What we imply by this is that the NN yields a strong *periodic* or *more frequent* signal when a pattern is recognized, and in between two consecutively recognized patterns, none of the trained patterns are recalled. Finally, and most importantly, if an untrained pattern is presented, the system yields a chaotic signal. The basic model that we use here is the Adachi Neural Network (AdNN), which we modify in a random manner. The AdNN is a fascinating NN which has been shown to possess chaotic properties, and to also demonstrate Associative Memory (AM) and PR, and some of its variants have also been used to obtain other PR phenomena, including blurring. All these NNs require a quadratic number of computations in the training phase. This computation was reduced to be linear in [1] by resorting to a Maximum Spanning Tree topology, and a gradient search method. In this paper, we mainly consider the issue of how the network topology can be modified by involving randomized connections so as to render the new network much closer to "*real*" NNs. At the same time, we require that the newly obtained network still displays PR characteristics. To achieve this, we first construct a random network by means of the E-R model and then address the problem of computing the weights for the new network. This is done by constraining the the modified random connection-based NN to have approximately the same input-output characteristics using a gradient-based algorithm. Through a detailed experimental analysis, we show that the new random AdNN-like network possesses PR properties for appropriate settings. As far as we know, such a random AdNN has not been reported, and our present results are novel.
Keywords: Chaotic Neural Networks, Chaotic Pattern Recognition, Adachi-like Neural Networks, Random Networks.

1 Introduction

The goal of the field of *Chaotic* Pattern Recognition (PR) systems can be summarized as follows: We do not intend a chaotic PR system to report the identity

of a testing pattern with a "class proclamation" indicating the class to which the pattern belongs. Rather, what we want to achieve is to have the chaotic PR system give a strong *periodic* or *more frequent* signal when a pattern is recognized. Furthermore, between two consecutively recognized patterns, none of the trained patterns must be recalled. Finally, and most importantly, if an untrained pattern is presented, the system must give a chaotic signal.

The use of Artificial Neural Networks (ANNs) is one of the four best approaches for PR. However, one of the limitations of most ANN models is the dependency on an external stimulation. Once an output pattern has been identified, the ANN remains in that state until the arrival of a new external input. This is in contrast to real biological NNs and the brain, which exhibit sequential memory characteristics. Indeed, once a pattern is recalled from a memory location, the brain is not "stuck" in it; it is also capable of recalling other associated memory patterns without being prompted by any additional external inputs. This ability to "jump" from one memory state to another *in the absence of a stimulus* is one of the hallmarks of the brain, which is *one phenomenon that a chaotic PR system has to emulate.*

This paper deals with the Adachi Neural Network AdNN [2], which possesses a spectrum of very interesting chaotic, AM and PR properties, as described in [1,3–7,9–12]. The fundamental problem associated with the AdNN and its variants are their quadratic computational requirements. We shall show that by using the E-R model and an effective gradient search strategy, this burden can be significantly reduced, and yet be almost as effective with regard to the chaotic and PR characteristics.

We are currently working on reducing the complexity of the AdNN and the associated computations by invoking the so-called "small-world" model.

2   Limitations of the Current Schemes

Adachi *et al* and Calitoiu *et al* have done a lot of ground-breaking work in this area [2–4], and we have built on these results in various avenues [3–5], including that of designing a NN that can yield *ideal* chaotic PR [8]. Generally speaking, the computational burden of the family of AdNNs is excessive, rendering it impractical. Besides this, most of current NNs have a regular topology, e.g., a completely connected graph or a neighbor-coupled graph. This is in contrast with "real" NNs which usually have irregular topologies, e.g., a random graph, a small-world graph or even a scale-free graph. The contribution of this paper is to present a novel NN which is connected in a randomized AdNN way, which we refer to as the "Random-AdNN".

3   Designing the Random-AdNN

3.1   The Topology of the Random-AdNN

To present the new characteristics of the Random-AdNN, we shall first arrive at a topology with randomly-chosen edges. Such a modified random AdNN is obtained in two steps. Firstly, we connect the neurons by using the E-R model. The second step involves the computation of the weights associated with this new structure, which we will address subsequently.

Algorithm 1 Topology_Random-AdNN

Input: N, the number of neurons in the network, and a set of P patterns which the network has to "memorize".

Output: The topology and initial weights of the Random-AdNN.

Method:

1: Create a fully-connected graph $\mathcal{G}$ with N vertexes which represents the AdNN.
2: For each edge, we delete it with a fixed probability, p_d.
3: Continue this process for all the $\binom{N}{2}$ edges.
4: Compute the initial weights of the edges of $\mathcal{G}$, $\{w_{ij}\}$ as follows:
   $w_{ij} = \frac{1}{P}\sum_{s=1}^{P}(2x_i^s - 1)(2x_j^s - 1)$, where x_i^s is the ith component of the sth pattern.
5: If there is no edge between vertex i and j, $w_{ij} = 0$;

End Algorithm Topology_Random-AdNN

3.2   The Weights of the Random-AdNN: Gradient Search

Since we have removed most of the "redundant" edges from the completely-connected graph by using the E-R model, it is clear that the NN at hand will not adequately compare with the original AdNN. Thus, our next task is to determine a new set of weights so as to force the Random-AdNN to retain some of its PR properties, namely those corresponding to the trained patterns. We briefly explain below (the details are omitted in the interest of space, and one can refer to [13] for more details) the process for achieving this.

The Random-AdNN is defined by the following equations:

$$x_i^R(t+1) = f(\eta_i^R(t+1) + \xi_i^R(t+1)), \tag{1}$$

$$\eta_i^R(t+1) = k_f\eta_i^R(t) + \sum_{e_{ij}\in T} w_{ij}^{R^*} x_j^R(t), \tag{2}$$

$$\xi_i^R(t+1) = k_r\xi_i^R(t) - \alpha x_i^R(t) + a_i. \tag{3}$$

where $\{w_{ij}^{R^*}\}$, x_i^R, ξ_i^R and η_i^R are the weights, outputs, and state variables of the Random-AdNN respectively, and have similar meanings to $\{w_{ij}\}$, x_i, ξ_i and η_i of the AdNN.

In order to find the optimal values of $\{w_{ij}^{R^*}\}$, we define the square error between the original output of the AdNN and new output at the nth step as:

$$E_p = \frac{1}{2}\sum_{i=1}^{N}(x_i^{A,p} - x_i^{R,p}(n))^2, \tag{4}$$

where $x_i^{A,p}$ and $x_i^{R,p}$ imply the outputs of the ith neuron when the pth pattern is presented to the AdNN network and the Random-AdNN network respectively. The overall global error is $E = \sum_{p=1}^{P} E_p$, where there are P training patterns.

In order to adjust w_{ij}^R to obtain the smallest global error E, we consider the gradient, Δw_{ij}^R, and move w_{ij}^R by an amount which equals Δw_{ij}^R in the direction where the error is minimized. This can be formalized as follows:

$$\Delta w_{ij}^R = -\beta\frac{\partial E}{\partial w_{ij}^R} = -\beta\frac{\partial \sum_{p=1}^{P} E_p}{\partial w_{ij}^R} = -\beta\sum_{p=1}^{P}\frac{\partial E_p}{\partial x_i^{R,p}(n)}\cdot\frac{\partial x_i^{R,p}(n)}{\partial w_{ij}^R}$$

$$= \beta \sum_{p=1}^{P} (x_i^{A,p} - x_i^{R,p}(n)) \cdot \frac{1}{\varepsilon} \cdot x_i^{R,p}(n) \cdot (1 - x_i^{R,p}(n)) \cdot x_j^{R,p}(n), \qquad (5)$$

where β is the learning rate of the gradient search. The formal algorithm which achieves the update can be found [14].

The results of a typical numerical experiment which proceeds along the above gradient search on the Adachi data set (shown in Fig. 5) are displayed in Fig. 1 and 3. In these, we have chosen the learning rate β to be 0.05. To clarify issues, we catalogue our experiments for three specific cases, namely when the probability p_d for deleting an edge is 0.9, 0.5 and 0.1 respectively.

If p_d is 0.9, the total error E and average values of Δw_{ij}^R do not converge to 0, as shown in Fig. 1. However, as p_d decreases, e.g., 0.5, then E and Δw_{ij}^R converge to 0, as shown in Fig. 3 (a) and (b). If p_d is even less, E and Δw_{ij}^R also converge to 0 but with a faster rate, as shown in Fig. 3 (c) and (d). This phenomenon can be easily explained: The larger the value of p_d, the smaller is the number of edges and vice versa. Thus, if $p_d = 0$, it means that the Random-AdNN is exactly the same as the original AdNN. On the other hand, if $p_d = 1$, it means that all the vertexes are isolated and remain as disconnected units. Of course, the "fitting" effect that we obtain by the approximate graph, the Random-AdNN, is more precise as the number of edges increases.

The experimental results obtained for the LOVE data set (also shown in Fig. 5) are quite similar, and are displayed in Fig. 2 and 4.
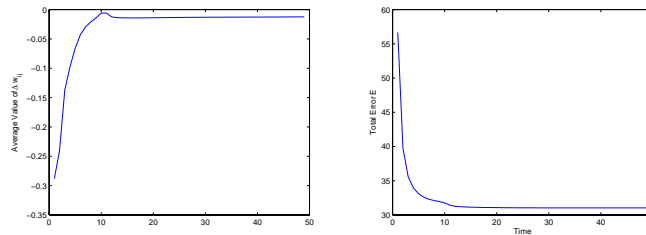

Fig. 1. For the Adachi data set: The figure on the left shows the variation of the average of Δw_{ij}^L (averaged over all values of i and j) over the first 50 iterations of the gradient search scheme. The average converges to a value arbitrarily close to zero after 12 time steps. The figure on the right shows the variation of the global error over the same time frame. Observe that this quantity does not converge to *zero*.

The Lyapunov analysis of the Random-AdNN is also available, but omitted here in the interest of space. It can be found in [13].

4   Chaotic and PR Properties of the Random-AdNN

We now briefly report the PR properties of the Random-AdNN. These properties have been discovered as a result of examining the Hamming distance between the input pattern and the patterns that appear in the output. The experiments were conducted using two data sets described below.
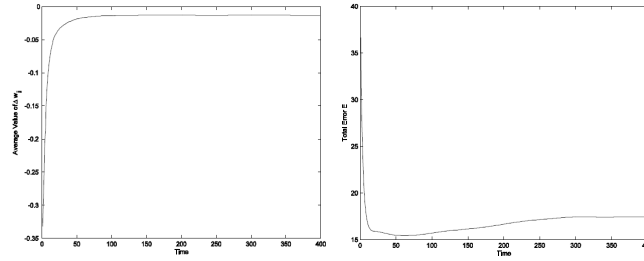
Fig. 2. For the LOVE data set: The figure on the left shows the variation of the average of Δw_{ij}^L over the first 400 iterations of the gradient search scheme. The average converges to a value arbitrarily close to zero after 50 time steps. The figure on the right shows the variation of the global error over the same time frame, which does not converge to *zero* either.
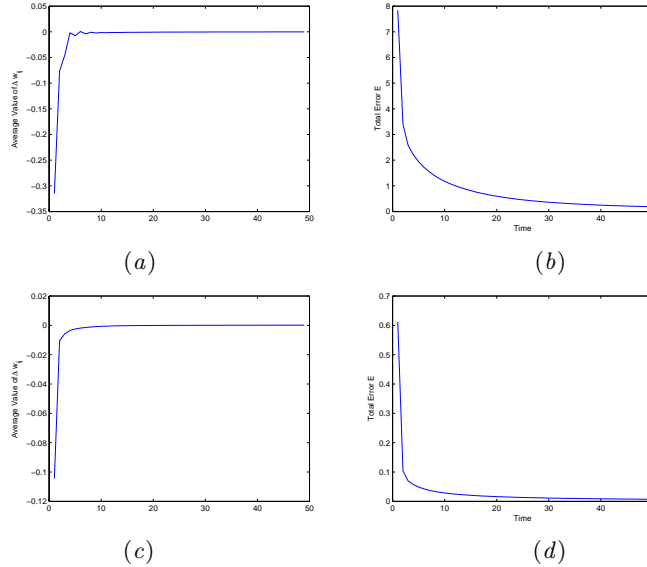

(a) (b)

(c) (d)

Fig. 3. For the Adachi data set: The figures show the variation of the average of Δw_{ij}^L and the global error over the same time frame. The probability of edge deletion is $p_d = 0.5$ (for (a) and (b)) and $p_d = 0.1$ (for (c) and (d)) respectively.

In the ideal setting we would have preferred the Random-AdNN to be chaotic when exposed to untrained patterns, and the output to appear periodically or more frequently when exposed to trained patterns. Besides yielding this phenomenon, the Random-AdNN also goes through a chaotic phase and a PR phase as some of its parameters change.

We summarize the results for the Random-AdNN, obtained by using different settings of p_d. The others parameters are: $k_f = 0.2$, $k_r = 1.02$, $\alpha = 10$, $\varepsilon = 0.015$, $\beta = 0.05$.

From these tables we see clearly that, the Random-AdNN is able to "resonate" the input patterns with the corresponding output patterns. Consider Table 1 (a) as an example. If the input is P1, then the network outputs P1 accordingly, and
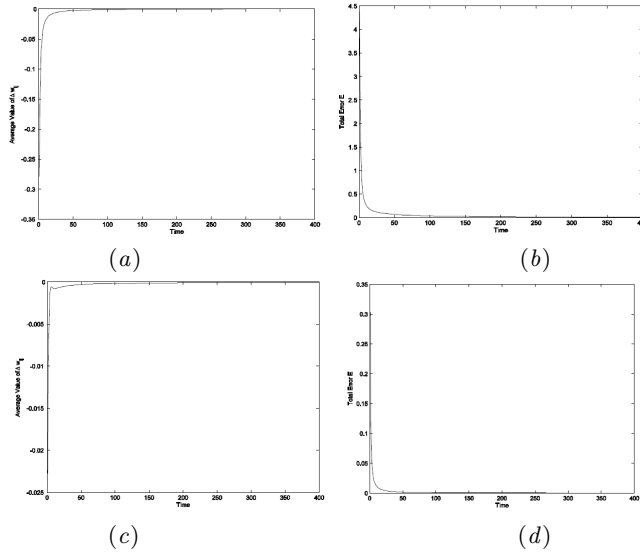
Fig. 4. For the LOVE data set: The figures show the variation of the average of Δw_{ij}^L and the global error over the same time frame. The probability is $p_d = 0.5$ (for (a) and (b)) and $p_d = 0.1$ (for (c) and (d)) respectively.

Fig. 5. The patterns used by Adachi *et al* (a) and Inoue *et al* (b). The first four patterns in (a) and (b) are used to train the network. The fifth pattern in (a) is obtained from the fourth pattern by including 15% noise. The sixth pattern in (a) and the fifth pattern in (b) are the untrained patterns.

at the same time, no other trained patterns appear in the output sequence. Even when a noisy pattern is presented to the system, e.g., P5, which is a noisy pattern of P4 with 15% noise, the network still "resonates" P4 instead of P5 in the output sequence. Furthermore, if the input is an untrained pattern, e.g., P6, then none of the trained patterns will be recalled. Observe that even the input pattern P6, will itself be retrieved only a few times, which is much less than the other diagonal entries in the table, i.e., when the inputs are P1 – P4. The difference between (a) – (c) is that in Table (c), the network "resonates" the input patterns more frequently than in (a) and (b). This is because when $p_d = 0.1$, the Random-AdNN is almost the same as the original AdNN since the Random-AdNN has most of the edges of the AdNN. However, in this case, the Random-AdNN also needs a quadratic number of computations, which is computationally much more intensive than for the case when $p_d = 0.9$. In this regard, we comment that $p_d = 0.9$ is good enough for PR, which has only a very small computational burden. By a simple computation we can see that the expected degree for each vertex of the Random-AdNN is only $N(1-p_d) = 10$ for the Adachi data set, which implies that

Table 1. The frequency of the Hamming distance between the input and the output patterns for the Random-AdNN. The probability p_d is 0.9, 0.5, 0.1 for (a), (b), (c) respectively.

$p_d = 0.9$		Input Patterns					
		P1	P2	P3	P4	P5	P6
	P1	151	0	0	0	0	0
	P2	0	422	0	0	0	0
Retrieved	P3	0	0	161	0	0	0
Patterns	P4	0	0	0	106	177	0
	P5	0	0	0	10	2	0
	P6	0	0	0	0	0	46

(a)

$p_d = 0.5$		Input Patterns					
		P1	P2	P3	P4	P5	P6
	P1	202	0	0	0	0	0
	P2	0	285	0	0	0	0
Retrieved	P3	0	0	234	0	0	0
Patterns	P4	0	0	0	211	206	0
	P5	0	0	0	4	3	0
	P6	0	0	0	0	0	33

(b)

$p_d = 0.1$		Input Patterns					
		P1	P2	P3	P4	P5	P6
	P1	238	0	0	0	0	0
	P2	0	331	0	0	0	0
Retrieved	P3	0	0	258	0	0	0
Patterns	P4	0	0	0	237	189	0
	P5	0	0	0	9	20	0
	P6	0	0	0	0	0	34

(c)

the computational load has been greatly reduced when compared to the original AdNN, which has a vertex degree of 99.

5   Conclusions

In this paper we have concentrated on the field of Chaotic Pattern Recognition (PR), which is a relatively new sub-field of PR. Such systems, which have only recently been investigated, demonstrate chaotic behavior under normal conditions, and resonate when it is presented with a pattern that it is trained with. The network that we have investigated is the Adachi Neural Network (AdNN) [2], which has been shown to possess chaotic properties, and to also demonstrate Associative Memory (AM) and Pattern Recognition (PR) characteristics. In this paper we have considered how the topology can be modified so as to render the network much closer to "real" neural networks. To achieve this, we have changed the network structure to be a random graph, and then computed the best weights for the new graph by using a gradient-based algorithm. By a detailed experimental suite, we showed that the new Random-AdNN possesses chaotic and PR properties for different settings.

References

1.Qin, K., Oommen, B.J.:   Adachi-like chaotic neural networks requiring linear-time computations by enforcing a tree-shaped topology.   IEEE Transactions on Neural

Networks **20**(11) (2009) 1797–1809

2. Adachi, M., Aihara, K.: Associative dynamics in a chaotic neural network. Neural Networks **10**(1) (1997) 83–98

3. Calitoiu, D., Oommen, B.J., Nussbaum, D.: Desynchronizing a chaotic pattern recognition neural network to model inaccurate perception. IEEE Transactions on Systems Man and Cybernetics Part B-Cybernetics **37**(3) (2007) 692–704

4. Calitoiu, D., Oommen, B.J., Nussbaum, D.: Periodicity and stability issues of a chaotic pattern recognition neural network. Pattern Analysis and Applications **10**(3) (2007) 175–188

5. Qin, K., Oommen, B.J.: Chaotic pattern recognition: The spectrum of properties of the Adachi neural network. In: Lecuture Notes in Computer Science. Volume 5342., Florida, USA (2008) 540–550

6. Chen, L., Aihara, K.: Global searching ability of chaotic neural networks. IEEE Transactions on Circuits and Systems I: Fundamental Theory and Applications **46**(8) (1999) 974–993

7. Qin, K., Oommen, B.J.: An enhanced tree-shaped adachi-like chaotic neural network requiring linear-time computations. In: Proceedings of CHAOS'09, the 2009 Chaotic Modeling and Simulation International Conference, Chania, Greece (2009) 284–293

8. Qin, K., Oommen, B.J.: Ideal chaotic pattern recognition is achievable: The Ideal-M-AdNN - its design and properties. In: Transactions on Computational Collective Intelligence (2013) 22–51

9. Luo, G.C., Ren, J.S., Qin, K.: Dynamical associative memory: The properties of the new weighted chaotic Adachi neural network. IEICE Transactions on Information and Systems **E95d**(8) (2012) 2158–2162

10. Qin, K., Oommen, B.J.: Networking logistic neurons can yield chaotic and pattern recognition properties. In: IEEE International Conference on Computational Intelligence for Measure Systems and Applications, Ottawa, Canada (2011) 134–139

11. Hiura, E., Tanaka, T.: A chaotic neural network with Duffing's equation. In: Proceedings of International Joint Conference on Neural Networks, Orlando, Florida, USA (2007) 997–1001

12. Qin, K., Oommen, B.J.: The entire range of chaotic pattern recognition properties possessed by the Adachi neural network. Intelligent Decision Technologies **6**(1) (2012) 27–41

13. Qin, K.: Generic Analysis of Chaotic Neural Networks and Their Applications in Pattern Recognition and Crypto-systems. PhD thesis. (2010) University of Electronic Science and Technology of China, Chengdu, China.

14. Qin, K., Oommen, B.J.: *Chaotic* pattern recognition using the Adachi neural network modified in a random manner. In: Proceedings of CHAOS'13, the 2013 Chaotic Modeling and Simulation International Conference, Istanbul, Turkey (2013) 540–550.

SIGNALS OF CHAOS IN THE TRANSIENT CURRENT THROUGH $As_2S_3(Ag)$ and $As_2Se_3(Al)$ THIN FILMS

A. S. Hacinliyan[1], Y. Skarlatos[2], O. Ozgur Aybar[3], I. Kusbeyzi Aybar[4], E.Kandiran[5], A. C. Keles[6], and E. C. G. Artun[7]

[1] Yeditepe University, Department of Information Systems and Technologies, Istanbul, Turkey
Yeditepe University, Department of Physics, Istanbul, Turkey
Bogazici University, Department of Physics, Istanbul, Turkey
(E-mail: ahacinliyan@yeditepe.edu.tr)
[2] Bogazici University, Department of Physics, Istanbul, Turkey
Yeditepe University, Department of Physics, Istanbul, Turkey
(E-mail: sakarlat@boun.edu.tr)
[3] Gebze Institute of Technology, Department of Mathematics, Kocaeli, Turkey
Yeditepe University, Department of Information Systems and Technologies, Istanbul, Turkey
(E-mail: oaybar@yeditepe.edu.tr)
[4] Yeditepe University, Department of Computer Education and Instructional Technology, Istanbul, Turkey
(E-mail: ikusbeyzi@yeditepe.edu.tr)
[5] Bogazici University, Department of Physics, Istanbul, Turkey
(E-mail: engin.kandiran@boun.edu.tr)
[6] Yeditepe University, Department of Information Systems and Technologies, Istanbul, Turkey
Yeditepe University, Department of Physics, Istanbul, Turkey
(E-mail: ali.keles@yeditepe.edu.tr)
[7] Yeditepe University, Department of Physics, Istanbul, Turkey
(E-mail: ecgartun@hotmail.com)

Abstract: The transient current through a sample of $As_2S_3(Ag)$ and $As_2Se_3(Al)$ glass substrate has been analyzed in order to study possible chaotic behavior using methodology similar to that in work on polymers [1,2]. Rescaled range analysis (R/S) shows the presence of two regimes of fractal behavior, one of which can be attributed to short time scale relaxation and the other can be attributed to long term chaotic behavior. The mutual information data indicates the necessity of noise reduction using a moving average. Extending the moving average window gives correspondingly large delay times as expected. The indicated delay time starts at 20*s* and grows up to 250*s*. The false nearest neighbor results also indicate a value around 10. A robust increase in the Lyapunov exponent stretching graphs confirm long term chaos; the result is not sensitive to the precise values of the delay time and embedding dimension. Possible relaxation mechanisms [3] in the short time range include parametrizations involving stretched

exponential relaxation and logarithmic relaxation, the latter suggested by a proposal of Trachenko [4,5].

Keywords: Chaotic Behavior, Lyapunov Exponents, Rescaled Range Analysis.

1. Introduction

The specimens under investigation were prepared as sandwiched metal-glass-metal structures with the glass as the isolating layer. 300 nm thick aluminum electrodes were thermally evaporated at 10^{-6} mbar on microscope glass slides cleaned in a detergent solution. Subsequently, aluminum top contacts were evaporated. The I-V measurement was performed via a programmable picoammeter/voltage source (Keithley, model 487) and a temperature controller (Lake Shore, model 300). The picoammeter and the temperature controller were interfaced to a computer through an interface card that automated data taking, schematically presented in Fig. 1. The picoammeter model 478 used is capable of reading currents in the range 10 fA to 2 mA. It also serves as a DC voltage supply in the range up to 500V.
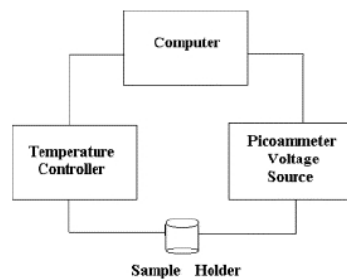
Fig. 1. Schematic of the experimental setup

The data of transient current against time for $As_2S_3(Ag)$ and $As_2Se_3(Al)$ are presented in Fig. 2 and Fig. 3. One horizontal unit represents 30 ms. Examining the graphs, we find that there is an overall relaxation in $As_2Se_3(Al)$ but not in $As_2S_3(Ag)$. However for both materials the data looks more like the behavior of the transient current data for polymer thin films such as PMMA [6] or PEG-Si[2].
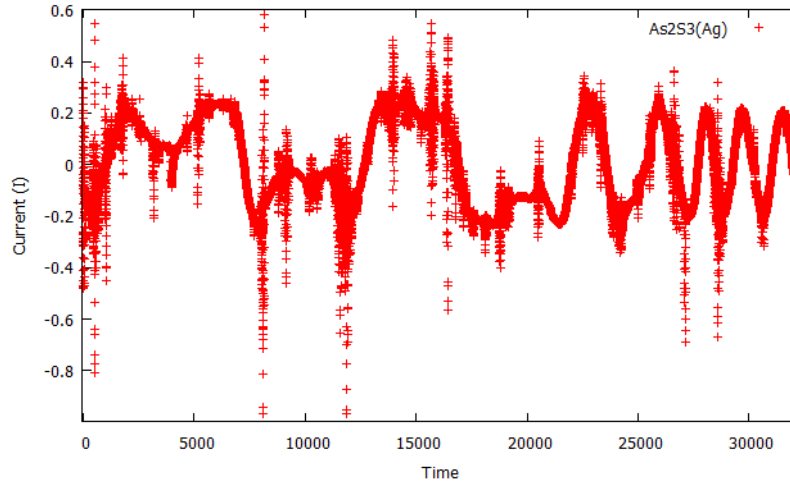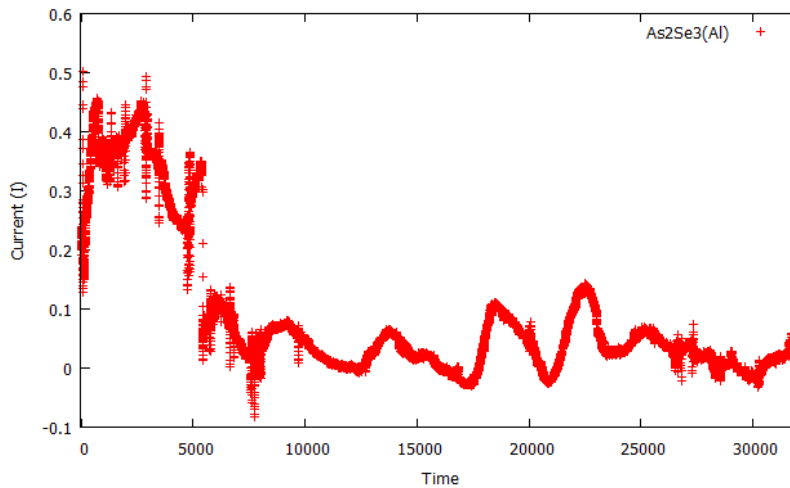
Fig. 2. The data of $As_2S_3(Ag)$

Fig. 3. The data of $As_2Se_3(Al)$

2. Time Series Analysis

Time series analysis is used for analysing the data of $As_2S_3(Ag)$ and $As_2Se_3(Al)$ using TISEAN [7,8] software package. The formulas used are part of the standard literature and are omitted. We observe one dimensional signal in uniform time intervals, x(0), x(T), …, x(nT). In fact the signal x(T) depends on an unknown number of parameters. To determine the number of parameters (dimensionality of the system), we find the meaningful time delay τ and the meaningful embedding dimension to construct time delay vectors. We find the embedding dimension by using the False Nearest Neighbors (FNN) method. We

find the delay time by using Mutual Information (MUT) or correlation function (CORR). We calculate the autocorrelation function, which is the Fourier transform of the power spectrum and we present the results in Fig.4.
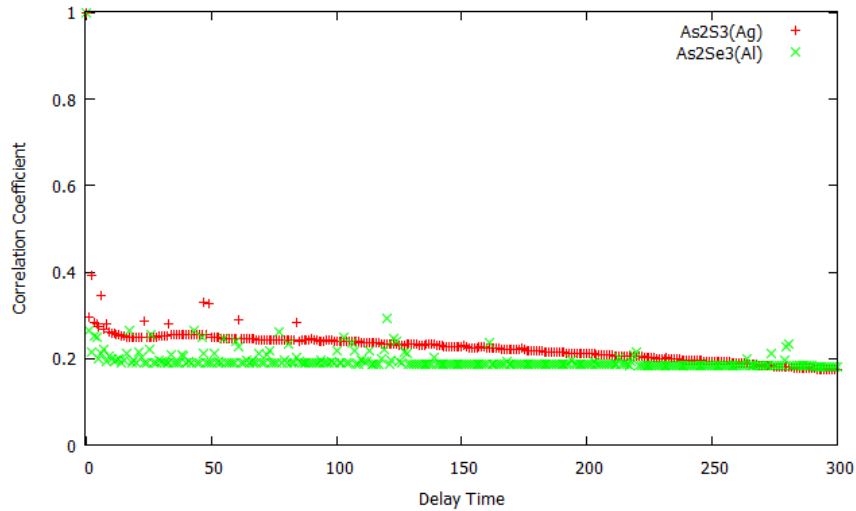
Fig. 4. Correlation coefficient

Another method for obtaining the delay time is to find the first minimum of the mutual information as presented in Fig. 5. We wish to represent a random variable with actual probability distribution $p(x)$ with a code whose average length is $H(p)$. In practice, because of missing information or sampling, we may not know the actual distribution $p(x)$, so that we have to take the distribution to be $q(x)$. In such a situation, we may need a longer code to represent the random variable. This difference in length, $D(p(x)\|q(x))$ is known as the relative entropy. The knowledge that one random variable includes about another random variable is known as mutual information. We can only examine the information that we send to one channel in terms of information output from there. Let x and y be random variables with mutual distribution $p(x,y)$. If variables x and y have distributions $p(x)$ and $p(y)$, the mutual information is the entropy between the mutual distribution and product distribution. If it is chosen to be too small, $x(t)$ and $x(t+\tau)$ will be very close to each other and it will be difficult to distinguish them. If it is chosen too large, $x(t)$ and $x(t+\tau)$ coordinates will be too far apart, will behave independently and cause loss of information.
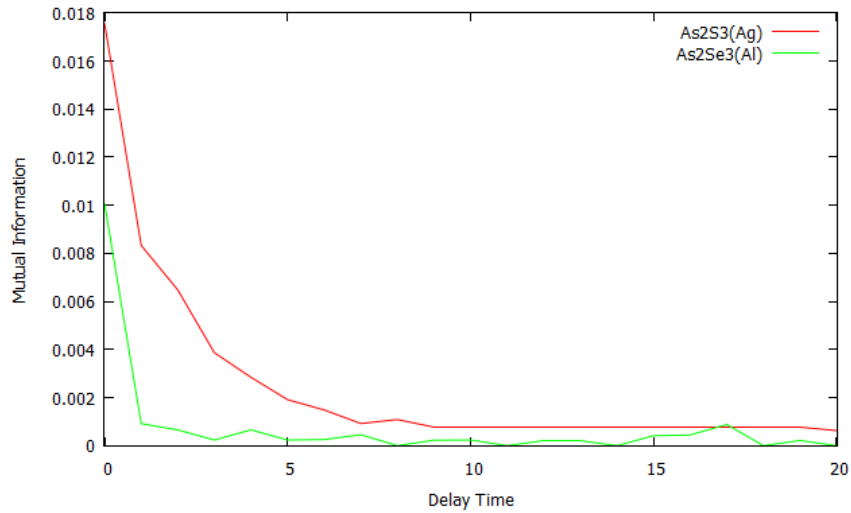
Fig. 5. Mutual information

False nearest neighbors graph (FNN) presented in Fig. 6. is useful for determining the minimal embedding dimension. The purpose is to find points near each other in the embedded space. If the embedding dimension is too small, points that are close in embedded space will appear as false neighbors. If the embedding dimension is too large, we lose statistics and information. By expressing the distance in (d+1) dimensions in terms of the distance in d dimensions, we can calculate the number of neighbors in d and d+1 dimensions, R_{d+1}/R_d. If this ratio is above a critical value, we have false nearest neighbors.
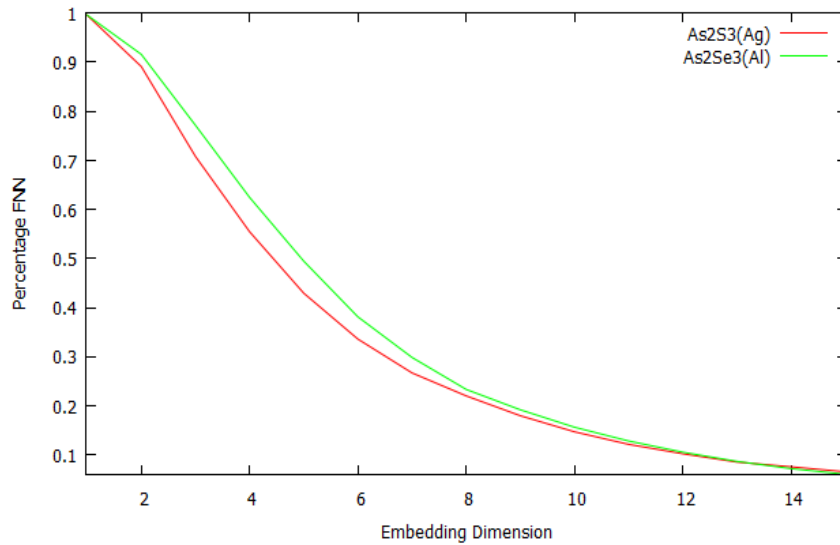

Fig. 6. False nearest neighbors

The largest lyapunov exponent presented in Fig.7 is usually used as an indicator of chaos. This is obtained by calculating the quantity

$$S(\Delta n) = \frac{1}{N} \sum_{n0=1}^{N} \ln \left[\frac{1}{|U(S_{n0})|} \sum_{S_n \in Y(S_{n0})} \left| [S_{n0+\Delta n} - S_{n+\Delta n}] \right| \right] \qquad (1)$$

S_{n0} is our reference point, U is a hypersphere of distance ε to this point. If ε is too small, we can not find a sufficient number of points, if it is too large, a periodic component may be missed. For a few ε values, calculating the number of points in the hypersphere $S(\Delta n)$, plotting it against Δn gives the largest Lyapunov Exponent. A positive slope implies a positive Lyapunov Exponent.
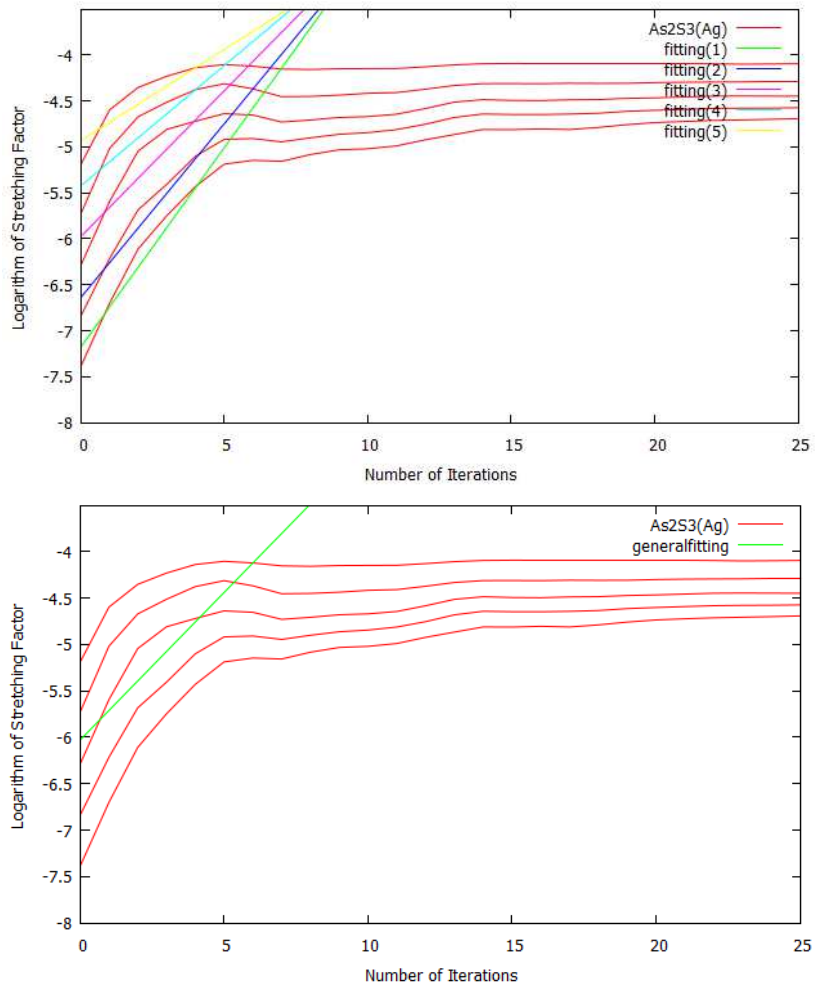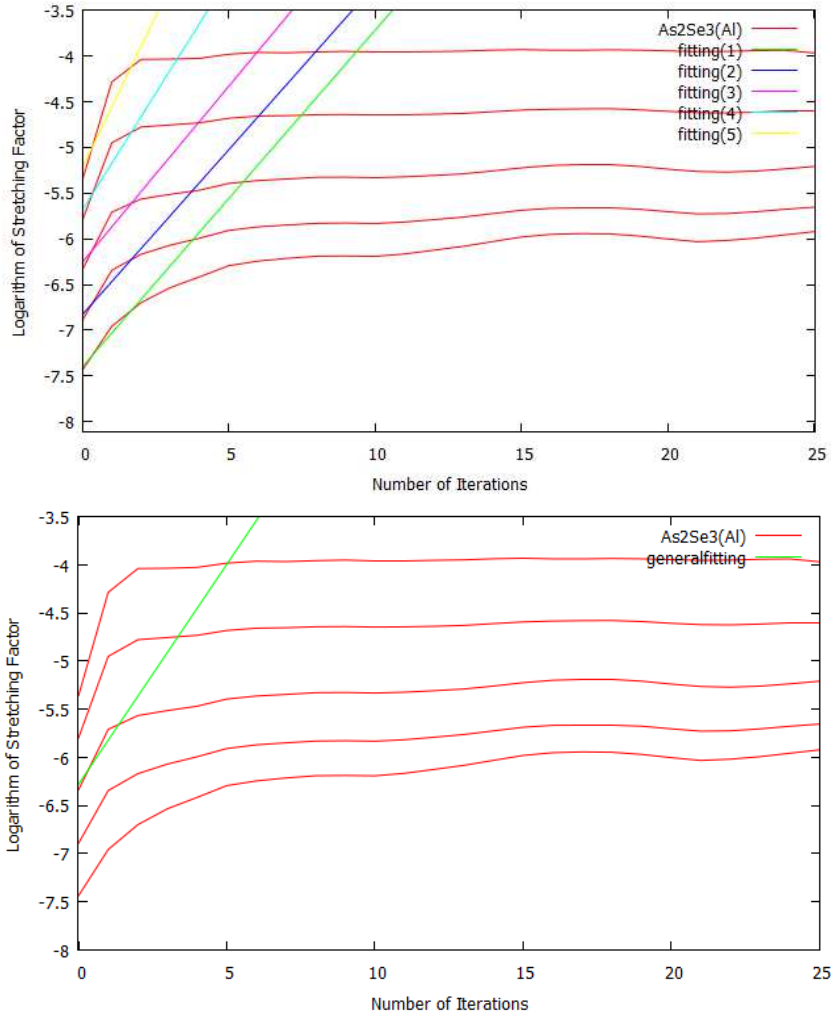
Fig. 7. Largest Lyapunov exponents

Thin Films	Lyapunov Exponent (slope)
$As_2S_3(Ag)$	0.317
$As_2Se_3(Al)$	0.456

3. Hurst (R/S) Analysis

The Hurst exponent is calculated using the standard approach and as presented in Fig. 8 it is a numerical approach to the predictability of a time series. If the Hurst exponent (H) is close to 0.5, the process is a random walk. (Brownian motion) A Hurst exponent (H) in the range $0 < H < 0.5$ implies non random behavior in the time series. A Hurst exponent (H) in the range $0.5 < H < 1$ implies a time series with long range, continuous evolution.
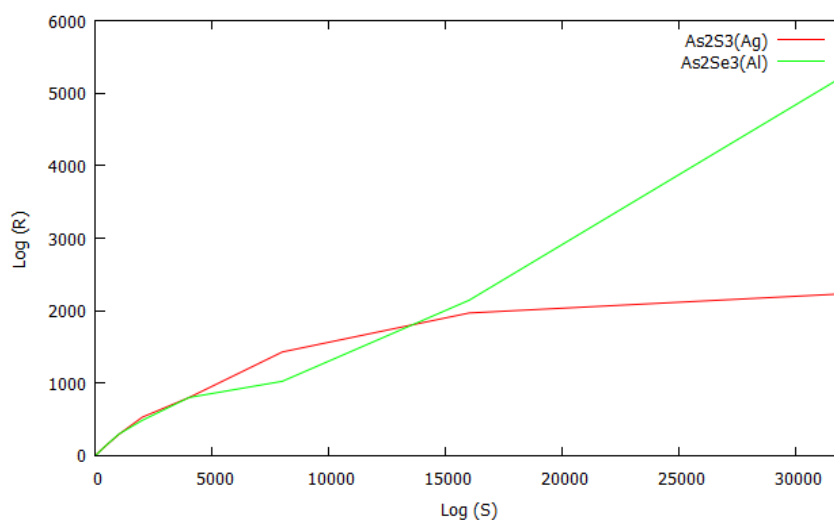

Fig. 8. Hurst Analysis

4. Conclusions

The complex structure of chalcogenites suggests many degrees of freedom and a multi-fractal structure. The transient current through the samples of $As_2S_3(Ag)$ and $As_2Se_3(Al)$ glass substrates has been analyzed in order to study possible chaotic behavior similar to that in our work on polymers. The conductivity mechanism measured by the time dependent behavior of transient current was analyzed by nonlinear considerations such as time series analysis, maximal Lyapunov exponent, Hurst (R/S) analysis. Intermediate dimensional chaos with positive maximal Lyapunov exponents was observed. The behaviors of the system with possibly two different regions, one with short range and another with long range correlation were seen by comparing the correlation coefficient and mutual information. As suggested by studies of other amorphous materials with irregular behavior, the use of nonlinear methods for analyzing the conductivity mechanisms in such materials seems crucial in modelling and show that the behaviors are comparable.

References

1. O. O. Aybar, A. Hacinliyan, Y. Skarlatos, G. Sahin, K. Atak, Possible Stretched Exponential Parametrization for Humidity Absorption in Polymers, *European Physical Journal E* 28: 369-376, 2009.

2. O. O. Aybar, A. Hacinliyan, Y. Skarlatos, G. Sahin, K. Atak, Chaoticity analysis of the current through pure, hydrogenated and hydrophobically modified PEG-Si thin films under varying relative humidity, *Central European Journal of Physics* 7:568-574, 2009.

3. O. Shpotyuk, J. Filipecki, M. Hyla, A. Ingram, Critical comments on speculations with open and closed free-volume defects in ion-conducting Ag/AgI - As_2S_3 glasses, *Solid States Ionics* 208: 1-3, 2012.

4. K. Trachenko, Slow dynamics and stress relaxation in a liquid as an elastic medium, *Physical Review B* 75, 2007.

5. K. Trachenko, Local events and stretched-exponential relaxation in glasses, *Physical Review B* 70, 2004

6. Y. Skarlatos, G. Şahin and G. Akın "Signals of Chaotic Behavior in PMMA" Chaos Solitons and Fractals, 17, 575-583(2003).

7. R. Hegger, H. Kantz, T. Schreiber, Chaos 94, 413 (1999).

8. Kantz, H.and T.Schreiber, Nonlinear Time Series Anaylsis, Cambridge University Press, Cambridge, 1997.

The Fractional Laplacian as continuum limit of self-similar lattice models

Thomas M. Michelitsch, Gérard A. Maugin[1], Shahram Derogar[2], and Franck C.G.A Nicolleau[3], Andrzej F. Nowakowski[3]

[1] Sorbonne Universités, Université Pierre and Marie Curie, Paris 6, Institut Jean le Rond d'Alembert, CNRS UMR 7190 Paris, France
(E-mail: `michel@lmm.jussieu.fr`)
[2] Department of Architecture, Yeditepe University, Istanbul, Turkey
(E-mail: `derogar@yeditepe.edu.tr`)
[3] Sheffield Fluid Mechanics Group, Department of Mechanical Engineering, University of Sheffield, United Kingdom
(E-mail: `f.nicolleau@sheffield.ac.uk`)

Abstract. We show that the fractional Laplacian (FL) $-(-\Delta)^{\frac{\alpha}{2}}$ is the principal characteristic operator of harmonic systems with self-similar interparticle interactions. We demonstrate that the FL can be rigorously defined by Hamilton's variational principle as "*fractional continuum limit*" of a spring model with self-similar, in some cases fractal harmonic interactions which we introduced recently (Michelitsch *et al.*[5]). We generalize that approach to the multi-dimensional physical space of dimensions $n = 1, 2, 3, ...$ In this way we demonstrate the interlink between fractal discrete behavior (discrete self-similar Laplacian) and its fractional continuum field counterpart (FL) and give the latter a physical justification. The dispersion relation of the discrete model is obtained as self-similar Weierstrass-Mandelbrot fractal function which takes in the fractional continuum limit the form of a smooth self-similar power law. The density of states (density of normal modes) takes the form of a characteristic scaling law which depends only on the scaling exponent of the FL and the dimension of the physical space. The approach has a wide range of interdisciplinary applications of self-similar dynamic problems such as anomalous diffusion (Levi flights), self-similar wave propagation, and may also be useful to model self-similar chaotic processes and dynamics in turbulence.
Keywords: Fractional Laplacian, fractional continuum limit, linear chain, Fractals, Weierstrass-Mandelbrot function, self-similarity, scaling laws.

1   Introduction

Despite fractional calculus has a long history, recently a new increasing interest has emerged to employ fractional operators and the so called *fractional Laplacian* (FL) (often also referred to as Riesz fractional derivative) $-(-\Delta)^{\frac{\alpha}{2}}$ where α indicates a fractional in general non-integer exponent. The reason for this

new interest is the conclusion that the fractional approach is a highly powerful mathematical tool to model complex and chaotic phenomena in various disciplines.

The goal of this note is to demonstrate that the FL is the "natural" characteristic linear operator, in a sense most basic operator that can be generated from a physical "self-similar" spring model and its generalizations. Due to its non-local "long tail" and self-similar invariant characteristics of the FL we raise the question what is the interlink of the FL with fractal and chaotic features often chosen in nature.

Recently many models where developed which employ the *FL* in various physical contexts, among them the description of "complex" dynamic phenomena including anomalous diffusion (Lévi flights) [1–3,8,10] and see also the numerous references therein.

This note is organized as follows: As point of departure we introduce a 1D harmonic spring model with harmonic elastic potential energy which describes *self-similar interparticle interactions* which we developed recently [5]. This discrete model leads to fractal dynamic vibrational characteristics such as a dispersion relation of the form of Weierstrass-Mandelbrot fractal functions. Application of Hamilton's variational principle defines a discrete self-similar Laplacian with all good properties of a Laplacian: The self-similar Laplacian is self-adjoint, elliptic, negative (semi-) definite (indicating elastic stability), and translational invariant. We introduce a *fractional continuum limit* which yields in rigorous manner the FL. In this way the FL is physically justified being a continuum description of a self-similar spring model. The approach is generalized to n dimensions of the physical space.

2   Linear chain model with self-similar harmonic interactions

We consider an infinite sequence of points $\{h_p\}$ generated by a non-linear invertible mapping $h \to N(h)$ with (initial value $h = h_0$)

$$h_p = N(h_{p-1}), \qquad p \in Z_0 \tag{1}$$

where we exclude for convenience periodic orbits and fixed points. All points of the sequence are assumed to fulfil $h_p \neq h_q$ for $p \neq q$ ($-\infty < p < \infty$). Define a function Φ for a arbitrary generated by the series

$$\Phi(h) = \sum_{s=-\infty}^{\infty} a^{-\delta s} f(h_s) \tag{2}$$

where the sum is performed over the infinite sequence of points h_s of (1). $\Phi(h)$ is defined (convergent) for sufficiently good functions f. Function Φ behaves self-similar under the (in general non-linear) transformation $h \to N(h)$ of its argument, namely

$$\Phi(N(h)) = a^{\delta} \sum_{s=-\infty}^{\infty} a^{-\delta(s+1)} f(h_{s+1}) = a^{\delta} \Phi(h) \tag{3}$$

For the sake of simplicity but without loss of generality let us consider here a sequence generated by a linear mapping

$$N(h) = ah, \qquad a > 1 \tag{4}$$

Then we introduce the self-similar elastic potential in the form of a self-similar function (3), namely

$$\mathcal{W}(x,h) = \frac{1}{4} \sum_{s=-\infty}^{\infty} a^{-\delta s} \left\{ (u(x+ha^s) - u(x))^2 + (u(x-ha^s) - u(x))^2 \right\} \tag{5}$$

which is self-similar in the sense of (3) with respect to h. The elastic potential describes a homogeneous mass distribution where each material point x is connected with other material points $x \pm ha^s$ by a self-similar distribution of linear springs of spring constants $\sim a^{-\delta s}$. In general this potential can be defined also for nonlinear sequence h_s of (1). The notion of self-similarity at a point was coined by Peitgen *et al.*[9].

The total elastic energy of (5) is given by

$$V(h) = \int_{-\infty}^{\infty} \mathcal{W}(x,h)\, \mathrm{d}x \tag{6}$$

A self-similar Laplacian is then defined by Hamilton's principle

$$\Delta_{\delta,h} u(x) = -\frac{\delta V}{\delta u(x)} \tag{7}$$

where $\frac{\delta(..)}{\delta u}$ stands for a functional derivative, and where

$$\Delta_{(\delta,a,h)} u(x) = \sum_{s=-\infty}^{\infty} a^{-\delta s} \left(u(x+ha^s) + u(x-ha^s) - 2u(x) \right), \qquad 0 < \delta < 2 \tag{8}$$

fulfilling self-similarity condition $\Delta_{\delta,ah} = a^{\delta} \Delta_{\delta,h}$. This Laplacian has all required good properties. The dispersion relation (negative eigenvalues) of this Laplacian are obtained in the form of Weierstrass-Mandelbrot functions

$$\omega_{(\delta,a)}^2(kh) = 4 \sum_{s=-\infty}^{\infty} a^{-\delta s} \sin^2 \left(\frac{kha^s}{2} \right), \qquad 0 < \delta < 2 \tag{9}$$

which are self-similar $\omega_{(\delta,a)}^2(kah) = a^{\delta} \omega_{(\delta,a)}^2(kh)$ within its entire interval of existence $0 < \delta < 2$. The dispersion relation (9) is within $0 < \delta < 1$ a nowhere differentiable fractal function of estimated Hausdorff dimension $2 - \delta$ [4,5]. In figures 1-3 cases of increasing fractal dimension (decreasing δ) are plotted. Note that for $1 \le \delta < 2$ (9) is a non-fractal function of Hausdorff dimension $D = 1$ (see figure 1). For increasing fractal dimension D (decreasing exponent δ) fractal dispersion curves have increasingly erratic characteristics. For more details we refer to our paper Michelitsch *et al.*[5].
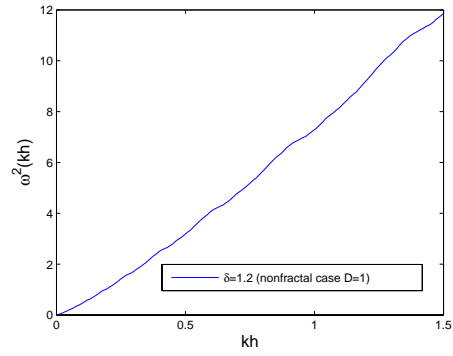
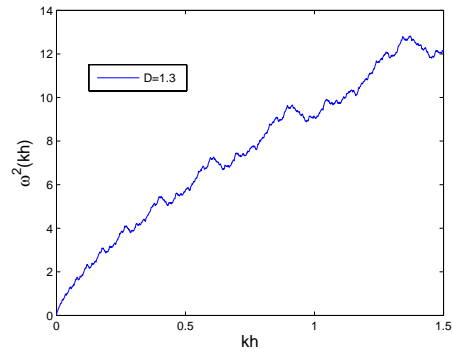**Fig. 1.** Dispersion relation (9) for a fractal case.

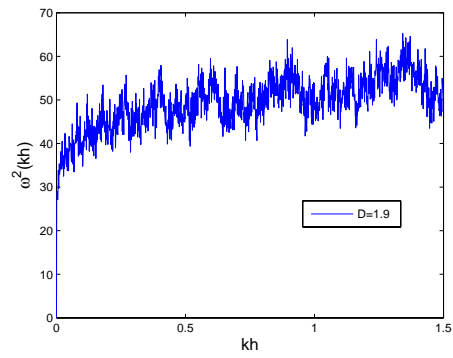**Fig. 2.** Dispersion relation (9) for a non-fractal case.

Fig. 3. Dispersion relation (9) for a fractal case.

3   The FL as fractional continuum limit of the discrete chain Laplacian and its generalization to n dimensions

Now we define the *fractional continuum limit* as follows [6,7]

$$\Lambda_a(h) = \lim_{a \to 1} \sum_{s=-\infty}^{\infty} a^{-\delta s} f(a^s h) \approx \frac{h^{\delta}}{\zeta} \int_0^{\infty} \frac{f(\tau)}{\tau^{\delta+1}} \mathrm{d}\tau \tag{10}$$

where $a = 1 + \zeta \to 1$ and $0 < \zeta << 1$. The *fractional continuum limit* of the elastic potential (5) takes then the form

$$\mathcal{W}(x,h) \approx \frac{h^{\delta}}{4\zeta} \int_0^{\infty} \frac{(u(x+\tau) - u(x))^2 + (u(x-\tau) - u(x))^2}{\tau^{\delta+1}} \mathrm{d}\tau, \qquad 0 < \delta < 2 \tag{11}$$

which can be generalized to n dimensions as

$$\mathcal{W}(\mathbf{x},h,\alpha) \approx \frac{h^{\alpha}}{4\zeta} \int_0^{\infty} \frac{(u(\mathbf{x}+\mathbf{r}) - u(\mathbf{x}))^2 + (u(x-\mathbf{r}) - u(\mathbf{x}))^2}{\tau^{\alpha+n}} \mathrm{d}^n\mathbf{r} \tag{12}$$

where $0 < \alpha < 2$. Hamilton's principle yields from (12) the fractional continuum limit of the self-similar Laplacian in n dimensions

$$\Delta_{n,\alpha,h} u(x) =: -\frac{\delta V}{\delta u(x)} = \frac{h^{\alpha}}{2\zeta} \int_0^{\infty} \frac{(u(\mathbf{x}+\mathbf{r}) + u(x-\mathbf{r}) - 2u(\mathbf{x}))}{\tau^{\alpha+n}} \mathrm{d}^n\mathbf{r} \tag{13}$$

with $0 < \alpha < 2$. (13) recovers for $n = 1$ also the fractional continuum limit of the self-similar Laplacian (8). The dispersion relation is obtained by $\Delta_{n,\alpha,h} e^{ikx} = -\omega_{n,\alpha,h}^2(kh) e^{ikx}$ and yields [8] a power-law of the form

$$\omega_{n,\alpha,h}^2(kh) = \mathcal{A}_{n,\alpha} k^{\alpha}, \qquad 0 < \alpha < 2 \tag{14}$$

with the positive constant [8]

$$\mathcal{A}_{n,\alpha} = \frac{h^{\alpha}}{\zeta} \frac{\pi^{\frac{n}{2}}}{2^{\alpha-1}\alpha} \frac{\Gamma(1 - \frac{\alpha}{2})}{\Gamma(\frac{\alpha+n}{2})} > 0, \qquad 0 < \alpha < 2 \tag{15}$$

The positiveness of this constant is a consequence of the elastic stability.

   The following observation is crucial: The fractional continuum limit Laplacian (13) coincides (up to a normalization factor) with the FL which is defined, e.g. [2,3,10]

$$\Delta_{n,\alpha,h} = -\mathcal{A}_{n,\alpha} (-\Delta)^{\frac{\alpha}{2}} \tag{16}$$

where the constant (15) is consistent with the normalization factor given by in the literature e.g. [2,3,8,10] and where (13) recovers with (16) and (15) the standard representation of the FL. Our self-similar chain model represents hence a discrete lattice counterpart which corresponds in the fractional continuum approximation the FL fractional approach.

With (15) it is straight-forward to obtain the density of normal modes ("density of states") $\mathcal{D}(\omega)$ where $\mathcal{D}(\omega)\mathrm{d}\omega$ measures the number of eigenmodes of frequency ω. It is obtained as [8]

$$\mathcal{D}_{\alpha,n}(\omega) = B_{n,\alpha}\omega^{\frac{2n}{\alpha}-1}, \quad 0 < \alpha < 2 \tag{17}$$

with

$$B_{n,\alpha} = \frac{2^{2-n}}{\pi^{\frac{n}{2}}\Gamma(\frac{n}{2})\alpha\mathcal{A}_{n,\alpha}^{\frac{n}{\alpha}}} \tag{18}$$

We observe that the state density $\mathcal{D}_{\alpha,n}(\omega)$ scales as $\sim \omega^{\frac{2n}{\alpha}-1}$ with a positive exponent where $0 < n - 1 < \frac{2n}{\alpha} - 1$ depending only on physical dimension n and α. Because of $0 < \alpha < 2$ the scaling exponent of the self-similar density of states (17) is always greater than the exponent $n-1$ of the standard Laplacian which is asymptotically approached by (17) when α approaches the forbidden value $\alpha \to 2$.

4   Conclusions

We have demonstrated in this brief note that the fractional Laplacian can be rigorously defined as the fractional continuum limit by a self-similar linear spring model and its generalization to $n = 1, 2, 3..$ dimensions. In this way a physical justification for the FL is introduced. The model also reveals the interlink between fractal vibrational Weierstrass-Mandelbrot characteristics and its smooth fractional continuum counterpart. The present approach allows to develop a smooth fractional field theory of phenomena with fractal and erratic - chaotic features [8]. Especially noteworthy is a vast potential of applications which include dynamic processes such as anomalous diffusion (Lévi flights), wave propagation and turbulence problems.

References

1. D. Brockmann and L. Hufnagel, Front Propagation in Reaction-Superdiffusion Dynamics: Taming Levy Flights with Fluctuations, Phys. Rev. Lett. 98, 178301 (2007.
2. Z.-Q. Chen, P. Kim, R. Song, Heat kernel estimates for the Dirichlet FL, J. Eur. Math. Soc. 12, 1307-1329 (2008).
3. A. Hanyga, Multi'dimensional solutions of space-time fractional diffusion equations, Proc. R. Soc. Lond. A, 458, 429-450 (2002). doi: 10.1098/rspa.2001.0893
4. G.H. Hardy, Weierstrass's non-differentiable function. In: Trans. Amer. Math. Soc.. Bd. 17, Nr. 3, 1916, S. 301-325, doi:10.1090/S0002-9947-1916-1501044-1.
5. T.M. Michelitsch, G.A. Maugin, F. C. G. A. Nicolleau, A. F. Nowakowski, S. Derogar. Dispersion relations and wave operators in self-similar quasicontinuous linear chains. *Physical Review E* 80, 011135, 2009.
6. T. M. Michelitsch, The self-similar field and its application to a diffusion problem, J. Phys. A: Math. Theor. 44 465206, 2011.

7. T.M. Michelitsch, G.A. Maugin, M. Rahman, S. Derogar, A.F. Nowakowski, F. C. G. A. Nicolleau, A continuum theory for one-dimensional self-similar elasticity and applications to wave propagation and diffusion, European Journal of Applied Mathematics, vol. 23, pp. 709-735, 2012).

8. T.M. Michelitsch, G.A. Maugin, A.F. Nowakowski, F. Nicolleau, The fractional Laplacian as a limiting case of a self-similar spring model and applications to n-dimensional anomalous diffusion. Fractional Calculus and Applied Analysis, Vol. 16, No 4 (2013), pp. 827-859; DOI:10.2478/513540-013-0052-5.

9. H.O. Peitgen, H. Juergens, D. Saupe, Fractals for the Classroom" Part Two, Springer-Verlag, New York, und NCTM, 1992.

10. J. L. Vazquez (2010), Nonlinear Diffusion with Fractional Laplacian Operators. In Nonlinear partial differential equations: the Abel Symposium 2010; Holden, Helge & Karlsen, Kenneth H. eds., Springer, 2012. Pp. 271-298.

Self-organization in the thin gas-sensitive
Ag-containing polyacrylonitrile films

V. Petrov, N. Plugotarenko, T. Semenistaya

Southern Federal University, Rostov-on-Don, Russia
E-mail: plugotarenkonk@sfedu.ru

Abstract: The surface of thin gas-sensitive Ag-containing polyacrylonitrile films is investigated by a method of atomic force microscopy. The assumption of existence in the studied spatial distributed system of signs of the determined chaos is confirmed with calculation of parameters of nonlinear dynamics. The interrelation between extent of self-organization in films of polyacrylonitrile and their gas-sensitive properties is found.
Keywords: electroconductive organic polymers, gas-sensitive materials, self-organization, theory of information, atomic force microscopy

1. Introduction
Nanocomposite films of metallcontaining polyacrylonitrile (PAN), represent an organic matrix, which structure and properties are changed under the influence of various temperatures, and the particles of a modifying additive dispersed in it, are perspective material for gas sensors [1]. Ag-containing PAN films are fabricated by pyrolysis method under the influence of incoherent IR-radiation from film-forming solutions, undergo transition from a liquid state of substance to the solid-state – this stage is process of self-organization of a material. The structure of the disorder material is formed in nonequilibrium conditions, the substance when hardening changes the properties in time and is distributed non-uniformly in space. Thus a spatial ordered structure is formed in the disorder environment [2]. Methods of nonlinear dynamics and theory of information are applied to the analysis of processes of self-organization in structure of materials: surface structure research of materials with various structural organization and revealing long-range correlations in these structures [3]. It is possible to investigate dynamics of system, measuring any of dynamic variables in one point at regular intervals. Thus the look and dimension of an attractor, number of degrees of freedom, correlation and fractal dimensions of a surface, Lyapunov exponents, average mutual information and other parameters of dynamics are defined. These methods which have been originally developed for the research of systems behavior, changing the condition in time, are adapted for studying of the spatial distributed systems what surfaces of the materials are.

2. Results and discussion

For carrying out researches a set of samples of Ag-containing PAN films while using different technological regimes was fabricated.

Sensitivity of the films was evaluated using factor of gas-sensitivity S, which is calculated as:

$$S = (R_o - R_g)/R_o, R_o > R_g,$$

where R_o – value of resistance of a film in air, R_g – value of resistance of a film in the atmosphere of detected gas.

In view of the material surface is a fractal object, general idea of fractal objects is used for its analysis [4].

The Takens method, well-known in the theory of nonlinear systems, is used to research the dynamics of formation of solid phase of gas-sensitive material of PAN films [2]. Patterns of self-organization processes at the formation of disordered materials, which the PAN films are, can be studied by means of the study of their surface, because their surface is a "snapshot" processes of solidification. Proceeding from this, the fractal dimension D_f of Ag-containing PAN films of the surface profile, obtained with scanning probe microscope Solver P47 Pro (NT-MDT) in tapping mode on the air in the size of areas 5×5 mkm^2 was measured. Step of scanning was determined by the choice of the linear dimensions of the scanning area. Surface scan is carried out with the help a fixed number of points $N = 256 \times 256$ regardless of the scanned area. Distribution function of the altitude profile of the surface $\rho = f(h)$ of studied film, begins on some level of h, taken as zero. Using Image Analysis package we processed 65536 points on the surface image of each sample for constructing this feature. This number of points is sufficient to identify the topology of attractor [2]. As a result of measurement of height profile for the samples, which were carried out along the surface through discrete intervals, get a three-dimensional image of the square surface. In the course of the processing of three-dimensional images of square surface areas by using the Image Analysis program received a graph of the distribution function of the height profile. For data processing Grassberger-Prokaččia algorithm was used [2].

The first Lyapunov exponent λ_r was calculated using Wolf's algorithm [5]. Lyapunov exponents are topological invariants that characterize the spatio-temporal evolution and stability of the system: dynamics of formation of solid-state is determined by the spatial-temporal chaos of a small dimension.

The calculation of the average mutual information I (AMI) was carried out by methods of the theory of information, described in [3]. AMI is the main characteristic of the correlations in nonlinear systems. AMI invariant is relative to the different technologies and allows you to evaluate the impact of different technological factors on the structure of the material.

The studies have shown that application of different temperature and time regimes while forming the polymer nanocomposite films and modifying its transition metal with different percentage concentration lead to significant changes in the morphology of its surface.

Fig. 1 presents the image, obtained by AFM measurements of the surface morphology of a sample of Ag-containing PAN film. The distribution function of height profile h (ρ is the density of probability) (Fig.2) and the dependence of the correlation dimension $D = f(log_2 r)$ (Fig. 3) are given too.
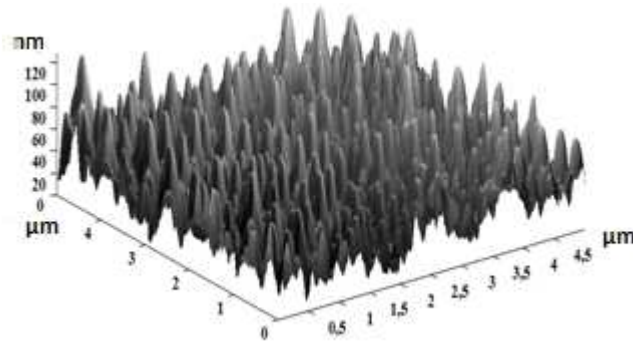

Fig. 1. AFM-image of the surface morphology of Ag-containing PAN film

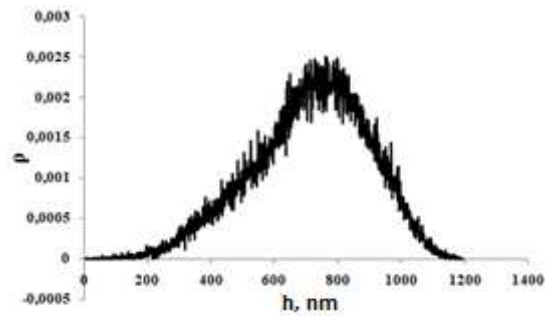Fig. 2. Distribution function of height profile of Ag-containing PAN film
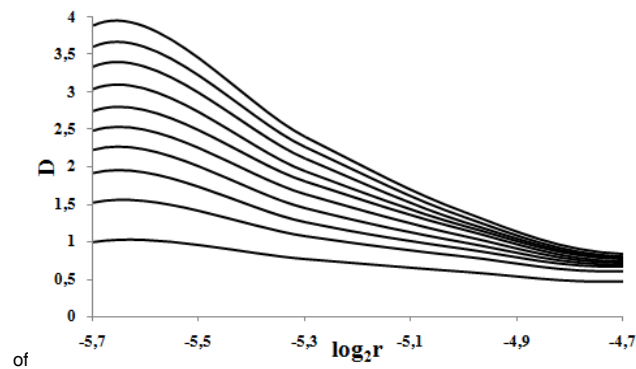

Fig. 3. Dependence $D = f(log_2 r)$ of Ag-containing PAN film

Dependence of correlation dimension $D = f(log_2 r)$ allows to testify the presence or absence of self-organizing structures in nanocomposite materials PAN/Ag. The analysis showed the presence of deterministic chaos in the system. It is noted that the surface of the films with the best gas-sensing properties is formed by three levels of self-similar structures.

The studies of the samples revealed that AMI has rather big range in values. AMI increases with the increase of the height of surface profile of films. The samples with the disordered structure represent hundredths of units in AMI values that correspond to theoretical calculations for the amorphous material. Sufficiently high AMI values are observed in the samples with small value of the height of the surface profile (up to 30 nm) and good gas sensitivity (S = 0,46 ÷ 0,53). High AMI values prove presence of long-range correlations in the system, which may be evidence of order as a result of self-organization processes [3].

The dependence of factor of gas-sensitivity on chlorine (107 ppm) and the dependence of AMI value on mass silver content in PAN films fabricated at the same technological regimes, is resulted on fig. 4. Character of the received dependences is similar. The maximal AMI value corresponds the maximal value of factor of gas-sensitivity.

Thus, the calculation of AMI allows to reveal correlations in disordered materials, which conclude a certain interrelation of electrophysical and gas-sensing properties of PAN/Ag films with its morphology of the surface.
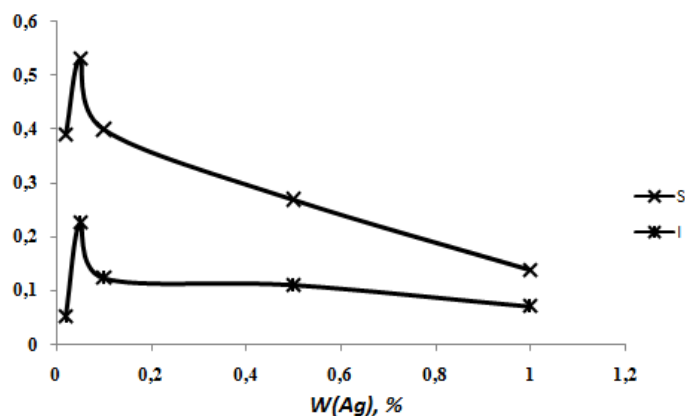

Fig. 4. Dependence of factor of gas-sensitivity (S) and AMI values (I) from silver content by weight in PAN films

For the investigated samples Lyapunov first spatial exponent λ_r which have appeared positive have been calculated. It means, that distribution of substance in space differs from equilibrium. The analysis of Lyapunov exponent testifies, that stability of structure of a material depends on technological parameters of its formation: higher values of temperature of second stage of IR-annealing tend to increase Lyapunov exponent. It is necessary to note absence of correlation

between values of spatial Lyapunov exponent and percentage concentration of the modifying additive in samples.
The results are shown in Table 1.

Table 1. Results of the research the samples of films

The method of film deposition*	The mass content Ag in percent	Sensitivity on Cl_2 (107 ppm)	The correlation dimension	The first Lyapunov exponent	AMI
I	0.1	0.2	1.7	0.0383	0.0898
I	0.02	0.39	1.7 0.9	0.0489	0.0523
C	0.02	0.59	1.6	0.0525	0.1173
I	0.05	0.53	-	-	0.2265
C	0.05	0.63	1.8 1.3 0.7	0.0596	0.0601
I	0.1	0.4	0.8	0.0459	0.1233
I	0.5	0.27	1.4 0.9	0.0415	0.1105
I	1	0.14	0.95 0.65	0.0537	0.0704
C	0.05	0.22	1.1	0.0682	0.1620
C	0.07	0.46	--	--	0.2658

*I – the method of irrigation; C – the centrifugation method

3. Conclusions

The structure of the disorder materials is formed in strongly non-equilibrium conditions with violation of symmetry in the thermodynamically open, non-linear system. These are all the properties inherent in the self-organization. As a result of complex researches the presence of the spatially-ordered structures in the disorder amorphous organic matrix of polymer is confirmed.

During the research it has been established, that greater value of the average mutual information and higher degree of self-organizing answers more ordered structure of the material and the highest values of gas-sensitivity factor.

Thus, on the basis of knowledge of type of dynamics management of nonlinear system of synthesis of a material should be carried out coordinated with internal dynamic processes of substance. It will allow not only to operate effectively the process of growth of the disorder materials, but also to program synthesis of materials for micro - and nanoelectronics with new unique properties.

References

1. Korolev A. N., Semenistaya T.V., Al-Hadrami I. S., Loginova T. P., Bruns M. Nanocomposite copper-containing polyacrylonitrile films: composition, structure, morphology of the surface. // Perspective materials. 2010. №5. P. 52 – 56.

2. Vihrov S.P, Bodyagin N.V., Larina T.G., Mursalov S.M. Processes of height of unregulated semiconductors from positions of theory of self-organization. // Physics and technique of semiconductors. 2005. V. 39. №8. P. 953 – 959.

3. Avacheva T.G., Bodyagin N.V., Vihrov S.P, Mursalov S.M. Research of self-organization of unregulated materials with the use of theory of information. // Physics and technique of semiconductors. 2008. V. 42. №5. P. 513 – 518.

4. Douketis. C., Wang Z., Haslett T. L., Moskovits M. Fractal character of cold-deposited silver films determined by low-temperature scanning tunneling microscopy. // Physical Review B. 1995. V. 51. № 16. P. 11022 – 11031.

5. Wolf A., Swift J.B., Swinney H.L., Vastano J.A. Determining Lyapunov exponents from a time series. // Physica D. 1985. V. 16. P. 285 – 317.

Stochastic Model Reduction for Polynomial Chaos Expansion Using Proper Orthogonal Decomposition

Mehrdad Raisee[1], Dinesh Kumar[2] and Chris Lacor[2]*

[1] Center of Excellence in Design and Optimization of Energy Systems (CEDOES)
   School of Mechanical Engineering, College of Engineering, University of Tehran,
   P.O.Box: 11155-4563, Tehran, IRAN
   (E-mail: `mraisee@ut.ac.ir`)
[2] Fluid Mechanics and Thermodynamics Research Group, Department of
   Mechanical Engineering, Vrije Universiteit Brussel, Pleinlaan 2, 1050 Brussels,
   BELGIUM
   (E-mail: `dkumar@vub.ac.be, chris.lacor@vub.ac.be`)

Abstract. In this paper, a non-intrusive stochastic model reduction scheme is developed for polynomial chaos representation using proper orthogonal decomposition. The main idea is to extract the optimal orthogonal basis via inexpensive calculations on a coarse mesh and then use them for the fine discretization analysis. The developed reduced-order model is implemented to the stochastic steady-state heat diffusion equation. The random conductivity field is approximated via the Karhunen-Loeve (KL) expansion. Input random variables are uniformly distributed so that the Gauss-Legendre quadrature scheme is utilized for the numerical integration. The numerical results showed that the non-intrusive model reduction scheme is able to accurately reproduce mean and variance fields. It is found that the computation-time of the reduced-order model is lower than that of the full-order model.
Keywords: Uncertainty Quantification, Polynomial Chaos, Reduced-order Model.

1   Introduction

In many engineering applications, uncertainty in physical properties, input data and model parameters result in uncertainties in the system output. A representative practical example is design of turbomachineries where uncertainties in flow conditions and small variations in structural parameters of components(e.g. blade profile) can have a significant impact on the performance. For design refinement of such complex mechanical devices, it is necessary to include all uncertainty information in the output results using uncertainty quantification (UQ) schemes. However, many complex applications require a fine 3D

---

* Corresponding Author

computational mesh, small time-step and high-dimensional space for stochastic analysis. This dramatically increases the computational cost which is not desirable for design proposes. Thus, it is necessary to employ efficient numerical schemes for stochastic analysis of complex industrial flows. A variety of different uncertainty quantification methods such as Monte Carlo approach, sensitivity method, perturbation method, regression method and polynomial chaos have been proposed for uncertainty quantification. All of these techniques have positive and negative features, and no single technique is optimum for all situations. Following our previous work on UQ (Dinescu *et al.* [1] and Wang *et al.* [7]), here we employed Polynomial Chaos (PC) approach to model uncertainty propagation. Polynomial chaos methods have been successfully applied to solid mechanics problems by several researches (See for example Ghanem and Spanos [3] and Doostan *et al.* [2]). PC schemes have also been employed for a number of fluid mechanics problems by a number of researchers such as: Walters and Huyse [6], Mathelin *et al.* [4] and Dinescu *et al.* [1]. The polynomial chaos representation can be used for different Probability Density Functions (PDFs) and can be implemented through either intrusive or non-intrusive methods. The intrusive approach requires the modification of the CFD codes and this may be difficult, expensive, and time consuming for many CFD problems. Moreover, the source codes of most commercial CFD softwares are not accessible and thus it is impossible to implement the intrusive PC approach to such softwares. For these reasons, here we focused on non-intrusive PC methodology with uniform PDF for uncertainty quantification. The main shortcoming of all PC methods is the *curse of dimensionality*. Developing efficient reduced-order models for shortening the computational cost associated with the stochastic analysis is of great interest for prediction of complex industrial flows with large number of uncertain parameters. In recent years, several model reduction techniques have been proposed for uncertainty quantification. Two informative examples of such works are: Nouy [5] and Doostan *et al.* [2]. In Nouy [5] a Generalize Spectral Decomposition (GSD) was proposed that gives the reduced basis independent of the stochastic discretization scheme. The GSD implementation to a class of Stochastic Partial Differential Equations (SPDE) leads to drastic computational saving though does not circumvent the curse of dimensionality. Doostan *et al.* [2] proposed an intrusive model reduction technique for chaos representation of a SPDE to tackle the curse of dimensionality. A 2D test case from solid mechanics is chosen to illustrate the accuracy and convergence of the model.

In this work, a non-intrusive reduced-order technique is developed and applied to the 2D steady-state stochastic heat diffusion equation. This paper is organized as follows. In Section 2 we present the details of mathematical formulation and problem under investigation. In Section 3, the model reduction methodology is described. Finally, in Section 4 the numerical results are presented and discussed.

2   Mathematical Formulation

To demonstrate the non-intrusive stochastic model reduction algorithm, 2D steady-state stochastic heat conduction in a square plate of side $2a$ is considered (see Figure 1). The 2D heat diffusion with random thermal conductivity is described by the following SPDE:

$$\frac{\partial}{\partial x}(k(x,y;\zeta)\frac{\partial T}{\partial x}) + \frac{\partial}{\partial y}(k(x,y;\zeta)\frac{\partial T}{\partial y}) = 0 \tag{1}$$

As shown in Figure (1), the top boundary of the plate is at hot temperature
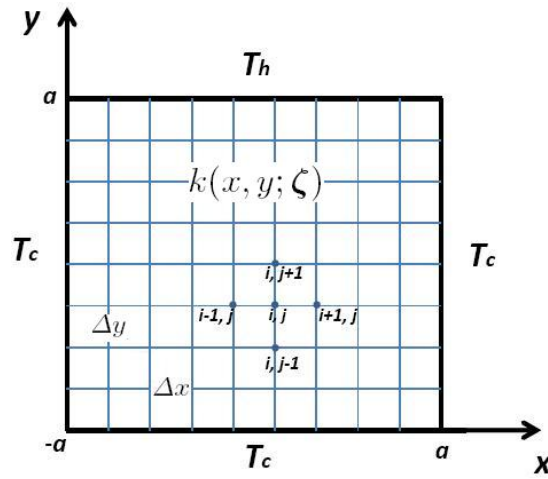

Fig. 1. Schematic of computational domain.

T_h whilst the side and bottom boundaries of the plate are at cold temperature T_c. The thermal conductivity of the plate, $k(x,y;\zeta)$, is assumed to be a two-dimensional homogeneous random process with known mean $\bar{k}(x,y)$ and known covariance function:

$$R(x_1,y_1;x_2,y_2) = \sigma_k{}^2 e^{-|x_1-x_2|/b_x - |y_1-y_2|/b_y} \tag{2}$$

where b_x and b_y are the correlation lengths in x and y directions, respectively, and σ_k is the standard deviation on the thermal conductivity.

A key ingredient here is the representation of stochastic thermal conductivity field as a Karhunen-Loeve (KL) expansion, a type of Fourier expansion for random functions, which amounts to a discretization in the space of random events. According to the KL expansion, the eigenvalues and eigenfunctions are obtained by solving the following 2D integral equation:

$$\int_D R(x_1,y_1;x_2,y_2)\phi_n(x_2,y_2)dx_2dy_2 = \lambda_n\phi_n(x_1,y_1) \tag{3}$$

Separation of kernel (2) as $R(x_1,y_1;x_2,y_2) = \sigma_k{}^2 e^{-|x_1-x_2|/b_x}.e^{-|y_1-y_2|/b_y}$ and substitution in (3) leads to two identical 1D integral eigenvalue equations in

x and y directions. Solution of the integral equations give eigenvalues (i.e. $\lambda_i^{(x)}$ and $\lambda_j^{(y)}$) and their corresponding eigenfunctions (i.e. $\phi_i^{(x)}$ and $\phi_j^{(y)}$). As described in Ghanem and Spanos [3], the complete form of KL expansion for random process $k(x, y; \boldsymbol{\zeta})$ is:

$$k(x, y; \boldsymbol{\zeta}) = \bar{k}(x, y) + \sum_{i=1}^{\infty} \sum_{j=1}^{\infty} \left\{ \sqrt{\lambda_i^{(x)} \lambda_j^{(y)}} \zeta_{i,j} \frac{1}{\sqrt{2}} [\phi_i^{(x)}(x) \phi_j^{(y)}(y) + \phi_j^{(x)}(x) \phi_i^{(y)}(y)] \right\}$$

(4)

Having obtained an analytical expression for the thermal conductivity, the SPDE (Equation (1)) is discretized using an explicit central differencing scheme in a uniform grid ($\Delta x = \Delta y$), see Figure 1. Thus, for any set of $\boldsymbol{\zeta} \equiv \{\zeta_i\}_{i=1}^n$, first thermal conductivity is calculated in the computational domain using KL expression (Equation (4)). Then, the new temperature T^{n+1} at grid node (i, j) is obtained from old nodal temperature T^n of neighbouring nodes. The solution is converged when the maximum error between the old and new temperature values is sufficiently small($\epsilon \simeq 10^{-9}$).

3   Model Reduction Methodology

In the classical polynomial chaos expansion, the random temperature field $T(x, y; \boldsymbol{\zeta})$ can be decomposed into deterministic and stochastic components. The PC representation of temperature field of order p for n random variable $\boldsymbol{\zeta} \equiv \{\zeta_i\}_{i=1}^n$ can be written as:

$$T(x, y; \boldsymbol{\zeta}) - < T(x, y) > = \sum_{i=1}^{P} T_i(x, y) \psi_i(\boldsymbol{\zeta})$$

(5)

where the total number of terms are $P + 1 = (p + n)!/p!n!$ and the mean value of $T(x, y; \boldsymbol{\zeta})$ is expressed as:

$$< T(x, y) > = \int_{\omega} T(x, y; \boldsymbol{\zeta}) f(\boldsymbol{\zeta}) d\boldsymbol{\zeta}$$

(6)

In the above equation, f is Probability Density Function (PDF). Here we assumed random variables are uniformly distributed over interval [-1,1] and thus the PDF is $f = 1/2^n$ for n random variables $\{\zeta_i\}_{i=1}^n$. The non-intrusive method uses spectral projection to find the PC expansion coefficients $T_i(x, y)$ in Equation (5). Projecting Equation (5) onto the kth basis and use of orthogonality gives:

$$T_i(x, y) = \frac{1}{< \psi_i^2(\boldsymbol{\zeta}) >} \int_{\omega} T(x, y; \boldsymbol{\zeta}) \psi_i(\boldsymbol{\zeta}) f(\boldsymbol{\zeta}) d\boldsymbol{\zeta}$$

(7)

The objective of the spectral projection method is to compute the polynomial coefficients by evaluating numerator in Equation (7) numerically, while the

dominator can be computed analytically for multi-variant orthogonal polynomials. Here we used the n-dimensional *Gauss-Legendre quadrature* to compute the projection integrals in Equation (7) as:

$$T_i(x,y) = \frac{1}{<\psi_i^2(\boldsymbol{\zeta})>} \sum_{i_1=1}^{q} ... \sum_{i_n=1}^{q} (w_1^{i_1} \otimes ... \otimes w_n^{i_n}) T(x,y;\zeta_1^{i_1},..,\zeta_n^{i_n})$$

$$\psi_i(\zeta_1^{i_1},..,\zeta_n^{i_n}) f(\zeta_1^{i_1},..,\zeta_n^{i_n}) \tag{8}$$

where $(\boldsymbol{\zeta}^k, \boldsymbol{w}^k)$, $k = 1, 2, .., q$ are the one-dimensional (1D) Gauss-Legendre integration points and weights.

The above classical expansion dose not represent an optimal PC representation of $T(x,y,\boldsymbol{\zeta})$. To find the optimal PC expansion one can consider the fact that spatial discretization errors and random discretization errors may be decoupled. Therefore, one can minimize the random discretization errors on the coarse grid and then solve the real physical problem on a fine mesh by using limited number of optimal random basis $\{z_i\}_{i=1}^{m}$ (obtained in the coarse grid analysis) where m is the number of dominated eigenvalues. The first step in the model reduction scheme is to find optimal PC basis using POD; a well-known procedure for extracting a basis for a model decomposition from an ensemble of realizations. To this end, suppose in a coarse grid, expression (9) represents an optimal PC expansion of the stochastic temperature field $T(x,y,\boldsymbol{\zeta})$;

$$T(x,y;\boldsymbol{\zeta})- < T(x,y) >= \sum_{i=1}^{m} T^i(x,y) z_i(\boldsymbol{\zeta}) \tag{9}$$

Now in the coarse grid, the covariance function $C(x_1,y_1;x_2,y_2)$ of temperature field can be obtained from:

$$C(x_1,y_1;x_2,y_2) = \sum_{i=1}^{P} T_i(x_1,y_1) T_i(x_2,y_2) < \psi_i^2 > \tag{10}$$

The corresponding eigenvalues ν_i and eigenfunctions $\phi_i(x,y)$ are the solution of the following eigenvalue problem:

$$\int_D C(x_1,y_1;x_2,y_2)\phi_i(x_2,y_2)dx_2 dy_2 = \nu_i \phi_i(x_1,y_1) \tag{11}$$

The upper limit m in the Equation (9) can be found by the size of dominant eigenspace (10) such that $\sum_{i=1}^{m}\nu_i/\sum_i \nu_i \geq 0.99$.

Having obtained $T_i(x,y)$ from classical PC on the coarse grid and eigenfunctions $\phi_i(x,y)$ from the solution of eigenvalue problem (11), the set of optimal basis $\{z_i\}_{i=1}^{m}$ can be now represented as a linear combination of the set of classical polynomial chaos; $\{\psi_i\}_{i=1}^{P}$ using the following scalar product:

$$z_i(\boldsymbol{\zeta}) = [T(x,y;\boldsymbol{\zeta})- < T(x,y) >, \phi_i(x,y)] = \sum_{j=1}^{P} \alpha_{ij}\psi_j(\boldsymbol{\zeta}) \tag{12}$$

The scalar product of functions v and w is defined as: $[v,w] = \int_x v.w dx$.

where coefficient α_{lj} are obtained via the scalar product:

$$\alpha_{ij} = \int_R T_j(x,y)\phi_i(x,y)d\overrightarrow{x}d\overrightarrow{y} \tag{13}$$

One now dose the classical polynomial chaos on a fine mesh, where z_i are used instead of ψ_i. For $1 \leq i \leq m$, the coefficients in expansion (9) are obtained from:

$$T^i(x,y) = \frac{< T(x,y;\zeta), z_i >}{< z_i, z_i >} = \frac{1}{\nu_i}\sum_{j=1}^{P} \alpha_{ij} < T(x,y;\boldsymbol{\zeta}), \psi_j > \tag{14}$$

4   Results and Discussion

We now examine the performance of the reduced-order model by analyzing the 2D steady-state heat conduction equation. It is assumed that the top wall is at $T_h = 300°C$ and side and bottom walls at $T_c = 100°C$.   First, a 2D KL expansion is performed using the exponential kernel with a standard deviation of $\sigma_k = 1.0\ W/m.K$ and correlation lengths of $b_x = b_y = 10.0\ m$. The mean thermal conductivity is assumed to be $\bar{k} = 5.0\ W/m.K$. The first six largest terms in the KL expansions are chosen for further analysis.

Figures 2 and 3 respectively show the distributions of eigenvalues and $\mid \alpha_{ij} \mid$ coefficients obtained from the coarse discretization analysis on a 5×5 mesh when a second-order Legendre polynomial ($p = 2$) is employed. From these figures it can be concluded that only two ($m = 2$) basis functions (i.e. z_1 and z_2) are adequate for the fine discretization analysis. Thus, fine discretization analysis is performed using the new z_1 and z_2 basis functions on a 41×41 mesh. The computed mean and variance fields using full- and reduced-order models are compared in Figure 4. It is visible the fine grid computations via reduced- and full-order models resulted in identical results for the mean temperature field. Moreover, full- and reduced-order analysis on the fine mesh produced very similar variance fields. In Figure 4(f), regions of high absolute relative error (about 10%) are visible in the top corners of the domain. This error can be reduced by considering more basis functions (e.g. z_3) in the PC expansion but the reduced-order computational cost will also increase.

The ratio of computation-time for the reduced-order analysis to the time needed for the full-order calculation using five fine meshes of 21×21, 26×26, 31×31, 36×36 and 41×41 is shown in Figure 5. A coarse mesh with 10×10 grid nodes is used for the coarse grid analysis. This figure shows that for the present problem with six random variables, the reduced-order model is less expensive than the full-order model when a 21×21 mesh is used. By increasing the size of the fine mesh to 26×26 the advantage of the reduced-order model over the standard PC becomes more evident. It is seen that with the reduced-order model about 20% saving in CPU-time can be obtained when a mesh with 41×41 nodes is used for the fine scale discretization. Further saving in the CPU-time may be achieved by combination of the current reduced-order model with other efficient numerical schemes such as for example sparse sampling schemes for the stochastic discretization and multi-grid methods for the spatial discretization.
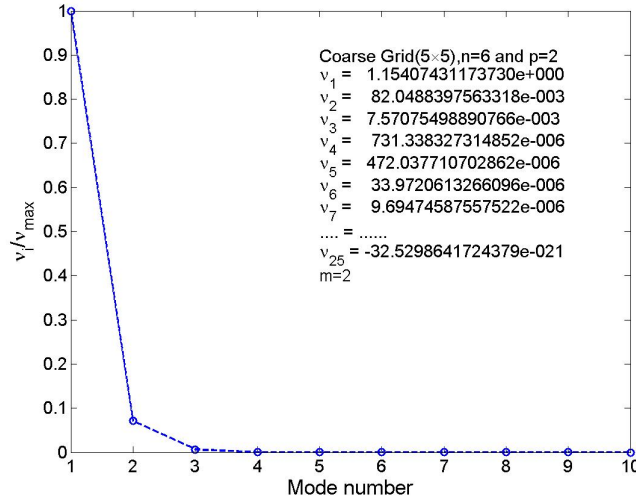
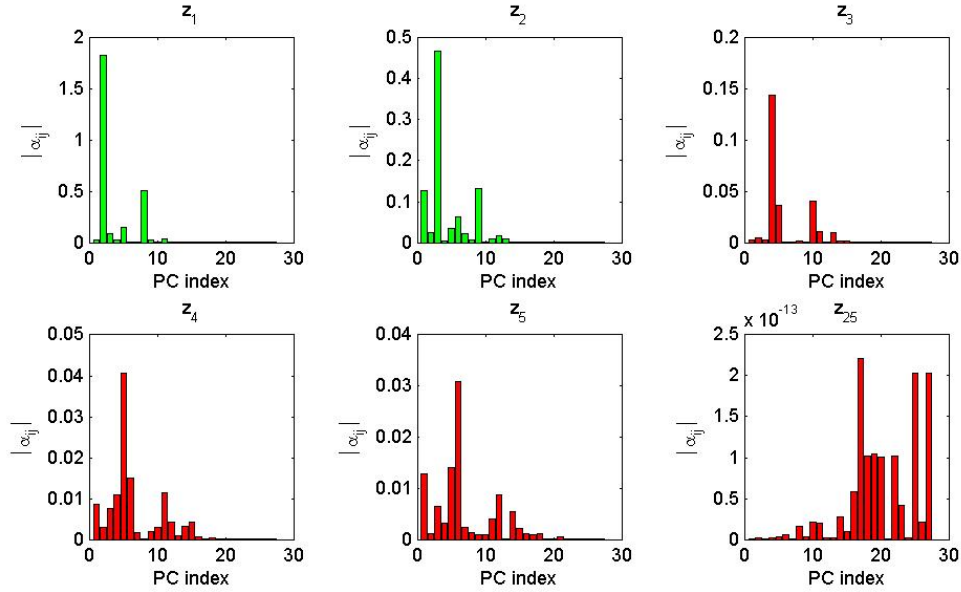**Fig. 2.** Computed eigenvalues using coarse discretization analysis.

Fig. 3. Computed $\mid \alpha_{ij} \mid$ using coarse discretization analysis.

Conclusion

In this paper, a non-intrusive model reduction technique for PC expansion is presented and discussed. The reduced-order model is applied to the 2D steady-state heat diffusion equation. Distributions of mean and variance obtained from the reduced-order model are compared with those of full-order model. The numerical results show that the developed reduced-order model is able to
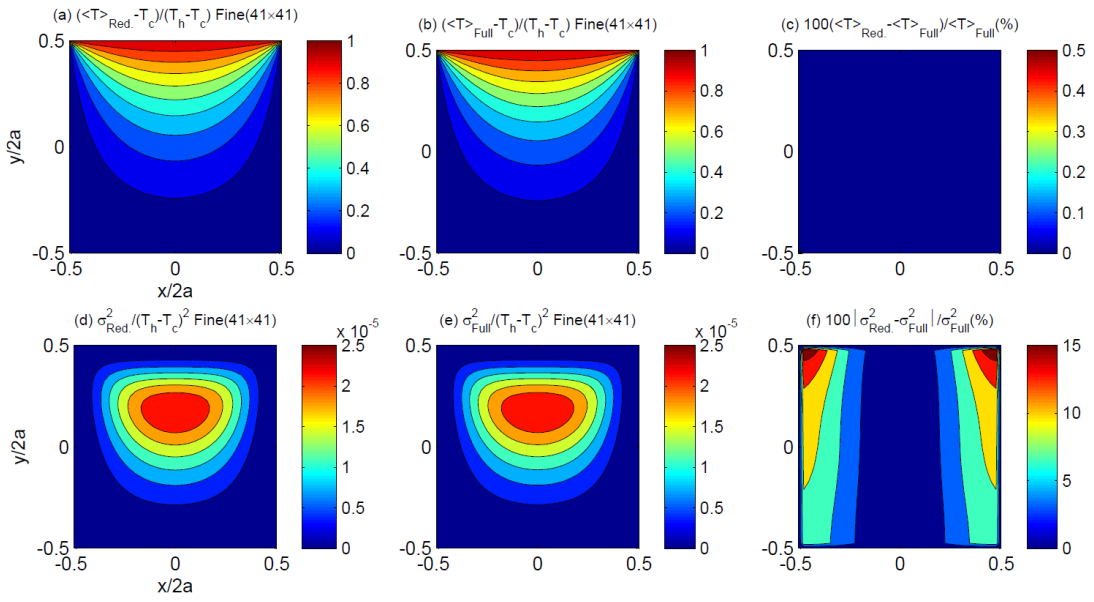
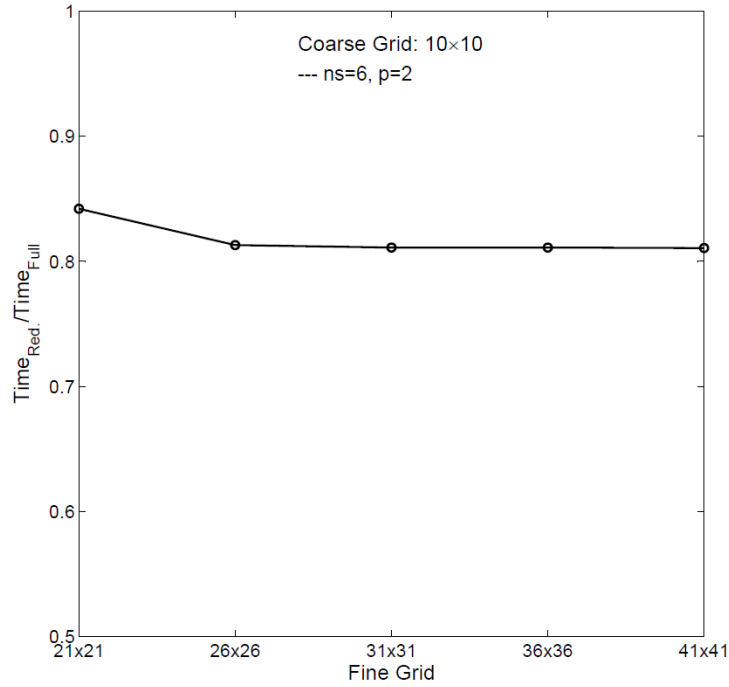**Fig. 4.** Comparison of mean and variance fields.

Fig. 5. Ratio of reduced-order computation-time to the full-order computation-time.

produce acceptable results for such statistical quantities. Computation-time of the reduced-order model is found to be lower than that of the full-order model.

Acknowledgment

References

1. C. Dinescu, S. Smirnov, Ch. Hirsch, and C. Lacor. Assessment of intrusive and non-intrusive non-deterministic CFD methodologies based on polynomial chaos expansions. *Int. J. of Eng. Systems Modeling and Simulation*, 2:87-98, 2010.
2. A. Doostan, R. Ghanem, and J. Red-Horse. Stochastic model reduction for chaos representations. *Comp. Meth. in Appl. Mech. and Eng.*, 196:3951-3966, 2007.
3. R. Ghanem, and O. Spanos. Stochastic Finite Elements: A Spectral Approach, 1991, Springer Verlag.
4. L. Mathelin, M. Y. Hussaini, and T. A. Zang. Stochastic approaches to uncertainty quantification in CFD simulations. *Numer. Algorithms*, 38:209-236, 2007.
5. A. Nouy. A generalized spectral decomposition technique to solve a class of linear stochastic partial differential equations. *Comp. Meth. in Appl. Mech. and Eng.*, 196:4521-4537, 2007.
6. R. W. Walters, and L. Huyse. Uncertainty analysis for fluid mechanics with applications. NASA/CR 2002-211449.
7. X. Wang, Ch. Hirsch, Z. Liu, S. Kang, and C. Lacor. Uncertainty-based robust aerodynamic optimization of rotor blades. *Int. J. Numer. Meth. Eng.*, 94:111-127, 2013.

Exponential dichotomy and bounded solutions of the Schr*ö*dinger equation

Oleksander A. Pokutnyi[1]

Institute of mathematics of NAS of Ukraine, , 01601 Kiev, Ukraine
(E-mail: `lenasas@gmail.com`)

Abstract. Necessary and sufficient conditions for existence of bounded on the entire real axis solutions of Schrödinger equation are obtained under assumption that the homogeneous equation admits an exponential dichotomy on the semi-axes. Bounded analytical solutions are represented using generalized Green's operator.

Keywords: exponential dichotomy, normally-resolvable operator, pseudoinverse Moore-Penrose operator.

Numerous papers deal with problems of the existence of bounded solutions of linear and nonlinear differential equations in Banach spaces and condition of exponential dichotomy on both semi-axes. We note the well-known paper [1], where such problems were considered in finite-dimensional spaces. Boundary value problems for linear differential equations in Banach spaces which admit exponential dichotomy on both semi-axes with bounded and unbounded operators in linear part was investigated in [2], [3]. The normal solvability of a differential operator was considered in [4]. The present paper dealt with the derivation of necessary and sufficient conditions for the existence of generalized bounded solutions of the Schrödinger equation in the Hilbert space.

1 Linear case

1.1 Statement of the Problem

Consider the next differential Shrödinger equation

$$\frac{d\varphi(t)}{dt} = -iH(t)\varphi(t) + f(t), t \in J \tag{1}$$

in a Hilbert space $\mathcal{H}$, where, for each $t \in J \subset R$, the unbounded operator $H(t)$ has the form $H(t) = H_0 + V(t)$ (here $H_0 = H_0^*$ is unbounded self-adjoint operator with domain $D = D(H_0) \subset \mathcal{H}$), the mapping $t \to V(t)$ is strongly continuous. Define as in [5] operator-valued function

$$\tilde{V}(t) = e^{itH_0}V(t)e^{-itH_0}.$$

In this case for $\tilde{V}(t)$ Dyson's [5, p.311] representation is true and its propagator we define as $\tilde{U}(t,s)$. If $U(t,s) = e^{-itH_0}\tilde{U}(t,s)e^{isH_0}$ then $\psi_s(t) = U(t,s)\psi$ is a weak solution of (1) with condition $\psi_s(s) = \psi$ in the sense that for any $\eta \in D(H_0)$ function $(\eta, \psi_s(t))$ is differentiable and

$$\frac{d}{dt}(\eta, \psi_s(t)) = -i(H_0\eta, \psi_s(t)) - i(V(t)\eta, \psi_s(t)), t \in J.$$

The present part dealt with the derivation of necessary and sufficient conditions for the existence of weak (in different senses) bounded solutions of the inhomogeneous equation (1) with $f \in BC(J, H) = \{f : J \to \mathcal{H};$ the function f is continuous and bounded $\}$. Here the boundedness is treated in the sense that $|||f||| = sup_{t \in J}||f(t)|| < \infty$. For simplicity we suppose that D dense in $\mathcal{H}$. The operator $U(t,s)$ is a bounded linear operator for fixed t, s, and since the set D is dense in $\mathcal{H}$, we find that it can be extended to the entire space $\mathcal{H}$ by continuity, which is assumed in forthcoming considerations. The extension of the family of evolution operators to the entire space is denoted in the same way.

1.2   Bounded solutions

Throughout the following, we use the notion of exponential dichotomy in the sense of [6]. It is of special interest to analyze the exponential dichotomy on the half-lines $R_s^- = (-\infty, s]$ and $R_s^+ = [s; \infty)$. [In this case, the projection-valued functions defined on half-lines will be denoted by $P_-(t)$ for all $t \geq s$ and $P_+(t)$ for all $t < s$ with constants M_1, α_1 and M_2, α_2, respectively (α_1, α_2 - entropy or Lyapunov coefficients on the half-lines).] Most of the results obtained below follows directly from [3]. The main result of this section can be stated as follows.

Theorem 1. *Let $\{U(t,s), t \geq s \in R\}$ be the family of strongly continuous evolution operators associated with equation (1). Suppose that the following conditions are satisfied.*

1. The operator $U(t,s)$ admits exponential dichotomy on the half-lines R_0^+ and R_0^- with projection-valued operator-functions $P_+(t)$ and $P_-(t)$, respectively.

2. The operator $D = P_+(0) - (I - P_-(0))$ is generalized-invertible.

Then the following assertions hold.

1. There exist weak solutions of equation (1) bounded on the entire line if and only if the vector function $f \in BC(R, \mathcal{H})$ satisfies the condition

$$\int_{-\infty}^{+\infty} H(t)f(t)dt = 0, \tag{2}$$

where $H(t) = \mathcal{P}_{N(D^*)}P_-(0)U(0,t)$.

2. Under condition (2), the weak solutions of (1) bounded on the entire line have the form

$$\varphi_0(t,c) = U(t,0)P_+(0)\mathcal{P}_{N(D)}c + (G[f])(t,0)\forall c \in \mathcal{H}, \tag{3}$$

where

$$(G[f])(t,s) = \begin{cases} \int_s^t U(t,\tau)P_+(\tau)f(\tau)d\tau - \int_t^{+\infty} U(t,\tau)(I - P_+(\tau))f(\tau)d\tau + \\ \quad + U(t,s)P_+(s)D^+[\int_s^\infty U(s,\tau)(I - P_+(\tau))f(\tau)d\tau + \\ \quad + \int_{-\infty}^s U(s,\tau)P_-(\tau)f(\tau)d\tau], \quad t \geq s \\ \int_{-\infty}^t U(t,\tau)P_-(\tau)f(\tau)d\tau - \int_t^s U(t,\tau)(I - P_-(\tau))f(\tau)d\tau + \\ \quad + U(t,s)(I - P_-(s))D^+[\int_s^\infty U(s,\tau)(I - P_+(\tau))f(\tau)d\tau + \\ \quad + \int_{-\infty}^s U(s,\tau)P_-(\tau)f(\tau)d\tau], \quad s \geq t \end{cases}$$

is the generalized Green operator of the problem on the bounded, on the entire line, solutions

$$(G[f])(0+,0) - (G[f])(0-,0) = - \int_{-\infty}^{+\infty} H(t)f(t)dt;$$

$$\mathcal{L}(G[f])(t,0) = f(t), \quad t \in R$$

and

$$(\mathcal{L}x)(t) = \frac{dx}{dt} - iH(t)x(t),$$

D^+ *is the Moore-Penrouse pseudoinverse operator to the operator* D; $\mathcal{P}_{N(D)} = I - D^+D$ *and* $\mathcal{P}_{N(D^*)} = I - DD^+$ *are the projections [7] onto the kernel and cokernel of the operator* D.

Remark 1. A similar theorem holds for the case in which the family of evolution operators $U(t,s)$ admits exponential dichotomy on the half-lines R_s^+ and R_s^-.

Now we show that condition 2 in theorem 1 can be omitted and in the different senses equation (1) is always resolvable. From the proof of the theorem 1 follows that equation (1) have bounded solutions if and only if the operator equation

$$D\xi = g, \tag{4}$$

$$g = \int_{-\infty}^0 U(0,\tau)P_-(\tau)f(\tau)d\tau + \int_0^{+\infty} U(0,\tau)(I - P_+(\tau))f(\tau)d\tau$$

is resolvable and its number depends from the dimension of $N(D)$.

Consider next 3 cases.

1) Classical strong generalized solutions.

Consider case when the operator D is normally-resolvable ($R(D) = \overline{R(D)}$ is the set of values of D). Then [7] $g \in R(D)$ if and only if $\mathcal{P}_{N(D^*)}g = 0$ and the set of solutions of (4) can be represented in the form [7] $\xi = D^+g + \mathcal{P}_{N(D)}c, for all c \in \mathcal{H}$.

2) Strong generalized solutions.

Consider the case when $R(D) \neq \overline{R(D)}$. We show that operator D may be extended to $\overline{D}$ in such way that $R(\overline{D})$ is closed.

Since the operator D is bounded the next representations of $\mathcal{H}$ in the direct sum are true

$$H = N(D) \oplus X, \mathcal{H} = \overline{R(D)} \oplus Y,$$

with $X = N(D)^\perp$ and $Y = \overline{R(D)}^\perp$. Let $E = H/N(D)$ is quotient space of $\mathcal{H}$ and $\mathcal{P}_{\overline{R(D)}}$ is orthoprojector, which projects onto $\overline{R(D)}$. Then operator

$$\mathcal{D} = \mathcal{P}_{\overline{R(D)}} D j^{-1} p : X \to R(D) \subset \overline{R(D)},$$

is linear, continuous and injective (here $p : X \to E$ is continuous bijection and $j : \mathcal{H} \to E$ is a projection. The triple $(\mathcal{H}, E, j)$ is a locally trivial bundle with typical fiber $\mathcal{P}_{N(L)} H$). In this case [8, p.26,29] we can define strong generalized solution of equation

$$\mathcal{D}\xi = g, \xi \in X.$$

We complete the space X with the norm $||\xi||_{\overline{X}} = ||\mathcal{D}\xi||_F$, where $F = \overline{R(D)}$ [8]. Then the extended operator

$$\overline{\mathcal{D}} : \overline{X} \to \overline{R(D)}, X \subset \overline{X}$$

is a homeomorphism of $\overline{X}$ and $\overline{R(D)}$. Operator $\overline{D} := \overline{\mathcal{D}} \mathcal{P}_{\overline{X}} : \overline{\mathcal{H}} \to \mathcal{H}$ is normally-resolvable. By the construction of a strong generalized solution [8], the equation

$$\overline{D}\,\overline{\xi} = g,$$

has a unique generalized solution, which we denote $\overline{D}^+ g$ which is called the strong generalized solution of (4). Then the set of strong generalized solutions of (4) has the form

$$\xi = \overline{D}^+ g + \mathcal{P}_{N(D)} c, \, for \, all \, c \in \mathcal{H}.$$

3) Strong pseudosolutions.

Consider an element $g \notin \overline{R(D)}$. This condition is equivalent $\mathcal{P}_{N(D^*)} g \neq 0$. In this case there are elements from $\overline{\mathcal{H}}$ that minimize norm $||\overline{D}\xi - g||_{\overline{\mathcal{H}}}$ for $\xi \in \overline{\mathcal{H}}$:

$$\xi = \overline{D}^+ g + \mathcal{P}_{N(D)} c, \, for \, all \, c \in \mathcal{H}.$$

These elements are called strong pseudosolutions by analogy of [7].

Remark 2. It should be noted that in each cases 1) - 3) the form of bounded solutions (4) isn't change.

Remark 3. As follows from 1) and 3) the notion of exponential dichotomy is equivalent of existence of bounded on the entire real axis solutions of (1).

2   Main result (Nonlinear case)

In the Hilbert space $\mathcal{H}$, consider the differential equation

$$\frac{d\varphi(t)}{dt} = -iH(t)\varphi(t) + \varepsilon Z(\varphi, t, \varepsilon) + f(t). \tag{5}$$

We seek a bounded solution $\varphi(t, \varepsilon)$ of equation (5) that becomes one of the solutions of the generating equation (1) for $\varepsilon = 0$.

To find a necessary condition on the operator function $Z(\varphi, t, \varepsilon)$, we impose the joint constraints

$$Z(\cdot, \cdot, \cdot) \in C[\|\varphi - \varphi_0\| \leq q] \times BC(R, \mathcal{H}) \times C[0, \varepsilon_0],$$

where q is some positive constant.

Let us show that this problem can be solved with the use of the operator equation for generating constants

$$F(c) = \int_{-\infty}^{+\infty} H(t) Z(\varphi_0(t, c), t, 0) = 0. \tag{6}$$

Theorem 2 (necessary condition). Let the equation (1) admits exponential dichotomy on the half-lines R_0^+ and R_0^- with projection-valued operator functions $P_+(t)$ and $P_-(t)$, respectively, and let the nonlinear equation (5) have a bounded solution $\varphi(\cdot, \varepsilon)$ that becomes one of the solutions of the generating equation (1) with constant $c = c^0$, $\varphi(t, 0) = \varphi_0(t, c^0)$ for $\varepsilon = 0$. Then this constant should satisfy the equation for generating constants (6).

The proof of this theorem is the same as in [3, Theorem 1].

To find a sufficient condition for the existence of bounded solutions of (1), we additionally assume that the operator function $Z(\varphi, t, \varepsilon)$ is strongly differentiable in a neighborhood of the generating solution ($Z(\cdot, t, \varepsilon) \in C^1[\|\varphi - \varphi_0\| \leq q]$).

This problem can be solved with the use of the operator

$$B_0 = \int_{-\infty}^{+\infty} H(t) A_1(t) U(t, 0) P_+(0) \mathcal{P}_{N(D)} dt : \mathcal{H} \to \mathcal{H},$$

where $A_1(t) = Z^1(v, t, \varepsilon)|_{v = \varphi_0, \varepsilon = 0}$ (the Fréchet derivative).

Theorem 3 (sufficient condition). Suppose that the equation (1) admits exponential dichotomy on the half-lines R_0^+ and R_0^- with projection-valued functions $P_+(t)$ and $P_-(t)$, respectively. In addition, let the operator B_0 satisfy the following conditions.

1. The operator B_0 is Moore-Penrose pseudoinvertible.
2. $\mathcal{P}_{N(B_0^*)} \mathcal{P}_{N(D^*)} P_-(0) = 0$.

Then for an arbitrary element of $c = c^0 \in \mathcal{H}$ satisfying the equation for generating constants (6), there is exists bounded solution. This solution can be found with the use of the iterative process

$$\overline{y}_{k+1}(t, \varepsilon) = \varepsilon G[Z(\varphi_0(\tau, c^0 + y_k, \tau, \varepsilon))](t, 0),$$

$$c_k = -B_0^+ \int_{-\infty}^{+\infty} H(\tau)\{A_1(\tau)\overline{y}_k(\tau, \varepsilon) + \mathcal{R}(y_k(\tau, \varepsilon), \tau, \varepsilon)\} d\tau,$$

$$\mathcal{R}(y_k(t, \varepsilon)) = Z(\varphi_0(t, c^0) + y_k(t, \varepsilon), t, \varepsilon) - Z(\varphi_0(t, c^0), t, 0) - A_1(t) y_k(t, \varepsilon),$$

$$\mathcal{R}(0, t, 0) = 0, \qquad \mathcal{R}_x^{(1)}(0, t, 0) = 0,$$

$$y_{k+1}(t, \varepsilon) = U(t, 0) P_+(0) \mathcal{P}_{N(D)} c_k + \overline{y}_{k+1}(t, 0, \varepsilon),$$

$$\varphi_k(t, \varepsilon) = \varphi_0(t, c^0) + y_k(t, \varepsilon), \quad k = 0, 1, 2, ..., \quad y_0(t, \varepsilon) = 0, \quad \varphi(t, \varepsilon) = \lim_{k \to \infty} \varphi_k(t, \varepsilon).$$

2.1   Relationship between necessary and sufficient conditions

First, we formulate the following assertion.

Corollary. *Let a functional $F(c)$ have the Fréchet derivative $F^{(1)}(c)$ for each element c^0 of the Hilbert space $\mathcal{H}$ satisfying the equation for generating constants (6). If $F^1(c)$ has a bounded inverse, then equation (5) has a unique bounded solution on the entire line for each c^0.*

Remark 4. If assumptions of the corollary are satisfied, then it follows from its proof that the operators B_0 and $F^{(1)}(c^0)$ are equal. Since the operator $F^{(1)}(c)$ is invertible, it follows that assumptions 1 and 2 of Theorem 3 are necessarily satisfied for the operator B_0. In this case, equation (5) has a unique bounded solution for each $c^0 \in \mathcal{H}$. Therefore, the invertibility condition for the operator $F^1(c)$ relates the necessary and sufficient conditions. In the finite-dimensional case, the condition of invertibility of the operator $F^{(1)}(c)$ is equivalent to the condition of simplicity of the root c^0 of the equation for generating amplitudes [7].

In such way we obtain the modification of the well-known method of Lyapunov-Schmidt. It should be emphasized that theorem 2 and 3 give us possible condition of chaotic behavior of (5) [9].

References

1. *K. J. Palmer.* Exponential dichotomies and transversal homoclinic points. J. Different. Equat. **55**.-1984. P. 225–256.

2. *Boichuk A.A., Pokutnyi O.A.* Dichotomy and boundary value problems on the whole line. - Proceedings, 5th Chaotic Modeling and Simulation International Conference, 12-15 June 2012, Athens Greece. - p.81-89.

3. *Pokutnyi A.A.* Bounded solutions of linear and weakly nonlinear differential equations in a Banach space with unbounded operator in the linear part. Differential equations (in Russian), 2012, vol.48, No.6 - pp.803-813.

4. *A. A. Boichuk and A.A. Pokutnij.* Bounded solutions of linear differential equations in Banach space. *Nonlinear Oscillations,* **9**, no 1. - 2006. - P. 3-14; http://www.springer.com/.

5. *Reed M., Symon B.* Methods of modern mathematical physics: in 4 vol. - .:World, 1978. - v.2: Harmonic analysis. Selfadjointness. - 1978. – 395p.(in Russian)

6. *Henry D.* Geometric theory of semilinear parabolic equations. - .:Mir, 1985. - 376p.(in Russian)

7. *Boichuk A.A., Samoilenko A.M.* Generalized Inverse Operators and Fredholm Boundary Value Problems. – VSP, Utrecht-Boston, 2004. – 317 p.

8. *Klyushin D.A., Lyashko S.I., Nomirovskii D.A., Petunin Yu. I., Semenov V.V.* Generalized Solutions of Operator Equations and Extreme Elements. Springer, 2012. 202+xxi p.

9. *Chueshov I.D.* Introduction to the theory of infinite-dimensional dissipative systems. Acta, 2002. - 416p.

Stability and bifurcation in a two species predator-prey model with quintic interactions

I. Kusbeyzi Aybar[1] and I. Hacinliyan[2]

[1] Department of Computer Education and Instructional Technology, Yeditepe University, 26 August Campus, Kayisdagi Street, Istanbul, 34755, Turkey
(E-mail: `ikusbeyzi@yeditepe.edu.tr`)
[2] Department of Mathematics, Istanbul Technical University, Maslak, Istanbul, 34469, Turkey
(E-mail: `hacinliy@itu.edu.tr`)

Abstract. In this work, the generalization of Lotka-Volterra model including the addition of symmetrically coupled quintic polynomial interaction is analyzed. Stability and bifurcation properties of this model are studied. It is also shown that the model has a family of limit cycles bifurcating from the Hopf points by using a numerical method.
Keywords: Predator-Prey Models, Stability, Bifurcation Analysis.

1 Introduction

Predator-prey problem attempts to model the relationship between the populations of two or more species in interaction. The simplest model of predator-prey interactions, called the classical Lotka-Volterra (LV) model, is given by the following system of differential equations [1]:

$$\dot{x} = x(a - by), \qquad \dot{y} = -y(c - dx), \qquad (1)$$

where the parameters a, b, c and d characterize the predator-prey environment, dots denote the time derivatives, $x(t)$ and $y(t)$ are the prey and predator populations, respectively. Due to its unrealistic stability characteristics, the LV model serves as a starting point of many generalized models which should predict a single closed orbit, or perhaps finitely many, but not a continuous family of neutrally stable cycles. Among many ways to improve stability in the LV model, a simple approach is to add polynomial interactions. One of the generalizations considered by Nutku has been to suggest a cubic self-interaction term, instead of a quadratic self-interaction [2]. The Nutku generalization introduces additional stability in a simple way; beside a further generalization involving coupling of the form $x^k y$, where k is a positive integer and $k \leq 2$, provides a rich spectrum of equilibrium points leading to Hopf, pitchfork, saddle node

and cusp bifurcations [3]. Moreover, the limit cycles of the Hopf bifurcation point tend to a specific solution of an equation in [3]. Meanwhile, it is shown that the Gause type predator-prey model with holling type III functional response and allee effect on prey, which is another type generalization of the LV model, topologically equivalent to the differential equations, are given by a fifth order polynomial system in [4,5]. On the other hand, Giné and Romanovski have obtained necessary and sufficient integrability co! nditions at the origin for a complex generalization of the LV model where a quintic nonlinearity is introduced [6]. By the help of this motivation, we will examine stability and bifurcation properties of this model with the symmetrically coupled interaction by using approximate techniques near equilibrium points.

2   The Model, Stability and Bifurcation Scenarios

The quintic Lotka-Volterra model with symmetrically coupled interaction is given as,

$$\dot{x} = x(1 - Ax^4 - Bx^3y - Cx^2y^2 - Dxy^3 - Ey^4)$$
$$\dot{y} = -y(1 - Ay^4 - Bxy^3 - Cx^2y^2 - Dx^3y - Ex^4), \qquad (2)$$

where parameters A, B, C, D and E are positive. System (2) with $A(-B + 3D) = E(3B-D)$ has an integrating factor of the form $V = (xy)^{(-4B+2D)/(B-D)}$ which allows us to find the algebraic integral

$$(xy)^{\frac{r_1}{r_2}} \left(\frac{r_2}{r_1} + \frac{r_2}{2} xy(x^2 + y^2) + \frac{Cr_2}{r_3} x^2 y^2 - \frac{Ar_2}{r_1}(x^4 + y^4) \right) = \text{constant}, \quad (3)$$

where $r_1 = -3B + D$, $r_2 = B - D$ and $r_3 = B + D$.

System (2) has 13 trivial equilibrium points, which are $(0,0)$, $(A^{-1/4}, 0)$, $(-A^{-1/4}, 0)$, $(iA^{-1/4}, 0)$, $(-iA^{-1/4}, 0)$, $(0, A^{-1/4})$, $(0, -A^{-1/4})$, $(0, iA^{-1/4})$, $(0, -iA^{-1/4})$, $(T_1^{-1/4}, T_1^{-1/4})$, $(-T_1^{-1/4}, -T_1^{-1/4})$, $(iT_1^{-1/4}, iT_1^{-1/4})$ and $(-iT_1^{-1/4}, -iT_1^{-1/4})$ with $T_1 = A+B+C+D+E$; and nontrivial ones depending on the values of the coefficients, which are summarized below.

(i) If $T_2 = A - B + C - D + E > 0$ then $(T_2^{-1/4}, -T_2^{-1/4})$, $(-T_2^{-1/4}, T_2^{-1/4})$, $(iT_2^{-1/4}, -iT_2^{-1/4})$ and $(-iT_2^{-1/4}, iT_2^{-1/4})$ are also equilibrium points.

(ii) If $T_2 = A - B + C - D + E < 0$ then there are four complex equilibrium points: $(\sqrt{2}(1 + i)(-T_2)^{-1/4}/2, -\sqrt{2}(1 + i)(-T_2)^{-1/4}/2)$, $(\sqrt{2}(-1 + i)(-T_2)^{-1/4}/2, \sqrt{2}(1 - i)(-T_2)^{-1/4}/2)$ and their complex conjugates.

(iii) If $A = E$ and $B = D$ then there are infinitely many equilibrium points.

(iv) If $A \neq E$, $B = D$ and $T_3 = A - C + E > 0$ then $(T_3^{-1/4}, iT_3^{-1/4})$, $(-T_3^{-1/4}, -iT_3^{-1/4})$, $(iT_3^{-1/4}, -T_3^{-1/4})$, $(-iT_3^{-1/4}, T_3^{-1/4})$ and their complex conjugates are also equilibrium points.

(v) If $A \neq E$, $B = D$ and $T_3 = A - C + E < 0$ then there are eight complex equilibrium points: $(\sqrt{2}(1 + i)(-T_3)^{-1/4}/2, \sqrt{2}(-1 + i)(-T_3)^{-1/4}/2)$,

$(\sqrt{2}\,(1+i)\,(-T_3)^{-1/4}/2,\ \sqrt{2}\,(1-i)\,(-T_3)^{-1/4}/2),\ (\sqrt{2}\,(-1+i)\,(-T_3)^{-1/4}/2,$
$\sqrt{2}\,(-1-i)\,(-T_3)^{-1/4}/2),\ (\sqrt{2}\,(-1+i)\,(-T_3)^{-1/4}/2,\ \sqrt{2}\,(1+i)\,(-T_3)^{-1/4}/2)$
and their complex conjugates.

(vi) If $A \neq E$, $B \neq D$ and $|B - D| > 2\,|A - E|$ then there are 4 real and 4 complex, or 2 real and 6 complex equilibrium points. One can find these points by solving the system of the equations $x = (-\alpha \pm \sqrt{\alpha^2 - 1})y$, $2\alpha = (B - D)/(A - E)$, and $Ax^4 + Bx^3y + Cx^2y^2 + Dxy^3 + Ey^4 = 1$.

(vii) If $A \neq E$, $B \neq D$ and $|B - D| < 2\,|A - E|$ then one can find equilibrium points by solving the system of the equations $x = (-\alpha \pm i\sqrt{1 - \alpha^2})y$ and $Ax^4 + Bx^3y + Cx^2y^2 + Dxy^3 + Ey^4 = 1$.

On the other hand, system (2) is Lyapunov unstable for the chosen values of the parameters, which can be very easily demonstrated using the Lyapunov function $V = (E - A)(x^2 + y^2) + 2Bxy$ which is positive definite if and only if $E > A$ and $E - A > B$. Therefore, we obtain

$$\dot{V} = 2(x^2 - y^2)\,[\beta A(x^4 + y^4) + ((A + E)^2 + B(D - B) + \beta C)x^2y^2 - \beta], \quad (4)$$

where $\beta = A - E < 0$. Although the second factor has negative definite dominant term, the first factor changes sign as $|x| = |y|$. Hence there is a regime where the system is Lyapunov unstable so that we can limit our discussion to local stability. At this stage, we focus on trivial equilibrium points to examine stability. Nontrivial ones will be taken into account for a spacial case.

Linearized eigenvalues about the first real trivial equilibrium point $(0, 0)$ are $\{\pm 1\}$; thus the origin is a saddle point. Eigenvalues for the points $(A^{-1/4}, 0)$ and $(-A^{-1/4}, 0)$ are $\{-4, -1 + E/A\}$, so these points are saddle when $A < E$, and stable nodes when $A > E$. Eigenvalues associated with points $(0, A^{-1/4})$ and $(0, -A^{-1/4})$ are $\{4, 1 - E/A\}$. If $A < E$, these equilibrium points are saddle, otherwise they are unstable nodes. On the other hand the eigenvalues for both of equilibrium points $(T_1^{-1/4}, T_1^{-1/4})$ and $(-T_1^{-1/4}, -T_1^{-1/4})$ are $\{\pm i\sqrt{8[2(E - A) + (D - B)]/T_1}\}$, a pair of purely imaginary eigenvalues, if $2(E - A) + (D - B) > 0$ and $\{\pm\sqrt{8[2(A - E) + (B - D)]/T_1}\}$ if $2(E - A) + (D - B) < 0$. Thus the first purely imaginary values satisfy the resonance conditions and the system can be expanded into a resonant normal form, which gives Hopf bifurcation under the condition $2(E - A) + (D - B) > 0$. For the other condition, these points are also saddle.

Let $A = 1$ and $B = C = D = E = 2$. In this special case, the real equilibrium points of the system are $(0,0)$, $(1,0)$, $(-1,0)$, $(0,1)$, $(0,-1)$, $A_1(1/\sqrt{3}, 1/\sqrt{3})$, $A_2(-1/\sqrt{3}, -1/\sqrt{3})$, $A_3(1, -1)$, $A_4(-1, 1)$; and there are 16 complex equilibrium points. Trivial equilibrium point at the origin is a saddle point with the eigenvalues $\{\pm 1\}$. $(1,0)$ and $(-1,0)$ are also saddle points with the eigenvalues $\{-4, 1\}$. Similarly $(0,1)$ and $(0,-1)$ are saddle points with the eigenvalues $\{4, -1\}$. On the other hand, the points A_1 and A_2 with the eigenvalues $\{\pm i4/3\}$; and also the points A_3 and A_4 with the eigenvalues $\{\pm i4\}$ are also Hopf points. The third order normal form about the point A_1 is

$$\dot{u} = 4iu(1 - 14uv)/3, \qquad\qquad \dot{v} = -4iv(1 - 14uv)/3, \qquad (5)$$

where u and v refer to the variables in the near identity transformation. This normal form indicates Hopf bifurcation. From the linearized eigenvalues of system (5), it is clear that the normal form will be $\dot{u} = i\alpha u f(uv)$, $\dot{v} = -i\alpha v f(uv)$ which admits the solution $uv =$constant. Hence the inclusion of higher order terms in the normal form will only change the purely imaginary eigenvalues, since the only change will be the constant value of $f(uv)$ to the normal form approximation. This implies that the character of the local bifurcation will not change by including further terms. Normal form analysis for the other equilibrium points is omitted for brevity.
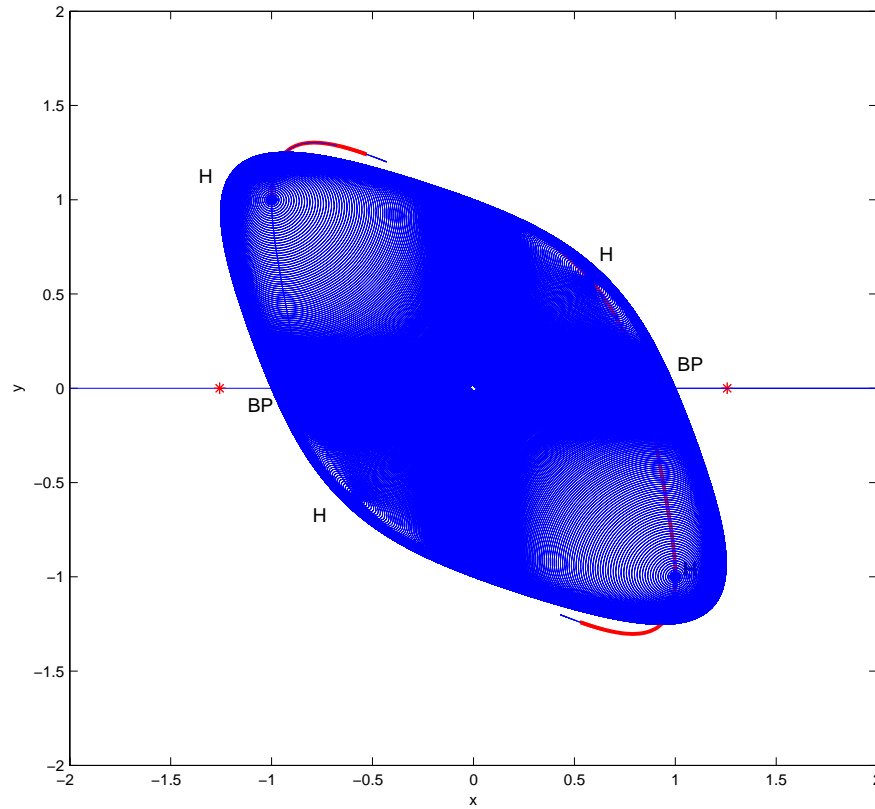

Fig. 1. Family of limit cycles of the system (2) when A is varied

The bifurcation analysis when A is varied is given in Figure 1. In this special case, two supercritical Hopf bifurcation points, A_1 and A_2, and two subcritical Hopf bifurcation points, A_3 and A_4, are observed. All of the limit cycles lie between the coordinate axes and the curve in one of quadrants. They also form a double throw-and-catch mechanism around a pitchfork bifurcation point in the middle.

3   Conclusion

In this work, a special case of the quintic generalization of the LV model has been studied. The model is globally Lyapunov unstable, however local stability indicates several instances of Hopf bifurcation to a family of bounded orbits. It is also numerically observed that there is a discontinuous family of stable cycles in the same way as in the cubic nonlinear intersection.

References

1.A. Lotka. *Elements of Physical Biology*, 1st edition, Williams and Wilkins Company, Baltimore, 1925.
2.Y. Nutku. Hamiltonian structure of the Lotka-Volterra equation. *Phys. Lett. A*, 145: 27-28, 1990.
3.I. Kusbeyzi, O. O. Aybar, and A. Hacinliyan. Stability and bifurcation in two species predotor-prey models. *Nonlinear Anal. RWA*, 12: 377-387, 2011.
4.F. Dumortier, J. Llibre and J. C. Artés. *Qualitative theory of planar differential systems*, Spring, Berlin, 2006.
5.E. González-Olivares and A. Rojas-Palma. Multiple limit cycles in a Gause Type Predator-Prey Model with Holling Type III Functional Response and Allee Effect on Prey. *Bull. Math. Biol*, 73: 1378-1397, 2011.
6.J. Giné and V. G. Romanovski. Integrability conditions for Lotka-Volterra planar complex quintic systems. *Nonlinear Anal. RWA*, 11: 21002105, 2010.

Model Order Reduction for Nonlinear Schrödinger Equation

Canan Akkoyunlu[1], Murat Uzunca[2], and Bülent Karasözen[3]

[1] Department of Mathematics and Computer Sciences, Istanbul Kültür University, 34156, Istanbul, Turkey
(E-mail: `c.kaya@iku.edu.tr`)
[2] Department of Mathematics, Middle East Technical University, 06800 Ankara, Turkey
(E-mail: `uzunca@metu.edu.tr`)
[3] Department of Mathematics and Institute of Applied Mathematics, Middle East Technical University, 06800 Ankara, Turkey
(E-mail: `bulent@metu.edu.tr`)

Abstract. Proper orthogonal decomposition (POD) is a method for deriving reduced order models of dynamical systems. In this paper, the POD is applied to the nonlinear Schrödinger equation (NLS). The NLS equation is discretized in space by finite differences and is solved in time either by structure preserving symplectic or energy preserving average vector field (AVF) integrators. Numerical results for one dimensional NLS equation with soliton solutions show that the low-dimensional approximations obtained by POD reproduce very well the characteristic dynamics of the system, such as preservation of energy and phase space structure of the NLS equation.
Keywords: Nonlinear Schrödinger equation, model order reduction, periodic solutions .

1 Introduction

The nonlinear Schrödinger (NLS) equation arises as the model equation with second order dispersion and cubic nonlinearity describing the dynamics of slowly varying wave packets in nonlinear optics and fluid dynamics and it appears in Bose-Einstein condensate theory. We consider in this paper the NLS equation

$$\psi_t = i\psi_{xx} + i\gamma \mid \psi \mid^2 \psi \tag{1}$$

with the periodic boundary conditions $\psi(x + L, t) = \psi(x, t)$. Here $\psi = \psi(x, t)$ is a complex valued function, γ is a parameter and $i^2 = -1$. The NLS equation is called focusing if $\gamma > 0$ and defocusing if $\gamma < 0$; for $\gamma = 0$, it reduces to

the linear Schrödinger equation. In last two decades various numerical methods were applied for solving NLS equation, among them are the well-known symplectic and multisymplectic integrators, discontinuous Galerkin methods.

There is a strong need for model reduction techniques to reduce the computational costs and storage requirements in large scale simulations. They should yield low-dimensional approximations for the full high-dimensional dynamical system, which reproduce the characteristic dynamics of the system. Among the model order reduction techniques the proper orthogonal decomposition (POD) is one of the most widely used method. Surprisingly good approximation properties are reported for POD based model order reduction techniques in the literature. It has been successfully used in different fields including signal analysis and pattern recognition Fukunaga[3], fluid dynamics and coherent structures Berkooz *et al.*[2] and more recently in control theory Kunisch and Volkwein[4]. The POD is applied mostly to linear and nonlinear parabolic equations Kunisch and Volkwein[5]. In this paper, we apply the POD to the NLS equation. To the best of our knowledge, there is only one paper where POD is applied to NLS equation Schlizerman *et al.*[7], where the authors use only one and two modes approximations of the NLS equation. In this paper, the NLS equation is discretized in space and time by preserving the symplectic structure and the energy. Then, from the snapshots of the fully discretized dynamical system, the POD basis are computed using the singular value decomposition (SVD). It turns out that most of the energy of the system can be accurately approximated by using few POD modes. Numerical results for a NLS equation with soliton solutions confirm the energy and phase space preserving properties of the POD.

The paper is organized as follows. Section 2 and Section 3 are devoted to reviewing the POD method and its application to semi-linear dynamical systems. Numerical solution of the semi-discrete NLS equation and the POD reduced form are described in Section 4. In the last section, Section 5, the numerical results for the reduced order models of one-dimensional NLS equation are presented.

2   The Proper Orthogonal Decomposition

Let X be a real Hilbert space endowed with inner product $\langle \cdot, \cdot \rangle_X$ and norm $\|\cdot\|_X$. For $y_1, \ldots, y_n \in X$ we set

$$V = span\left\{y_1, \cdots, y_n\right\},$$

and refer to V as the ensemble consisting of the snapshots $\{y_j\}_{j=1}^n$. Let $\{\psi_k\}_{k=1}^d$ denote an orthonormal basis of V with $d = dimV$. Then each member of the ensemble can be expressed as

$$y_j = \sum_{k=1}^d \langle y_j, \psi_k \rangle_X \psi_k, \quad j = 1, \ldots, n \tag{2}$$

The POD is constructed by choosing the orthonormal basis such that for every $l \in \{1, \ldots, d\}$ the mean square error between the elements y_j, $1 \le j \le n$, and the corresponding $l - th$ partial sum of (2) is minimized on average:

$$\min_{\{\psi_k\}_{k=1}^l} \frac{1}{n} \sum_{j=1}^n \left\| y_j - \sum_{k=1}^l \langle y_j, \psi_k \rangle_X \psi_k \right\|_X^2 \tag{3}$$

$$\langle \psi_i, \psi_j \rangle_X = \delta_{ij}, \quad 1 \le i \le l, \quad 1 \le j \le i$$

A solution $\{\psi_k\}_{k=1}^l$ to (3) is called a POD-basis of rank l. We introduce the correlation matrix $K = \{K_{ij}\} \in \mathbb{R}^{n \times n}$ corresponding to the snapshots $\{y_j\}_{j=1}^n$ by

$$K_{ij} = \frac{1}{n} \langle y_j, y_i \rangle_X$$

The matrix K is positive semi-definite and has rank d. Let $\lambda_1 \ge \ldots \ge \lambda_d > 0$ denote the positive eigenvalues of K and $v_1, \ldots, v_d \in \mathbb{R}^n$ the associated eigenvectors. Then a POD basis of rank $l \le d$ is given by

$$\psi_k = \frac{1}{\sqrt{\lambda_k}} \sum_{j=1}^n (v_k)_j y_j$$

where $(v_k)_j$ is the $j - th$ component of the eigenvector v_k. Moreover, we have the error formula

$$\frac{1}{n} \sum_{j=1}^n \left\| y_j - \sum_{k=1}^l \langle y_j, \psi_k \rangle_X \psi_k \right\|_X^2 = \sum_{j=l+1}^d \lambda_j$$

The choice of l is based on heuristic considerations combined with observing the ratio of the modeled to the total energy contained in the system Y which is expressed by

$$\epsilon(l) = \frac{\sum_{i=1}^l \lambda_i}{\sum_{i=1}^d \lambda_i}$$

2.1 POD and SVD

There is a strong connection between POD and singular value decomposition (SVD) for rectangular matrices.

Let Y be a real-valued $m \times n$ matrix of rank $d \le \min\{m, n\}$ with columns $y_j \in \mathbb{R}^m$, $1 \le j \le n$. In the context of POD, it will be useful to think of the columns $\{Y_{\cdot, j}\}_{j=1}^n$ of Y as the spatial coordinates vectors of a dynamical system at time t_j. Similarly, we consider the rows $\{Y_{i, \cdot}\}_{i=1}^m$ of Y as the time trajectories of the dynamical system evaluated at the locations x_i.

SVD guarantees the existence of real numbers $\sigma_1 \ge \sigma_2 \ge \ldots \ge \sigma_d > 0$ and orthogonal matrices $U \in \mathbb{R}^{m \times m}$ with columns $\{u_i\}_{i=1}^m$ and $V \in \mathbb{R}^{n \times n}$ with columns $\{v_i\}_{i=1}^n$ such that

$$U^T Y V = \begin{pmatrix} D & 0 \\ 0 & 0 \end{pmatrix} := \Sigma \in \mathbb{R}^{m \times n} \tag{4}$$

where $D = diag(\sigma_1, \sigma_2, \ldots, \sigma_d) \in \mathbb{R}^{d \times d}$ and the zeros in (4) denote the matrices of appropriate dimensions. Moreover, the vectors $\{u_i\}_{i=1}^d$ and $\{v_i\}_{i=1}^d$ satisfy

$$Y v_i = \sigma_i u_i, \quad Y^T u_i = \sigma_i v_i, \quad i = 1, \cdots, d.$$

One of the central issues of POD is the reduction of the data expressing their essential information by means of a few basis vectors. Let us now interpret SVD in terms of POD by the following theorem.

Theorem : (Kunisch and Volkwein[5]) Let $Y = [y_1, \ldots, y_n] \in \mathbb{R}^{m \times n}$ be a given matrix with rank $d \leq min\{m, n\}$. Further, let $Y = U \Sigma V^T$ be the SVD of Y, where $U = [u_1, \ldots, u_m] \in \mathbb{R}^{m \times m}, V = [v_1, \ldots, v_n] \in \mathbb{R}^{n \times n}$ are orthogonal matrices and the matrix $\Sigma \in \mathbb{R}^{m \times n}$ has the form (4). Then, for any $l \in \{1, \ldots, d\}$ the solution to

$$\max_{\widetilde{u}_1, \ldots, \widetilde{u}_l \in \mathbb{R}^m} \sum_{i=1}^l \sum_{j=1}^n \left| \langle y_j, \widetilde{u}_i \rangle_{\mathbb{R}^m} \right|^2, \quad \langle \widetilde{u}_i, \widetilde{u}_j \rangle_{\mathbb{R}^m} = \delta_{ij}, \quad 1 \leq i, j \leq l \tag{5}$$

is given by the singular vectors $\{u_i\}_{i=1}^l$. A necessary optimality condition for (5) is given by the eigenvalue problem $YY^T u_i = \lambda_i u_i$.

3   Application to Semi-linear Time Dependent Systems

We consider the semi-linear initial value problem

$$\dot{y}(t) = Ay(t) + f(t, y(t)), \quad t \in [0, T], \quad y(0) = y_0, \tag{6}$$

where $f : [0, T] \times \mathbb{R}^m \to \mathbb{R}^m$ is continuous in both arguments and locally Lipschitz-continuous with respect to the second argument. The NLS equation (1) is a semi-linear equation, where the cubic nonlinear part is locally Lipschitz continuous.

Suppose that we have determined a POD basis $\{u_j\}_{j=1}^l$ of rank $l \in \{1, \ldots, m\}$ in $\mathbb{R}^m$. Then we make the ansatz

$$y^l(t) = \sum_{j=1}^l \underbrace{\langle y^l(t), u_j \rangle}_{=:y_j^l(t)} u_j, \quad t \in [0, T], \tag{7}$$

where the Fourier coefficients y_j^l, $1 \leq j \leq l$, are functions mapping $[0, T]$ into $\mathbb{R}^m$, and the inner product $\langle \cdot, \cdot \rangle$ represents the Euclidean inner product $\langle \cdot, \cdot \rangle_{\mathbb{R}^m}$ to make the notation simple. Since

$$y(t) = \sum_{j=1}^m \langle y(t), u_j \rangle u_j, \quad t \in [0, T]$$

holds, $y^l(t)$ is an approximation for $y(t)$ provided $l < m$. Inserting (7) into (6) yields

$$\sum_{j=1}^{l} \dot{y}_j^l(t)u_j = \sum_{j=1}^{l} y_j^l(t)Au_j + f(t,y^l(t)), \quad t \in [0,T], \quad \sum_{j=1}^{l} y_j^l(0)u_j = y_0 \quad (8)$$

Note that (8) is an initial-value problem in $\mathbb{R}^m$ for $l \leq m$ coefficient functions $y_j^l(t), \quad 1 \leq j \leq l$ and $t \in [0,T]$, so that the coefficients are overdetermined. Therefore, we assume that (8) holds after projection on the l dimensional subspace $V^l = span \{u_j\}_{j=1}^{l}$. From (8) and $\langle u_j, u_i \rangle = \delta_{ij}$ we infer that

$$\dot{y}_i^l(t) = \sum_{j=1}^{l} y_j^l(t) \langle Au_j, u_i \rangle + \langle f(t, y^l(t)), u_i \rangle \quad (9)$$

for $1 \leq i \leq l$ and $t \in (0, T]$. Let us introduce the matrix

$$B = \{b_{ij}\} \in \mathbb{R}^{l \times l}, \quad b_{ij} = \langle Au_j, u_i \rangle$$

and the non-linearity $F = (F_1, \cdots, F_l)^T : [0, T] \times \mathbb{R}^l \to \mathbb{R}^l$ by

$$F_i(t, y) = \left\langle f(t, \sum_{j=1}^{l} y_j u_j), u_i \right\rangle, \quad t \in [0, T], \quad y = (y_1, \cdots, y_l) \in \mathbb{R}^l$$

Then, (9) can be expressed as

$$\dot{y}^l(t) = By^l(t) + F(t, y^l(t)), \quad t \in (0, T] \quad (10)$$

For initial condition, we derive $y^l(0) = y_0$ where

$$y_0 = (\langle y_0, u_1 \rangle, \ldots, \langle y_0, u_l \rangle)^T \in \mathbb{R}^l$$

This system is called the POD-Galerkin projection for (6). In case of $l << m$ the $l-$dimensional system is a low-dimensional approximation for (6). Therefore, it is the reduced-order model for (6).

4   Numerical solution of NLS equation

One dimensional NLS equation (1) can be written by decomposing $\psi = p + iq$ in real and imaginary components

$$p_t = -q_{xx} - \gamma(p^2 + q^2)q, \quad q_t = p_{xx} + \gamma(p^2 + q^2)p \quad (11)$$

as an infinite dimensional Hamiltonian pde in the phase space $u = (p, q)^T$

$$\dot{u} = \mathcal{D}\frac{\delta \mathcal{H}}{\delta u}, \quad \mathcal{H} = \int \frac{1}{2}\left(p_x^2 + q_x^2 - \frac{\gamma}{2}(p^2 + q^2)^2\right)dx, \quad \mathcal{D} = \begin{pmatrix} 0 & 1 \\ -1 & 0 \end{pmatrix}.$$

After discretizing the Hamiltonian in space

$$H = \frac{1}{2\Delta x^2} \sum_{j=1}^{n}((p_{j+1} - p_j)^2 + (q_{j+1} - q_j)^2) - \frac{\gamma}{4}\sum_{j=1}^{n}(p_j^2 + q_j^2)^2.$$

we obtain the semi-discretized Hamiltonian ode's

$$p_t = -Aq - \gamma q(p^2 + q^2), \quad q_t = Ap + \gamma p(p^2 + q^2), \tag{12}$$

where A is a circulant matrix.

To solve (12) we apply the second order Strang split-step method by adapting the linear, non-linear splitting

$$u_t = \mathcal{N}u + \mathcal{L}u, \quad \mathcal{L}u = iu_{xx}, \quad \mathcal{N}u = i\gamma|u|^2u.$$

4.1 POD Basis for NLS equation

Suppose that we have determined POD bases $\{u_j\}_{j=1}^{l}$ and $\{v_j\}_{j=1}^{l}$ of rank $l = \{1, \ldots, m\}$ in $\mathbb{R}^m$. Then we make the ansatz

$$p^l = \sum_{j=1}^{l}\alpha_j u_j(x), \quad q^l = \sum_{j=1}^{l}\beta_j v_j(x) \tag{13}$$

where $\alpha_j = <p^l, u_j>$, $\beta_j = <q^l, v_j>$ and p^l, q^l are approximations for p and q, respectively. Inserting (13) into (12), and using that $\langle u_i, u_j \rangle = \delta_{ij}$ and $\langle v_i, v_j \rangle = \delta_{ij}$, $i, j = 1, \cdots, l$, we obtain

$$\dot{\alpha}_i = -\sum_{j=1}^{l}\beta_j\langle Av_j, u_i\rangle - \gamma\left\langle\left(\sum_{j=1}^{l}\beta_j v_j\right)\left(\sum_{j=1}^{l}\alpha_j u_j\right)^2, u_i\right\rangle - \gamma\left\langle\left(\sum_{j=1}^{l}\beta_j v_j\right)^3, u_i\right\rangle$$

$$\dot{\beta}_i = \sum_{j=1}^{l}\alpha_j\langle Au_j, v_i\rangle + \gamma\left\langle\left(\sum_{j=1}^{l}\alpha_j u_j\right)\left(\sum_{j=1}^{l}\beta_j v_j\right)^2, v_i\right\rangle + \gamma\left\langle\left(\sum_{j=1}^{l}\alpha_j u_j\right)^3, v_i\right\rangle$$

As defining $V = [v_1, v_2, \cdots, v_l] \in \mathbb{R}^{m \times l}$, $\beta \in \mathbb{R}^l$, $U = [u_1, u_2, \cdots, u_l] \in \mathbb{R}^{m \times l}$, $\alpha \in \mathbb{R}^l$, $B = \{b_{ij}\}$, $b_{ij} = \langle Av_j, u_i\rangle$, $B^T = \{c_{ij}\}$, $c_{ij} = \langle Au_j, v_i\rangle$, we obtain

$$\dot{\alpha} = -B\beta - \gamma U^T\left((V\beta) \cdot (U\alpha)^2\right) - \gamma U^T\left((V\beta)^3\right)$$
$$\dot{\beta} = B^T\alpha + \gamma V^T\left((U\alpha) \cdot (V\beta)^2\right) + \gamma V^T\left((U\alpha)^3\right) \tag{14}$$

with both the operation '·' and the powers are hold elementwise.

The reduced order system (14) is solved, as the unreduced one (1), with the energy preserving AVF method and symplectic midpoint method applying

linear-nonlinear Strang spliting Weideman and Herbst[8]. The nonlinear parts of the equations are solved by Newton-Raphson method. For solving the linear system of equations, we have used the Matlab toolbox **smt** Redivo-Zaglia and Rodriguez[6], which is designed for solving linear systems with a structured co-efficient matrix like the circulant and Toepltiz matrices. It reduces the number of floating point operations for matrix factorization to $O(n \log n)$.

5   Numerical Results

For the one dimensional NLS equation we have taken the example in Celle-doni *et al.*[1] with $\gamma = 1$, and the periodic boundary conditions in the interval $[-20, 20]$. The initial conditions are given as $p(x,0) = \exp(-(x-1)^2/2)$, $q(x,0) = \exp(-x^2/2)$. As mesh sizes in space and time we have used $dx = 40/20$ and $dt = 0.1$, respectively.

We compare the energy error and the norm error with ROM-AVF and ROM-MID using with and without difference quotients in Table 1. With increasing number of POD basis l, the errors in the energy and discrete solutions of the fully discretized NLS equation and the reduced order model decreases. The singular values of the snapshot matrix are rapidly decaying (Figure 4) so that the only few POD modes would be sufficient to approximate the fully discetized NLS equation. For POD basis with $l = 3$ (Figure 3), hence, the energy is well preserved as for the fully discretized form (Figure 2) and more accurate solutions are obtained with increasing number of POD modes (Figure 4).

Table 1. L_∞-errors of the energy and solutions

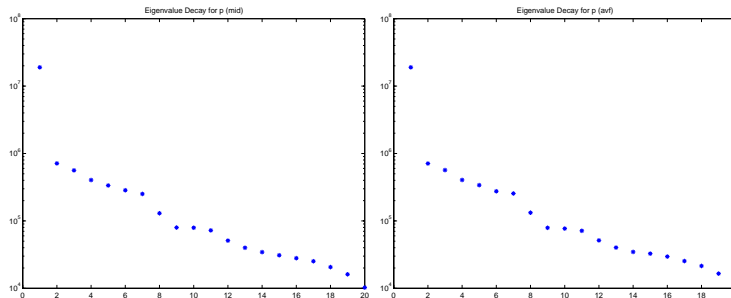| POD	Energy (ROM-AVF)	Energy (ROM-MID)	Solution (ROM-AVF)	Solution (ROM-MID)
2	6.125e-002	6.107e-002	2.164e-001	2.159e-001
3	5.529e-002	5.528e-002	2.010e-001	2.011e-001
4	4.612e-002	4.609e-002	1.847e-001	1.835e-001
5	4.100e-002	4.095e-002	1.838e-001	1.817e-001

Fig. 1. Singular values: left: mid-point, right: AVF
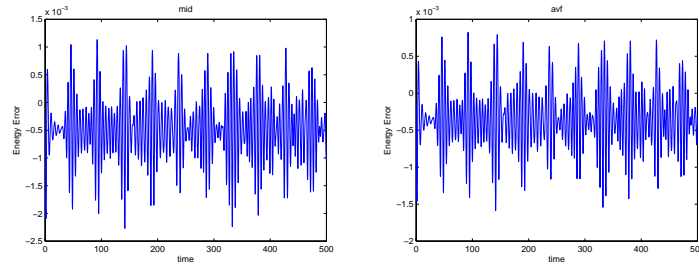
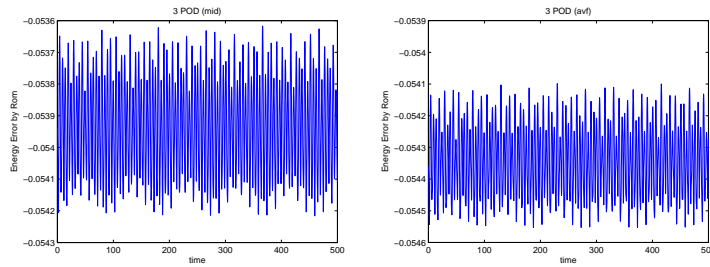**Fig. 2.** Energy (full discretization): left: mid-point, right: AVF

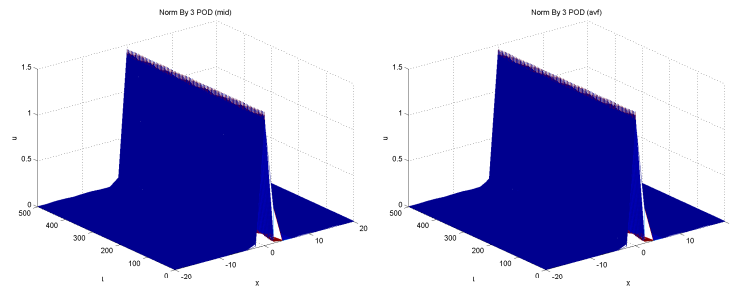**Fig. 3.** Energy (POD, l=3) : left: mid-point, right: AVF

Fig. 4. ROM solutions with 3 POD modes: left: mid-point, right: AVF

References

1. E. Celledoni, V. Grimm, R. I. McLachlan, D. I. McLaren, D. O'Neale, B. Owren and G.R.W. Quispel. : Preserving energy resp. dissipation in numerical PDEs using the "Average Vector Field" method, Journal of Computational Physics, 231:6770-6789, 2012.
2. G. Berkooz, P. Holmes and J.L. Lumley. Turbulence, Coherent Structuress, Dynamical Systems and Symmetry, Cambridge University Press: Cambridge Monographs on Mechanics, 1996.
3. K. Fukunaga. Introduction to statistical pattern recognition. Computer Science and Scientific Computing. Academic Press Inc., Boston, MA, second edition, 1990.
4. K. Kunisch and S. Volkwein. Control of Burgers' equation by a reduced order approach using proper orthogonal decomposition, J. Optimization Theory and Applications 102:345-371, 1999.

5. K. Kunisch and S. Volkwein. Galerkin proper orthogonal decomposition methods for parabolic problems. Numer. Math., 90:117-148, 2001.
6. M. Redivo-Zaglia and G. Rodriguez, SMT: a Matlab structured matrices toolbox. Numer. Algorithm, 59:639-659, 2012.
7. E. Schlizerman, E. Ding, O.M. Williams and J.N. Kutz. The Proper Orthogonal Decomposition for Dimensionality Reduction in Mode-Locked Lasers and Optical Systems, International Journal of Optics, 831604, 2012.
8. J.A.C. Weideman and B.M. Herbst : Split-step methods for the solution of the nonlinear Schrödinger equation. SIAM J. Numer. Anal. 23:485-507, 1986.

Layer-Recurrent Neural Network Modelling of Reactive Distillation Process

Abdulwahab GIWA[1] and Saidat Olanipekun GIWA[2]

[1] Federal University of Technology, School of Engineering and Engineering Technology, Chemical Engineering Department, Gidan Kwano, Minna, Nigeria
[2] Ankara University, Ankara, Turkey
E-mails: a.giwa@futminna.edu.ng and giwa@ankara.edu.tr

Abstract: Reactive distillation is one of the complex processes encountered in process industries as a result of the integration of both reaction and separation in a single unit. Nowadays, the modelling of this process has become a big challenge to Process Engineers. The use of a reliable model that can handle complex functions is very necessary to represent this complex process. It has been discovered that Neural Network can be used to handle complex functions very well. Therefore, the modelling of the reactive distillation process considered in this work has been carried out with the aid of a dynamic neural network known as Layer-Recurrent Neural Network. The simulated results obtained from the developed Neural Network models were compared with the measured results to confirm the validities of the developed models.

1. Introduction

In recent years, integrated reactive separation processes have attracted considerable attentions in both academic research and industrial applications (Völker et al., 2007; Giwa and Karacan, 2012a). One of these processes which is known as reactive distillation is potentially attractive whenever conversion is limited by reaction equilibrium (Balasubramhanya and Doyle III, 2000; Giwa and Karacan, 2012a).

Reactive Distillation (RD) combines the benefits of equilibrium reaction with a traditional unit operation (in this case, distillation) to achieve a substantial progress in not only promoting the reaction conversion through constant recycling of unconverted materials and removal of products but also reducing the capital and operating costs in one way by reducing the number of equipment units (Giwa and Karacan, 2012a). Moreover, its other advantages include improved selectivity, lower energy consumption, scope for difficult separations and avoidance of azeotropes (Jana and Adari, 2009). However, due to the integration of reaction and separation, reactive distillation exhibits complex behaviours (Khaledi and Young, 2005) such as steady state multiplicity, process gain sign changes (bidirectionality) and strong interactions between process variables (Jana and Adari, 2009). These complexities have

made the modelling of Reactive Distillation Process extremely difficult (Giwa and Karacan, 2012b; Giwa and Giwa, 2012). As such, a robust tool that can handle complex functions very well is needed to represent this complex process. One of these tools has been discovered to be Neural Network model because, according to Beale et al. (2010), Neural Network can be trained to handle complex functions.

Neural Network model can be viewed as a nonlinear empirical model that is especially useful in representing input-output data, in making predictions in time, and in classifying data (Himmelblau, 2000). Neural Network can be highly nonlinear, can learn easily, requires little or no a priori knowledge of model structure, is fault-tolerant and can handle complex problems that cannot be satisfactorily handled by the traditional methods (MacMurray and Himmelblau, 2000). There are many kinds of Neural Network models available in the literature. For instance, a simple classification can be: Static Neural Network and Dynamic Neural Network. It is perceived that a dynamic network, especially Layer-Recurrent Network (LRN), will be better in representing this complex Reactive Distillation Process because of the presence of a delay ensuring proper dynamics in each of its layers except in the last one.

According to the information gathered from the literature, Giwa and Karacan (2012a) used three different types of delayed neural network (Nonlinear AutoRegressive (NAR), Nonlinear AutoRegressive with eXogenous inputs (NARX) and Nonlinear Input-Output (IO)) models to represent a reactive distillation column in predicting the temperatures of the top and the bottom sections of the reactive distillation column used for the production of ethyl acetate and they were able to obtain very good results from both NAR and NARX models while the results given by IO models were found not to be satisfactory. Also, Giwa and Karacan (2012c) developed two nonlinear black-box (treepartition and sigmoid network NARX) models for the Reactive Distillation Process used for the production of ethyl acetate from the esterification reaction between acetic acid and ethanol and found that sigmoid network NARX model was better than treepartition NARX model for the reactive distillation process studied in their work.

In this work, Reactive Distillation Process is aimed to be modelled with the aid of Layer-Recurrent Neural Network using the metathesis reaction of trans-2-pentene to trans-2-butene and trans-2-hexene as the case study.

2. Procedures
The methods used for the accomplishment of this work are as outlined below.

2.1 Data Acquisition
The diagram of the metathesis reactive distillation column, developed with the aid of Aspen HYSYS (Aspen, 2011), used for the production of trans-2-butene (obtained in high purity at the top segment of the column) and trans-2-hexene (obtained in high purity at the bottom segment of the column) from trans-2-pentene, and from which the measured data used for the neural network

model development were generated is as shown in Figure 1 below. As can be seen from the figure, the column had one feed stream and two product streams. The olefin metathesis reaction that occurred in the column was a reversible type given as shown in Equation 1.
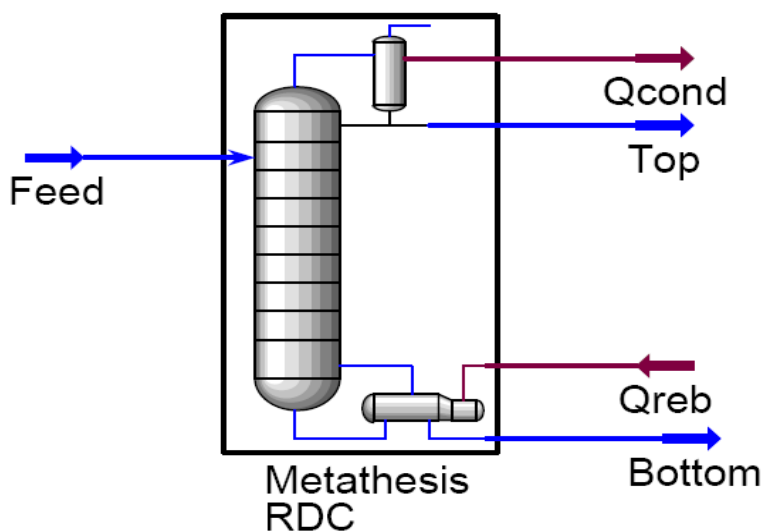

Fig. 1. Process flowsheet for metathesis reactive distillation process

$$2C_5H_{10} \xleftrightarrow{K_{eq}} C_4H_8 + C_6H_{12} \tag{1}$$

The data used for the development of the process in Aspen HYSYS environment are as given in Table 1.

Table 1. HYSYS metathesis reactive distillation process development data

Parameter	Value
Feed	
Flow rate (mL/min)	35
Temperature (K)	298.15
Pressure (atm)	1.11
Feed Composition (Mole fraction)	
trans-2-pentene	0.999998
trans-2-butene	1.00E-06
trans-2-hexene	1.00E-06
Fluid Package	UNIQUAC

Column	
Type	Packed
Packing type	Raschig Rings (Ceramic) 0.25 inch
No. of segment	15
Feed segment	8
Reaction	
Type	Equilibrium
Segment	6 - 10 and reboiler
K_{eq} source	Gibbs Free Energy
Basis	Molar concentration
Phase	Liquid

In the process development, reflux ratio and reboiler duty were chosen as the manipulated (input) variables while top segment and bottom segment temperatures were selected as the process (output) variables. By using the random data set values of the manipulated variables built with the aid of Parametric Utility of Aspen HYSYS, the column was run and the top segment and the bottom segment temperatures were obtained as the measured values of the output variables. Two different data sets were generated from the Aspen HYSYS system of the process. One was used for the training while the other was used for the testing of the Layer-Recurrent Neural Network models.

2.2 Modelling and Simulation

In the modelling of the Reactive Distillation Process in MATLAB (Mathworks, 2012) environment, the data sets obtained from Aspen HYSYS system of the process were converted from concurrent types to sequential ones because those were the types required by the dynamic Layer-Recurrent Neural Network. The parameters used for the formulation of the Neural Network models of the process considered in this work are as given in Table 2.

Table 2. Layer-Recurrent Neural Network model formulation parameters

Parameter	Value
Number of inputs	2
Number of outputs	2
Number of layers	2
Number of neurons in hidden layer	7
Hidden layer transfer function	*tansig*
Output layer transfer function	*purelin*
Training algorithm	*Levenberg-Marquardt*

Owing to the fact that there were two outputs, and even with two inputs, the structure of the neural network had two models in it – one for each process variable; that is, one model was for top segment temperature and the other was for bottom segment temperature. The structure of the developed models is shown below in Figure 2.
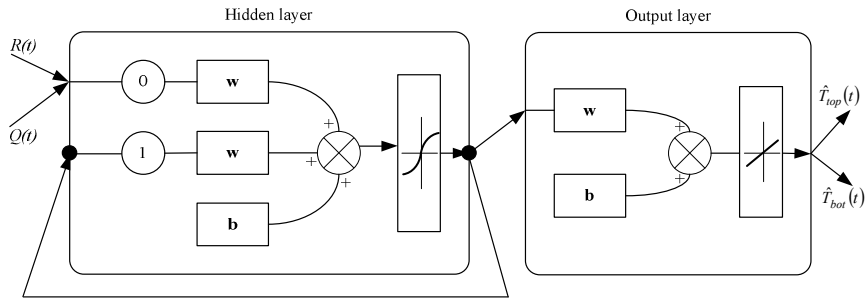

Fig. 2. Layer-Recurrent Neural Network of metathesis RD process

In order to determine the validities of the developed models, they were simulated and their performance values were calculated. The performance criteria used were fit values (indicating the percentage of the data accounted for by the developed models), means of absolute errors and sums of squared errors.

3. Results and Discussions

The acquired measured data sets of the input and the output variables used for training and testing the neural network models are given in Figures 3 and 4 respectively for the top segment and the bottom segment temperatures.
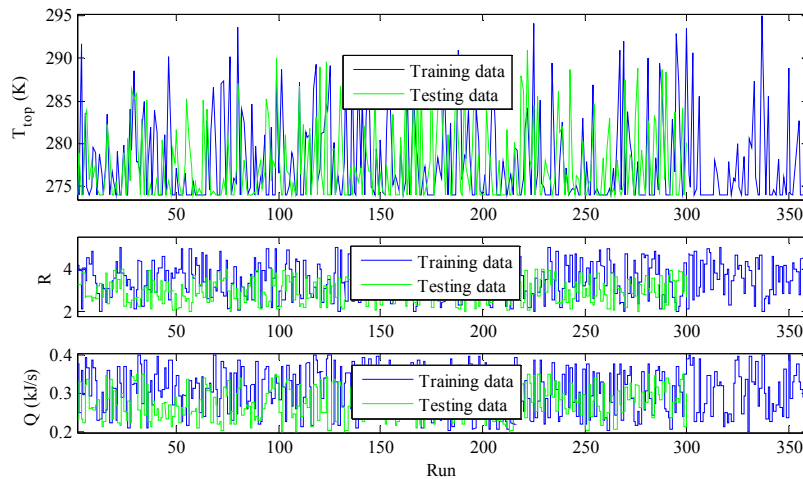

Fig. 3. Top segment temperature training and testing data sets

As can be seen from Figures 3 and 4, there were corresponding changes in the responses of the two segment temperatures as a result of the changes in the input variables. Also noticed from the results shown in Figures 3 and 4 was that the lengths of the training and the testing data for both segment temperatures were not the same but the overall limits of the testing manipulated variables used were within the ones used for the generation of the training data. The different data length was made so in order to test the robustness of the developed neural network model to another data with length different from that of the one used for its training.
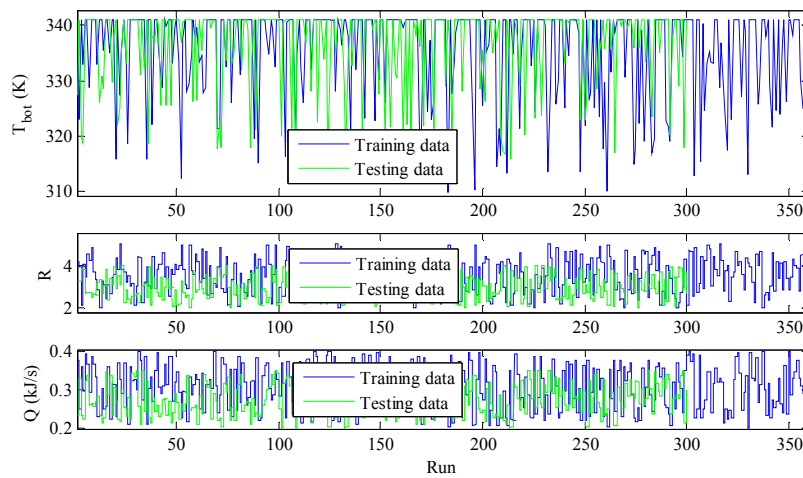

Fig. 4. Bottom segment temperature training and testing data sets

After training the Layer-Recurrent Network Models of the process, even though the models could not be obtained as physical ones, they were simulated using the manipulated variable values used for the training and the performance values of the models obtained from the training simulation are as shown in Table 3. It was observed from the table that the fit values of the models were appropriately very high and the means of absolute errors and the sums of squared errors were low enough to say that the models were well trained. Further considering the fit values of the training simulations, it was discovered that the developed neural network models could account for approximately 99% of the data used for developing them.

Table 3. Performance values of network training simulation

Performance criterion	Performance value	
	T_{top}	T_{bot}
Fit value	99.08	99.27
Mean of absolute errors	0.04	0.04
Sum of squared errors	0.80	1.33

In addition, the top and the bottom segment temperatures obtained from the training simulations of the developed neural network models were plotted together with the measured ones and their graphs are as shown in Figures 5 and 6 respectively for the top segment temperature and the bottom segment temperature profiles. From Figure 5, it was observed that there was a good relationship between the measured and the simulated top segment temperature profiles because, as seen from the graph, the trends of the two plots were found to follow each other very well. Also, as noticed from Figure 6, good relationship was found to exist between the profiles of the bottom segment temperatures measured and those estimated with the developed model. The good relationships between the plots contained in Figures 5 and 6 have been discovered to be in support of the excellent performance values of the models (see Table 3).
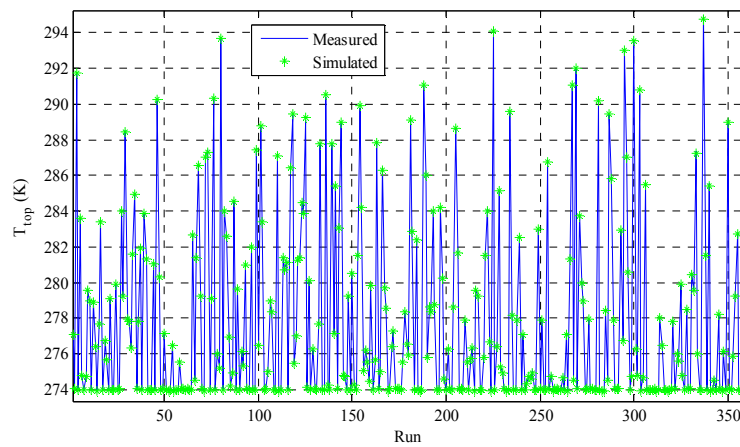

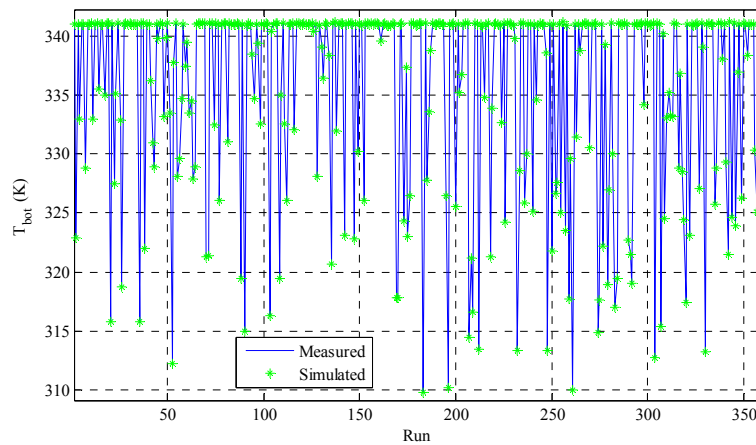Fig. 5. Measured and simulated top segment temperatures

Fig. 6. Measured and simulated bottom segment temperatures

Apart from simulating the developed models with the manipulated (input) variables used for the training, testing data set generated for the purpose of model testing, and which was not used for the training of the models, was also used to simulate the developed models and the performance values obtained from the testing simulations are as given in Table 4. As can be seen from the table, in the testing simulation also, the fit values were found to be very high. In addition, the means of absolute errors and the sums of squared errors for both the top and the bottom segment temperatures were obtained to be very low and appropriate enough for good models.

Table 4. Performance values of network testing simulation

Performance criterion	Performance value	
	T_{top}	T_{bot}
Fit value	98.74	98.63
Mean of absolute errors	0.05	0.07
Sum of squared errors	0.95	3.15

In addition, the representations of the Reactive Distillation Process of this work by the developed neural network models were as well investigated by plotting the testing simulation results of both the top and the bottom segment temperatures against the measured ones as shown in Figures 7 and 8, respectively.
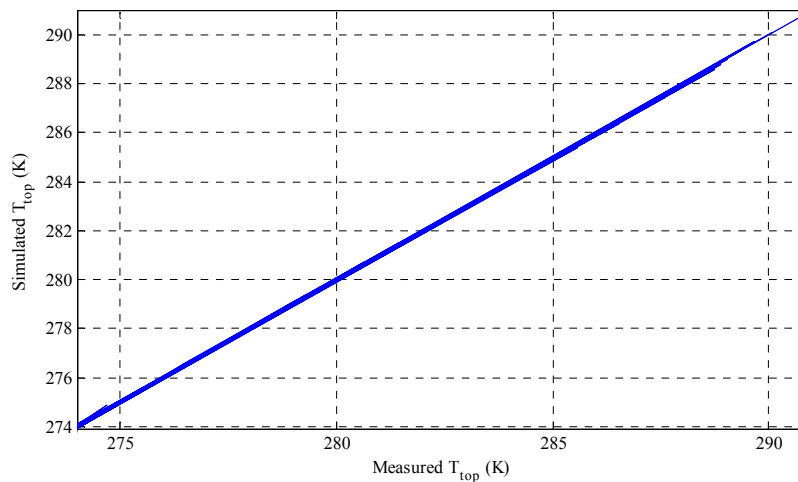

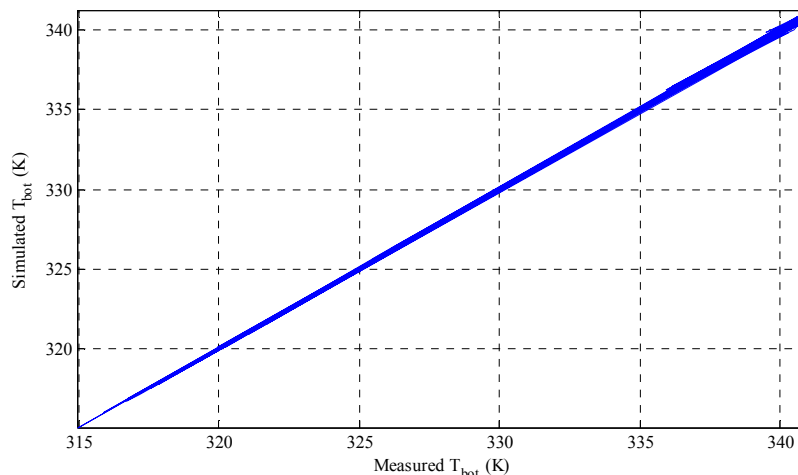Fig. 7. Top segment simulation results of neural network testing

Fig. 8. Bottom segment simulation results of neural network testing

According to the results shown in Figures 7 and 8, the 45 degree lines given by the plots of the testing simulations of the top and the bottom segment temperatures against the measured ones were found to be other indications of the good representations of the Reactive Distillation Process by the developed neural network models.

It has thus been seen that the developed neural network models for the top and the bottom segment temperatures of the reactive distillation column have been found to perform very well both in the training and in the testing simulations. The good performances obtained from the developed models have demonstrated the versatility of neural network in representing complex processes very well.

4. Conclusions

The very high fit values, the low means of absolute errors and the low sums of squared errors obtained from the training and the testing simulations of the Layer-Recurrent Neural Network models developed for the olefin metathesis Reactive Distillation Process, used for the production of trans-2-butene and trans-2-hexene from trans-2-pentene, have confirmed the validities of the developed models for the top and the bottom segment temperatures of the column in which the process was accomplished. Therefore, Layer-Recurrent Neural Network model has been revealed to be an excellent tool in representing the complex Reactive Distillation Process.

Acknowledgement

References

1. A. Giwa and S. Karacan. Black-Box Modelling of Ethyl Acetate Reactive Packed Distillation Column, *AU Journal of Technology,* 15(3):172-178, 2012b.

2. A. Giwa and S. Karacan. Modeling and Simulation of a Reactive Packed Distillation Column Using Delayed Neural Networks, *Chaotic Modeling and Simulation,* 2(1):101-108, 2012a.

3. A. Giwa and S. Karacan. Nonlinear Black-Box Modeling of a Reactive Distillation Process, *International Journal of Engineering Research & Technology,* 1(7):1-10, 2012c.

4. A. Giwa and S.O. Giwa. Optimization of Transesterification Reaction Integrated Distillation Column Using Design Expert and Excel Solver, *International Journal of Advanced Scientific and Technical Research,* 2(6):423-435, 2012.

5. A.K. Jana and P.V.R.K. Adari. Nonlinear State Estimation and Control of a Batch Reactive Distillation. *Chemical Engineering Journal,* 150(2-3):516-526, 2009.

6. Aspen. AspenONE V7.3, *Aspen Technology,* 2011.

7. D. M. Himmelblau. Applications of Artificial Neural Networks in Chemical Engineering, *Korean Journal of Chemical Engineering,* 17(4):373–392, 2000.

8. J. C. MacMurray and D. M. Himmelblau. Modeling and Control of a Packed Distillation Column Using Artificial Neural Networks, *Computers and Chemical Engineering,* 19(10):1077–1088, 1995.

9. L. S. Balasubramhanya and F. J. Doyle III. Nonlinear Model-Based Control of a Batch Reactive Distillation Column, *Journal of Process Control,* 10(2-3):209-218, 2000.

10. M. H. Beale, M. T. Hagan and H. B. Demuth. Neural Network Toolbox 7, *The MathWorks Inc.,* Apple Hill Drive, Natick MA, 2010.

11. M. Völker, C. Sonntag and S. Engell. Control of Integrated Processes: A Case Study on Reactive Distillation in a Medium-Scale Pilot Plant, *Control Engineering Practice,* 15(7):863–881, 2007.

12. Mathworks. MATLAB R2012b, The Language of Technical Computing, *The MathWorks, Inc.,* Natick, 2012.

13. R. Khaledi and B.R. Young. Modeling and model predictive control of composition and conversion in an ETBE reactive distillation column, *Industrial & Engineering Chemistry Research,* 44(9):3134-3145, 2005.

Nonlinear Dynamical Systems Theory
and Economic Complexity

Aleksander Jakimowicz

University of Warmia and Mazury in Olsztyn, Faculty of Economic Sciences,
Department of Quantitative Methods, Poland
E-mail: aleksander.jakimowicz@uwm.edu.pl

Abstract: Catastrophe theory and deterministic chaos constitute basic elements of the science of complexity. Elementary catastrophes were the first form of nonlinear, topological complexity that were seriously studied in economics. Deterministic chaos and other types of complexity succeeded catastrophe theory. In general, chaos means the seemingly random behavior of a deterministic system, which stems from high sensitivity to its initial conditions. Nonlinear dynamical systems theory, which unites various manifestations of complexity into one integrated system, is contrary to the assumptions that markets and economies spontaneously strive for a state of equilibrium. To the contrary, their complexity seems to grow due to the influence of classic economic laws. In my paper, I indicate that with time, model economic systems strive for a state we call "the edge of chaos". I consider two cases. The first case concerns an economy based on a two-stage accelerator, where the economic cycle adopts the form of chaotic hysteresis. The second case concerns a Cournot-Puu duopoly model in which striving for the edge of chaos stems from profit maximization by entrepreneurs. The evolution of systems at the edge of chaos can be sudden, which makes it necessary to consider it in terms of elementary catastrophes.
Keywords: Cusp catastrophe, Chaotic hysteresis model, Cournot-Puu duopoly model, Edge of chaos, System classification, Economic transformation, Rule of progressive complexity.

1. Introduction: Foundations of catastrophe theory
1.1. Classification Theorem
The theory of catastrophes, also known as the theory of morphogenesis, appeared in science in the mid-1970s [25]. It is a general method of system modeling focusing on the way in which discontinuous effects can emerge from continuous causes. Let the dynamic system be represented by a smooth function:

$$f : \mathbf{R}^k \times \mathbf{R}^n \to \mathbf{R}, \tag{1}$$

where $\mathbf{R}^k$ is a control space representing a set of causes, whereas $\mathbf{R}^n$ is a space of states (behavior) representing a set of effects. The function f is called a potential function. If the internal dynamics of the system consist in striving for a

local maximum, then the potential function can represent the probability of it being found.

The basis of catastrophe theory is the classification theorem [26]. This states that if the co-dimension k of elementary catastrophes is bigger than 5, they create a finite family of discontinuous transition types. Every sudden dynamic change can be assigned to one of those types. The relation between the number of catastrophes and the co-dimension is shown in Table 1.

Table 1. Elementary catastrophe classification in relation to the co-dimension k

Co-dimension value (k)	1	2	3	4	5	6	7 …
Number of elementary catastrophes	1	2	5	7	11	∞	∞

From an application point of view, the case $k = 4$ is important, since $\mathbf{R}^4$ can be interpreted as a physical space-time in which all events take place. There are seven types of singularities in this case: fold, cusp, swallowtail, butterfly, hyperbolic umbilic, elliptic umbilic, and parabolic umbilic [5].

The application of the catastrophe theory in economics is possible only when the law governing a given phenomenon or process has been well-defined. In such a case, the catastrophe theory will facilitate the choice of the easiest mathematical structure, which will generate a behavior closest to real. Another equally point is to use metaphors properly [8].

1.2. The cusp catastrophe
The cusp catastrophe is one of the most common elementary catastrophes in economic applications. The potential function has the following form:

$$f : \mathbf{R}^2 \times \mathbf{R}^1 \rightarrow \mathbf{R}, \tag{2}$$

Thus, the control space is two-dimensional, whereas the state space is one-dimensional. The function (2) has a simple multinomial representation:

$$f(c_1, c_2, x) = \frac{1}{4} x^4 + \frac{1}{2} c_1 x^2 + c_2 x, \tag{3}$$

where x stands for the state variable, whereas c_1 and c_2 are the control parameters [28]. The manifold of the catastrophe defining the surface area of the system equilibrium is dependent on the following formula:

$$M_3 = \left[\left(c_1, c_2, x \right) : \frac{df}{dx} = 0, \frac{df}{dx} = x^3 + c_1 x + c_2 \right].$$ (4)

The system proceeds along this surface in a continuous way, until it comes across a set of singularities. There is then a sudden jump to another equilibrium surface and the continuous evolution continues until the next jump.

2. Deterministic chaos

2.1. Nonlinearity as a necessary condition for complexity

In order to define nonlinearity it is necessary to clearly define linearity. In all linear systems, the binding rule is the rule of superposition. This states that the system's reaction to two or more stimuli is the sum of reactions triggered individually by each of these stimuli. If factor *A* triggers reaction *X*, and factor *B* reacts to *Y* then the factor (*A* + *B*) results in (*X* + *Y*). In other words, linear systems are additive.

The rule of superposition implies the linearity of the system if we supplement it with the condition of homogeneity. A lack of additiveness and homogeneity implies the nonlinearity of the system. The main causes of nonlinearity in economics are:

- Limitations imposed on the economic variables [2].
- Technical-balance laws of production [15].
- Technical-organizational factors [10].
- Bounded rationality [24].
- Processes of expectation formation [4].
- Adaptive processes of economic-agent learning [3].
- The shape (protuberance) of the indifference curves.
- Aggregation processes of some variables [27].
- Evolution of competition rules [3].
- Psychological laws [14].

Nonlinearity is a necessary condition, but it is not enough to trigger chaos. Statistical tests confirm that nonlinearity is a phenomenon that is common in economic time series, and part of them proves that deterministic chaos exists. There are strong grounds to claim that in the future, the role of nonlinearity in economic explorations will become more significant.

2.2. The butterfly effect

Deterministic chaos means a seemingly random behavior of the deterministic system, thus one which is strictly subject to specific rules. The reason for the stochastic behavior of some nonlinear deterministic systems is their unusually sensitive dependence on initial conditions, which was named 'the butterfly effect' by Lorenz [16]. A slight disturbance in the initial conditions after some time causes significant changes in the system behavior as trajectories begin to disperse exponentially. As picturesquely described Lorenz, a proverbial flap of butterfly wings in Brazil can cause a tornado in Texas.

The Lyapunov exponents are amongst the most frequently-used quantitative measures of the trajectory divergence. This notion has been used by Oseledec [20] in a well-known multiplicative ergodic theorem. The Lyapunov exponent for one-dimensional map is as follows:

$$W^L = \lim_{n \to \infty} \lim_{\varepsilon \to 0} \frac{1}{n} \ln \left| \frac{f^n(x_0 + \varepsilon) - f^n(x_0)}{\varepsilon} \right| = \lim_{n \to \infty} \frac{1}{n} \ln \left| \frac{d f^n(x_0)}{d x_0} \right|. \quad (5)$$

Symbols $f^1, f^2, \ldots, f^n$ stand for subsequent iterations, x_0 and $x_0 + \varepsilon$ are the initial conditions for the two trajectories. The number $\varepsilon > 0$ is very small. With every iteration, the distance between the trajectories increases exponentially. This definition can also be generalized with multi-dimensional systems. The number of exponents has to correspond to the number of dimensions. If the largest exponent of a dynamical system is positive, this indicates a chaotic trajectory, while an exponent equal to zero indicates the bifurcation point, and a negative value means convergence of the trajectory with the constant point of attraction or a periodic attractor.

The basic notion of nonlinear dynamical systems theory is also the notion of an attractor, primarily a chaotic attractor. Let *F* stand for a map of *m*-dimensional space into itself. The compact set *A*, which is situated in the *m*-dimensional space, we call the attractor for *F* if it meets the conditions of invariance, density, stability and attraction. An attractor is a chaotic attractor if it contains a chaotic trajectory [19].

2.3. System classification in nonlinear dynamical systems theory

In order to compare the subjects of conventional science, the theory of deterministic chaos, and the theory of complexity, we can classify systems based on the following criteria: the number of constituents of the system *N* and the average number of links between these elements *K* (see [11, 12, 13]). Depending on the relationship between these parameters, we can distinguish three types of the *NK* systems:

- Type I – subcritical systems. The number of links is very small, given the number of elements. Every element is technically independent from others, thus the behavior of the whole system can be treated as a simple sum of its parts. Because the rule of superposition is met in such a case, systems of this type are approximately linear. Their dominating behavior is striving for states of equilibrium.
- Type II – critical systems. The average number of links is substantially greater than in the subcritical systems. These systems are characterized by more complex dynamics and can reveal emergent properties [7]. Local changes can be dispersed in a system so they usually do not bring about global consequences. These types of systems often balance on the edge of chaos (this is a state when the system's ability to survive is the greatest and its computing power reaches maximum value).
- Type III – supercritical systems. The ratio of the number of links to the number of elements approaches one. It is a state in which almost every

element is interlinked with all the rest. It includes deterministic systems, which are characterized by complex dynamics.

The largest Lyapunov exponent for subcritical systems is negative, for critical systems it oscillates around zero, whereas for supercritical systems it is positive. Classical science deals with systems of type I, the theory of chaos explores systems of type III, whereas the subject of interest for the theory of complexity is type II and the transitions between various types of systems (see [7, 21]).

3. Applications in economics

3.1. The theory of economic transformation

The first step towards elaborating a theory of transformation was taken by American researchers who formulated a model of chaotic hysteresis (see [22, 23]). Two basic nonlinear dynamical systems theory methods were applied concurrently, i.e. elementary catastrophes and deterministic chaos. The starting point is a socialist economy. According to the Marxist convention, the economy was divided into two sectors: consumption-goods and capital-goods. The notion of a technological gap and the cusp catastrophe were used to describe social-economic crises. The attractor in the form of a chaotic hysteresis that appears in a reformed economy is a result of a two-phase activity of a nonlinear accelerator.

The dynamic system is described by a two-dimensional formula:

$$I_t = I_{t-1} + Z_t, \tag{6}$$

$$Z_t = u\left(Z_{t-1} - Z_{t-1}^3\right) - v I_{t-1}, \tag{7}$$

where: I_t – total investment within the period t, Z_t – increase in the investment, whereas symbols u and v means respectively the values of accelerators in the capital-goods sector and in the consumption-goods sector. These formulas cannot be solved analytically, but they can be the subject of numerical explorations.

An analysis of the system (6)–(7) was conducted assuming the constant value of the accelerator in the sector of capital goods $u = 2$, whereas the value of the parameter v was gradually decreased. For $0.01 \leq v \leq 0.1395$ in the phase space of the system there is an investment cycle in the form of a chaotic attractor. Lowering the value of the accelerator of the consumption-goods sector means the metamorphosis of the attractor – eventually for the value of $v = 0.00005$ it takes on the form of chaotic hysteresis. The attractor in this form is featured in Figure 1. In the model, there is a trade-off between complexity (chaos) and instability, understood as the increase of period and amplitude of oscillation of investment [6].

The next element of the theory is the technological gap (G), which stems from the higher rate of capital-intensive nature of production in socialism compared to a capitalist economy. Paradoxically, this phenomenon is a result of pursuing the postulates of stability of production and full employment, which were to make socialism a system more bearable for people than capitalism with its chronic unemployment and crises.
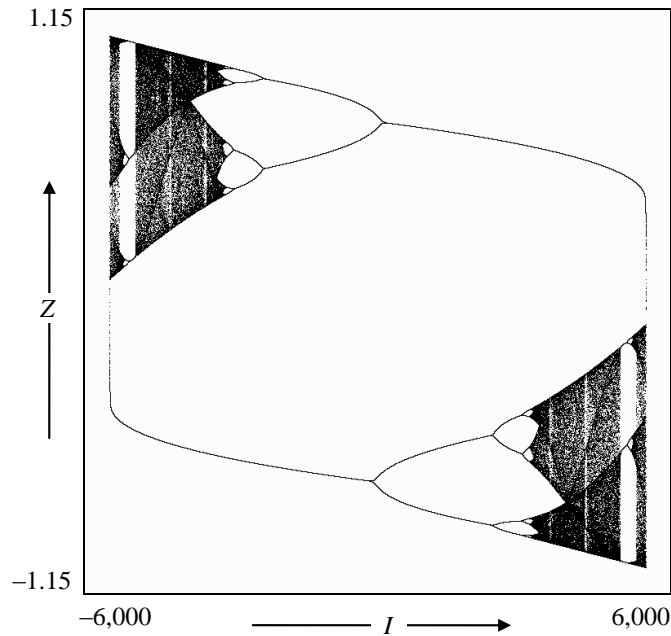
Figure 1. The chaotic attractor in the form of chaotic hysteresis for
$u = 2$, $v = 0.00005$

Another step is to introduce the cusp catastrophe, whose space area of equilibrium meets condition (4). In the theory under investigation, the variable of this state is the probability of an introduction of market reforms $x = P(s)$, the bifurcation parameter is the dimensions of the technological gap $c_1 = G$, whereas the asymmetric parameter is the rate of growth of investment $c_2 = Z/I$. In the Figure 2 there is a geometrical interpretation of the morphogenetic model of transformation.

The space of the catastrophe equilibrium describes various scenarios of economic crises and the corresponding reforms that sought to answer them. For $G = 0$ we have an example market economy. The occurrence of the technological gap, which happens after passing through the beginning of catastrophe, causes a division of the equilibrium space into two layers – an upper and lower. They suggest the occurrence of nonlinear changes in the probability of transformation, whenever the rate of investment growth reaches a necessary value. Sudden leaps take place when the asymmetric factor crosses the bifurcation set of the catastrophe located in the parameter space marked by the following formula:
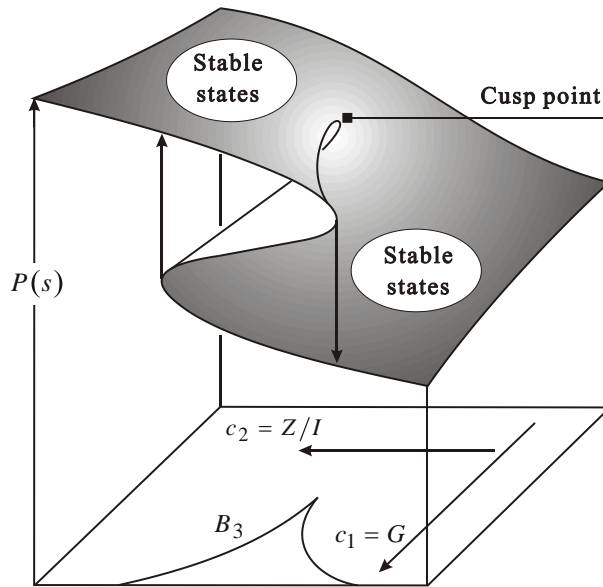
Figure 2. Geometrical interpretation of a morphogenetic transformation model

$$B_3 = \left[(c_1, c_2) : 4c_1^3 + 27c_2^2 = 0 \right]. \tag{8}$$

Numerical explorations of model (6)–(7) have shed new light on a certain macroeconomic problem which has been neglected by mainstream economics regarding the macroeconomic costs of the reform complexity. An intuitive understanding of this category of costs is known from the theory of the corporation [18]. The global financial crisis prompted a wider look at the complexity of economic processes and the accompanying problems [1]. An economy under transformation is vulnerable to falling victim to trade-offs between complexity and instability, which accounts for the fact that benefits stemming from reforms can, over a long period of time, consolidate below the costs of complexity. It is a new, quality-based position in the balance of transformation. Future research should focus on methods of its measurement. In addition, it constitutes a challenge to economic policy, which should seek to simplify economic life.

3.2. The rule of progressive complexity

Mathematical studies of standard nonlinear economic models have revealed an interesting regularity, which I called "the rule of progressive complexity" [9]. It appears that there are two active forces in economic systems. The first force is short term in nature, and its source stems from rational, typical endeavors of

business entities. One of the manifestations of this activity is profit maximization by producers and maximization of utility by consumers. As a result, these systems seek a state of short-term equilibrium. The second force is active over a long period of time and even though its source is identical to the first one, the effects are totally different. It destabilizes the short-term states of equilibrium and pushes market structures towards a state known as "the edge of chaos". It is a transition field between a periodic behavior and chaotic behavior, where the computing power of systems, which means their ability to collect and process information, reaches its maximum. The complexity of a system, which can been measured by Lapunov exponents, increases in this field.

Let us consider a duopoly model using the following equations:

$$x_{t+1} = \sqrt{\frac{y_t}{a}} - y_t, \tag{9}$$

$$y_{t+1} = \sqrt{\frac{x_t}{b}} - x_t, \tag{10}$$

where: x – the production output of the first entrepreneur, y – the production output of the second entrepreneur, whereas a and b stand for their marginal costs, respectively. In the static version, these equations set the reaction functions. Each of them describes the choice of the production output made by an entrepreneur assuming that the production output of their competitor is known. The collision of these two functions takes place at the point known as the Cournot-Nash equilibrium point.

The standard analysis of the model's stability allows us to set two critical values of the marginal costs ratio:

$$\frac{a}{b} \vee \frac{b}{a} = 3 \pm 2\sqrt{2} \ . \tag{11}$$

This is where the analytical methods give up. We do not know what happens to this model when the stability threshold is crossed, or how it behaves over a long period.

It is best to start numerical explorations of a duopoly (9)–(10) with making a period plot [19]. This is a two-dimensional space of parameters in which various behavior of the system has been specified (with emphasis on periodic behavior). In order to do this, one should define the interval of changeability of both parameters and the initial condition of the trajectory bundle. A plot of this type allows us to follow the dynamics of the system depending on a simultaneous change in two control parameters.

Numerical explorations of parameter space reveal the following types of behavior: states of short-term equilibrium, periodic dynamics, chaos and divergent trajectories (see Figure 3). Pairs of parameters responsible for states of stable equilibrium account for 82.77% of the parameter space, whereas pairs of

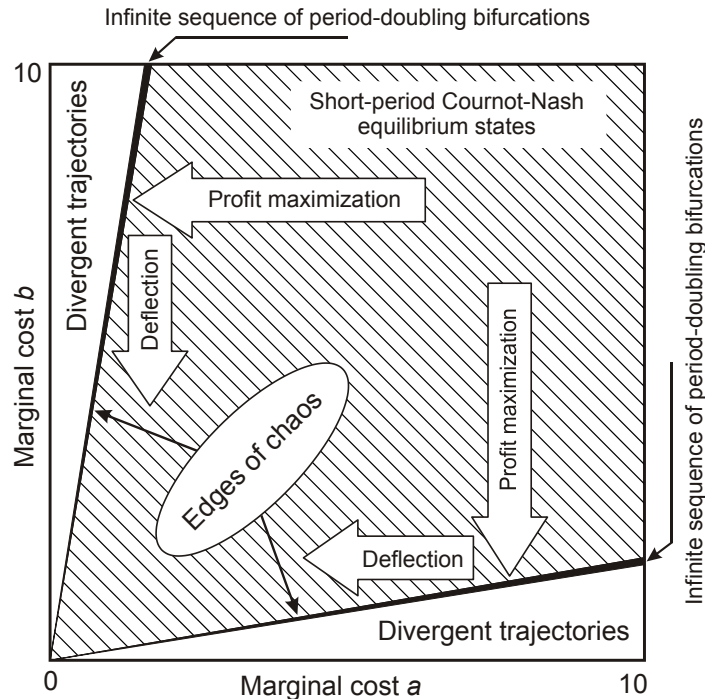Infinite sequence of period-doubling bifurcations

Fig. 3. Dynamics of the Cournot-Puu duopoly in the parameter space

chaotic parameters account for mere 0.15% of this space. Consequently, it seems that stability predominates and the claims of conventional economics have been confirmed. However, it is a false conclusion. Entrepreneurs are interested not only in maximizing profit over a short time, but also in the long run. Maximizing profit in the long run requires introducing technical-organizational progress and it results in lowering marginal costs. Consequently, every producer strives for one of the two edges of chaos (11), i.e. states with growing complexity [9].

The system displays a certain type of globally rational behavior which contributes to its survival. As of the moment the efficient producer achieves the edge of chaos, his long-term profit decreases, and the long-term profit of the inefficient producer begins to grow [17]. This leads to role reversal, and in the diagram, the market bounces off the edge of chaos.

4. Conclusions

Catastrophe means a violent, sudden transition of the tested system into a new state. What is important here is the rapidity of the changes in the behavior of an object as compared with the mean change in the past. Catastrophe theory merges two apparently contradictory and unrelated kinds of phenomena descriptions to form one coherent notion system: evolutionism and revolutionism, continuity and discontinuity. In economics, the application of catastrophe theory is of great

cognitive importance, particularly in issues of explanation and forecasting in economics.

In transitional economies, there is a trade-off between complexity and instability. In the economic calculation of transformations, a new type of cost needs to be considered – the social costs connected with the change of the dynamic complexity of the systems. Numerical explorations of an archetypal duopoly model have proven that states of equilibrium are stable only for a short period. In the long run, such systems strive for the edge of chaos.

References

1. J. C. Bogle. Dość. *Prawdziwe miary bogactwa, biznesu i życia*, PTE, Warszawa, 2009.

2. J. R. Hicks. *A Contribution to the Theory of the Trade Cycle*, Clarendon Press, Oxford, 1951.

3. C. H. Hommes. Economic dynamics. In: Scott AC (ed) *Encyclopedia of Nonlinear Science*. Routledge, New York, pp. 245–248, 2005.

4. C. H. Hommes. Heterogeneous agent models in economics and finance. In: Tesfatsion L, Judd KL (eds) *Handbook of Computational Economics*, vol. 2: *Agent-Based Computational Economics*. North-Holland, Amsterdam, pp. 1109–1186, 2006.

5. A. Jakimowicz. *Od Keynesa do teorii chaosu. Ewolucja teorii wahań koniunkturalnych*, Wydawnictwo Naukowe PWN, Seria: „Współczesna Ekonomia", Warszawa, 2005.

6. A. Jakimowicz. Interdisciplinary Matrix in Economics: Two Applications to the Transition from Socialism to Capitalism, *Nonlinear Dynamics, Psychology, and Life Sciences*, vol. 13, no. 4, 393–421, 2009a.

7. A. Jakimowicz. O niektórych implikacjach nieliniowości w keynesizmie, *Ekonomista*, no. 1, 15–48, 2009b.

8. A. Jakimowicz. Catastrophes and Chaos in Business Cycle Theory, *Acta Physica Polonica A*, vol. 117, no. 4, 333–339, 2010a.

9. A. Jakimowicz. *Źródła niestabilności struktur rynkowych*, Wydawnictwo Naukowe PWN, Seria „Współczesna Ekonomia", Warszawa, 2010b.

10. M. Kalecki. Zarys teorii wzrostu gospodarki socjalistycznej. In: Kalecki M, *Dzieła*, vol. 4: *Socjalizm. Wzrost gospodarczy i efektywność inwestycji*. PWE, Warszawa, pp. 17–124, 1984.

11. S. A. Kauffman. *The Origins of Order: Self-Organization and Selection in Evolution*, Oxford University Press, New York, 1993.

12. S. A. Kauffman and S. Levin. Towards a General Theory of Adaptive Walks on Rugged Landscapes, *Journal of Theoretical Biology*, vol. 128, no. 1, 11–45, 1987.

13. H. Kaul and S. H. Jacobson. Global Optima Results for the Kauffman NK Model, *Mathematical Programming*, vol. 106, no. 2, 319–338, 2006.

14. J. M. Keynes. *Ogólna teoria zatrudnienia, procentu i pieniądza*, PWN, Warszawa, 1985.

15. O. Lange. Prawa ekonomiczne. In: O. Lange, *Dzieła*, vol. 3: *Ekonomia polityczna*. PWE, Warszawa, pp. 260–304, 1975.

16. E. N. Lorenz. *The Essence of Chaos*, UCL Press, London, 1995.

17. A. Matsumoto. Controlling the Cournot-Nash Chaos, *Journal of Optimization Theory and Applications*, vol. 128, no. 2, 379–392, 2006.

18. A. Noga. *Teorie przedsiębiorstw*, PWE, Warszawa, 2009.

19. H. E. Nusse and J. A. Yorke. *Dynamika. Badania numeryczne*, Wydawnictwo Naukowe PWN, Warszawa, 1998.

20. V. I. Oseledec. Мультипликативная эргодическаяа теорема. Характеристичес-кие показатели Ляпунова динамических систем, *Труды Московского Математического Общества*, vol. 19, 179–210, 1968.

21. M. Pigliucci. Chaos and Complexity. Should We Be Skeptical?, *Skeptic*, vol. 8, no. 3, 62–70, 2000.

22. J. B. Rosser and M. V. Rosser. Discrete Dynamics in Transitional Economies, *Discrete Dynamics in Nature and Society*, vol. 1, 269–281, 1998.

23. J. B. Rosser, M. V. Rosser, S. J. Guastello and R. W. Bond. Chaotic Hysteresis and Systemic Economic Transformation: Soviet Investment Patterns, *Nonlinear Dynamics, Psychology, and Life Sciences*, vol. 5, no. 4, 345–368, 2001.

24. T. J. Sargent. *Bounded Rationality in Macroeconomics*, Clarendon Press, Oxford, 1993.

25. R. Thom. *Structural Stability and Morphogenesis. An Outline of a General Theory of Models*, Benjamin, London, 1975.

26. D. Trotman and E. C. Zeeman. Klasyfikacja elementarnych katastrof kowymiaru ≤ 5. In: Cieślak M, Smoluk A (eds) *Zbiory rozmyte. Rozpoznawanie obrazów. Teoria katastrof. Wybór tekstów*. PWN, Warszawa, pp. 123–194, 1988.

27. H. R. Varian. *Mikroekonomia. Kurs średni. Ujęcie nowoczesne*, Wydawnictwo Naukowe PWN, Warszawa, 1995.

28. E. C. Zeeman. *Catastrophe Theory: Selected Papers, 1972–1977*, Addison-Wesley, London, 1977.

Some aspects of stochastic calculus and approximation in chaotic systems analysis

Gabriel V. Orman[1]

Department of Mathematics and Computer Science, "Transilvania" University of
Braşov, 500091 Braşov, Romania.
(E-mail: `ogabriel@unitbv.ro`)

Abstract. Frequently when we refer to *chaos* and *chaotic and complex systems* to
describe the comportment of some natural phenomena, in fact we consider phenomena
of the type of a *Brownian motion* which is a more realistic model of such phenomena.
Thus one can talk about a passing *from chaotic and complex systems to Brownian
motion*. Some aspects regardind the Brownian motion and its Markovian nature will
be developed, in short, in this paper; we try also to emphasize their impact for some
practical problems.
Keywords: stochastic differential equations, stochastic calculus, Markov processes,
Brownian motion..

1 Introduction

It is known that a chaotic perpetual motion of a Brownian particle is the result
of the collisions of particle with the molecules of the fluid in which there is.

But this particle is much bigger and also heavier than the molecules of the
fluid which it collide, and then each collision has a negligible effect, while the
superposition of many small interactions will produce an observable effect.

On the other hand, for a Brownian particle such molecular collisions ap-
pear in a very rapid succession, their number being enormous. For a so high
frequency, evidently, the small changes in the particle's path, caused by each
single impact, are too fine to be observable. For this reason the exact path of
the particle can be described only by statistical methods.

We emphasize that L. Bachélier derived the law governing the position of
a single grain performing a 1-dimensional Brownian motion starting at $a \in R$
at time $t = 0$; and A. Einstein also derived the same law from statistical
mechanical considerations and applied it to the determination of molecular
diameters.

Also Paul Lévy found a construction of the Brownian motion and given
a profound description of the fine structure of the individual Brownian path.
D. Ray obtained some results in the case when the motion is *strict Markov*;

and W. Feller obtained that the generator of a strict Markovian motion with continuous paths (diffusion) can be expressed as a *differential operator*.

And in the last time we can speak about Markov processes from Kiyosi Itô's perspective (according to D.W. Stroock). The usual class of Markov processes which we consider has many times some restrictions which do not cover many interesting processes. This is the reason for which we try often to obtain some extensions of this notion.

Researches in this direction are due especially to K. Itô and in this context we shall refer below, in short, to some of them.

2   On Markov processes - an extended definition

We start with the concept of a random variable which encodes an experimental outcome as a number, or a vector of real numbers in the multidimensional case. When a random variable has a multidimensional state space, we emphasize that fact by calling it a *random space*.

Let (E, ξ) be a measurable space and $X : (\Omega, \mathcal{K}, P) \to (E, \xi)$ a random variable (i.e. a measurable map).

The image μ of P under X is a probability measure on (E, ξ) called the *law of X* and denoted by $\mathcal{L}(X)$. The events $\{\omega \,|\, X(\omega) \in A\}$ for $A \in \xi$ form a sub-σ-field of $\mathcal{K}$ called the σ-field *generated* by X and denoted by $\sigma(X)$.

More general, given a family X_α, $\alpha \in I$, of random variables on $(\Omega, \mathcal{K}, P)$ taking values in measurable spaces (E_α, ξ_α), $\alpha \in I$, respectively, the σ-field generated by X_α, $\alpha \in I$, denoted by $\sigma(X_\alpha, \alpha \in I)$, is the smallest sub-$\sigma$-field with respect to which they are all measurable.

They may be situations where it is preferable to view $\{X_\alpha, \alpha \in I\}$ as a single random variable taking values in the product space $\prod E_\alpha$ endowed with the product σ-field $\prod \xi_\alpha$.

If so, this definition reduces to the following:

Definition 21 *Let $(\Omega, \mathcal{K}, P)$ be a probability space and let us denote by E a subset of R^n. A "random variable" X is a function from Ω into E.*

E is referred to as the *state space* of the random variable.

Suppose we have n random variables $X_1(\omega), \cdots, X_n(\omega)$ defined on a probability space.

The random variables $X_1, \cdots, X_n$ are said to be *independent* if the fields (σ-fields) $\mathcal{K}_{X_1}, \cdots, \mathcal{K}_{X_n}$ generated by them are independent.

Definition 22 *A "stochastic process" is a family of real random variables*

$$\{X_t\}_{t \in T}$$

defined on a probability space $(\Omega, \mathcal{K}, P)$, indexed with a time parameter t and assuming values in R^n.

The parameter space T may be the halfline $[0, +\infty)$, or it may also be an interval $[a, b]$, or the non-negative integers and even subsets of R^n, for $n \geq 1$.

Now, for each $t \in T$ fixed, we have a random variable $\omega \to X_t(\omega)$, $\omega \in \Omega$. A stochastic process will be denoted by $X(t)$.

Now let S be a *state space* and consider a particle which moves in S. Also, suppose that the particle starting at x at the present moment will move into the set $A \subset S$ with probability $p_t(x, A)$ after t units of time, "irrespectively of its past motion", that is to say, this motion is considered to have a *Markovian character*.

The *transition probabilities* of this motion are $\{p_t(x, A)\}_{t,x,A}$ and we considered that the time parameter $t \in T = [0, +\infty)$.

The state space S is assumed to be a *compact Hausdorff space with a countable open base*. The σ-field generated by the open sets (the topological σ-field on S) is denoted by $K(S)$. Therefore, a *Borel set A* is a set in $K(S)$ (i.e. $A \in K(S)$).

The *mean value*

$$m = M(\mu) = \int_R x \, \mu(dx)$$

is used for the center and the scattering degree of a one-dimensional probability measure μ having the second order moment finite, and the *variance* of μ is defined by

$$\sigma^2 = \sigma^2(\mu) = \int_R (x - m)^2 \mu(dx).$$

On the other hand, from the Tchebychev's inequality, for any $t > 0$, we have

$$\mu(m - t\sigma, m + t\sigma) \leq \frac{1}{t^2},$$

so that several properties of 1-dimensional probability measures can be derived.

Remark 1. In the case when the considered probability measure has no finite second order moment, σ becomes useless. In such a case one can introduce the central value and the dispersion that will play similar roles as m and σ for general 1-dimensional probability measures.

The *dispersion δ* is defined as follows

$$\delta = \delta(\mu) = -\log \int \int_{R^2} e^{-|x-y|} \mu(dx)\mu(dy).$$

Furthermore it is assumed that the following conditions are satisfied by the transition probabilities $\{p_t(x, A)\}_{t \in T, x \in S, A \in K(S)}$:

1 for t and A fixed,
    a) the transition probabilities are Borel measurable in x;
    b) $p_t(x, A)$ is a probability measure in A;
2 $p_0(x, A) = \delta_x(A)$ (i.e. the δ-measure concentrated at x);
3 $p_t(x, \cdot) \xrightarrow{\text{weak}} p_t(x_0, \cdot)$ as $x \to x_0$ for any t fixed, that is

$$\lim_{x \to x_0} \int f(y) p_t(x, dy) = \int f(y) p_t(x_0, dy)$$

for all continuous functions f on S;

4 $p_t(x, U(x)) \longrightarrow 1$ as $t \searrow 0$,   for any neighborhood $U(x)$ of x;
5 the Chapman-Kolmogorov equation holds:

$$p_{s+t}(x, A) = \int_S p_t(x, dy) p_s(y, A).$$

Remark 2. The "transition operators" can be defined in a similar manner. Consider $C = C(S)$ to be the space of all continuous functions (it is a separable Banach space with the supremum norm).

The operators p_t, defined by

$$(p_t f)(x) = \int_S p_t(x, dy) f(y), \quad f \in C$$

are called "transition operators".

Remark 3. Let us consider $R \cup \{\infty\}$ as the one-point compactification of R. Then it can be observed that the conditions $(1) - (5)$ above are satisfied for the "Brownian transition probabilities". One can define

$$p_t(x, dy) = \tfrac{1}{t\sqrt{2\pi}} e^{-\frac{(y-x)^2}{2t^2}} dy \quad \text{in } R$$
$$p_t(\infty, A) = \delta_\infty A.$$

We can give now the definition of a Markov process as follows:

Definition 23 *A "Markov process" is a system of stochastic processes*

$$\{X_t(\omega), t \in T, \omega \in (\Omega, K, P_a)\}_{a \in S},$$

that is for each $a \in S$, $\{X_t\}_{t \in S}$ is a stochastic process defined on the probability space (Ω, K, P_a).

It can be observed that a definition as it is given above not correspond to many processes that are of a real interest so that it is useful to obtain an extension of this notion. An extended notion has been proposed by K. Itô and it is given below.

Let E be a separable Banach space with real coefficients and norm $||\cdot||$ and let also $L(E, E)$ be the space of all bounded linear operators $E \longrightarrow E$. It can be observed that $L(E, E)$ is a linear space.

Definition 24 *The collection of stochastic processes*

$$X = \{X_t(\omega) \equiv \omega(t) \in S, \, t \in T, \, \omega \in (\Omega, K, P_a)\}_{a \in S}$$

is called a "Markov process" if the following conditions are satisfied:

1) *the "state space" S is a complete separable metric space and $K(S)$ is a topological σ-algebra on S;*
2) *the "time internal" $T = [0, \infty)$;*
3) *the "space of paths" Ω is the space of all right continuous functions $T \longrightarrow S$ and K is the σ-algebra $K[X_t : t \in T]$ on Ω;*

4) *the probability law of the path starting at a, $P_a(H)$, is a probability measure on (Ω, K) for every $a \in S$ which satisfy the following conditions:*

4a) $P_a(H)$ is $K(S)$-measurable in a for every $H \in K$;

4b) $P_a(X_0 = a) = 1$;

4c) $P_a(X_{t_1} \in E_1, \cdots, X_{t_n} \in E_n) =$

$$\int \cdots \int_{a_i \in E_i} P_a(X_{t_1} \in da_1) P_{a_1}(X_{t_2 - t_1} \in da_2) \ldots$$
$$\ldots P_{a_{n-1}}(X_{t_n - t_{n-1}} \in da_n) \qquad for \quad 0 < t_1 < t_2 < \ldots < t_n.$$

Remark 4. Evidently there are some differences between this definition and Definition 23 of a Markov process. Thus

   i.   The space S is not necessary to be compact;

  ii.   it is not assumed the existence of the left limits of the path;

 iii.   the transition operator $f \longrightarrow G_t f(\cdot) = E$.

    $(f(X_t))$ do not necessarily carry $C(S)$ into $C(S)$ ($C(S)$ being the space of all real-valued bounded continuous functions on S).

3   The Markovian nature of the Brownian path

As we already emphasized the Brownian motion, used especially in Physics, is of ever increasing importance not only in Probability theory but also in classical Analysis. Its fascinating properties and its far-reaching extension of the simplest normal limit theorems to functional limit distributions acted, and continue to act, as a catalyst in random analysis.

It is probable the most important stochastic process.

As some authors remarks too, the Brownian motion reflects a perfection that seems closer to a law of nature than to a human invention.

In 1828 the English botanist Robert Brown observed that pollen grauns suspended in water perform a continual swarming motion. The chaotic motion of such a particle is called *Brownian motion* and a particle performing such a motion is called a *Brownian particle.*

He was not the first to mention this phenomenon and had many predecessors, starting with Leeuwenhoek in the 17th century.

However, Brown's investigation brought it to the attention of the scientific community, hence *Brownian.*

Brownian motion was frequently explained as due to the fact that particles were alive. Poincaré thought that it contradicted the second law of Thermodynamics.

Today we know that this motion is due to the bombardament of the particles by the molecules of the medium. In a liquid, under normal conditions, the order of magnitude of the number of these impacts is of 1020 per second.

It is only in 1905 that kinetic molecular theory led Einstein to the first mathematical model of Brownian motion. He began by deriving its possible existence and then only learned that it had been observed.

Let us imagine a chaotic motion of a particle of colloidal size immersed in a fluid. As we already emphasized such a chaotic motion of a particle is

called, usually, *Brownian motion* and the particle which performs such a motion is referred to as a *Brownian particle*. Such a chaotic perpetual motion of a Brownian particle is the result of the collisions of particle with the molecules of the fluid in which there is.

But this particle is much bigger and also heavier than the molecules of the fluid which it collide, and then each collision has a negligible effect, while the superposition of many small interactions will produce an observable effect.

On the other hand, for a Brownian particle such molecular collisions appear in a very rapid succession, their number being enormous. For a so high frequency, evidently, the small changes in the particle's path, caused by each single impact, are too fine to be observable. For this reason the exact path of the particle can be described only by statistical methods.

Thus, the influence of the fluid on the motion of a Brownian particle can be described by the combination of two forces in the following way.

1. The considered particle is much larger than the particle of the fluid so that the cumulated effect of the interaction between the Brownian particle and the fluid may be taken as having a hydrodynamical character. Thus, the first of the forces acting on the Brownian particle may be considered to be the forces of *dynamical friction*. It is known that the frictional force exerted by the fluid on a small sphere immersed in it is determined from the Stockes's law: *the drag force per unit mass acting on a spherical particle of radius a is given by* $-\beta\mathbf{v}$, *with* $\beta = \dfrac{6\pi a \eta}{m}$, where m is the mass of the particle, η is the coefficient of dynamical viscosity of the fluid, and $\mathbf{v}$ is the velocity of particle.

2. The other force acting on the Brownian particle is caused by the individual collisions with the particles of the fluid in which there is. This force produces instantaneous changes in the acceleration of the particle. Furthermore, this force is *random both in direction and in magnitude*, and one can say that it is a *fluctuating force*. It will be denoted by $\mathbf{f(t)}$. For $\mathbf{f(t)}$ the following assumptions are made:

   i The function $\mathbf{f(t)}$ is statistically independent of $\mathbf{v}(t)$.

   ii $\mathbf{f(t)}$ has variations much more frequent than the variations in $\mathbf{v}(t)$.

   iii $\mathbf{f(t)}$ has the average equal to zero.

A completely different origin of mathematical Brownian motion is a game theoretic model for fluctuations of stock prices due to L. Bachélier from 1900.

In his doctoral thesis L. Bachélier hinted that it could apply to physical Brownian motion.

Therein, and in his subsequent works, he used the heat equation and, proceeding by analogy with *heat propagation* he found, albeit formally, distributions of various functionals of mathematical Brownian motion.

Heat equations and related parabolic type equations have been used rigorously by Kolmogorov, Petrovsky, Khintchine.

Bachélier, L. *Théorie de la spéculation.* Ann. Sci. École Norm. Sup., 17, 1900, 21-86.

L. Bachélier derived the law governing the position of a single grain performing a 1-dimensional Brownian motion starting at $a \in \mathbf{R^1}$ at time $t = 0$:

$$P_a[x(t) \in db] = g(t, a, b)db \qquad (t, a, b) \in (0, +\infty) \times \mathbf{R^2}, \qquad (1)$$

where g is the source (Green) function

$$g(t, a, b) = \frac{e^{-\frac{(b-a)^2}{2t}}}{\sqrt{2\pi t}} \qquad (2)$$

of the problem of heat flow:

$$\frac{\partial u}{\partial t} = \frac{1}{2} \frac{\partial^2 u}{\partial a^2} \qquad (t > 0). \qquad (3)$$

Bachélier also pointed out the Markovian nature of the Brownian path expressed in

$$P_a[a_1 \leq x(t_1) < b_1, \, a_2 \leq x(t_2) < b_2, \, \cdots, \, a_n \leq x(t_n) < b_n] =$$

$$= \int_{a_1}^{b_1} \int_{a_2}^{b_2} \cdots \int_{a_n}^{b_n} g(t_1, \, a, \, \xi_1) \, g(t_2 - t_1, \xi_1, \xi_2) \cdots$$

$$\cdots g(t_n - t_{n-1}, \, \xi_{n-1}, \, \xi_n) \, d\xi_1 \, d\xi_2 \cdots d\xi_n, \quad 0 < t_1 < t_2 < \cdots t_n \qquad (4)$$

and used it to establish the law of maximum displacement

$$P_0 \left[\max_{s \leq t} x(s) \leq b \right] = 2 \int_0^b \frac{e^{-\frac{a^2}{2t}}}{\sqrt{2\pi t}} \, da \qquad t > 0, \, b \geq 0. \qquad (5)$$

It is very interesting that A. Einstein, in 1905, also derived (1) from statistical mechanical considerations and applied it to the determination of molecular diameters.

We emphasize again that a rigorous definition and study of Brownian motion requires measure theory.

But as soon as the ideas of Borel, Lebesgue and Daniell appeared, it was possible to put the Brownian motion on a firm mathematical foundation and this was achived in 1923 by N. Wiener.

Consider the space of *continuous* path $w : t \in [0, +\infty) \to R$ with coordinates $x(t) = w(t)$ and let $\mathbf{B}$ be the smallest Borel algebra of subsets B of this path space which includes all the simple events $B = (w : a \leq x(t) < b), \, (t \geq 0, \, a < b)$. Wiener established the existence of nonnegative Borel measures $P_a(B), \, (a \in R, \, B \in \mathbf{B})$ for which (4) holds. Among other things, this result attaches a precise meaning to Bachélier's statement that *the Brownian path is continuous.*

As we already emphasized at the beginning, Paul Lévy found another construction of the Brownian motion and gives a profound description of the fine structure of the individual Brownian path.

The standard Brownian motion can be now defined.

A. Einstein, *Investigations on the theory of the Brownian movement*, New York, 1956.
N. Wiener, *Differential space.* J. Math. Phys. 2, 1923, 131-174.

Definition 31 *A continuous-time stochastic process $\{B_t \mid 0 \le t \le T\}$ is called a "standard Brownian motion" on $[0, T)$ if it has the following four properties:*

 i *$B_0 = 0$.*
 ii *The increments of B_t are independent; that is, for any finite set of times $0 \le t_1 < t_2 < \cdots < t_n < T$, the random variables*

$$B_{t_2} - B_{t_1}, \, B_{t_3} - B_{t_2}, \, \cdots, B_{t_n} - B_{t_{n-1}}$$

 are independent.
 iii *For any $0 \le s \le t < T$ the increment $B_t - B_s$ has the normal distribution with mean 0 and variance $t - s$.*
 iv *For all ω in a set of probability one, $B_t(\omega)$ is a continuous function of t.*

The Brownian motion can be represented as a random sum of integrals of orthogonal functions. Such a representation satisfies the theoretician's need to prove the existence of a process with the four defining properties of Brownian motion, but it also serves more concrete demands. Especially, the series representation can be used to derive almost all of the most important analytical properties of Brownian motion. It can also give a powerful numerical method for generating the Brownian motion paths that are required in computer simulation.

Remark 5. Let us consider $R \cup \{\infty\}$. Then one can define

$$p_t(x, dy) = \frac{1}{t\sqrt{2\pi}} e^{-\frac{(y-x)^2}{2t^2}} \, dy \quad \text{in } R$$
$$p_t(\infty, A) = \delta_\infty A.$$

Let us observe that the conditions 1b) and 2-5 assumed on the transition probabilities $\{p_t(x, A)\}_{t \in T, x \in S, A \in K(S)}$, given in Section 2, are satisfied in this case for "Brownian transition probabilities" where $R \cup \{\infty\}$ is considered as the one-point compactification of R.

Finally we shall give an interesting result regarding to a 3-dimensional Brownian motion.

Let X be a Markov process in a generalized sense as it is given in Definition 24. Let us denote by $\mathbf{B}(S)$ the space of all bounded real $K(S)$-measurable functions and let us consider a function $f \in \mathbf{B}(S)$.

It is supposed that

$$E_a \left(\int_0^\infty |f(X_t)| dt \right) \tag{6}$$

is bounded in a. Then, the following

$$U f(a) = E_a \left(\int_0^\infty f(X_t) dt \right) \tag{7}$$

is well-defined and is a bounded $K(S)$-measurable function of $a \in S$.

The Uf is called *the potential* of f with respect to X. Having in view that $Uf = \lim_{\alpha \downarrow 0} R_\alpha f$, it is reasonable to write R_0 instead of U. Based on this fact, $R_\alpha f$ will be called *the potential of order α* of f.

Remark 6. It is useful to retain that $R_\alpha f \in \mathbf{B}(S)$ for $\alpha > 0$; and generally $f \in \mathbf{B}(S)$ while $R_0 f (= Uf) \in \mathbf{B}(S)$ under the condition (6).

Now the name *potential* is justified by the following theorem on *the 3-dimensional Brownian motion*

Theorem 31 *(K. Itô). Let X be the 3-dimensional Brownian motion. If $f \in$ $\mathbf{B}(S)$ has compact support, then f satisfies (6) and*

$$Uf(a) = \frac{1}{2\pi} \int\limits_{R^3} \frac{f(b) db}{|b - a|} = \frac{1}{2\pi} \times Newtonian \; potential \; of \; t. \qquad (8)$$

Remark 7. Many other details, proofs and related problems can be found in [1], [2], [3], [4], [14], [6], [13], [12], [9].

Conclusion 31 *The Brownian motion can be represented as a random sum of integrals of orthogonal functions. Such a representation satisfies the theoretician's need to prove the existence of a process with the four defining properties of Brownian motion, but it also serves more concrete demands, one of the most important being the "chaotic and complex systems analysis".*

Especially, the series representation can be used to derive almost all of the most important analytical properties of Brownian motion.

It can also give a powerful numerical method for generating the Brownian motion paths that are required in computer simulation.

At the same time, as we have said at the beginning, we think that when, in various problems, we say "chaos" or "chaotic and complex systems" or we use another similar expression to define the comportment of some natural phenomena, in fact we imagine phenomena similarly to a Brownian motion which is a more realistic model of such phenomena. And this opinion lie at the basis of this paper.

References

1. A. T. Bharucha-Reid. Elements of the Theory of Markov Processes and Their Applications. Mineola, New York, Dover Publications, Inc., 1997.
2. K. Itô, *Selected Papers*, Springer, 1987.
3. K. Itô and H. P. McKean Jr. Diffusion Processes and their Sample Paths. Berlin Heidelberg, 1996, Springer-Verlag.
4. K. Itô. Stochastic Processes. Ole E. Barndorff-Nielsen, Ken-iti Sato, editors. Springer-Verlag, Berlin Heidelberg, 2004.
5. B. Øksendal. Stochastic Differential Equations: An Introduction with Applications. Sixth Edition, New York, 2003, Springer, Berlin-Heidelberg.
6. P. Olofsson, and M. Andersson. Probability, Statistics and Stochastic Processes, 2nd Edition. John Wiley & Sons, Inc., Publication, 2012.

7. G. V. Orman. Lectures on *Stochastic Approximation Algorithms. Theory and Applications*. Preprint, Univ. "Gerhard Mercator", Duisburg, 2001.
8. G. V. Orman. Handbook of Limit Theorems and Sochastic Approximation. Transilvania University Press, Brasov, 2003.
9. G. V. Orman. *On Markov Processes: A Survey of the Transition Probabilities and Markov Property*. In Christos H. Skiadas and Ioannis Dimotikalis, editors, Chaotic Systems: Theory and Applications. World Scientific Publishing Co Pte Ltd, 2010, 224-232.
10. G. V. Orman. *On a problem of approximation of Markov chains by a solution of a stochastic differential equation*. In Christos H. Skiadas, Ioannis Dimotikalis and Charilaos Skiadas, editors, Chaos Theory: Modeling, Simulation and Applications. World Scientific Publishing Co Pte Ltd, 2011, 30-40.
11. G. V. Orman and I. Radomir. *New Aspects in Approximation of a Markov Chain by a Solution of a Stochastic Differential Equation*. Chaotic Modeling and Simulation (CMSIM) International Journal, 2012, pp. 711-718.
12. G. V. Orman. Aspects of convergence and approximation in random systems analysis. LAP Lambert Academic Publishing, Germany, 2012.
13. Z. Schuss. Theory and Application of Stochastic Differential Equations. John Wiley & Sons, New York, 1980.
14. D. W. Stroock. *Markov Processes from K. Itô Perspective*. Princeton Univ. Press, Princeton, 2003.